Progenitor Stars of Hydrogen- and Helium-Deficient Astrophysical Transients

Dissertation
zur
Erlangung des Doktorgrades (Dr. rer. nat.)
der
Mathematisch-Naturwissenschaftlichen Fakultät
der
Rheinischen Friedrich-Wilhelms-Universität Bonn

von
David Ramon Aguilera Dena
aus
Mexiko-Stadt, Mexiko

Bonn, 30.09.2020

Dieser Forschungsbericht wurde als Dissertation von der Mathematisch-Naturwissenschaftlichen Fakultät der Universität Bonn angenommen und ist auf dem Hochschulschriftenserver der ULB Bonn `http://hss.ulb.uni-bonn.de/diss_online` elektronisch publiziert.

1. Gutachter: Prof. Dr. Norbert Langer
2. Gutachter: Prof. Dr. Cristiano Porciani

Tag der Promotion:
Erscheinungsjahr:

Als das Kind Kind war,
war es die Zeit der folgenden Fragen:
Warum bin ich ich und warum nicht du?
Warum bin ich hier und warum nicht dort?
Wann begann die Zeit und wo endet der Raum?
Ist das Leben unter der Sonne nicht bloss ein Traum?
— *Lied Vom Kindsein*, Peter Handke

Abstract

Massive stars are among the most influential components of the Universe. They house nuclear reactions that transmute hydrogen and helium, the two elements produced with the highest abundance after the Big Bang, into heavier elements. They enrich their host galaxies with them, and output a significant amount of energy through radiation and stellar winds.

Massive stars end their lives with the collapse of their iron cores, which can lead to energetic transient events such as supernovae (SNe) and gamma-ray bursts (GRBs). These explosions release large amounts of matter and energy into their environment in short time scale. Core-collapse in massive stars is also responsible for the formation of objects such as black holes (BHs) and neutron stars (NSs), often observed as radio and X-ray sources, and more recently as sources of gravitational waves.

There are many uncertainties massive stellar evolution. In particular, uncertainties in the effects of rotation, metallicity and mass loss in stellar evolution remain, and permeate our understanding about the formation of energetic transients. In this thesis, we explore certain channels of massive star evolution, and propose them as possible formation channels for the formation of hydrogen- and helium-deficient transients.

First, we present evolutionary models of fast-rotating, low metallicity, massive stars, focusing on their late evolution. The combination of low metallicity and fast rotation induces strong mixing in the stellar interior, leading to chemically homogeneous evolving (CHE) stars. As a consequence, no hydrogen and only a small amount of helium are retained at the time of core collapse. We find that neutrino emission during the late phases of evolution causes CHE stars to contract in an accelerated manner, leading to surface spin-up and episodes of strong, rotationally-induced mass loss. Due to their composition and high angular momentum content, we propose these models as progenitors both for hydrogen-free superluminous SNe (SLSNe) and long GRBs.

Using similar models, we suggest that the core structure of CHE stars, which varies non-monotonically with initial mass, determines the types of transient they produce at the end of their evolution. We suggest that the non-monotonic variation is the origin of the variety in the observed properties in SLSNe and GRBs. We find that our models can reproduce the observed properties of most SLSNe in the context of the magnetar model. We predict that signatures of mass loss in the last years of evolution should be present in the observations of both SLSNe and long GRBs.

Finally, we present evolutionary models of massive helium stars with different metallicities. These systems are representative of the late evolution of progenitors of hydrogen-deficient SNe of Type Ib and Ic. They can be formed by mass loss in very massive stars, or as the result of binary interactions. We characterize the impact of metallicity in their evolution, which alters their stellar winds. We propose a method to explain the observed lower limit in luminosity observed in populations of Wolf-Rayet stars. We simulate helium star populations in different metallicities, and find the properties of the transients they produce. We finally comment on the resulting populations of compact objects.

Contents

1 Introduction **1**

1.1 The Discovery of Supernovae 1
1.2 The Physics of Supernovae and Massive Stars 4
1.2.1 Massive Star Evolution: Basic Understanding from Birth to Death 4
1.2.2 Characteristics and Classification of Supernovae and Other Astrophysical Transients 11
1.2.3 Missing Ingredients in Stellar Evolution and the Massive Star-Transient Connection 15
1.3 Rapidly Rotating Massive Stars at Low Metallicity 22
1.4 Context of this Thesis 24
1.4.1 Method 24
1.4.2 A Unified Evolutionary Channel for Progenitors of Superluminous Supernovae and Gamma-ray Bursts 25
1.4.3 Precollapse Properties of Superluminous Supernovae and Long Gamma-Ray Burst Progenitor Models 25
1.4.4 Type Ibc Supernovae Progenitors and Wolf-Rayet Stars Evolving from Helium Stars in Different Metallicities 25

2 A Unified Evolutionary Channel for Progenitors of Superluminous Supernovae and Gamma-ray Bursts **27**

2.1 Method 27
2.2 Evolution of Chemically Homogeneously Evolving Massive Stars 28
2.2.1 Evolution of the Chemical Composition 31
2.2.2 The Radius of Chemically Homogeneous Stars 32
2.2.3 Angular Momentum Distribution 32
2.2.4 Rotationally Enhanced Mass Loss 35
2.2.5 Magnetic fields 35
2.3 Astrophysical Transients Produced by Chemically Homogeneously Evolving Stars . . 38
2.3.1 Shock Break-out 38
2.3.2 Interaction with the Circumstellar Medium 39
2.3.3 Expected Outcome for Different Models: Superluminous Supernovae 42
2.3.4 Expected Outcome for Different Models: Gamma-ray Bursts 43
2.3.5 Expected Outcome for Different Models: The Effect of Pair Instability 44
2.4 Discussion 44
2.5 Conclusions 45

3 Precollapse Properties of Superluminous Supernovae and Long Gamma-Ray Burst Progenitor Models **47**

3.1 Introduction 48

3.2 Method . . . 50
3.2.1 Physical and numerical parameters . . . 50
3.2.2 Comparison with ALMS18 . . . 52
3.3 Results . . . 54
3.3.1 Pre-collapse evolution . . . 54
3.3.2 Properties at core collapse . . . 59
3.4 Observable properties . . . 67
3.5 Conclusions . . . 70

4 Type Ibc Supernovae Progenitors and Wolf-Rayet Stars Evolving from Helium Stars in Different Metallicities 73
4.1 Introduction . . . 74
4.2 Method . . . 75
4.3 Helium Star Evolution . . . 76
4.3.1 The Impact of Metallicity in Helium Stars . . . 77
4.3.2 Helium Star Populations . . . 84
4.4 Properties of Helium Stellar Models at Core Collapse . . . 86
4.4.1 Final Masses and Chemical Compositions . . . 86
4.4.2 Supernova Explosions from Helium Stars . . . 91
4.5 Discussion . . . 98
4.6 Conclusions . . . 99

5 Outlook 101

Bibliography 105

List of Figures 119

List of Tables 125

Acknowledgements 127

CHAPTER 1

Introduction

1.1 The Discovery of Supernovae

Astronomy can be loosely described as the natural science that studies the stuff we observe in the sky that lies outside of our Earth; an attempt at understanding the dynamical lives of large-scale components of our Universe, using what we have learnt about physics here on Earth. Our understanding of astronomy is relatively modern. Although the study of stars and celestial bodies has been ubiquitous to most –if not all– human civilizations since prehistoric times, modern astrophysics could be said to have started during the Renaissance. Perhaps its most notable first leap was the publication of Nicolaus Copernicus' *De revolutionibus orbium coelestium* in 1543. Astronomy has always been tightly linked to history, culture, and identity of entire nations, and it is considered by some to be the oldest of the sciences. Prior to Copernicus's work, and the scientific revolution that it was part of, astronomy as a science was applied practically in time keeping and navigation. This made it become an essential tool for the survival and progress of civilizations, as it allowed them to master agriculture and explore further in land and sea (Cardona, 2013). Astronomy was also tightly wound to philosophy, mythology and religion in many cultures throughout all of human history. The positions of the stars and planets was woven into the shapes of stories, with entire cultures revolving around what they thought they could interpret from the motions of celestial bodies. Entire cities were built around the significance of astronomical phenomena. Changes in the sky served as omens and messages from deities, from comets to shooting stars, and other astronomical phenomena were no exception to this. Among these transient phenomena, however, supernovae –on which we focus in this thesis– hold a special place in the historical development of astronomy as a science. Their sudden appearance as "new stars" in an otherwise relatively unchanging night sky not only fueled the imaginations of those who saw them, but a few particular supernovae also fueled the explosion in scientific advances that started with the spark of Copernicus's publication, and allowed to convince many that astronomy was ready to be re-invented as a science, breaking apart from beliefs that were held by scholars since antiquity.

Copernicus' book put forth the idea that the Sun is at the center of the solar system, and the Earth and planets revolve around it, with the Moon revolving around the Earth in a similar way. Before this work was published, western scholars relied on models for the motions of planets and stars in the night sky that had been proposed by philosophers from the Greco-Roman world, and whose ideas had become a fundamental part of many philosophical and theological discussions since antiquity and throughout the middle ages. The astronomical model that prevailed in Europe during the middle ages, was the geocentric model that was preserved through Ptolemy's *Almagest*. Figure 1.1 illustrates the differences between the two.

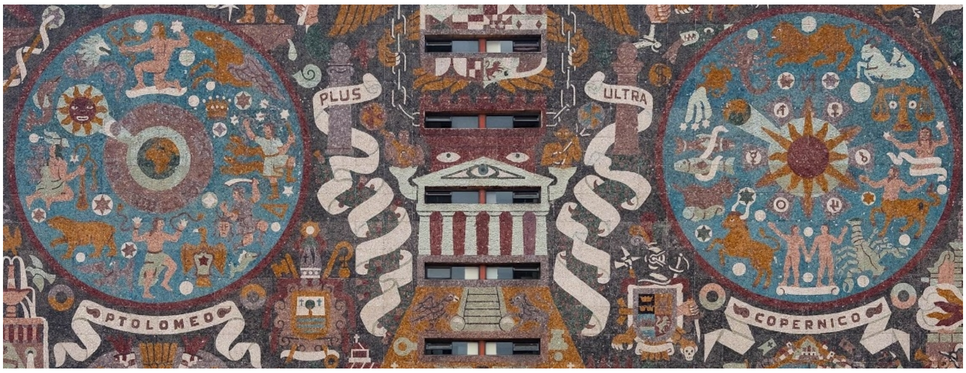

Figure 1.1: Detail of the mural *Historical Representation of Culture* created by Juan O'Gorman, located in the southern façade of the Central Library of the National Autonomous University of Mexico. It represents the Ptolemaic model of the Solar system, with the Earth at the center (left), and the Copernican model, with the Sun at the center. Figures around the two represent the locations of constellations and stars in the Celestial Sphere. Adapted from a photograph by Thomas Guignard. Source: Flickr.

The Ptolemaic model was based on the tenants of the so-called Aristotelian physics. One of the principles of Aristotelian physics, which was believed to be immutable and was directly challenged by Copernicus and his contemporaries, is the division of the Universe into the Terrestrial Spheres, which were set at the center of the Universe and were subject to the changes we observe on Earth; and Celestial spheres, which moved around the Terrestrial Spheres and contained the planets and stars, and were deemed sacred and eternal both in classical and medieval philosophies. The motion of planets and celestial bodies in this model was described by circular motions of objects in the celestial sphere.

Copernicus' heliocentric model was consequently a cause of some controversy during his time (and for quite some time), which led to dramatic episodes such as the trial and conviction of Galileo Galilei in the hands of the Inquisition in 1633. Notable support was received, however, from many scientists, including Tycho Brahe, considered by some to be the first empirical observational astronomer in the modern sense (on top of being an expert brawler and in general a rascal). Not only did he find that the Copernican model was more suited to interpret his measurements of the positions of stars and planets, but he was able to refute the Aristotelian belief of the unchanging celestial spheres. Proof of this came with the study of what he called the *stella nova*, a new bright star that quickly appeared in the night sky, and subsequently faded away after months of appearing to be one of the brightest stars in the sky.

This could be described as the serendipitous re-discovery of what today we know as supernovae, which we now know are astronomical transient phenomena. Supernovae and other transients are characterized by extremely high intrinsic brightness, and short durations, ranging from fractions of a second to months or a few years. A typical supernova at its peak is about 10^9 times brighter than our Sun, often even brighter than the entire galaxy that houses them. The brightest supernova known to date was observed to be about 5×10^{11} times more luminous than the Sun (Dong et al., 2016). Today, we know they are related to the explosions of certain stars, and leave behind remnants that can be recognized hundreds of years after their cataclysmic explosions. However, they have a long history.

Tycho's supernova was the first recorded supernova since the end of the Middle Ages, but others were observed and recorded by many sources in other historical periods. The oldest suggested record of a "guest star", suddenly appearing and slowly fading away, is argued to come from around the year 4,600 BC, found in a stone carving found in Kashmir, India. The vestiges of the alleged supernova recording are presented in Figure 1.2. This record is hypothesized to correspond to the supernova remnant HB9 (Joglekar et al., 2011). Several other historical records of supernova observations have been found. There

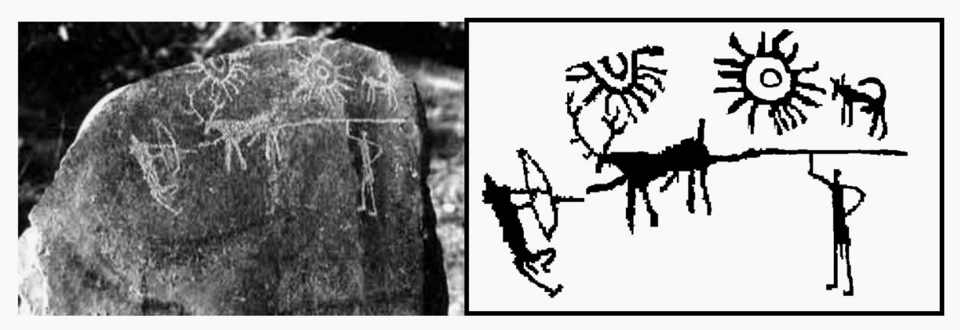

Figure 1.2: Photograph and recreation of the proposed oldest supernova recorded, a craving on a cave wall in Kashmir, India. Figure adapted from Joglekar et al. (2011).

are three of them in particular that were reported in several historical texts that took place before Tycho's supernova, in the years 1006, 1054 and 1181 AD. These supernovae were observed and documented by different Chinese astronomers, but also astronomers in Korea, Japan and several Arab lands, and their remnants have been identified. Other records include one from 185 AD, found in records of Chinese astronomers, and perhaps alluded to in Roman literature; and those of 369, 386, and 393, described only in single records by Chinese astronomers. Other possible texts detailing observations of strange celestial phenomena exist, dated as early as the 14th century BC, but these might be attributable to different astronomical sources (Clark et al., 1977; Green et al., 2017).

The last supernova in our Galaxy of which we have reliable contemporary records happened in 1604, and is commonly referred to as Kepler's Supernova, observed extensively by Johannes Kepler, an astronomer from the Holy Roman Empire who was a pupil of Tycho Brahe. Details and descriptions of his observations were published it in his book *De Stella Nova in Pede Serpentarii*. The remnants of two other such explosions have been discovered using modern telescopes. The supernova remnant Cas A is connected to a supernova that likely took place around 1680, and the remnant G1.9+0.3 in the constellation of Sagittarius is the youngest supernova remnant known in the Milky Way, originating from an explosion that took place between 1890 and 1908. Unfortunately, neither of them were likely visible to the unaided eye at the time they exploded. Not all hope is lost, though. Galaxies similar to the Milky Way have an approximate rate of one supernova per century, so I encourage even the least superstitious reader to keep their fingers crossed that it happens in our lifetimes.

While we sit and wait for the next celestial fireworks to be visible from the comfort of our balconies, however, a spectacular number of supernovae and other diverse astronomical transients are detected and studied every day using modern astronomical equipment. As opposed to the days of Kepler, when scientists were aware of only two of these events, today the Open Supernova Catalogue [1] reports more than 63,000 observed events. Some were observed and confirmed to be extragalactic sources in the late 19th and early 20th century, but it wasn't until the 30s that they were recognized as the beasts they really are. They were recognized to release more energy than previously known variable sources, known as novae (Baade et al., 1934b), which served as inspiration for Fritz Zwicky, who came up with the moniker "supernova". After the identification of these energetic transients, Zwicky launched the first supernova search, finding a few dozens in their first campaign. Ever since that first campaign, supernova and transient searches with ground and space based telescopes has been one of the most active fields in astronomy. Today, projects like the Zwicky Transient Factory (ZTF), Panoramic Survey Telescope and Rapid Response System (Pan-STARRS), amongst others, produce about 1 detection around every

---

[1] https://sne.space/ .

30 minutes, and the upcoming Vera C. Rubin Observatory will likely increase that number by at least a factor 10.

1.2 The Physics of Supernovae and Massive Stars

The first notion about how supernovae are powered came from Baade et al. (1934a), who correctly predicted that these transients originate from the energy released during the collapse of the core of a massive star into a neutron star. Ever since this idea was proposed in 1934, though, a lot of progress has been made to understand exactly how this process works, and which kinds of stars can actually experience this phenomenon. In the remainder of this Chapter, we discuss the necessary theoretical tools and the observational constrains we require to understand massive star evolution and their connection to astrophysical transients, and provide some context to the remainder of this thesis. The theory of massive star structure and evolution is introduced in Section 1.2.1, followed by an overview of the classification of supernovae and other astrophysical transient phenomena 1.2.2, and we conclude with a discussion about their connection, highlighting the mechanisms of their formation and what we know about progenitors of different stellar transients in Section 1.2.3.

1.2.1 Massive Star Evolution: Basic Understanding from Birth to Death

New stars are constantly being formed. Star formation regions are found within some galaxies and can form stars at different rates, depending on their physical properties. The process of star formation is complex, but in essence new stars are formed as a consequence of the gravitational collapse of giant molecular clouds. Giant molecular clouds have enough mass to form several hundreds of stars of many different masses during a single star formation episode, and stars formed from a single cloud have similar ages and initial chemical compositions, and will likely form a gravitationally bound group of stars, known as a star cluster. Star formation begins in giant molecular clouds if they become unstable, which occurs once their internal pressure becomes insufficient to counterbalance their self-gravity. This happens once they reach the so-called the Jeans mass, a theoretical value that depends on the cloud density and its thermal properties. Star formation can be triggered by cooling, or by clouds interacting with external sources of pressure that perturb their fragile equilibrium (see e.g. Carroll et al., 1996, for an introductory text).

Once the complex process of star formation is finished, stars settle into an equilibrium state. Here, a short overview of some general properties of massive stars is provided to shed light on how they live between the moment they settle into this state of equilibrium, and the moment where they reach their explosive deaths, but the reader is referred to Kippenhahn et al. (1990) for a more detailed discussion.

Stars are typically observed through photometry and spectroscopy. Photometry is the most accessible observation method, as it consists in observing a star's brightness in wide wavelength bands. This can be done as a function of time, to determine how brightness evolves as a function of time, and several objects can be observed simultaneously. Brightness is typically measured in *apparent magnitude*, defined as

$$m = -2.5 \log_{10} \left(\frac{F_x}{F_{x,\mathrm{ref}}} \right) \tag{1.1}$$

where F_x is the flux in a given band, and $F_{x,\mathrm{ref}}$ is a reference flux in the same given band. This system is calibrated to have the reference star Vega at magnitude 0, and decreases for increasing brightness. This can then be converted into *absolute magnitude*, which is defined as the apparent magnitude the same object would have if it was at a distance of 10 pc from the observer, and thus contains information about the distance to the observed object, and about its intrinsic brightness, or luminosity.

Spectroscopy on the other hand takes much more observing time, making it more difficult. It consists on decomposing the flux of light emitted by the star (or supernova, or any astrophysical object) into flux in different wavelengths at a given epoch. This method is useful, as it provides information about the chemical composition, temperature and velocity of the observed object, at the cost of requiring longer observing times.

Stars are classified according to their observed photometric and spectral properties. Most broadly, stars are divided in spectral classes O,B,A,F,G,K and M. They are distinguished by their spectral properties, which reflect their temperatures. Measuring a star's luminosity and temperature informs us about its physical size, since these two quantities are connected by the Stefan-Boltzmann law, due to the fact that stars are –to a very good approximation– black bodies.

Stars come in many flavors, and an important tool that is used to understand their properties and classify them in different families is the Hertzsprung-Russel diagram (HRD), which relates stars' luminosity to their effective temperature (with an inverted x-axis), or its observational counterpart, the color-magnitude diagram (CMD), which connects the related absolute magnitude of stars, related to their luminosity, to the difference between their brightness in two different bands (or in different colors), which is a proxy to their temperature. An example of this kind of diagram is given in Figure 1.3. As can be seen, spectral class, color difference and temperature are related to one another, and absolute magnitude is related to luminosity (typically measured in units of solar luminosity). Some of the different regions in this diagram are discussed further in this Chapter.

The structure and evolution of stars, once they settle in an equilibrium state after formation, is understood today on the basis of a few simple physical considerations. These principles provide the theoretical background for their study. Stellar structure and evolution is then summarized in five coupled differential equations, that are nowadays solved numerically for a number of different initial conditions, and thus allow us to understand the variety of phenomena that we observe from them (see Kippenhahn et al., 1990, for a summary). The system of coupled differential equations that describe stars stem from the following assumptions:

- Stars are spherical, and made of gas
- They are in a state of hydrostatic equilibrium, where the self gravity of the gas inside the star is exactly balanced by its pressure gradient
- They are in a state of global thermal equilibrium, where the energy they irradiate from their surface is balanced by the energy generated in their interior through nuclear reactions
- The gas inside stars is in local thermal equilibrium, and the energy that is generated in their interiors is transported either by the diffusion of radiation or by the bulk convective motion of the gas inside the star
- The chemical composition of stars is initially set by the composition of the cloud that formed them, and their composition and distribution change due to nuclear reactions, and processes that transport material across different parts of the star

Combining this set of insightful concepts together yields a set of equations that becomes closed once the thermal state of the gas is described by an equation of state, and a description for the opacity –which is a measure of how much light can be absorbed by the gas inside the star–, and the rates of nuclear reactions are provided; as well as a method to calculate the mass loss rate of the star, which is often

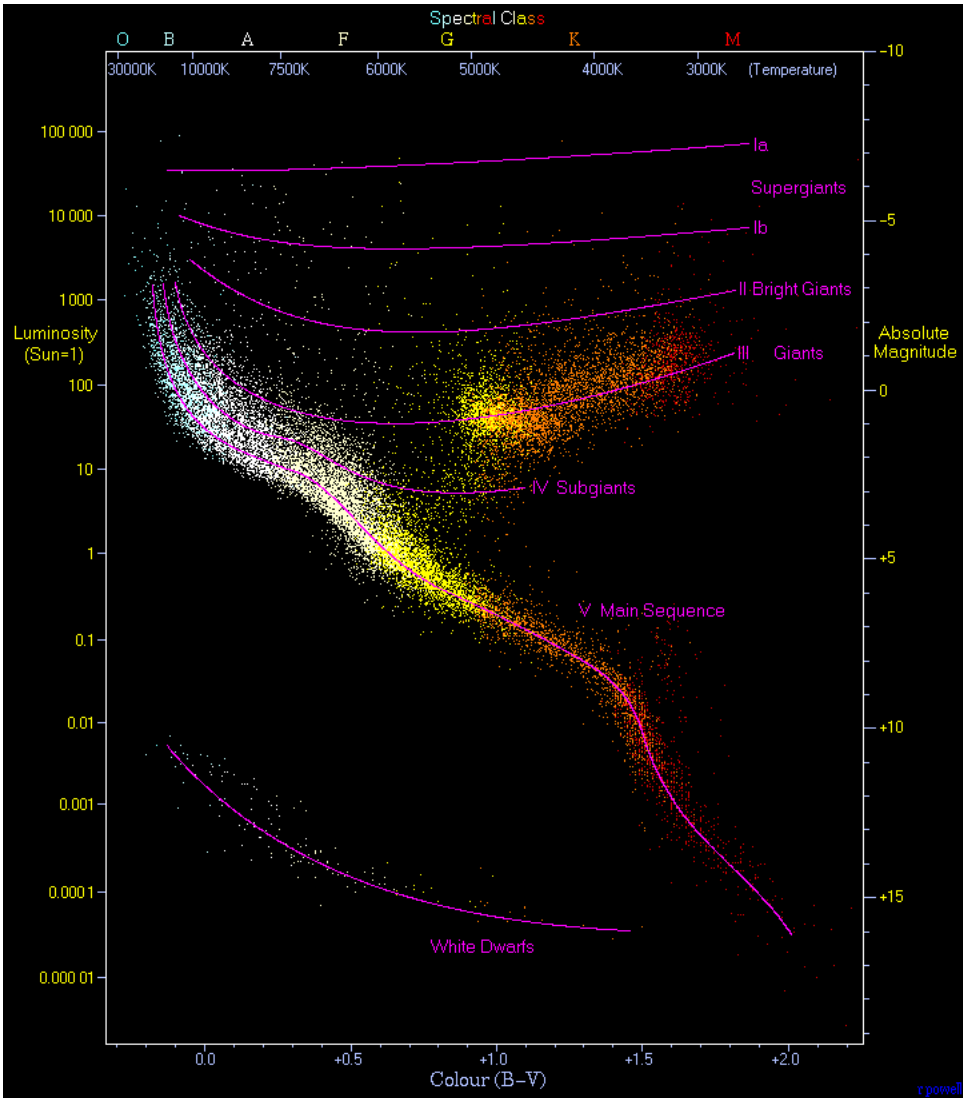

Figure 1.3: A Hertzsprung-Russell diagram showing the inferred luminosities (left y-axis, in units of a Solar luminosity $L_\odot$) and equivalent absolute magnitudes (right y-axis), as a function of color index B-V (bottom x-axis) and its equivalent effective temperature and spectral class (top y-axis) of 22,000 nearby stars from the *Hipparcos Catalogue* (Perryman et al., 1997), and 1,000 faint stars from the *Gliese Catalogue of Nearby Stars* (Gliese, 1957; Woolley et al., 1970). Figure adapted from Wikipedia.

obtained empirically. The equations can be solved once initial and boundary conditions have been set, and through these few principles we can understand the entire life cycle of many types of stars, and explain the properties of their populations.

The chemical composition stars are born with, as previously alluded to, is set by the chemical composition of the giant molecular cloud that they are made from. As stars evolve, nuclear reactions take place in their interior which transmute light elements into heavier ones, providing the energy to keep the star in thermal equilibrium. Thus, the interiors of stars become enriched with heavy elements, and through different processes enrich the interstellar medium, providing new chemical elements into the regions that will in the future form a new generation of stars. After the Big Bang, the first generation of stars formed was composed almost entirely of hydrogen and helium. It is the evolution of stars throughout cosmic history that has produced the largest amount of elements heavier than those two, subsequently enriching their host galaxy with their processed material. This results in new generations of stars, as well as the interstellar medium, the intergalactic medium, planets, and other astrophysical objects that have an increasingly richer chemical composition. This is what gives meaning to the famous Carl Sagan quote "The cosmos is within us. We are made of star-stuff".

The main process that generates energy in the interior of stars is hydrogen burning. The rate of nuclear reactions in the stellar gas is set by an interplay between the electromagnetic forces, that tend to push nuclei away from each other; the thermal state of the gas, which determines the velocity distribution of nuclei; and the quantum tunneling probability, which allows for nuclei to interact with each other, and fuse, even when their charges work to push them away from each other. Reactions are thus very sensitive to the composition, density and especially the temperature of their environment. The equilibrium state of stars implies that the rate of energy generation in their interior is matched by the rate at which they irradiate said energy at their surface, and this sets many important stellar properties.

There are two main channels through which stars burn hydrogen, known as the pp chain (or proton-proton chain) and the CNO cycle. The pp chain works most efficiently in stars with masses around and below 1.3 $M_{\odot}$, whereas the CNO cycle dominates the energy generation in more massive stars. A diagram detailing the main reaction in these cycles is presented in Figure 1.4. A single helium nucleus is generated in the pp chain from the fusion of four hydrogen nuclei, following a set of reactions that first generate deuterium (an isotope of hydrogen, ^{2}H) through the fusion of two protons. The resulting deuterium nucleus then interacts with a third proton, producing ^{3}He, and finally 2 ^{3}He nuclei interact with one another to produce one stable ^{4}He nucleus, and two protons as a byproduct. All in all, four protons produce one ^{4}He atom, and in the process produce photons that add thermal energy to the stellar gas, as well as neutrinos that escape the system immediately. The CNO cycle is slightly more complicated, but essentially repeats the process of turning 4 protons into a helium nucleus, except carbon, oxygen and nitrogen atoms act as catalysts that enable the reaction to occur more efficiently. The total number of carbon, oxygen and nitrogen atoms remains the same throughout the cycle, but their relative abundances change, favoring the production of nitrogen at the cost of carbon and oxygen.

Although the energy generation rates between the pp chain and the CNO cycle differ, they roughly produce the same amount of energy per reaction, and keep the star in equilibrium from birth, until hydrogen in the core of the star becomes depleted. A simple estimate of the duration of the hydrogen-burning lifetime of a star can be given by the nuclear time scale, $\tau_{\rm nuc}$, which is calculated as

$$\tau_{nuc} = \frac{E_{nuc}}{L} = \phi f_{nuc} X \frac{Mc^2}{L}, \tag{1.2}$$

where E_{nuc} is the total amount of nuclear energy available to the star, and L is the luminosity of the star; the rate at which this energy is released in the form of radiation at the stellar surface. E_{nuc} can

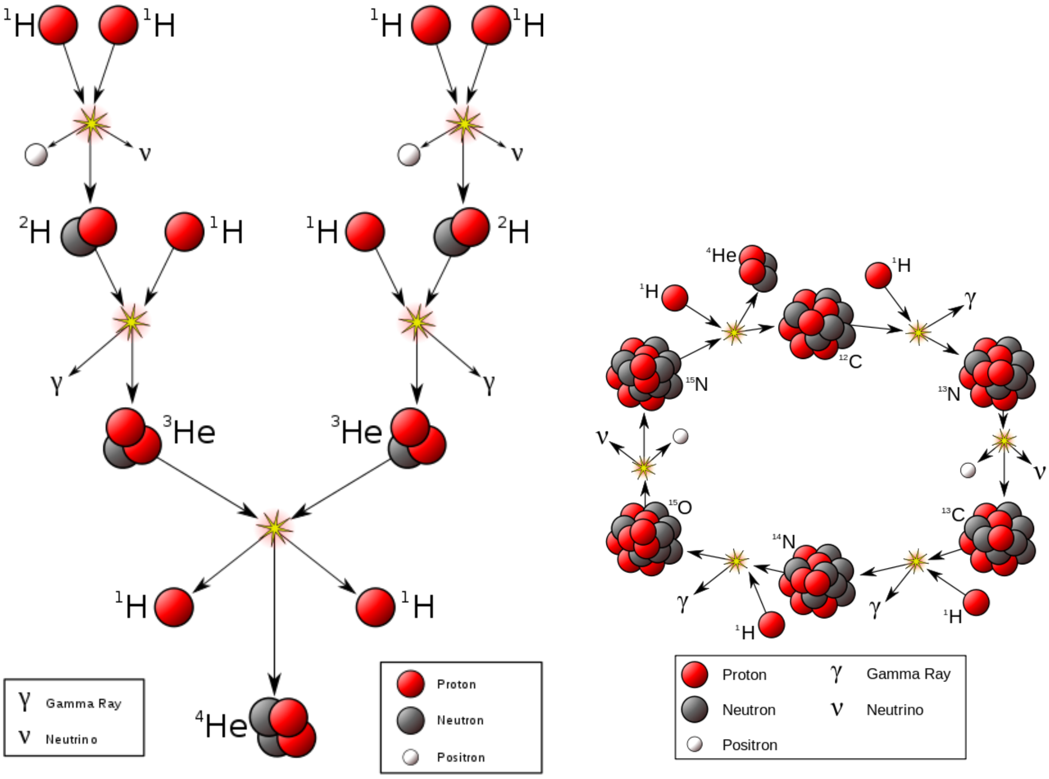

Figure 1.4: A schematic representation of the pp chain (left) and the CNO cycle (right); the nuclear fusion processes that most commonly take place inside of stars, and turn hydrogen into helium. Adapted from Wikipedia.

be approximated by the product of the mass of the star M times the speed of light, c, squared. This represents the total rest mass energy of the star, and multiplied by ϕ, the amount of rest mass energy that is released per reaction (which is about 0.007 for hydrogen burning), gives the total energy that could be released if all the star was made of hydrogen, and all the hydrogen was completely converted into helium. Multiplying this by f_{nuc}, the fraction of the stellar mass where this reaction takes place (otherwise known as the core of the star), removes the amount of the star that remains unchanged, and finally X, the mass fraction of hydrogen, takes into account that not all the material in the star is hydrogen. Calculating this time scale for the Sun yields a time scale of about 10^{10} years, meaning that the Sun has lived approximately half of its hydrogen-burning life. This simple estimate for how long a star lives decreases steeply for more massive stars, owing to the fact that they quickly become more luminous the more massive they are, following the old-school-cool motto of *live fast, die young*, albeit in a time scale that is still of the order of a few tens of millions of years for stars around 10 $M_\odot$.

The nuclear time scale roughly describes the total life time of stars. Since they are in hydrostatic and thermal equilibrium, all the changes that they are subject to during their evolution are fast compared to their nuclear time scale. There are two other important time scales are useful in describing the evolution of stars, and are therefore discussed below.

If a star is subject to changes in its structure that take the star slightly off of thermal equilibrium, such as the exhaustion of hydrogen in its core, these changes take place in the so-called thermal time scale (otherwise known as Kelvin-Helmholz time scale, named after its proponents). This time scale is typically several orders of magnitude shorter than the nuclear time scale. The thermal time scale is given by

$$\tau_{KH} = \frac{E_{thermal}}{L} \simeq \frac{GM^2}{RL}, \tag{1.3}$$

where $E_{thermal}$ is the total amount of nuclear energy available to the star, related to the gravitational energy of the star through the virial theorem, a direct consequence of hydrostatic equilibrium. It thus depends on the stellar mass M, the stellar radius R, and the gravitational constant G. For a star like the sun, the typical thermal time scale is about 10^7 years, considerably shorter than its nuclear time scale.

Finally, the shortest time scale that plays a role in the evolution of a star is the so-called dynamical time scale, which is the time scale at which perturbations to hydrostatic equilibrium propagate. This time scale can be approximated by assuming that gas pressure suddenly becomes negligible, and the stars structure reacts to a force. This assumption yields an a time scale given by

$$\tau_{dyn} = \sqrt{\frac{R^3}{2GM}}, \tag{1.4}$$

and it is useful to describe phenomena where pressure suddenly drops, or a force is suddenly exerted on some parts of the star. An example of this is the collapse of the core of a massive star, discussed below.

Having introduced these concepts, we can return to Figure 1.3, and explain some of is characteristics. The region with the highest density of stars is known as the main sequence. The high number of points in this luminosity and temperature regime is due to the fact that stars in that region of the diagram are burning hydrogen into helium, and this the longest stage of stellar evolution. At this stage, the luminosity and effective temperature are determined by the efficiency of energy generation and transport, and to the balance of gravitational and thermal energies; and land along this area of the diagram. Other relatively populated areas of the diagram correspond to different, relatively long lived stages of stellar evolution, and some relevant families are discussed below.

Once all the hydrogen inside a star's core has been turned into helium, the core will contract. If it is massive enough, it will then become hot enough in its core to burn the helium it created through the so-called triple α process, where three helium nuclei are turned into one ^{12}C nucleus, releasing energy as part of the reaction. A secondary process will also slowly turn some of the carbon produced into oxygen by interacting with a fourth helium nucleus, leaving behind a mix of carbon and oxygen after the end of helium burning. The time scale of helium burning is small compared to that of hydrogen burning, owing to the fact that nuclear reactions of elements heavier than hydrogen are less efficient in producing energy through fusion, as well as the fact that the fraction of the mass that a star burns is smaller. The helium burning lifetime is about 10% of hydrogen burning lifetime.

At some point between when a star exhausts its hydrogen supply in its core, and when it ignites the helium ashes left behind, the whole star contracts. During the contraction, the regions around the helium core become hot enough to burn hydrogen. Hydrogen burning in a shell immediately above the helium core has two main effects. On one hand, more helium will be produced, meaning that the helium core will grow in mass between this point, and the end of the star's life. On the other hand, the core will continue to contract until helium burning generates enough energy to stabilize it, while the envelope of the star will expand due to the energy that is created in the hydrogen burning shell, which needs to be dissipated. This is known as the *mirror principle*, and can take place multiple times when multiple shells develop in the interior of stars, alternatively increasing and decreasing their radius. Stars that go through this process populate the region to the right of the main sequence in Figure 1.3; the so-called giants and supergiants, with high luminosities and low surface temperatures. The region in between the main sequence and the red giant branch is less populated by stars due to the fact that the transition from

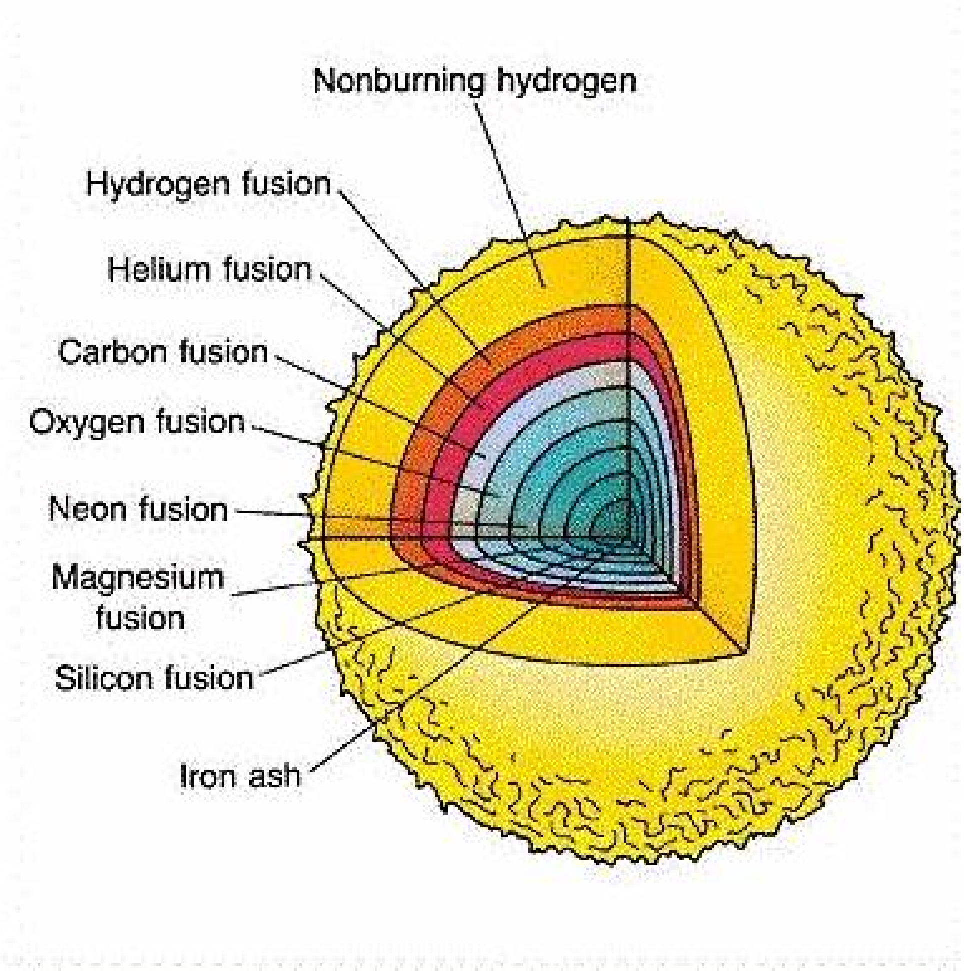

Figure 1.5: A schematic representation of the layers of different composition that a massive star will have at the end of its life. Figure adapted from Chaisson et al. (2005).

core hydrogen burning stars to red giants or supergiants occurs in a thermal time scale, much shorter than the life time of any star.

In some stars, if they are massive enough, the chain continues. Their massive carbon and oxygen core becomes hot enough to burn carbon, then neon, then oxygen, and finally silicon, producing a core that is composed of iron ashes. The process becomes accelerated at each phase, mainly due to the fact that the luminosity L in Equation 1.2 increases by many orders of magnitude due to the emission of neutrinos (which does not imply that the star emits more electromagnetic radiation, since energy is carried by said neutrinos, and not the radiation we observe at the surface). While helium burning can take something of the order of two million years for a star of about 10 $M_{\odot}$, burning silicon into iron takes about one day. A schematic of what a star could look like at this point (not to scale) is presented in Figure 1.5.

The cycle of taking light elements and making heavier ones ends at this point, due to the fact that fusing elements of the iron group (or heavier) is actually *consuming* energy, rather than creating it. Therefore, these reactions are not favored to occur in a star, and would not contribute to its stability (and, by the way, that is the reason that *fission*, the process employed in nuclear power plants in which heavy nuclei decay into lighter ones, which can release a very large amount of energy, takes place). Once an iron core is formed inside a star, it will reach a point where it can no longer sustain itself against gravity, and will collapse. This collapse might result in the formation of a neutron star or a black hole, and leads to explosive events with several degrees of intensity, that depend on the state of the star when it reaches this point. This is the canonical understanding of the subpopulation of stars that concerns this thesis, the so-called “massive stars”. Several authors define this term differently (or get away with vaguely hinting at its meaning), but what many of them mean, in essence, is stars that end their lives either exploding or imploding, likely due to the formation of an iron core that ultimately will collapse. In the canonical picture, a massive star would then release the gravitational binding energy that is produced when the iron core transforms into a neutron star, and this energy would power a bright supernova. However, as will be seen in Sections 1.2.2 and 1.2.3, this is hardly the whole story, and more ingredients are missing to fully explain the diversity of observed transients. A better understanding of stellar evolution and its connection to transients is, in essence, the aim of this thesis.

1.2.2 Characteristics and Classification of Supernovae and Other Astrophysical Transients

Astrophysical transients such as supernovae, gamma-ray bursts, gravitational wave mergers, fast radio bursts, and others are routinely discovered nowadays. Supernovae are perhaps the most ubiquitous among them, and they are a largely important for the results of this thesis, so they will be discussed first. The naming convention for individual supernova events starts with the prefix SN, followed by the year it was discovered, and letters that denote the order in which they were discovered, starting with A through Z for the first 26 supernovae in a year, and continuing with a pair of lowercase letters in the sequence aa, ab, etc. Historical supernovae are only known officially by the year they were observed in, such as SN 1604, Kepler’s supernova.

Supernovae are typically observed through photometry and spectroscopy, similar to how stars are studied. Photometry of supernovae is used to follow the evolution of their luminosity as a function of time, also known as their *light curve*, which contains information about the total energy that a particular supernova irradiates, and also provides clues about how the explosion is powered and how it interacts with its environment. They are nowadays most often discovered by “transient factories”, which observe regions of the sky through photometry, and have regular observations of the same regions with a determined cadence, so newly appearing objects can be discovered promptly.

Spectroscopy of supernovae reveals information about their temperature, velocity and composition, but it cannot be done for every possible transient, and even those that get observed spectroscopically may have only one or a few epochs during which they are observed. They come in several different varieties and are classified according to properties in their light curves and spectra, which are in turn linked to the properties at death of the progenitor star, as well as the source of energy that causes the cosmic fireworks.

Supernovae come in different varieties, and modern classification is based in the scheme described by Filippenko (1997). According to this scheme, supernovae are first subdivided into two categories, separating those whose spectra show hydrogen lines at the time of maximum brightness, classified as Type II supernovae, from those that do not show any hydrogen lines at this time, classified as Type I. Type I supernovae are further classified into Types Ia, Ib and Ic. Type Ia supernova spectra are characterized by the presence of strong silicon features, but also contain contributions from other elements between carbon and iron. Type Ib supernovae do not possess a silicon absorption feature, but show strong helium lines. Type Ic supernovae show neither silicon nor helium features. Characteristic spectra of these types of supernova are summarized in Figure 1.6.

Supernovae are further subdivided according to their light curves. Type II supernovae are classified as Type II-P when their light curves have a significant plateau in their brightness evolution (i.e. an extended period where brightness remains approximately constant), or as Type II-L when their light

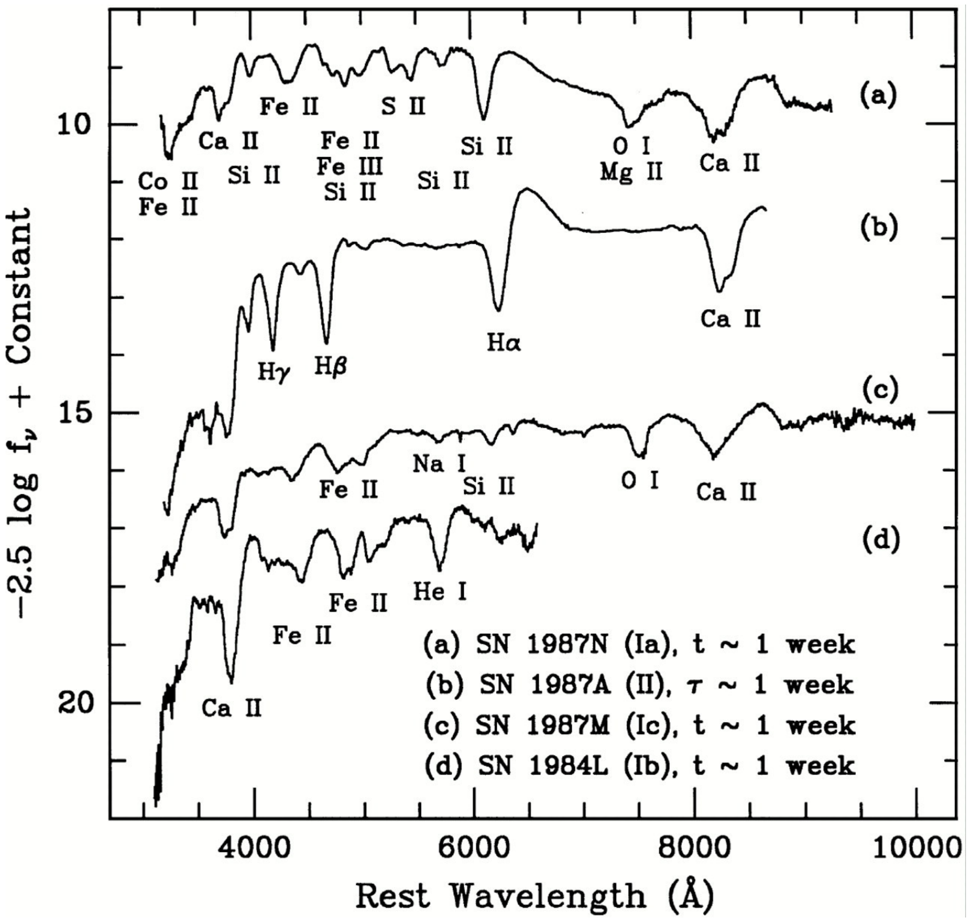

Figure 1.6: Example optical spectra near the time of maximum brightness of typical Type Ia (a), Type II (b), Type Ic (c) and Type Ib (d) supernovae. The different features in the spectra are caused by the presence of different elements near the photosphere. The elements and ionization states responsible for some features are highlighted. The variable t in this figure represents the time after B-band maximum, and the variable τ represents time after core collapse. Figure adapted from Filippenko (1997).

curves decay roughly linearly in magnitude. An example of typical light curves of different supernovae can be seen in Figure 1.7. Type Ia supernovae have a distinct light curve with properties that can be regularized (Phillips, 1993), likely due to the fact that they are formed in similar systems, although there is an increasing amount of systems with peculiar properties, and many competing progenitor models exist (see Maeda et al., 2016, for a recent review). Type Ib and Ic supernovae have light curves that are statistically indistinguishable from each other (Drout et al., 2011), implying that they can only be distinguished spectroscopically, but are often less luminous than those of Type II. Beyond the supernova classes that are described above, there is a large variety of supernovae that this classification scheme does not fully encompass (a few of them being discussed below), as shyly exemplified by the light curve of SN 1987A in Figure 1.7, the nearest supernova to have taken place in recent memory, in our neighboring galaxy, the Large Magellanic Cloud, and definitively a peculiar event.

Within this classification scheme, information about the physical mechanism that drives the explosions can be found. From it, we can infer the kinds of stars that are the progenitors of such events. Type Ia supernovae, which are observed to originate in old stellar populations, have spectra that show features of elements with atomic numbers between carbon and nickel. This led to the conclusion that these

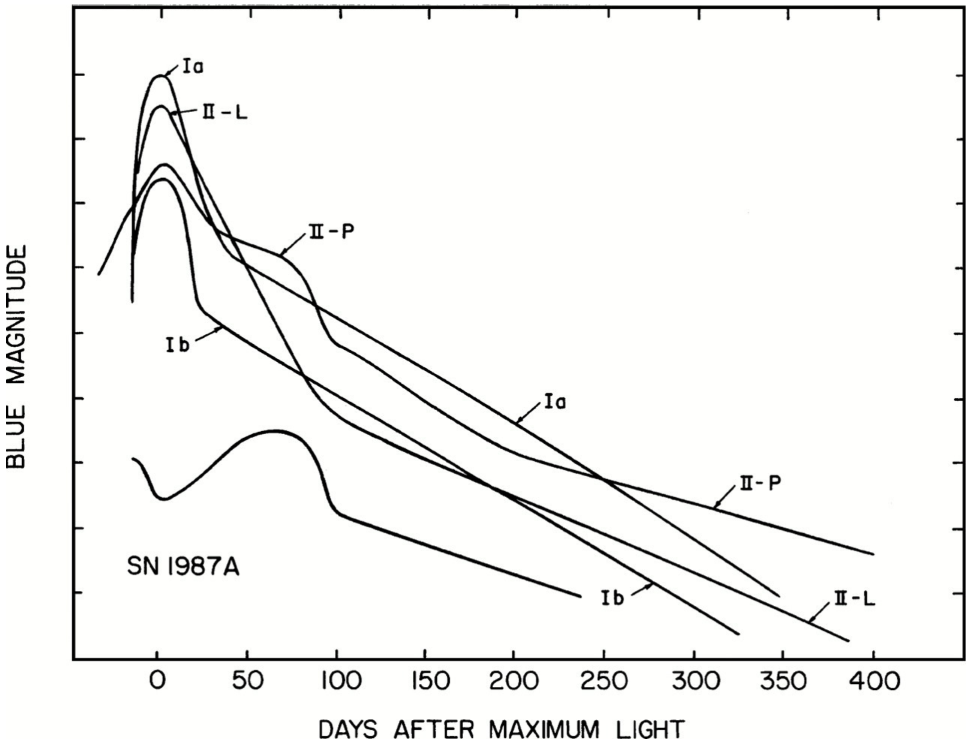

Figure 1.7: Schematic blue magnitude light curves representative of typical supernovae of different types. including a supernova Type II-L, a Type II-P, a Type Ia, a Type Ib, and the peculiar case of SN 1987A. Figure adapted from Filippenko (1997).

supernovae originate from white dwarfs that reach masses similar to the Chandrasekhar mass, which is the highest mass at which degenerate matter can balance its own gravitation through degeneracy pressure. White dwarfs that reach a mass similar to the Chandrasekhar mass ignite their remaining material in a degenerate state, triggering a number of thermonuclear reactions that subsequently power the explosion of the white dwarf, leaving no remnant behind and producing a high amount of iron (see Maeda et al., 2016, for a recent review). Type Ia supernovae are thus also known as thermonuclear supernovae, and they form a family of transients that have relatively homogeneous properties.

The rest of the "typical" classes, Type II, Type Ib and Type Ic supernovae, are known as core-collapse supernovae, as they originate from the collapse of the iron core of a massive star into a neutron star (Baade et al., 1934a). The large variation of their properties, even between members of one sub-class, is interpreted as a consequence of the evolutionary history of their progenitor star. Therefore, they provide us with a unique laboratory for the study of the physics of massive stars. This becomes especially important since massive stars, although bright, are intrinsically rare, since fewer of them are formed compared to less massive stars (Salpeter, 1955), and since they have shorter lives than their less massive counterparts (e.g. Kippenhahn et al., 1990). Studying the properties of massive stars through the transients they produce at death, owing to their extreme brightness, allows us to study them in distant galaxies, where a single star cannot possibly be detected individually. This not only allows us to dive deeper into the physics of massive stars, but also to have a glimpse at how the Universe behaves in regions with lower metallicity.

In addition to the classes of transients described by the classification scheme of Filippenko (1997), several other families of transients have been discovered in recent years, many of which are also linked

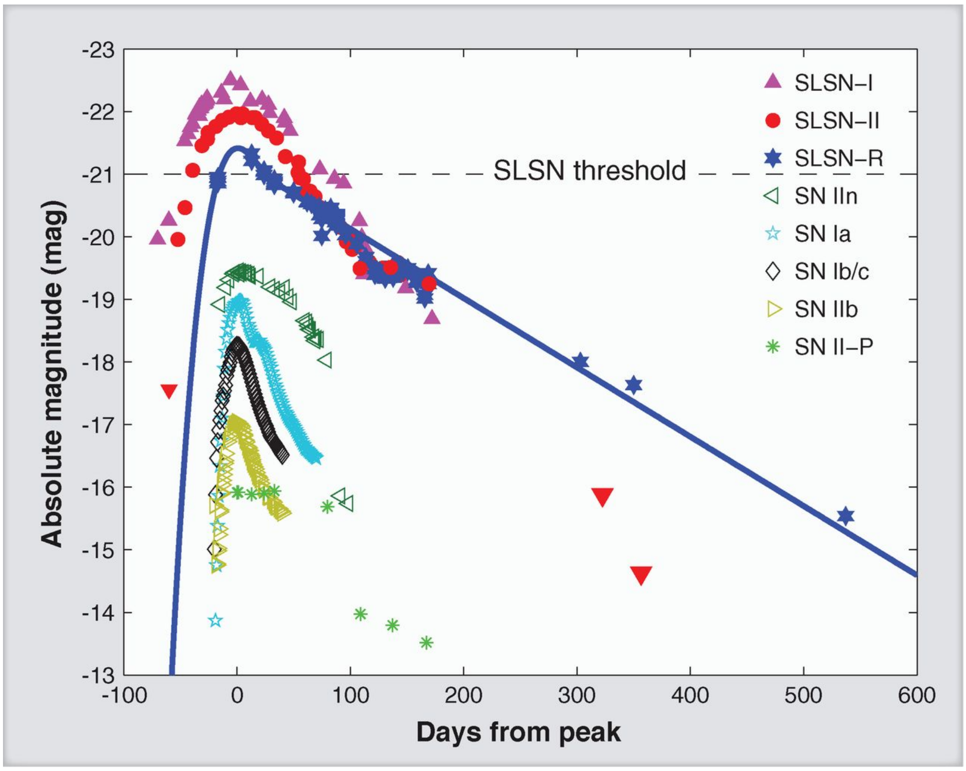

Figure 1.8: Examples of absolute magnitude light curves of superluminous supernovae of Type I (hydrogen poor, pink), Type II (hydrogen rich, red) and Type R (hydrogen poor, likely powered by ^{56}Ni, dark blue). For compatison, typical light curves of other supernova types are shown. Adapted from Gal-Yam (2012).

to massive stars. A subclass of Type II was recognized recently, known as Type IIb supernovae. Together with Type Ib and Ic, they are part of the so-called “stripped-envelope supernovae”, and are distinguished by spectra that resemble a Type II at early times, but as they evolve, they more resemble a Type Ib supernovae, with strong helium lines and weakening hydrogen lines. Several events such as SN 1987A are classified as “anomalous”, and can only vaguely be accommodated in the more ordinary classes. Other events have been discovered abundantly since the classification first came into use, and nowadays they form subclasses of their own right.

An important subclass that was recently discovered, and one that is very relevant to the results of this thesis, is the so-called superluminous supernovae (Gal-Yam, 2012). They are a rare class of supernova that are observed to be 10 to 100 times brighter than their “ordinary” counterparts, and are also subdivided into Type I, lacking obvious hydrogen and helium lines in their very hot spectra, and Type II, which have hydrogen lines. Examples of light curves of the both classes are given in Figure 1.8, displaying the immense power that these supernovae can output compared to the more ordinary transients.

Other transients that are related to massive stars, but do not fall in the categories above, are gamma-ray bursts. They were discovered serendipitously in the 1960s, in the midst of the Cold War, by military satellites, and inspired a large observational and theoretical campaign to try to understand their origin, since they are the most energetic electromagnetic explosion known to us. They fall into two categories, depending on their duration: long and short. Short gamma-ray bursts were hypothesized to form from the mergers of two neutron stars (e.g Ruffert et al., 1998), and this claim was confirmed quite recently, with the discovery of a short gamma-ray burst GRB 170817 A, detected by the Fermi and INTEGRAL satellites (B. P. Abbott et al., 2017), coincident with the gravitational wave source GW 170817 detected by the LIGO/Virgo collaboration (B. P. Abbott et al., 2017), and confirmed to be consistent with this model by subsequent observations, in what was perhaps the most thoroughly observed transient in history.

Long gamma-ray bursts on the other hand are related directly to the deaths of massive stars. They are observed in star-forming regions (Savaglio et al., 2009), indicative of their relationship with massive stars, and have environments that are similar to those of superluminous supernovae (Lunnan et al., 2014). Many are observed accompanied with a peculiar type of supernova known as Type Ic-BL (S. E. Woosley et al., 2006), characterized by broad spectral lines, indicative of very high velocity ejecta, and like the "normal" Type Ic supernovae, lacking hydrogen and helium lines in their spectra, although they differ greatly in their typical ejecta velocities, total energy and luminosity, and are very likely the product of a different process than their typical Type Ic counterparts.

Gamma-ray bursts are interesting due to the fact that they are the most energetic electromagnetic explosions known to date. They are observed, as the name suggests, as flashes of high energy gamma-ray emission lasting from a few seconds up to a a few hours. They are known to form from collimated, highly relativistic jets that emit gamma rays that are beamed into a small viewing angle, and as the jets decelerate, an afterglow is observable in wavelengths that range from radio to X-rays (Piran, 2004). They are preferably found in low metallicity galaxies, and are observable up to redshifts larger than any other stellar transient (Palmerio et al., 2019).

Besides gamma-ray bursts and exotic supernovae, a new variety of astrophysical transient was recently discovered: gravitational wave emission from compact object mergers. They were discovered by the LIGO/Virgo collaboration (B. P. Abbott et al., 2016), and much observational and theoretical progress has been achieved in the few years since their discovery. Mergers of binary black holes, binary neutron stars, and perhaps even binary systems composed of a neutron star and a black hole have been observed, posing a challenge to stellar evolution, since the evolution of close binaries that remain bound until the death of both components has proven difficult to explain.

The descriptions of properties of different transients listed above is far from complete. Several classes exist, and each of them have their own peculiar events which elude explanation. Here, we have described only the few that are relevant for the content of this thesis, but many new classes of transients, some of which potentially have their origins in massive stars, have been discovered and characterized in recent years, and many aspects of their formation are yet to be explored.

1.2.3 Missing Ingredients in Stellar Evolution and the Massive Star-Transient Connection

The link between massive stars and core-collapse supernovae is more than well established. Baade et al. (1934a) proposed that the source of energy for such an explosion was linked to the formation of a neutron star inside a massive star, and today we have observed several examples of "disappearing" stars at the sites of supernova explosions. Images of the progenitors of supernovae were first found fortuitously, starting with the systems that gave rise to SN 1987A (White et al., 1987) and SN 1993J (Aldering et al., 1994), both happening in nearby galaxies that have been thoroughly studied at the time (and both peculiar! One a rare Type II-P and the other a Type IIb). Nowadays, several groups routinely try to find observations of the progenitors of supernovae in archival images, and a sample of about fifteen progenitors for Type II-P and Type II-L supernovae exists (see e.g. Davies et al., 2020, and references therein), as well as five observed progenitors for Type IIb supernovae (e.g. Kilpatrick et al., 2017, and references therein), one candidate for the progenitor of a Type Ib (Cao et al., 2013; Folatelli et al., 2016), and one candidate for a Type Ic (Kilpatrick et al., 2018; Van Dyk et al., 2018). This unfortunately short list of observed progenitors contains only the "typical" supernovae. No progenitors of either gamma-ray bursts, supernovae Type Ic-BL or superluminous supernovae have been directly observed to date.

Although all these transients are believed to come from massive stars, not all massive stars produce transients. In some cases, the formation of a typical neutron star might not be able to produce enough energy to completely eject the envelope of a star, and it might instead directly become a stellar mass black hole (Oppenheimer et al., 1939). Many such black holes have been observed by the LIGO/Virgo collaboration in binary black hole mergers (e.g. B. P. Abbott et al., 2016), and there are a few candidate "disappearing" stars, that might have been too massive to successfully produce a supernova, and thus simply disappeared quietly from our field of view after collapsing and becoming black holes (Gerke et al., 2015; S. M. Adams et al., 2017; Allan et al., 2020).

Another aspect that provides clues on the nature of progenitors of different transients is the rate at which they occur. The last supernova that we know about in our Galaxy was observed in August 1680. However, different measurements put the rate of supernovae in the Galaxy at about one per 50 years (e.g. Diehl et al., 2006, , we are overdue for one, so keep looking up!). From the total number of supernovae in the local Universe, it has been inferred that around 24 % of them are thermonuclear supernovae, and the remaining fraction are core-collapse supernovae. Close to 70% of them are "normal" Type II events, and around 30% are stripped-envelope supernovae of different types (Shivvers et al., 2017), as exemplified in the diagram in Figure 1.9. This means that progenitors have been detected for the majority of supernovae, but for a large fraction of them, the type of stars that precede them remains uncertain. The relatively high rate of Types IIb, Ib and Ic suggest that whatever evolutionary channel is responsible for forming them has to be relatively common, so we should be able to associate their progenitors to observed types of stars.

In the simple picture of stellar evolution from birth to death described in Section 1.2.1, all massive stars would spend most of their lives on the main sequence, and then evolve into red supergiants. If this was the case, all supernovae would be of Type II. However, observations of evolved stars in different regions of the HRD, as well as the existence (and relative abundance) of Type Ibc and Type IIb supernovae reveal that this is not how all stars evolve in reality. The simple evolutionary channel described in Section 1.2.1 is missing (at least) three main factors that contribute to the variety of both observed massive stars and supernovae. First of all, stars lose mass from their surface, and this can have a very dramatic effect in the evolution of some stars, especially the most massive ones. Mass loss rates evolve differently for different families of stars in different regions of the HRD, but in general they increase both with increasing luminosity (which implies more massive stars lose mass faster), and with increasing metallicity.

Mass loss through winds can then make massive stars become *stripped*, completely losing their hydrogen envelopes and exposing their helium rich interior. Many such stars have been observed, and they typically inhabit the hot and luminous corner of the HRD, to the left of the main sequence (e.g. Crowther, 2007). Stars in this region of the HRD are typically known as Wolf-Rayet stars. This subclass of stars are often found in said region of the HRD, but are primarily distinguished by their spectra (some Wolf-Rayet stars are also found at lower surface temperatures).

Wolf-Rayet spectra are distinguished by strong, broad emission lines, opposed to most stars that only show absorption features. Emission lines are caused by the intense winds, that cause the circumstellar medium to have high opacities, rendering them *optically thick*, meaning that the intense winds of these stars are opaque, and radiation cannot directly escape the surface of the star, but is rather thermalized by the stellar wind. Therefore, what we actually observe is not the surface of the star itself, but rather the surface of the stellar wind where a transition between opaque and transparent, or optically thick to optically thin, occurs.

There is a large variety of Wolf-Rayet stars with different spectral features, reflecting different conditions in their surfaces and circumstellar media. The main subclasses are WNL, which show weak hydrogen lines, and helium and nitrogen lines, WNE which show helium and nitrogen lines, but often have no hydrogen lines, WC stars that show strong carbon lines, and WO type stars that show

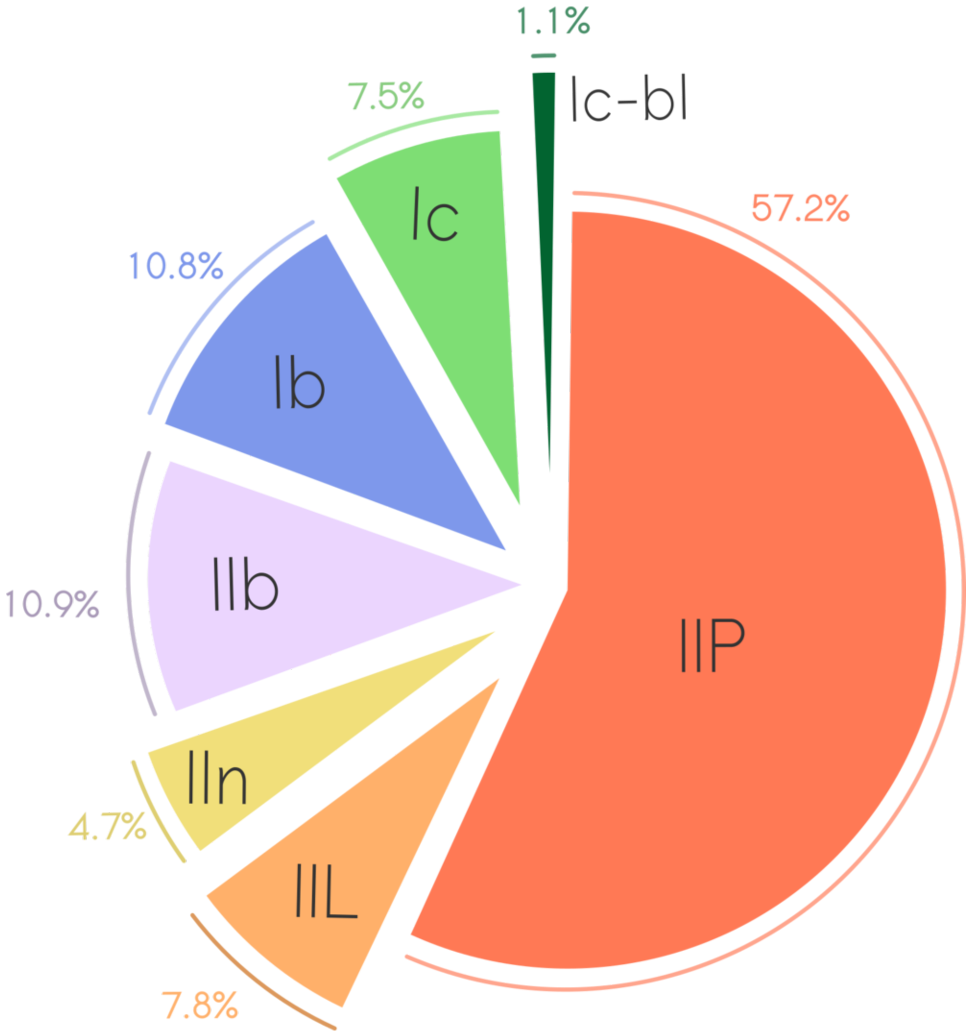

Figure 1.9: Pie chart representing the relative fractions of core-collapse supernovae of different types in a volume limited sample of supernovae with well determined type. Figure courtesy of H. F. Stevance, using data from from Shivvers et al. (2017).

oxygen lines. The differences between these different classes of Wolf-Rayet stars are believed to be connected with varying degrees of stripping. Wolf-Rayet stars also only appear above a certain luminosity, and the minimum luminosity depends on their metallicity (Shenar et al., 2020). Stripped stars below the minimum Wolf-Rayet luminosity are difficult to observe since they are likely compact and hot, and emit most of their radiation in the UV range (Götberg et al., 2017), and they are believed to have weaker winds than their Wolf-Rayet counterparts (Vink, 2017).

Another element that can contribute to producing stripped stars is binarity; i.e. pairs of stars evolving together while being in an orbit around one another. Massive stars are almost always found in binary or multiple systems, and most of them will interact in one of several possible ways before the end of their evolution (Sana et al., 2012). Binary systems are gravitationally bound, and the gravitational potential of such a system has 5 maxima, known as Lagrangian points, through which matter can flow from one component star to another, leave the system, or become accumulated. One of the potential maxima, known as L1, lies along the line that joins the two components, and is located between them. A particle located at this point would feel the same amount of gravitational attraction from both of the stars in the binary, meaning that if one of the stars expands enough so that some of its material reaches this point, it will be removed from it and fall onto its companion. The equipotential surface around each of the components of the binary that goes through this point is known as the Roche lobe, and the most long-lasting type of interaction between stars in a binary is stable mass transfer through L1 when stars overfill their Roche lobe. This interaction can last for relatively long periods of the life of a star, comparable to its nuclear time scale.

Stars in a binary can also interact dynamically through unstable mass transfer, which will lead to a so-called common envelope event (see Ivanova et al., 2013, for a recent review). In this kind of interaction, the star that overflows its Roche lobe grows at a faster rate than the Roche lobe increases in size, and ultimately engulfs its companion inside of its envelope. When this happens, viscosity will quickly lead to a constant decrease in the separation between the core of the expanding star, and its companion. If enough gravitational energy from the tightening of the binary orbit is injected into the envelope of the donor, this type of interaction can lead to the ejection of the envelope, and result in a close binary that includes a stripped star. If the gravitational energy is not enough, this will lead to the merger of both binary components. The details of this process are complicated and uncertain, but it is widely believed that it plays a key role in forming many of the close binary systems that have been observed.

Binarity likely plays a key role in the formation of stripped supernovae (Langer, 2012). Both types of binary interaction are crucial to explain many observed systems such as X-ray binaries, gravitational wave events, supernovae, Wolf-Rayet stars at low luminosity, and several other phenomena. The importance of binarity and mass transfer, and the variety of outcomes for such systems, are illustrated in Figure 1.10. It presents an evolutionary channel for a massive binary that leads to a double neutron star merger, where the binary experiences Roche lobe overflow twice, a common envelope event and survives two supernovae; a channel that is able to explain several known systems with a single initial condition.

Stellar rotation can contribute to forming stars that are hydrogen poor. Rotation has been observed to be common in massive stars (e.g. Ramírez-Agudelo et al., 2013), and it can be included in the one-dimensional description of stellar structure and evolution by considering that, although stars lose their spherical symmetry due to the presence of a centrifugal force that has a preferred axis, the star can still be described by the location of its isobaric surfaces with respect to a dimension that is typically chosen to be the equatorial radius of the rotating star (see, for example, Maeder, 2009, for a review).

Rotation has a lot of effects in the evolution of a star. It changes the structure of the star (Endal et al., 1976), enhances mass loss at the surface (Friend et al., 1986), it makes stars oblate and brighter at the poles than at the equator (von Zeipel, 1924), and it induces mixing of material through different layers of the star by several mechanisms (Heger et al., 2000a). Strong enough rotation to impact stellar evolution

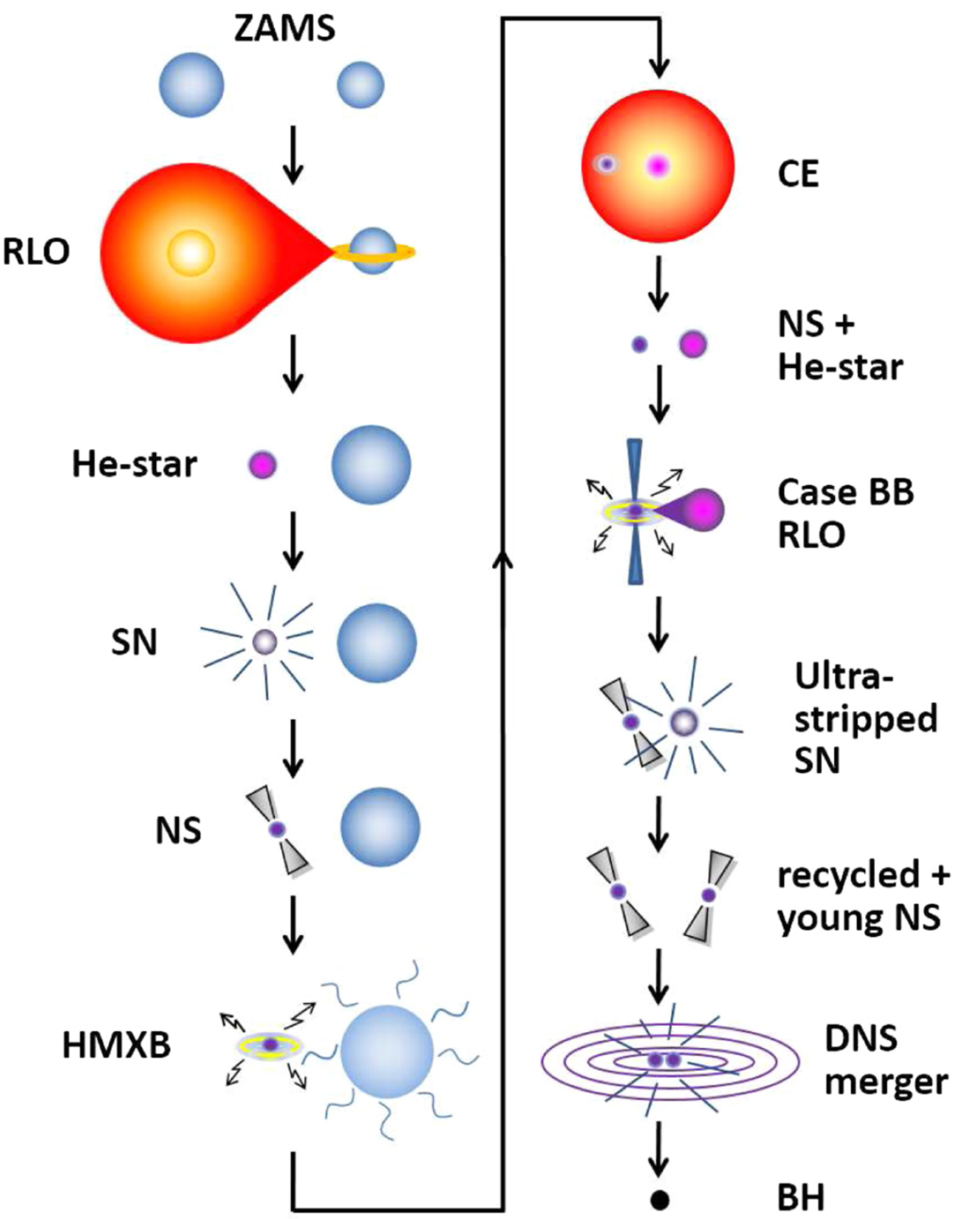

Figure 1.10: A schematic representation of an example evolutionary channel that a massive binary might go through to form a neutron star merger. Represents the evolution of a massive binary system co-evolving from the ZAMS. The system experiences an episode of mass transfer through Roche-lobe overflow (RLO), that strips the donor star from its hydrogen rich envelope. It subsequently evolves as a helium star and explodes as a supernova. The neutron star (NS) remains bound to its companion, and the system becomes a high mass X-ray binary (HMXB). Later, a common envelope (CE) event strips the secondary of its hydrogen-rich envelope, and becomes a helium star. The system experiences Case BB Roche-lobe overflow (after core helium depletion). After the secondary explosion, the system evolves as a neutron star binary, leading to a double neutron star (DNS) merger, creating a stellar mass black hole (BH). Figure adapted from Tauris et al. (2017).

has been observed in massive stars (e.g. Ramírez-Agudelo et al., 2013), and is required to explain the observed rotational velocities of stellar remnants such as white dwarfs and neutron stars (e.g. Suijs et al., 2008). In the most extreme case, stars can evolve chemically homogeneously, if rotational mixing is efficient enough to transport material from surface to core, and vice versa (Maeder, 1987). Chemically homogeneously evolving stars have different properties than those of normal stars, becoming compact and hot immediately instead of expanding and populating the right of the main sequence.

Another element that might affect the outcome of stellar evolution is the specific details of the collapse of the core. It is in itself a complicated phenomenon where the high energy physics of neutrino emission and the general relativistic effects present in high density environments are combined with complex hydrodynamics and energy transport. Therefore, simulations are complex and results are varied (B. Müller, 2016). However, many studies have attempted to parametrize the properties of massive stellar models to predict whether they will produce successful supernova explosions at core collapse, or instead form a black hole (e.g. O'Connor et al., 2011; Ugliano et al., 2012; Sukhbold et al., 2014; Ertl et al., 2016; B. Müller et al., 2016; Sukhbold et al., 2018). They point out the existence of "islands of explodability", and suggest that massive stars above a certain limit do not explode, which seems to be confirmed through observations of supernova progenitors (although the specifics are still a matter of debate; see, for example, Kochanek et al., 2008; Smartt et al., 2009; Davies et al., 2020).

Very massive stars might evolve differently than those stars that experience core collapse at the end of their evolution. As described in Section 1.2.1, the cores of massive stars contract and heat up several times, each time burning a different element to produce energy, starting with hydrogen and concluding with silicon, leaving behind a massive iron core. However, as illustrated in Figure 1.11, the cores of very massive stars may experience an instability in their core during oxygen burning caused by the high temperatures and relatively lower densities in their interiors, where the formation of electron positron pairs is favored for high energy photons in the stellar plasma. Since these stars rely on photons to provide their stabilizing pressure against gravity, the sudden absence of these photons leads to a contraction and heating of their cores. The contraction might be countered by the increase in nuclear energy generation, causing the star to pulsate one or several times, or may lead to an explosion caused by the thermonuclear reactions that leaves behind no remnant (S. E. Woosley, 2017). This type of transient is known as a pair instability supernova, and they are predicted to be luminous and hot (Kasen et al., 2011), likely forming superluminous supernovae (Gal-Yam et al., 2009), although this claim has not been confirmed. For stars of even higher mass, the thermonuclear reactions are not enough to prevent the collapse, and they form black holes directly again, which has consequences for gravitational wave sources, since a gap in the mass distribution is predicted by the existence of these transients (S. E. Woosley et al., 2020).

Although there is a large number of observed progenitors for core-collapse supernovae, many questions about their nature remain unanswered. It is clear that Type II supernovae originate in a class of massive stars called red supergiants, distinguished by low surface temperatures and high luminosities. However, the progenitors of all other classes of supernovae, as well as long gamma-ray bursts, remain a mystery. Many clues have been offered by both theoretical studies and extensive observational campaigns, but explaining the nature of the progenitors of energetic transients and stripped-envelope supernovae remains a challenge.

Superluminous supernovae and gamma-ray bursts, also linked to massive stars, cannot be simply explained by the collapse of the iron core of a massive star into a neutron star. They seem to require an additional (or alternative) source of energy to explain their high luminosities, ejecta velocities and durations. As discussed previously, one of the explanations for superluminous supernovae is pair instability, but the origin of their extreme brightness is still not well established. Several other models have been put forth to explain their luminosities and temporal properties. In the most successful model so far, the magnetar model (Kasen et al., 2010b), the high luminosity and long duration of these transients

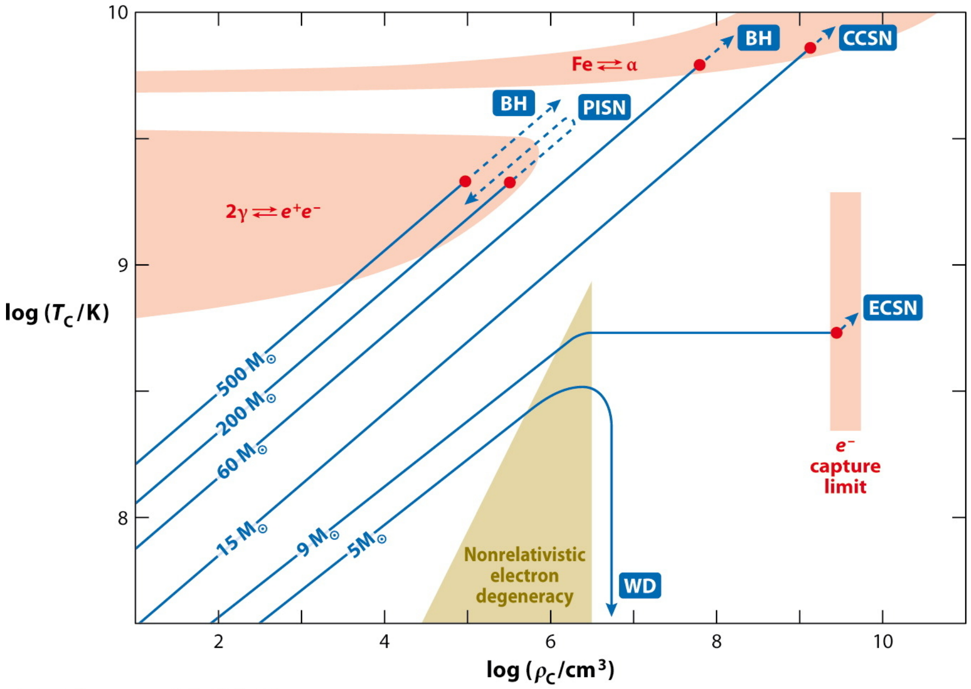

Figure 1.11: Schematic temperature-density diagram, showing approximate evolutionary tracks of stars of different masses (blue lines). Red shaded regions indicate the parameter space where different equations of state lead to instabilities that result in the formation of either a transient, the formation of a black hole, or the formation of a white dwarf. Fe$\rightleftharpoons \alpha$ indicates the region where iron photodisintegrates into alpha particles, leading to core-collapse supernovae (CCSN) or black hole (BH) formation. $2 \rightleftharpoons e^+e^-$ indicates the region where pair creation is favored to occur, leading to pair instability supernovae (PISN). Tracks in the e^- capture limit end up as electron capture supernovae (ECSN, not further discussed). The yellow region highlights the parameter space for low mass stars that become degenerate, and form white dwarfs (WDs). Adapted from Langer (2012).

are explained by the formation of a fast spinning magnetar during the explosion, that continuously deposits part of its rotational energy into the supernova ejecta. In the fallback accretion model (Dexter et al., 2013), similar to the magnetar model, it is sustained accretion of material onto a central compact object that then releases the extra energy that powers the luminous light curve. Other models include energy sources like an anomalous amount of ^{56}Ni being produced by the explosion of a very massive star (Gal-Yam et al., 2009), or the interaction between the explosion ejecta and a dense circumstellar medium (Chevalier et al., 2011). For some supernovae (e.g. T. .-.-W. Chen et al., 2017), several energy sources might have similar contributions to the light curve. However, how stars might evolve to become magnetar powered superluminous supernovae is not well understood, and the quest to constrain the nature of their progenitors, both theoretically and observationally, is ongoing.

On the other hand, the extreme luminosities and energies in gamma ray bursts can be explained by the so-called collapsar model, whereby a very massive and fast rotating star collapses into a fast rotating black hole, a process which generates relativistic jets that finally produced beamed emission of gamma-rays (S. E. Woosley, 1993). Another model that might explain their formation is the magnetar model (Usov, 1992), whereby instead of a critically rotating black hole, a fast spinning magnetar is formed during the collapse of a massive star, and fast rotation and strong magnetic fields power the high luminosity in the light curve, and provide means for the formation of a collimated jet. Therefore, rotation must also play an important role in the evolution of gamma-ray burst progenitors. Chemically homogeneously evolving stars have been proposed as possible progenitors for these transients, since they require to be very fast rotating, and extreme rotation might lead to the prevalence of such stars (e.g. Yoon et al., 2005). This might also help explain their prevalence in relatively low metallicity environments (Palmerio et al., 2019), since the formation of chemically homogeneously evolving stars is favored at lower metallicities (Brott et al., 2011a). Gamma-ray bursts are also connected to type Ic-BL supernovae, implying that the channel that explains their origin should also explain how they have low amounts of helium in their surface, a challenge in previous models.

1.3 Rapidly Rotating Massive Stars at Low Metallicity

Parts of this thesis are a continuation on the work conducted as a Master project, that were published in the Master Thesis titled *Pre-supernova Evolution of Rapidly Rotating Massive Stars at Low Metallicity* (Aguilera Dena, 2017). In this Section, the results from this thesis are summarized.

Two grids of simulations of the evolution of massive stars in the range of 5 to 100 $M_{\odot}$ was performed, from the main sequence to the formation of a massive iron core, using the open-source, 1-dimensional stellar evolution code *Modules for Experiments in Stellar Astrophysics* (MESA, Paxton et al., 2011; Paxton et al., 2013; Paxton et al., 2015), in its version 8845. The initial models have a metallicity of 0.00034, with abundances scaled from the solar abundance (Grevesse et al., 1996), which roughly corresponds to 1/50 $Z_{\odot}$, and have initial surface rotational velocities between 200 and 600 km s^{-1}. The two grids presented in Aguilera Dena (2017) are identical in their initial conditions, but one has the "standard" value of efficiency of rotational mixing (from Brott et al., 2011a, Series A), while the second one has this efficiency enhanced by a factor 10 (Series B).

Models with low metallicity and high rotational velocity may experience chemically homogeneous evolution depending on the strength of rotational mixing. The models of Aguilera Dena (2017) were observed to have a wide parameter space where this evolutionary channel prevailed. Chemically homogeneously evolving stars contract and become more luminous during the main sequence. During this time, rotational mixing is strong enough to keep the star homogeneous, and angular momentum transport is strong enough to keep the star rotating as a solid body.

A dichotomy in the behavior of models from Series A arises from this point on. Models with masses below about 20 $M_{\odot}$ develop helium burning shells at the end of core helium burning, which cause their envelopes to expand, akin to the expansion of red supergiants. Models above the 20 $M_{\odot}$ limit, due to a combination of mixing and mass loss, have less helium in their envelopes at the end of core helium burning and do not develop a helium envelope that ignites strongly enough to expand the star, and thus do not experience an expansion at this point.

Series B models with enhanced rotational mixing efficiency have a behaviour similar to the high mass models of Series A, never developing a helium burning shell and quickly contracting after core helium burning. As a consequence, they behave as C/O cores that have been stripped of hydrogen and helium, and are fast rotators.

The behavior of core contraction and envelope expansion in the sequences of Series A and Series B thus differ dramatically, particularly at lower initial masses, as summarized in Figure 1.12.

The contraction experienced by some of the models accelerates between the end of helium burning and the end of the evolution. The accelerated contraction takes place in the neutrino-mediated thermal time scale,

$$\tau_{\mathrm{KH},\nu} \simeq \frac{GM^2}{R(L+L_\nu)}, \tag{1.5}$$

where L_ν is the total neutrino luminosity. This time scale decreases by several orders of magnitude during

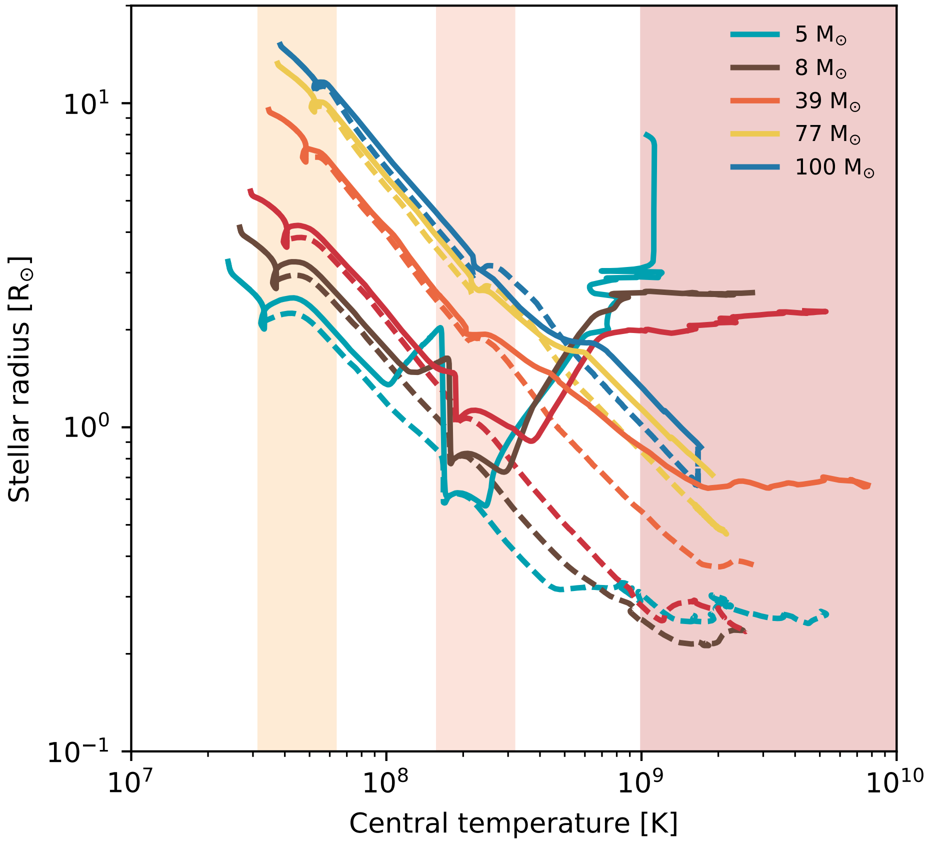

Figure 1.12: Stellar radius as a function of central temperature of the stellar evolutionary sequences of models of different initial mass in Series A (solid lines) and Series B (dashed lines). The temperature ranges where H (light orange), He (dark orange) and heavy element burning (red) occur are highlighted. This figure shows that massive models from Series A, and Series B models, continuously contract during their evolution. Lower mass Series A models develop hydrogen and helium burning shells, and expand during their late evolution. Adapted from Aguilera Dena (2017).

this period. It normally dictates the evolution of stellar cores, but since no core-envelope dichotomy is produced at this stage, the entire star behaves as a massive star core.

Low mass Series A models transport a significant amount of angular momentum from their core to the surface, while more massive stars do not develop these two regions and remain rotating approximately as a solid body. In later stages, starting after core helium burning, even the most massive stars develop a core-envelope structure and thus rotate differentially.

The combination of contraction and angular momentum transport works to increase the surface rotation velocity, bringing it above the critical rotation velocity and inducing mass loss. Thus, the dichotomy in expansion and contraction also creates a dichotomy in amount of mass lost. Models in Series B behave in a similar fashion as the high mass models in Series A, and thus have a similar pattern in mass loss.

Since a significant fraction of the mass that is lost due to rotation is ejected in the late burning phases, from core helium depletion to the end of the evolution, the transient that results from the evolution of these stars is thus expected to encounter and interact with a dense circumstellar medium. The exact structure of this environment is beyond the scope of 1D simulations and has to be resolved through 2D or 3D hydrodynamical simulations, but Aguilera Dena (2017) argue that the circumstellar medium might be very dense, with densities reaching around 10^{-6} g/cm^3. This yields optically thick environments for the higher mass models, despite the fact that this is not expected at their metallicity from the canonical understandig of single, non-rotating stars.

The properties of the circumstellar medium can significantly affect the transients that take place within them. One of the consequences discussed by Aguilera Dena (2017) include the fact that, since the circumstellar medium of some models at the time of supernova will be optically thick, radiation will be trapped within them. This implies that the rise time to its peak luminosity will be slowed down, and they will also slowly decay due to the interaction between the shock and the material it sweeps.

Spectrally, all the supernovae resulting from stars that evolve through this channel will be of Type I. Aguilera Dena (2017) argue that the models with small amounts of helium, like those of Series B, or those of Series A with masses larger than 20 $M_\odot$, will likely result in Type Ic supernovae, possibly superluminous supernovae, Type Ic-BL or long gamma-ray bursts, owing to the high amount of angular momentum they retain.

These results imply that such transients are expected to have signatures of interaction with a dense medium. Even if interaction is not the main source of luminosity of a particular transient, it is likely to have a significant effect. A final episode of mass loss caused by a neutrino-mediated contraction and spin-up might be common in most superluminous supernovae and gamma-ray bursts.

1.4 Context of this Thesis

As described in the previous Sections, the connection between massive star evolution and the physics of supernovae and other astrophysical transients is an extremely powerful tool to understand the physics of massive stars. Many open questions about the connection between transients and their progenitors remain, and it is the attempt of this thesis to help bridge the gap between what we know about massive stars from theory and observation, to what we observe (and what we do not observe as well) in the realm of astrophysical transients. The specific questions and answers that have been addressed in this thesis are described below.

1.4.1 Method

From the physical considerations described in Section 1.2.1, a set of five coupled, first order partial differential equations are obtained. With this set of equations, stellar structure and evolution can be described in one spatial dimension, taken as the Lagrangian mass coordinate, since spherical symmetry is assumed, as a function of time. However, the set of equations is highly non-linear, and exact solutions cannot be readily obtained. The results presented in this thesis rely instead on performing and analysing numerical solutions to this set of equations using the Modules for Experiments in Stellar Astrophysics code (MESA) (Paxton et al., 2011; Paxton et al., 2013; Paxton et al., 2015; Paxton et al., 2018), using different initial and boundary conditions, as well as different implementations of the physical descriptions of different phenomena that take place in the stellar interior.

MESA is an open-source, 1-dimensional code that simultaneously solves the set of equations for stellar evolution by discretizing the radial and temporal dimensions. It allows for choices of different parameters and physical ingredients designed for different problems in stellar evolution, and allows for *ad hoc* implementations of its different parts, determined by the user. The main parameters employed in each set of simulations presented in this thesis is detailed in each Chapter.

1.4.2 A Unified Evolutionary Channel for Progenitors of Superluminous Supernovae and Gamma-ray Bursts

Previous work on the evolution of fast rotating, massive stars in low metallicity environments (Aguilera Dena, 2017), summarized in Section 1.3, concluded that these conditions could lead to the occurence of quasi-chemically homogeneously evolving stars, likely progenitors of energetic transients. It was found that these stars experience heavy mass loss close to the end of their evolution, and it was suggested that the interaction between supernova ejecta and the mass lost to the star in previous evolutionary stages might have significant observable consequences in the spectra and light curves of the transients that result.

A continuation of this work is presented in Chapter 2. Here, the results of Aguilera-Dena et al. (2018) are presented, highlighting the advances made with respect to previous work. In particular, the focus is set of models from Series B, which are found to be able to reproduce several observed properties of both superluminous supernovae and gamma-ray bursts. Properties of their rotational properties, magnetic field distribution, possible circumstellar media are further discussed. The observable consequences of the evolutionary channel are explored in more depth, and we suggest which models might produce different transients, depending on their initial mass, and compare some properties to observations.

1.4.3 Precollapse Properties of Superluminous Supernovae and Long Gamma-Ray Burst Progenitor Models

Similarities in the environments and inferred chemical abundances of long gamma-ray bursts and hydrogen-poor superluminous supernovae, as well as in the power sources that had been proposed by theorists to power both events, led to the belief that they may have a common, related or at least similar origin. This idea was explored in the context of massive stellar evolution in Aguilera-Dena et al. (2018), where an evolutionary channel was proposed to try to give an explanation to the origin of these two types of transient. However, many questions were left open in that study. In particular, the final fate of our models after core collapse is uncertain, as well as what kind of remnant they will leave behind.

Chapter 3 focuses on this question. A set of low metallicity, rapidly rotating stellar models based on the models from Aguilera-Dena et al. (2018) is presented, with an improved treatment of angular momentum loss. These models evolve chemically homogeneously due to rotation, and are evolved from birth to core-collapse.

A comparison with previous models is presented, highlighting the differences that result from the improved physical treatment. Results that relate to an increase in resolution in initial mass are also discussed.

Later, a method to predict the nature of the transients that would be created from such an evolutionary channel is proposed, finding that the variety in both superluminous supernovae and long gamma-ray bursts is a natural outcome of the models.

1.4.4 Type Ibc Supernovae Progenitors and Wolf-Rayet Stars Evolving from Helium Stars in Different Metallicities

Although much is known about the progenitors of core-collapse supernovae, most existing observations are of Type II supernova progenitors. The evolutionary channel experienced by stars that form stripped-envelope supernovae is not completely understood. Yoon (2017) studied how the effect of mass loss from hydrogen-free Wolf-Rayet stars could impact the population of Type Ic and Type Ib supernovae, as well as the properties of Wolf-Rayet stellar populations. They also proposed a correction to typically used

Wolf-Rayet mass loss algorithms, to take the higher mass loss rate of WC stars into account (compared to WN stars of the same luminoisity), as well as to correct for other effects, such as clumping.

The effect of using this mass loss algorithm in stellar evolution was studied by S. E. Woosley (2019), who characterized the evolution of helium stars of different masses in a solar metallicity environment, and by Ertl et al. (2020), who characterized the possible effect it might have on the formation of core-collapse supernovae. This channel was also found by Dessart et al. (2020) to adequately reproduce the dichotomy of spectral properties between Type Ib and Type Ic supernovae, linking it to the effect of Wolf-Rayet mass loss.

Following these works, in Chapter 4 we study the properties of helium stars evolving in different metallicity environments, focusing on the effects that the metallicity dependence of the mass loss algorithm of Yoon (2017) has on helium stars. Through modeling and theoretical analysis, it is found that the mass loss rates of WNE and WC/WO stars can reproduce properties such as the minimum luminosities of Wolf-Rayet stars at different metallicities.

Later, predictions about properties of Wolf-Rayet populations and stripped-envelope supernova statistics are made, finding reasonable agreement with observations.

CHAPTER 2

A Unified Evolutionary Channel for Progenitors of Superluminous Supernovae and Gamma-ray Bursts

In this Chapter, we discuss a set of chemically homogeneously evolving (CHE) stellar models models of fast-rotating, low metallicity massive stars. They are a subset of those discussed in Aguilera Dena (2017), performed in an updated version of MESA. They are modified for better performance, and analysed in more detail, and are further discussed in Aguilera-Dena et al. (2018).

As discussed in Section 1.3, the evolution of CHE stars is dictated by rotational mixing. We find that they reach the end of their lives with no hydrogen or helium in their surface, and are thus are discussed in the context of hydrogen- and helium-deficient transients that are likely powered by rotation: long gamma-ray bursts (lGRBs) and superluminous supernovae (SLSNe), and discuss deeper consequences of the intense, rotationally induced mass loss they experience in their final years.

This Chapter is structured as follows: In Section 2.1 we describe in detail the numerical method employed to calculate these models, and how it differs from those of Aguilera Dena (2017). In Section 2.2 we present the general properties of the evolution and final configuration of the models, and in Section 2.3, we present the observable consequences of the evolutionary channel our models experience. Finally we provide a discussion of our results and our conclusions in Sections 2.4 and 2.5, respectively.

2.1 Method

The evolutionary calculations of massive, fast rotating stars at low metallicity massive stars presented in this Chapter are a an updated version of those performed by Aguilera Dena (2017). They were performed in the 1-dimensional stellar evolution code MESA, albeit in a more recent release (version 10000, Paxton et al., 2011; Paxton et al., 2013; Paxton et al., 2015; Paxton et al., 2018), which includes updated tables for reaction rates, diffusion coefficients, and a few technical improvements over the version used in Aguilera Dena (2017).

They have an initial metallicity of approximately 1/50 $Z_\odot$, scaled from solar metallicity (Grevesse et al., 1996). Their initial masses are in the range between 5 and 100 $M_\odot$, and they have uniform rotational velocity at the beginning of the calculation of 600 km s^{-1}, chosen based on the results of Aguilera Dena (2017) to guarantee CHE. The nuclear network employed in this calculation is the 21 isotope combination included in MESA as `approx21`.

Convection is treated using the Ledoux criterion for instability, and a mixing length parameter of

$\alpha = 1.5$. We include semiconvection following Langer (1991a) and overshooting following Brott et al. (2011a). Rotational mixing is computed following Heger et al. (2000b), including Eddington-Sweet circulation, secular and dynamical instabilities and the Goldreich-Schubert-Fricke instability. Two sets of models are carried out. The first of them, referred to hereafter as Series A, is computed with an efficiency factor for rotational mixing of $f_c = 1/30$, following Brott et al. (2011a), and a second set, Series B, is computed with an efficiency factor 10 times larger.

Rotational mixing guarantees that the models will evolve homogeneously throughout the main sequence, and the Eddington-Sweet circulation produces most of the mixing. After the main sequence, rotational mixing is not efficient enough for stars to remain homogeneous, and chemical composition barriers develop, depending on the structure of convective zones.

Wind mass loss is computed following a similar algorithm to Marchant et al. (2016a). Since metallicity is low, wind mass loss has very little effect on the evolution of our models. However, we include rotationally enhanced mass loss for stars rotating at $\Omega/\Omega_{crit} < 0.98$ following Friend et al. (1986) and and Bjorkman et al. (1993), and if a time step is encountered where this limit is exceeded, it is repeated with a mass loss high enough that guarantees that the star is below this limit at all times.

2.2 Evolution of Chemically Homogeneously Evolving Massive Stars

In this Section, we discuss the evolution of CHE stars, modelled as described in Section 2.1. We highlight the late stages of evolution, as they are the most important in determining the final fate of these systems. A summary of some relevant initial and final properties are presented in Tables 2.1 and 2.2, and are discussed below.

Table 2.1: Initial and final parameters of the evolutionary sequences in Series B. Table adapted from Aguilera-Dena et al. (2018).

Initial mass [$M_\odot$]	5	8	13	39	77	100
Initial $\Omega/\Omega_{\rm crit}$	0.89	0.84	0.79	0.69	0.67	0.67
CO core mass [$M_\odot$] [a]	4.08	6.13	9.18	23.17	41.75	52.47
Final mass [$M_\odot$]	3.36	5.23	8.27	22.05	40.68	51.47
$\Delta M_{\rm H\rightarrow He}$ [$M_\odot$] [b]	0.36	0.55	1.04	4.58	13.58	20.41
$\Delta M_{\rm He\rightarrow final}$[$M_\odot$] [c]	0.68	0.86	0.92	1.13	1.07	0.99
$f_{\rm M}$	0.27	0.19	0.12	0.06	0.20	0.62
Final Radius [cm]	2.15×10^{10}	2.27×10^{10}	1.52×10^{10}	2.72×10^{10}	3.31×10^{10}	4.14×10^{10}
Final $T_{\rm eff}$ [K]	1.63×10^{5}	1.72×10^{5}	1.16×10^{5}	2.68×10^{5}	3.63×10^{5}	2.96×10^{5}
Final H mass [$M_\odot$]	0	0	0	0	0	0
Final He mass [$M_\odot$]	0.04	0.05	0.03	0.06	0.03	0.04
Final $Y_{\rm surf}$	0.10	0.08	0.07	0.03	0.02	0.02
Radius at $\tau = 1$ [cm]	2.78×10^{12}	1.98×10^{12}	3.32×10^{13}	2.16×10^{13}	1.67×10^{13}	1.33×10^{13}
$\bar{j}_{1.5M_\odot}$ [cm^2 s^{-1}]	1.03×10^{15}	1.27×10^{15}	2.16×10^{15}	1.15×10^{15}	5.15×10^{15}	4.50×10^{15}
$\bar{j}_{2M_\odot}$ [cm^2 s^{-1}]	1.38×10^{15}	1.92×10^{15}	3.17×10^{15}	2.38×10^{15}	6.35×10^{15}	5.76×10^{15}
$\bar{j}_{5M_\odot}$ [cm^2 s^{-1}]	–	3.25×10^{16}	1.28×10^{16}	9.36×10^{15}	1.29×10^{16}	1.16×10^{16}
$P_{\rm rot}$ (1.5 $M_\odot$ NS) [ms] [d]	4.66	3.76	2.22	4.15	0.93	1.06
$E_{\rm rot}$ (1.5 $M_\odot$ NS) [erg] [d]	2.07×10^{51}	3.18×10^{51}	9.11×10^{51}	2.60×10^{51}	5.18×10^{52}	3.96×10^{52}
Final fate	CCSN	CCSN	CCSN	CCSN	PPISN	PPISN

[a] At core He depletion

[b] Mass lost from between H and He burning, defined as $\Delta M_{\rm H\rightarrow He} = \int_{T8_c>0.5}^{T8_c<1.2} \dot{M}\,dt$

[c] Mass lost from He core depletion to the end of the simulation

[d] Mass lost from He core depletion to the end of the simulation

Table 2.2: Initial and final parameters of the evolutionary sequences in Series A. Table adapted from Aguilera-Dena et al. (2018).

Initial mass [$M_\odot$]	5	8	13	39	77	100
Initial $\Omega/\Omega_{\rm crit}$	0.89	0.84	0.79	0.69	0.67	0.68
CO core mass [$M_\odot$] a	1.43	2.63	6.06	24.80	42.66	53.51
Final mass [$M_\odot$]	4.19	6.40	9.61	26.04	41.59	52.47
$\Delta M_{\rm H\rightarrow He}$ [$M_\odot$] b	0.51	0.58	1.05	4.48	13.21	19.84
$\Delta M_{\rm He\rightarrow final}$[$M_\odot$] c	0.01	0.25	0.83	1.27	1.06	1.00
$f_{\rm M}$	0.004	0.05	0.09	0.05	0.20	0.60
Final Radius [cm]	2.38×10^{11}	1.76×10^{11}	1.34×10^{11}	3.43×10^{10}	3.90×10^{10}	4.62×10^{10}
Final $T_{\rm eff}$ [K]	4.85×10^{4}	6.86×10^{4}	9.52×10^{4}	2.12×10^{5}	2.86×10^{5}	2.84×10^{5}
Final H mass [$M_\odot$]	0.01	0	0	0	0	0
Final He mass [$M_\odot$]	2.32	3.33	3.19	1.16	0.05	0.07
Final $Y_{\rm surf}$	0.98	1.00	0.99	0.90	0.03	0.03
Radius at $\tau = 1$ [cm]	–	–	–	9.05×10^{13}	1.61×10^{13}	1.22×10^{13}
$\bar{j}_{1.5M_\odot}$ [cm^2 s^{-1}]	2.46×10^{14}	2.83×10^{14}	8.88×10^{14}	1.88×10^{15}	5.20×10^{15}	4.48×10^{15}
$\bar{j}_{2M_\odot}$ [cm^2 s^{-1}]	8.32×10^{14}	3.57×10^{14}	8.88×10^{14}	3.72×10^{15}	6.41×10^{15}	5.73×10^{15}
$\bar{j}_{5M_\odot}$ [cm^2 s^{-1}]	–	2.73×10^{16}	3.40×10^{15}	1.12×10^{16}	1.31×10^{16}	1.15×10^{16}
$P_{\rm rot}$ (1.5 $M_\odot$ NS) [ms] d	19.42	16.89	5.39	2.54	0.92	1.07
$E_{\rm rot}$ (1.5 $M_\odot$ NS) [erg] d	1.19×10^{50}	1.57×10^{50}	1.54×10^{51}	6.93×10^{51}	5.29×10^{52}	3.92×10^{52}
Final fate	CCSN	CCSN	CCSN	CCSN	PPISN	PPISN

[a] At core He depletion

[b] Mass lost from between H and He burning, defined as $\Delta M_{\rm H\rightarrow He} = \int_{T8_c>0.5}^{T8_c<1.2} \dot{M}\,dt$

[c] Mass lost from He core depletion to the end of the simulation

[d] Mass lost from He core depletion to the end of the simulation

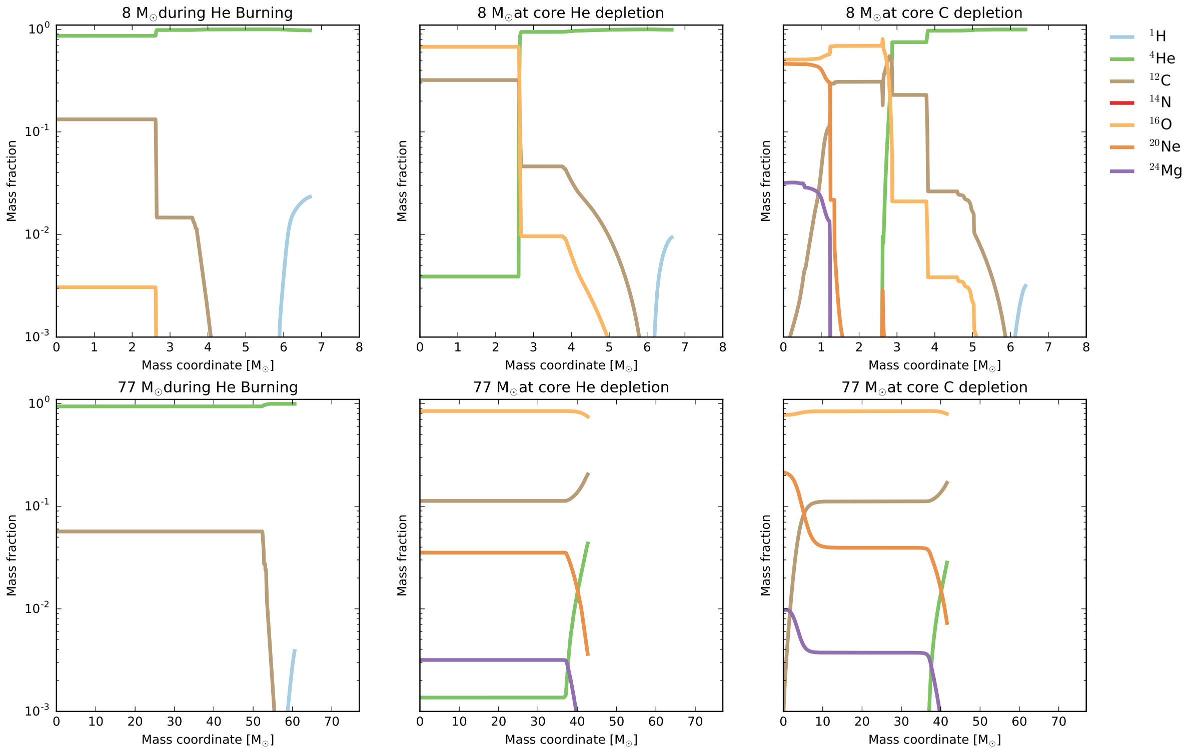

Figure 2.1: Mass fractions of the major chemical elements as function of mass in stellar models from two evolutionary sequences of Series A at three different times, during core He burning, at He core depletion, and at C core depletion. Figure adapted from Aguilera-Dena et al. (2018).

2.2.1 Evolution of the Chemical Composition

As found by Aguilera Dena (2017), during the main sequence, our models remain quasi-homogeneous in composition, quickly becoming enriched in helium and nitrogen due to hydrogen burning following the CNO cycle. At the end of hydrogen burning, they contract homologously until their core temperature becomes high enough to burn helium. Since the star contracts during this stage, its surface rotational velocity increases due to conservation of angular momentum. As the surface rotational velocity increases, so does the mass loss rate, so if any hydrogen is left close to the surface, most of it will be lost during the contraction.

High mass models (with initial masses above ~20 $M_\odot$) in Series A and all models in Series B remain quasi-homogeneous throughout most of helium burning, while low mass models in Series A develop a core-envelope structure and might even retain trace amounts of hydrogen at the surface. This is illustrated by two examples in Figure 2.1 for Series A models, and in Figure 2.2 for Series B models.

By the end of carbon burning, low mass models in Series A have developed a complex chemical structure, similar to that of the core of low-rotating massive stars (Heger et al., 2000b). More massive models and Series B models stop being homogeneous at this point, but they develop larger carbon-oxygen cores and retain a very small amount of helium at this stage.

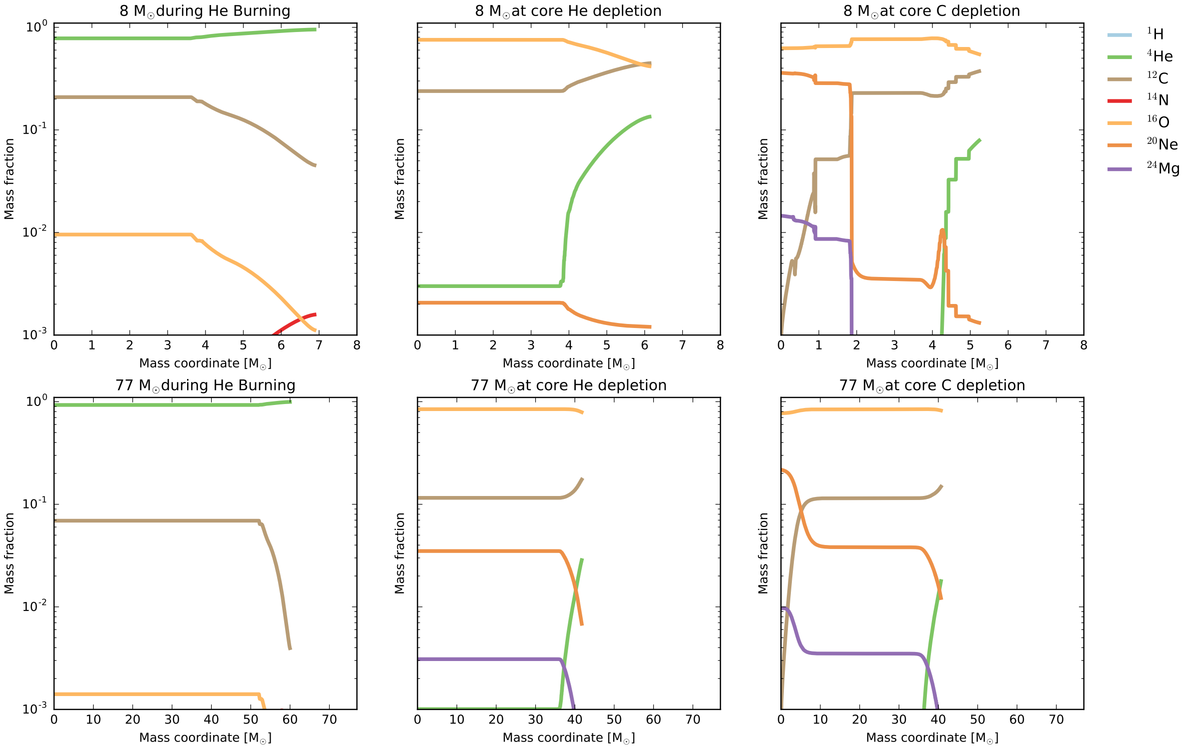

Figure 2.2: As Figure 2.1, but for the corresponding models from the B Series. Figure adapted from Aguilera-Dena et al. (2018).

2.2.2 The Radius of Chemically Homogeneous Stars

Non-rotating and slowly-rotating stars end their main sequence life time with a helium core and a helium envelope. As the core contracts and heats up before core helium burning, so do the layers immediately above. This causes a shell at the bottom of the hydrogen envelope to become hot enough to burn hydrogen, and this causes the envelope of such stars to expand, as the envelope continues to contract.

In CHE stars, the not a lot of hydrogen is left in the star after core hydrogen burning. Therefore these stars contract as a whole after core hydrogen depletion. As shown in Figure 1.12, only the lowest mass model in Series A experiences a weak expansion, but rotationally enhanced mass loss will cause the star to lose the rest of its remaining hydrogen, and it will continue to contract.

As observed in Aguilera Dena (2017) and Aguilera-Dena et al. (2018), high mass models in Series A, and models in Series B will contract throughout almost their entire evolution, and contraction will become accelerated by a reduction of the thermal timescale bought about by the sharp increase in neutrino luminosity (Equation 1.5).

2.2.3 Angular Momentum Distribution

Our models are initially set up to rotate as solid bodies. Changes in density cause the rotation velocity of contiguous layers to be different. If no mechanisms of angular momentum transport were present within the star, the stellar core would increase its rotational velocity due to core contraction, whereas the external layers of a star that expand would slow down, both by the effect of expansion and as a consequence of the loss of angular momentum attached to the mass the stars lose at their surface.

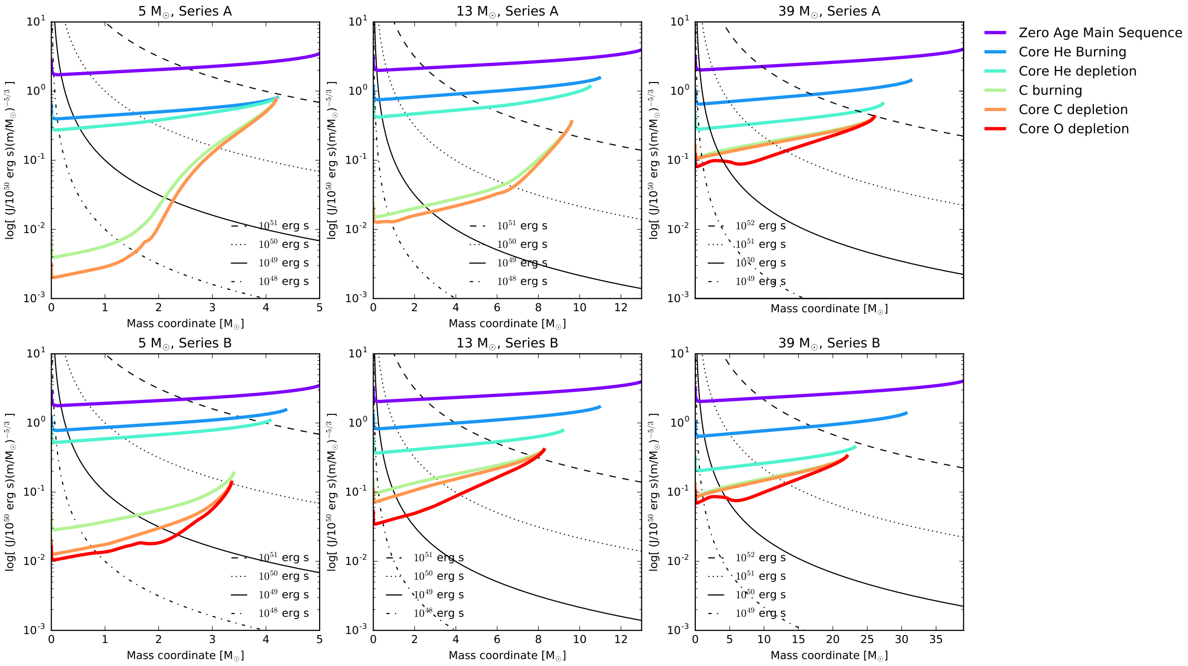
5 M$_\odot$, Series A

13 M$_\odot$, Series A

39 M$_\odot$, Series A

5 M$_\odot$, Series B

13 M$_\odot$, Series B

39 M$_\odot$, Series B

Figure 2.3: Integrated angular momentum divided by ($m^{5/3}$ as a function of mass coordinate m, plotted for several models of Series A (top) and Series B (bottom) during the ZAMS (purple), during core helium burning (blue), at core helium depletion (light blue), at the onset of carbon burning (green), at core carbon depletion (orange), and at core oxygen depletion (red). Black lines are contours of constant angular momentum. Figure adapted from Aguilera-Dena et al. (2018).

However, several mechanisms are at work that transport angular momentum between regions that experience differential rotation. Convection and hydrodynamic instabilities transport angular momentum efficiently but act on generally small areas of a star. A much more efficient mechanism is the so-called Spruit-Tayler dynamo. Differential rotation induces the formation of large scale magnetic fields, that induce torques in the star. This mechanism works to keep stars rotating uniformly, and has been used to explain the rotation velocities of white dwarfs (Suijs et al., 2008) and pulsars (Heger et al., 2005) which is otherwise overestimated in evolutionary models that do not include its effects.

To study how angular momentum is distributed throughout a star, Aguilera-Dena et al. (2018) follow the approach of Suijs et al. (2008), through the distribution of the quantity

$$m^{-5/3}J(m) = m^{-5/3}\int_0^m j(m')\mathrm{d}m', \tag{2.1}$$

where m is the Lagrangian mass coordinate of the star, $j(m)$ the specific angular momentum of the layer at m, and $J(m)$ is the total angular momentum integrated from $m' = 0$ to $m' = m$. This quantity is used as a tool to study the distribution of angular momentum in stars since a spherical object with constant density that rotates uniformly will have a constant value at every m. It is presented for a few models in different evolutionary stages in Figure 2.3.

As shown in Figure 2.3, a very significant amount of angular momentum is lost due to mass loss between different stages of the evolution in all models. Low mass models of Series A, however transport a large amount of angular momentum from the core to the envelope, since they rotate differentially. Whereas the high mass models in Series A, and those in Series B will likely be able to produce millisecond

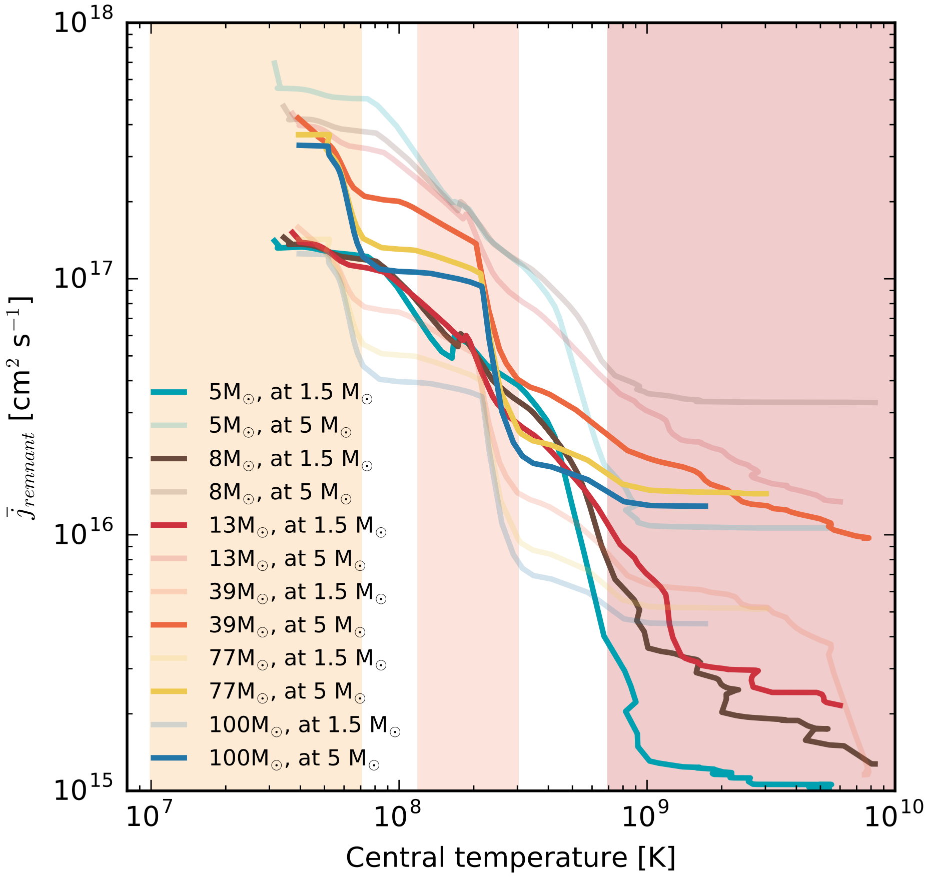

Figure 2.4: Mass average of the specific angular momentum of the innermost region of our Series B models as a function of central temperature. Solid lines show the average over the innermost 1.5 $M_\odot$ for models with initial mass below 20 $M_\odot$, representative of the region of the star that is likely to end up as a neutron star. For models with initial mass larger than 20 $M_\odot$, we show the average over the innermost 5 $M_\odot$, representative of the region that is likely to form a black hole, are shown in solid lines. In both cases, the corresponding average over the alternate representative mass of a potential remnant is shown in transparent lines of the same color. Figure adapted from Aguilera-Dena et al. (2018).

pulsars upon core collapse, low mass models in Series A will not retain enough angular momentum in their cores to do so.

Similarly, as found in Aguilera-Dena et al. (2018), enough angular momentum is retained in Series B and high mass Series A models to produce lGRBs in the collapsar scenario. This is shown in Figure 2.4, which shows the evolution of the average specific angular momentum that is retained in the innermost 1.5 $M_\odot$ (representative of a neutron star mass) and the innermost 5 $M_\odot$ (representative of the mass of a black hole). In all cases, if a neutron star is formed, the innermost 1.5 $M_\odot$ contain enough angular momentum to become a milisecond pulsar (above 10^{15} cm^{2}s^{-1}), and the innermost 5 $M_\odot$ contain enough angular momentum to form a critically rotating black hole (above 10^{16} cm^{2}s^{-1}).

2.2.4 Rotationally Enhanced Mass Loss

As discussed in Section 2.2.2, CHE stars will contract due to neutrino losses and the absence of an expanding envelope. This will make stars approach critical rotation in several stages of their evolution, particularly during the contraction phase between hydrogen depletion and helium core burning, and after core helium depletion. Aguilera Dena (2017) found that, despite the expectations that massive stars at low metallicity are not expected to lose a lot of mass, the combined effect of contraction and angular momentum transport to the surface will induce heavy mass loss, as high as $10^{-2}\ M_{\odot}\mathrm{yr}^{-1}$ in some cases, as shown in Figure 2.5.

As pointed out by Aguilera-Dena et al. (2018), the mass lost from the star due to rotation will probably remain close to the star, as it is not accelerated by radiation, as in the case of WR stars, but rather by centrifugal acceleration, which becomes weaker as the mass is displaced away from the stellar surface. However, since the star is rotating near-critically throughout its evolution, this mass will likely not be re-accreted and will accumulate close to the stellar surface. Assuming a wind velocity of 500 km s^{-1}, just a fraction of the observed wind velocities in Wolf-Rayet stars, the photon tiring limit is exceeded (Heger et al., 1996; Owocki et al., 1997; Grafener et al., 1998), implying that a wind with such velocity would violate energy conservation.

The momentum limit for mass to be accelerated at infinity is also violated, at even smaller mass loss rates. This limit has been observed to be violated in Wolf-Rayet stars due to multiple scattering events, by a factor of a few (Springmann, 1994). However, as shown in Figure 2.6, this limit is exceeded by more than a factor of ten during the period where mass loss becomes enhanced close to core collapse in our Series B models.

The mass lost in the stage between core helium depletion and the end of the evolution is close to 1 $\mathrm{M}_{\odot}$ in most Series B models, and in massive models of Series A (see Tables 2.1 and 2.1). Since the mass cannot be accelerated to infinity by radiation, Aguilera-Dena et al. (2018) concluded that this mass will be located near the stellar surface. Since mass loss is most likely concentrated along the rotation plane of the star, it will likely form a structure similar to that found by van Marle et al. (2008), who performed hydrodynamical simulations of the mass distribution that results from a critically rotating star losing mass due to its rotation. At the highest masses (models with 77 and 100 $\mathrm{M}_{\odot}$ in our figures), however, stars will likely experience pulsations due to pair instability. These will lead to additional, likely spherical mass loss, so that the structure of the circumstellar medium (CSM) will likely be different than in the cases where an iron core is formed and collapses.

2.2.5 Magnetic fields

As discussed in Section 2.2.3, the angular momentum distribution in our models is initially uniform, and its evolution is regulated by several mechanisms that transport angular momentum. Chief amongst these mechanisms is the Spruit-Tayler dynamo. Through this mechanism, magnetic fields that are generated due to the dynamo effect induced by differential rotation inside the star, and induce magnetic torques in regions of differential rotation, effectively transporting angular momentum from the faster spinning regions of the star, to the slower spinning regions. These are calculated in MESA following the implementation of Heger et al. (2005). Differential rotation in the stellar interior can occur during stages where certain parts of the star either contract or expand at a different rate than their neighboring layers.

The Spruit-Tayler dynamo will act to keep rotation uniform within the star, and will accomplish this if the time scale of angular momentum whenever the time scale for angular momentum diffusion is smaller than the time scale of contraction or expansion. Whenever differential rotation is present, magnetic fields will be generated inside the star, and these could persist throughout long periods, be present at the time

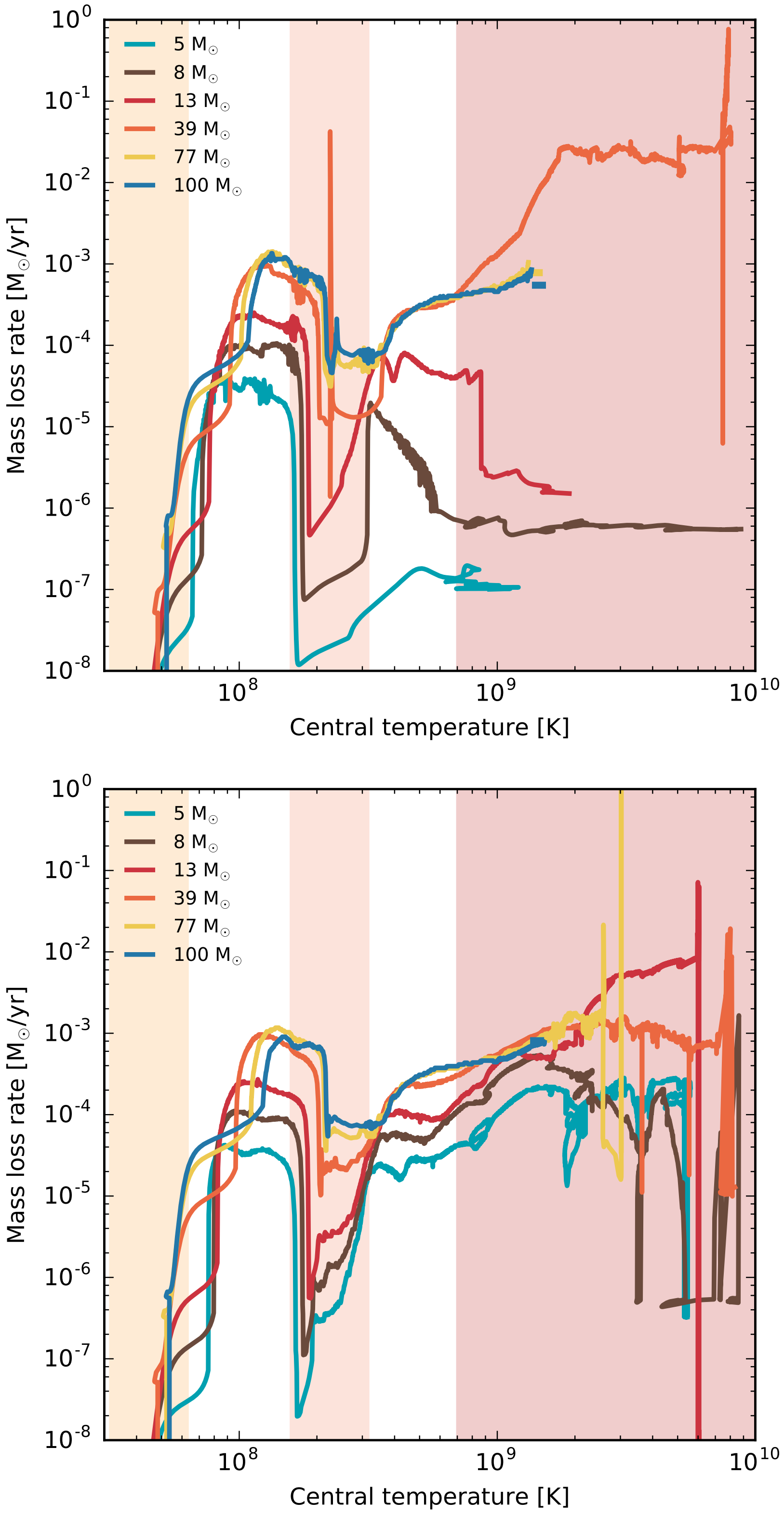

Figure 2.5: Mass loss rates of Series A models (top) and Series B models (bottom) as a function of central temperature. Highlighted areas show the temperature regimes where hydrogen burning (light orange), helium burning (dark orange) and heavy element burning (red) take place. Figure adapted from Aguilera-Dena et al. (2018).

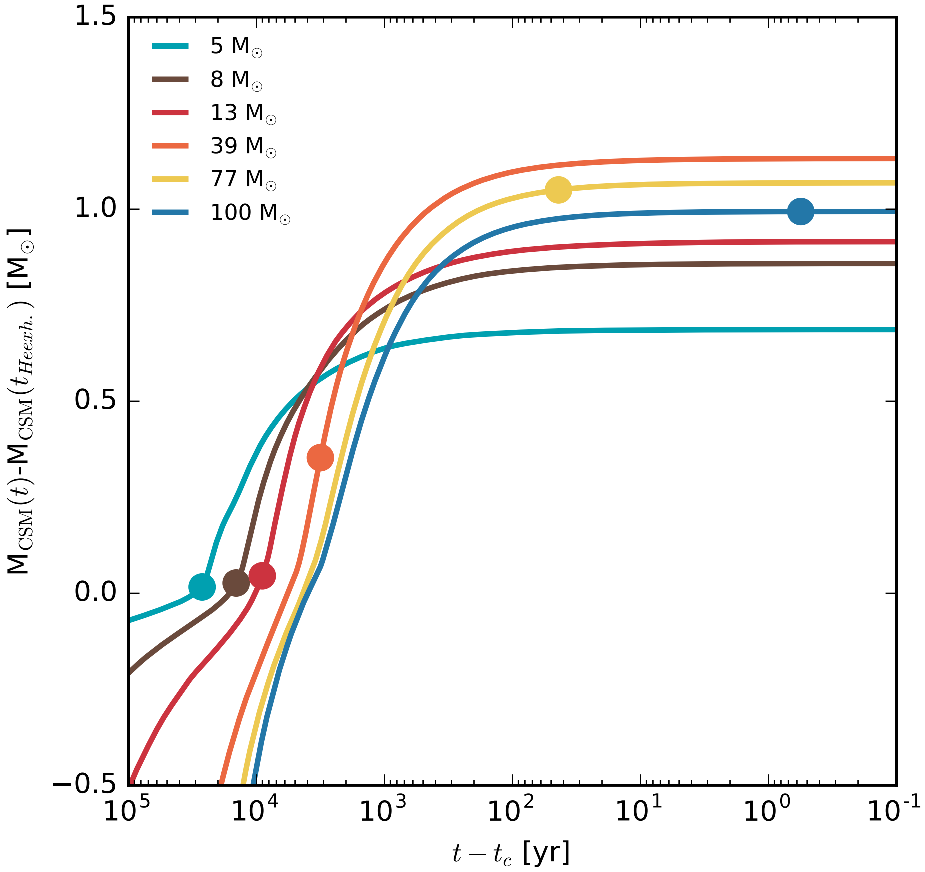

Figure 2.6: Time integrated mass loss rate with the end of core helium burning as zero point in time, as function of time, for six models of our Series B (bottom). Dots indicate where the mass loss rate becomes 10 times higher than that allowed by the momentum limit. Figure adapted from Aguilera-Dena et al. (2018).

of core collapse, and influence the explosion that results from it (Akiyama et al., 2003; Masada et al., 2015; Guilet et al., 2015; Mösta et al., 2015; Masada et al., 2012; Obergaulinger et al., 2018).

The configuration of the magnetic fields in the interior of some a few example models of Series B are presented in Figure 2.7, along with their final rotation profile. At the time of core collapse, the star is no longer chemically homogeneous (see, e.g. Figures 2.1 and 2.2), and therefore the rotation profiles of our models at this time has regions with vastly different rotation rates. As found by Aguilera-Dena et al. (2018), as different layers of CHE stars contract at different rates, strong magnetic fields are formed, trying to redistribute angular momentum throughout them. The toroidal component of the dynamo-generated magnetic fields in the innermost few solar masses of our models close to core collapse is of the order of 10^{10} – 10^{11} G, while the radial component is a few orders of magnitude smaller, although it can also reach very high values in the interfaces of layers that have very different rotation rates.

Magnetic fields of this magnitude are much larger than those found in stars that evolve normally (e.g. Heger et al., 2005). As discussed by Aguilera-Dena et al. (2018), assuming that magnetic flux is conserved during the formation of the neutron star, and assuming that it is formed with a mass of 1.5 M$_\odot$ and a radius of 15 km, the resulting magnetic fields will be amplified up to 10^{14} – 10^{15} G, in line with the observed values of magnetic fields in SLSNe, which are in the order of 10^{13} – 10^{15} G (Blanchard et al., 2020). However, the collapse of an iron core and formation of a neutron star is a complex problems, and magnetic flux is probably not conserved. Detailed simulations indicate that magneto-rotational instabilities can amplify and change the direction of seed magnetic fields, and affect the properties of the resulting transient (e.g. Rembiasz et al., 2016; Bugli et al., 2020; Obergaulinger et al., 2020). Therefore, we cannot predict the final strength of the magnetic fields from our stellar evolutionary calculations alone, but previous studies have found that magnetic fields comparable to the ones in our models can be dynamically important, and potentially produce magnetars.

We do not discuss the magnetic fields of models with 77 and 100 $M_\odot$, since they are not evolved until their pre-explosion configuration. These models will be subject to pair instability (see Section 1.2.3, and S. E. Woosley 2017 for information about pair instability in massive stars, the limit for the onset of pair instability is also discussed in Chapter 3). Pair instability can induce pulsations that remove mass and remove and redistribute angular momentum in the interior of such stars, and the extent of pair instability in rotation is not known.

2.3 Astrophysical Transients Produced by Chemically Homogeneously Evolving Stars

The possible transients that arise from the evolutionary channel described in this Chapter are discussed by Aguilera Dena (2017) and Aguilera-Dena et al. (2018), the latter focusing on the outcome of the evolution of Series B models.

The observable properties of transients resulting from CHE stars will be influenced by the properties discussed in Section 2.2. At the time of core collapse, they are free of hydrogen and have very little helium in their envelopes, so they are likely to produce Type Ic SNe. They are also very fast rotating and have high magnetic field strengths, and are surrounded by a dense CSM. In this Section, we discuss the consequences of these properties in the resulting transients.

Aguilera-Dena et al. (2018) discuss the possible explosive outcomes of CHE stars assuming that they change as a function of their initial mass. They subdivide the possible outcomes in four categories: Low mass, intermediate mass, high mass and very high mass. This question is explored in more detail in Chapter 3, but we discuss the insights of Aguilera-Dena et al. (2018) below.

2.3.1 Shock Break-out

The earliest SN electromagnetic emission is released when the shock formed within the star reaches layers near the stellar surface, and the medium becomes transparent enough for radiation to escape the shock (e.g. Colgate, 1974). This is known as shock break-out, and the properties of the signal are strongly dependent on the CSM (e.g. Ofek et al., 2010).

Compact massive stars are expected to have a shock break-out duration of the order of a few seconds, but if an optically thick CSM is present, the duration can extend to hundreds of seconds (e.g. Balberg et al., 2011; Svirski et al., 2014; Waxman et al., 2017).

The expected break-out signal from our models depends on the detailed distribution of CSM density, but if a spherically symmetric wind is assumed, Series B models will have an optically thick CSM, and therefore the signal could last up to a few hundred seconds.

However, our models are expected to have asymmetric CSM, due to the centrifugally induced mass loss of our models. If the material is concentrated in the equatorial plane, a shock break-out signal from our models could be expected to be very short. However, the interaction between the ejecta and the CSM along the rotation plane might influence the early light curve of a SN resulting from our models.

Detailed simulation is required to constrain the shape of the shock-breakout signal, that includes a realistic CSM, and the shape of the signal will likely depend on the angle between the event and the observer.

2.3.2 Interaction with the Circumstellar Medium

As the SN ejecta expands through a dense CSM, the collision can convert the kinetic energy of the expanding material into radiation. If enough matter is present in the CSM, this can lead to an effect in the light curve and spectra of SNe (e.g E. Sorokina et al., 2016).

Aguilera-Dena et al. (2018) estimate this via the parameter f_M, which is a measure of the fraction of the kinetic energy of the ejecta can be converted into radiation, and depends on the ejecta mass M_{ej} and the CSM shell mass M_{sh}, as

$$f_M = \frac{M_{sh}}{M_{ej} + M_{sh}}. \tag{2.2}$$

This quantity is derived by assuming that momentum is conserved during the collision of the ejecta with a shell of mass M_{sh}.

Assuming that the ejecta mass is given by the difference between the final model mass and the remnant that is left behind after the explosion, Aguilera-Dena et al. (2018) calculate this for the models in the grid, assuming remnant masses of 1.5 and 5 $\mathrm{M}_\odot$, representative of a neutron star and a black hole, and assuming that the mass of the shell corresponds to the mass lost by the star between the end of helium burning and the collapse of the iron core, denoted as $\Delta\mathrm{M}_{\mathrm{H}e\rightarrow final}$ in Table 2.1.

A result of this calculation is shown in the right y-axis of Figure 2.8. Since most models roughly have 1 $\mathrm{M}_\odot$ in their CSM, f_M decreases as the ejecta mass increases. However, in the models with the lowest initial mass, the fraction reaches up to 0.3, meaning that a very significant portion of the ejecta energy can be converted into radiation in this case. At the highest masses in Figure 2.8, it is assumed that a significant amount of mass is lost from the system due to pulsations induced by pair instability, and M_{sh} is approximated by interpolating the values obtained by S. E. Woosley (2017) for stars of the corresponding core mass as those of our models (See Section 2.3.5 for a discussion).

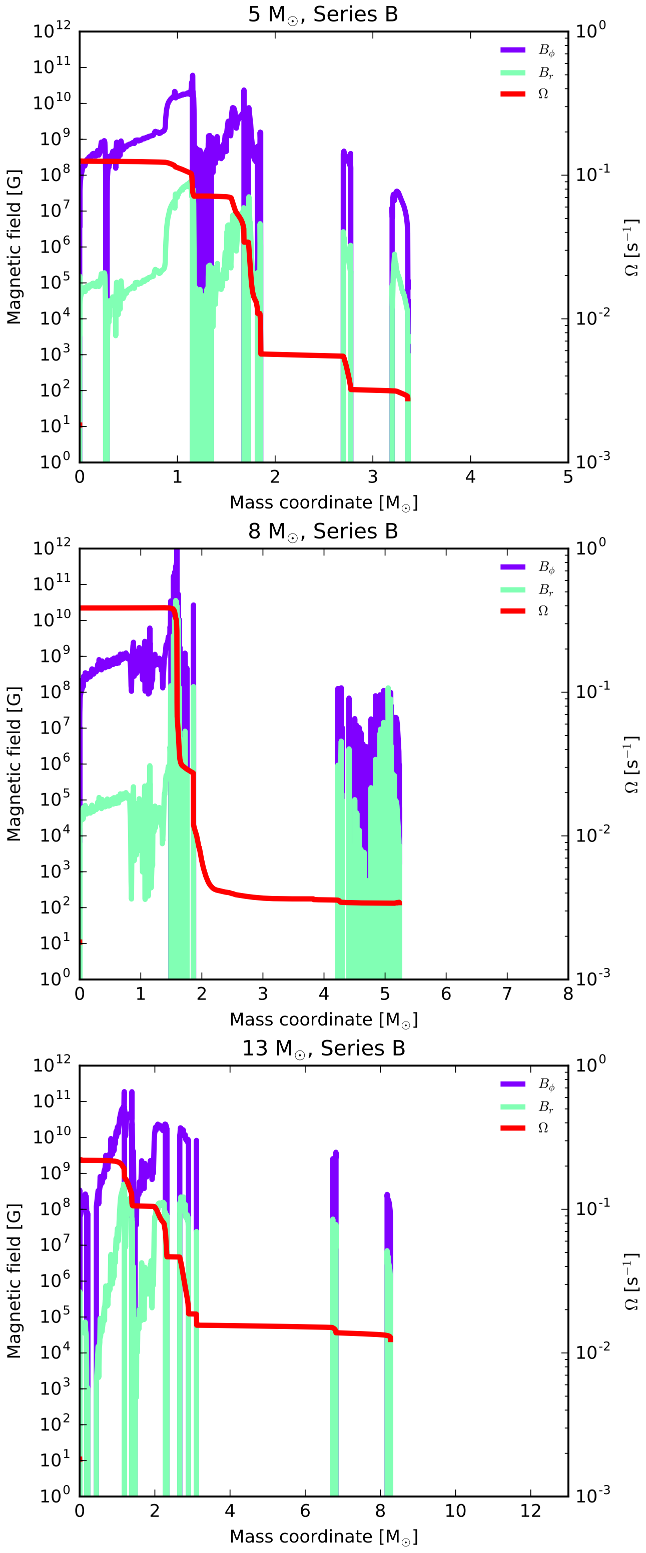

Figure 2.7: Polar and radial magnetic fields (left y-axis) and rotational frequency (right y-axis) of the final models of 3 different evolutionary sequences from Series B. Figure adapted from Aguilera-Dena et al. (2018).

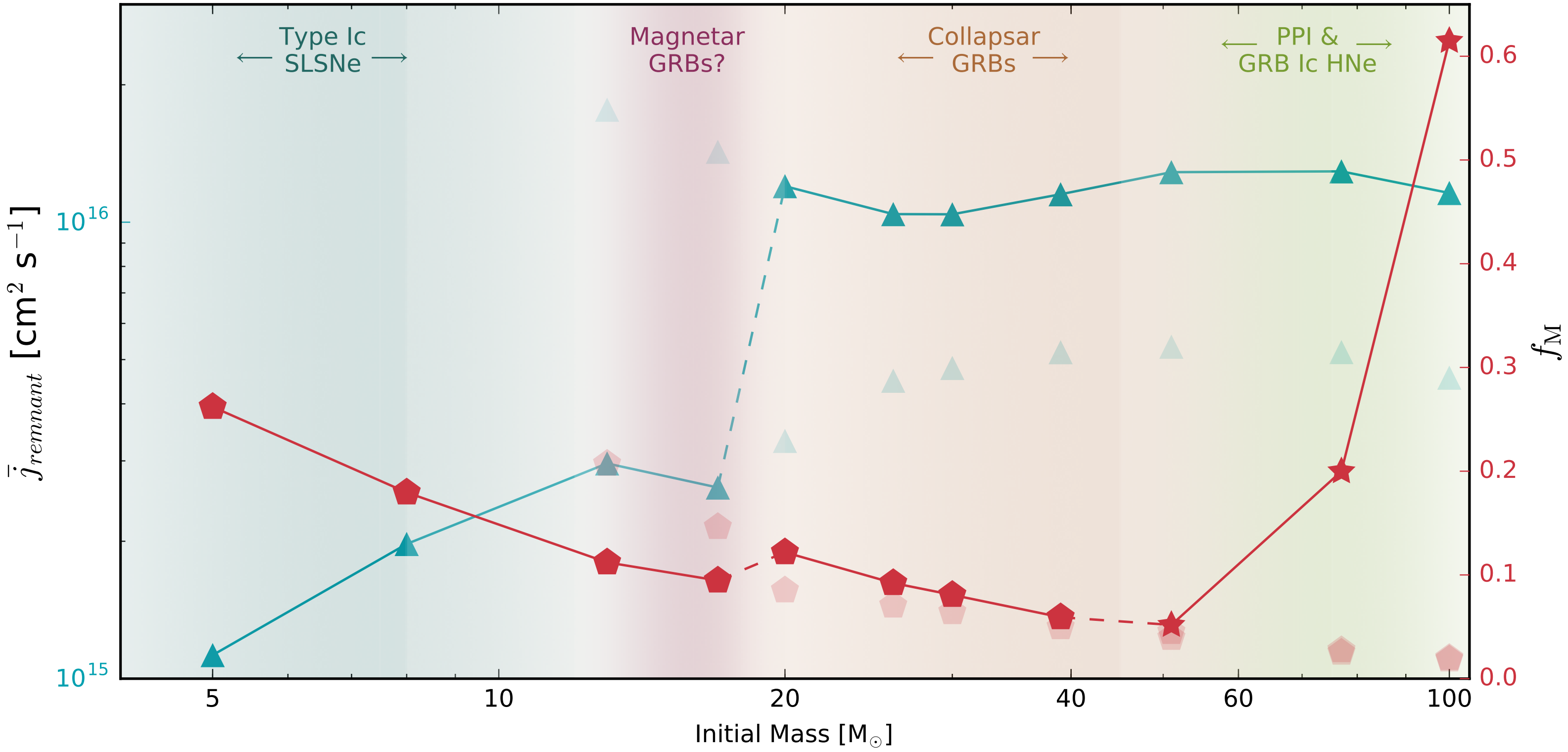

Figure 2.8: Average angular momentum at core O depletion of the first 1.5 $M_\odot$, for models with mass $M< 20$ $M_\odot$, and first 5 $M_\odot$ for the rest (left axis, blue triangles); and the ratio between shell and ejecta masses for the same remnant masses (right axis, red pentagons), as a function of initial mass for Series B models. The values for converse masses are added in lower saturation for comparison. The ratio between shell and ejecta mass for models that undergo pulsational pair instability is also calculated (red stars), with ejected shell masses according to S. E. Woosley (2017).

2.3.3 Expected Outcome for Different Models: Superluminous Supernovae

A large sample of SLSNe light curves has been analysed (Nicholl et al., 2017; Villar et al., 2018; Blanchard et al., 2018; Blanchard et al., 2019; Blanchard et al., 2020) assuming that their bright light curves are powered by fast spinning magnetars (Kasen et al., 2010a; S. E. Woosley, 2010). This analysis provides values for the ejecta masses, kinetic energies, magnetar spin periods and magnetic fields in SLSNe. The values of ejecta mass and spin period obtained from the observations correspond to the range of values obtained for our models, as shown in Figure 2.9.

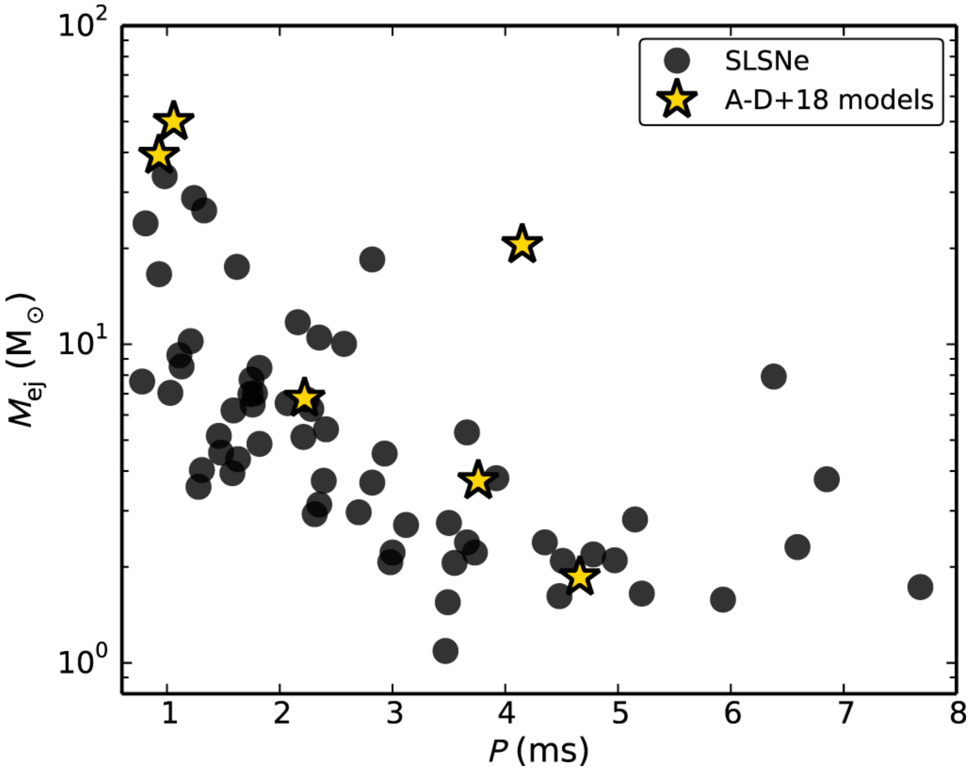

Figure 2.9: Ejecta masses and magnetar spin periods inferred for the sample in Blanchard et al. (2020) (black points), compared to the values inferred for the models presented in Aguilera-Dena et al. (2018) (yellow stars). Figure adapted from Blanchard et al. (2020).

Aguilera-Dena et al. (2018) assumed that lower mass models will give rise to magnetar powered SLSNe (see Figure 2.8), but the analysis provided in Chapter 3 shows that SLSN progenitors can come from a larger parameter space than that assumed. Progenitors in a larger parameter space are able to reproduce the SLSNe with the highest ejecta masses. However, it is found that the rotational energy of the neutron stars formed from the models is larger than the average kinetic energy inferred for observed SLSNe. This implies that rotation could contribute significantly in powering the observed explosions, and CSM interaction will still be important.

The magnetic fields (see Section 2.2.5 have the order of magnitude required to produce magnetars, but an exact value cannot be provided by stellar evolution calculations, and require detailed modelling. Magnetic fields could, however, also also be important sources of energy for the ejecta.

An order of magnitude estimate of the contribution of CSM interaction to the light curve is provided by Aguilera-Dena et al. (2018), assuming that the mass lost near the end of the evolution of CHE stars is distributed in a spherically symmetric wind with velocity of 0.2 km s^{-1}. The contribution to the light curve was estimated using Equation 2.2, assuming that the total kinetic energy of the ejecta is 4×10^{51} erg. The result of this estimation is presented in Figure 2.10, and it is compared with the observed light curve of SN 2015bn.

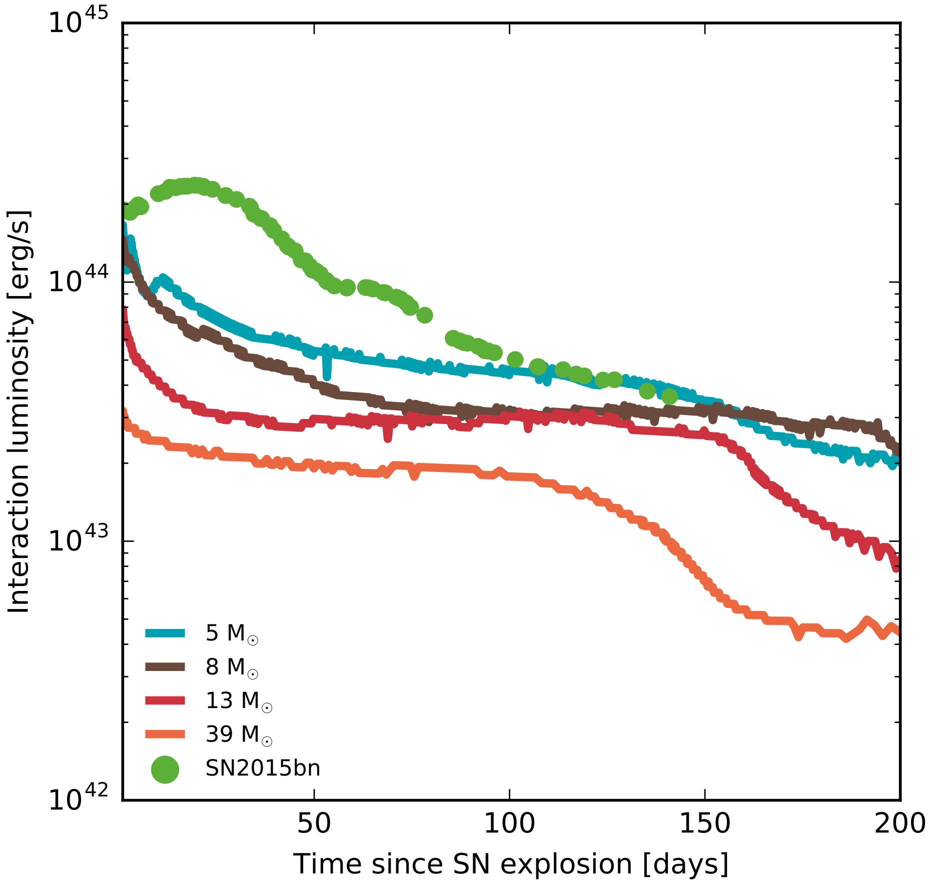

Figure 2.10: Inferred luminosity as a function of time, product of the interaction between a spherical SN ejecta and a spherical CSM. The kinetic energy of the SN ejecta is taken as 4×10^{51} erg. Ejecta mass corresponds to the final mass of the Series B models of Aguilera-Dena et al. (2018) with initial masses of 5 (blue), 8 (brown) 13 (red) and 39 $M_\odot$ (orange). The CSM is assumed to be a wind with velocity of 0.2 km s^{-1}, and have a density continuous density distribution given by the mass loss history of each model. Luminosity at each time is calculated using Equation 2.2. The light curve of SN 2015bn (Nicholl et al., 2016) is displayed alongside for comparison. Figure adapted from Aguilera-Dena et al. (2018).

Although this calculation provides only a rough estimate to the interaction luminosity, and also requires the mass to be distributed spherically, it demonstrates that the luminosity produced by the interaction between the ejecta and the dense CSM could be observable, even when it is not the main source of SLSN luminosity. It is suggested to help explain “bumps” (e.g. Inserra et al., 2017; T.-W. Chen et al., 2017) and “dips” (e.g. Nicholl et al., 2016) that have been observed in SLSNe.

2.3.4 Expected Outcome for Different Models: Gamma-ray Bursts

In certain mass ranges, discussed in Chapter 3, black hole formation is expected to be the outcome of the evolution of CHE stars. As shown in Figures 2.3 and 2.8, if a compact object more massive than a neutron star is formed, it will have a larger average specific angular momentum than that of a neutron star. For the chosen fiducial mass of 5 $M_\odot$, the average angular momentum often exceeds 10^{16} cm^2 g^{-1}, implying that they are suitable models for the formation of GRBs in the collapsar scenario (Yoon et al., 2005; S. E. Woosley et al., 2006; Yoon et al., 2006a).

It is unclear how the CSM would interact with the Type Ic-BL SN that is observed to accompany GRBs, but as shown in Figure 2.8, it is likely that the interaction luminosity is large, since f_M decreases for higher initial masses. However, since the material will likely be concentrated in the plane of rotation of the progenitor, it might induce an asymmetric ejecta.

On the other hand, the GRB jet will likely be launched along the polar direction of the progenitor, where the CSM is expected to be less dense. This implies that the GRB jet is unlikely to show signs of CSM interaction in the same magnitude as the case of its associated Type Ic-BL SN. However, some GRBs have been observed where an extended SN shock break-out is observed, implying a dense CSM (e.g. Irwin et al., 2016).

2.3.5 Expected Outcome for Different Models: The Effect of Pair Instability

At the highest masses (see Chapter 3 for an estimation of the mass boundary), pair instability will likely play a role in the outcome of the evolution of CHE stars. This can induce pulsations that can eject significant amounts of mass (S. E. Woosley, 2017), resulting in a CSM with much larger mass than that lost as a consequence of fast rotation.

The carbon-oxygen core mass of the models with initial masses of 77 and 100 $M_\odot$ suggest that a significant amount of mass will be lost as a result of their pulsations, but they will still undergo core-collapse. If the core retains enough angular momentum after the pulsations, the star could still explode as a GRB, Type Ic-BL SN or SLSN, which would then interact with a very dense CSM, and result in a SN with very high interaction luminosity (Figure 2.8). Models with higher masses than those modelled here could not present any pulsations at all, but explode directly as a consequence of pair instability. How rotation could affect them is also unclear.

It is not clear what kind of outcome this models would have, since their final structure is not known. However, models in this mass regime have been suggested to explain the unusual SNe such as SN Gaia2016apd (Yan et al., 2017) and more recently SN 2016iet (Gomez et al., 2019).

2.4 Discussion

As discussed in Aguilera Dena (2017), the scenario presented in this Chapter is not necessarily limited to CHE stars, but also to other evolutionary channels that might lead to the presence of fast rotating, hydrogen- and helium-free stars. Furthermore, it offers a possible explanation to the similarities between SLSNe and GRBs (e.g. Lunnan et al., 2014).

Aguilera-Dena et al. (2018) argue that the choice for enhanced efficiency of rotational mixing is justified by the uncertain effect of rotation in nearly-critically rotating massive stars, since the mixing coefficients are calculated by linear approximations that do not hold in this regime (Heger et al., 2000b). Furthermore, it is justified by the fact that models performed with this assumption reproduce the observed properties of SLSNe and GRBs simultaneously, while previous models of their progenitors found difficulties (e.g. Yoon et al., 2006b).

A testable prediction of this model is the expected interaction between SN ejecta and a dense CSM. Disproving that this interaction takes place would indicate that transients generate through an alternate channel, while a confirmation of its existence might still be consistent with other proposed evolutionary channels.

Although GRBs and SLSNe are preferentially found at relatively low metallicities, the metallicity of the models discussed above does not necessarily reflect the metallicity at which SLSNe and GRBs are found. This metallicity was chosen to guarantee a large parameter space of CHE stars, but the physical mechanisms that lead to our findings should also be present at higher metallicities, albeit in a smaller region of the velocity-rotational velocity parameter space, and therefore the rate of occurrence of this phenomenon.

2.5 Conclusions

By computing evolutionary tracks of fast rotating, massive stars at low metallicity with enhanced rotational mixing efficiency, we obtain bare carbon-oxygen cores with rotation rates that correspond to SLSNe, Type Ic-BL SNe and long GRBs.

A combination of angular momentum transport and mass loss induced by rotation renders the final composition in our models hydrogen- and helium-free. This is in agreement with the absence of hydrogen and helium lines in the spectra of these transients.

We find that the observed trend in spin and ejecta mass of SLSNe is reproduced, and conclude that this trend must be true for GRB progenitors, and perhaps also for stars experiencing pulsational pair instability.

Finally, predict that SLSNe and Type Ic-BL SNe should show signs of interaction between their ejecta and the dense CSM that is formed by a final episode of mass loss, consequence of neutrino-mediated contraction and critical rotation. We also predict that above the limit at which pulsational pair instability takes place, bright Type Ic SNe with very massive circumstellar shells can be formed.

CHAPTER 3

Precollapse Properties of Superluminous Supernovae and Long Gamma-Ray Burst Progenitor Models

David R. Aguilera-Dena[1,2], Norbert Langer[1,2], John Antoniadis[2,1,3] & Bernhard Müller[4]

[1]Argelander-Institüt für Astronomie, Universität Bonn, Auf dem Hügel 71, 53121 Bonn, Germany

[2]Max-Planck-Institut für Radioastronomie, Auf dem Hügel 69, 53121 Bonn, Germany

[3]Institute of Astrophysics, FORTH, Dept. of Physics, University of Crete, Voutes, University Campus, GR-71003 Heraklion, Greece

[4]School of Physics and Astronomy, Monash University, VIC 3800, Australia

The Astrophysical Journal, 2020, 901, 114A

Abstract. We analyze the properties of 42 rapidly rotating, low metallicity, quasi-chemically homogeneously evolving stellar models in the mass range between 4 and 45 $M_\odot$ at the time of core collapse. Such models were proposed as progenitors for both superluminous supernovae (SLSNe) and long duration gamma-ray bursts (lGRBs), and the Type Ic-BL supernovae (SNe) that are associated with them. Our findings suggest that whether these models produce a magnetar driven SLSN explosion or a near-critically rotating black hole (BH) is not a monotonic function of the initial mass. Rather, their explodability varies non-monotonically depending on the late core evolution, once chemical homogeneity is broken. Using different explodability criteria we find that our models have a clear preference to produce SLSNe at lower masses, and lGRBs at higher masses; but find several exceptions, expecting lGRBs to form from stars as low as 10 $M_\odot$, and SLSNe with progenitors as massive as 30 $M_\odot$. In general, our models reproduce the predicted angular momenta, ejecta masses and magnetic field strengths at core collapse inferred for SLSNe and lGRBs, and suggest significant interaction with their circumstellar medium, particularly for explosions with low ejecta mass.

Unified Astronomy Thesaurus concepts: Stellar evolution (1599); Late stellar evolution (911); Nonstandard evolution (1122); Stellar evolutionary models (2046); Neutron star cores (1107); Supernovae (1668); Gamma-ray bursts (629); Circumstellar matter (241); Black holes (162); Astrophysical black holes (98); Neutron stars (1108); Magnetars (992)

3.1 Introduction

Superluminous supernovae (SLSNe) and long duration gamma-ray bursts (lGRBs) are highly energetic transients that have generated great interest in astrophysics due to their extreme properties. Despite some differences in their environments and distributions (e.g. Leloudas et al., 2015; Angus et al., 2016), there is accumulating observational and theoretical evidence alluding to a similar origin (e.g. Lunnan et al., 2014; Japelj et al., 2016; Margalit et al., 2018).

Type I SLSNe (henceforth referred to simply as SLSNe) are characterized by intrinsic luminosities 10 to 100 times larger than those of "typical" supernovae (SNe; see Gal-Yam, 2012; Howell, 2017; Moriya et al., 2018; Inserra, 2019, for recent reviews). Their spectra show no hydrogen features, and helium features are rarely found in late time spectra of some events (Mazzali et al., 2016), suggesting that the envelopes of their progenitors contain no hydrogen very little to no helium; i.e., they are bare carbon and oxygen cores (Gal-Yam, 2019). This suggests that their progenitors undergo a phase of intense mass loss and/or mixing, during which these elements are efficiently depleted in their envelopes. Helium would likely be detectable in the SN spectra if $\gtrsim$0.1 $M_\odot$ of it was present in the ejecta (however, this estimate is somewhat sensitive to the distribution of ^{56}Ni in the SN ejecta, and the actual composition of the helium-rich layer, Hachinger et al., 2012; Dessart et al., 2015; Yoon et al., 2019). These SNe are found to prefer low metallicity environments (Perley et al., 2016; Japelj et al., 2016; Schulze et al., 2018), and their high bolometric luminosities of SLSNe are not easily explained by radioactive ^{56}Ni decay, and require an additional source of energy.

Although the nature of SLSN progenitors is still not known, some insight has been gained by studying the several mechanisms that have been proposed to explain their observational properties. Some of the leading theories invoke a continuous energy deposition into the ejecta by the spin-down of a newly-formed millisecond magnetar (e.g. Kasen et al. 2010b; S. E. Woosley 2010; Metzger et al. 2015; Nicholl et al. 2017), the accretion of fallback material onto a central compact object (e.g. Moriya et al., 2018), interaction between the SN ejecta and the circumstellar medium (CSM; e.g. Chatzopoulos et al., 2012), or the formation of large amounts of ^{56}Ni (more than 3 $M_\odot$), resulting from a pair-instability-driven explosion in a very massive star (e.g. Gal-Yam et al. 2009).

In the context of the magnetar model, which is considered the most likely explanation, a large sample of SLSN light curves have been analysed, setting constrains on the distribution of ejecta masses, magnetar spin periods and magnetic field strengths that are required to reproduce the observations (Nicholl et al., 2017; Villar et al., 2018; Blanchard et al., 2018; Blanchard et al., 2019; Blanchard et al., 2020). These studies have found that the ejecta masses of SLSNe range between 3.6 and 40 $M_\odot$, setting them significantly apart from type Ib/c SNe, and that the periods and magnetic fields of the millisecond pulsars that input energy into the ejecta are in the range of 1 to 8 ms and 0.3 to 10 $\times 10^{14}$ G, respectively. In this work, we present an evolutionary channel for progenitors of SLSNe, relying on efficient rotational mixing in massive, low-metallicity stars, that can reproduce many of the properties inferred from the SLSN light curve samples.

lGRBs on the other hand, are distinguished by beamed emission of energetic gamma-rays formed in collimated relativistic jets (see, for example Vedrenne et al., 2009, for a review). They are observed preferentially in low metallicity environments (e.g. Palmerio et al., 2019), and their host galaxies are similar to those hosting SLSNe. Furthermore, they are associated with a sub-class of hydrogen- and helium-deficient SNe known as Type Ic-BL (Hjorth et al., 2012). These SNe are less luminous than SLSNe, but still have large ejecta velocities with kinetic energies that are typically 10 times larger than those of "typical" Type Ic SNe.

In the framework of the collapsar model (S. E. Woosley, 1993), lGRBs form from the collapse of a rapidly rotating stellar core into a black hole (BH). A corresponding progenitor evolution is provided by rapidly rotating, rotationally mixed models which undergo so called quasi-chemically homogeneous evolution (Maeder, 1987; Langer, 1992; Heger et al., 2000; Brott et al., 2011b), predicting lGRBs to occur in massive, rapidly rotating low metallicity single stars (Yoon et al., 2005; S. E. Woosley et al., 2006; Yoon et al., 2006b) and in massive close binaries (Detmers et al., 2008; Cantiello et al., 2007). Notably, homogeneously evolving massive close binaries may also explain massive BH mergers (S. E. de Mink et al. 2009; Marchant et al. 2016b; Hastings et al. 2020) and ultra-luminous X-ray sources (Marchant et al., 2017). Given that SLSNe and lGRBs present similarities in their environments, spectra, and energetics, (Aguilera-Dena et al., 2018, henceforth ALMS18) suggested a unified scenario for both types of transients, based on chemically homogeneous evolution, which leads to fast-rotating pre-collapse models with hydrogen- and helium-depleted envelopes.

The mass loss and late evolution of these models is influenced significantly by intense neutrino cooling after core helium exhaustion. This accelerates the contraction of the core and enhances centrifugally-driven mass loss. ALMS18 advocated that the end-product is either a "collapsar" and a fast-spinning BH (S. E. Woosley, 1993), or a rapidly-spinning, highly-magnetized neutron star (NS; Kasen et al., 2010b; S. E. Woosley, 2010) — giving rise to a lGRB or a SLSN respectively. It was suggested that lower mass progenitor models might correspond to SLSNe while more massive ones could correspond to lGRBs, but the analysis performed by Blanchard et al. (2020) suggests that SLSN progenitors must have a wide range of final masses, from 3.6 to 40 $M_\odot$, in great contrast to progenitors of "normal" stripped-envelope SNe that have a strong cutoff in progenitor mass distribution above 10 $M_\odot$. We address the problem in this paper by studying the properties of such progenitor models at core-collapse.

While determining which stars will form a NS or a BH is a highly complex astrophysical problem, several recent studies have established a series of simple diagnostic indicators to predict the final fate based on the pre-collapse stellar structure (e.g. O'Connor et al., 2011; Ugliano et al., 2012; Sukhbold et al., 2014; Ertl et al., 2016; B. Müller et al., 2016; Sukhbold et al., 2018). One such diagnostic is the so-called core compactness parameter, $\xi_{\rm M}$, which is motivated by hydrodynamic simulations of neutrino-driven SN explosions (O'Connor et al., 2011). The behavior of this variable was found to be non-monotonic with initial mass, and depends mainly on the detailed core behavior of an evolutionary sequence and the core mass it develops, but is strongly affected by whether carbon burning proceeds radiatively or in a number of convective flames (Sukhbold et al., 2019), and more weakly in other properties, such as the ratio of carbon to oxygen after helium burning, the chosen wind prescriptions, and the numerical treatment employed. Other proposed diagnostics of explodability (e.g Ertl et al., 2016; B. Müller et al., 2016) generally yield similar results, i.e. they predict a transition around the dividing line between radiative and convective core carbon burning, with regimes where stars explode generally behaving non-monotonically.

Motivated by the findings of ALMS18, in this paper we explore the late burning stages and the progenitor-remnant connection for rapidly-rotating, chemically homogeneous massive stars. Expanding on our previous results, we evolve, for the first time, 42 rapidly-spinning stellar models to core collapse. We then apply the aforementioned diagnostic tools to predict their final fate and diagnose their relevance to lGRBs and magnetar-driven SLSNe. The text is organized as follows: In Section 3.2 we briefly describe the assumptions we employed to perform our calculations, and compare with the results of ALMS18. We present our analysis in Section 4.3, highlighting that detailed core evolution during and after carbon burning will determine whether a chemically homogeneously evolving stellar model might result in a lGRB or a magnetar driven SLSN. In Section 3.4 we infer observable properties of SLSNe from our models. We finalize this paper with a brief summary and conclusions in Section 4.6.

3.2 Method

The simulations presented in this work are similar to those performed in ALMS18. In this Section we review the methods and assumptions used, highlighting the similarities and differences to the previous simulations in Section 3.2.1, and describe the consequences of these changes in Section 3.2.2.

3.2.1 Physical and numerical parameters

We performed simulations of the evolution of massive single stars using the Modules for Experiments in Stellar Astrophysics code (MESA) in its version 10398 (Paxton et al., 2011; Paxton et al., 2013; Paxton et al., 2015; Paxton et al., 2018). To remain consistent to the simulations presented by ALMS18, our models have an initial equatorial rotation velocity of 600 km s^{-1}, and a metallicity of $1/50Z_{\odot}$, scaled from solar metallicity (Grevesse et al., 1996). The initial value for the equatorial rotational velocity is chosen to represent the fastest rotating known O type star (Ramírez-Agudelo et al., 2013), and the combination of fast rotation and low metallicity are chosen to guarantee quasi-chemically homogeneous evolution. The choice of metallicity was initially conceived to be consistent with the results of Szécsi et al. (2015), who modelled chemically homogeneously evolving massive stars to study the stellar population of the low metallicity galaxy I Zw 18. This value is smaller than the mean values observed for both SLSNe and lGRBs (e.g. Lunnan et al., 2014), but chemically homogeneous evolution has been observed to be present at higher metallicities (although all of them subsolar, e.g. Brott et al., 2011b), so we expect that different parameter choices will produce similar progenitors, albeit probably over a smaller region of the parameter space, at such metallicities. Thus, the effect of varying metallicity and initial rotational velocity in the context of enhanced rotational mixing efficiency is beyond the scope of this paper.

The models cover the mass range between 4 and $45M_{\odot}$ with a step size of $1M_{\odot}$. Evolutionary sequences with an initial mass larger than $45M_{\odot}$ were not computed since they are subject to pulsational pair instability near the core in their late burning stages. Likewise, models with masses smaller than $4M_{\odot}$ were excluded because the initial rotational velocity applied was above their breakup velocity at the zero-age main sequence (ZAMS). Our simulations are carried out from ZAMS to core collapse.

These calculations have similar parameters as the Series B evolutionary sequences from ALMS18. They include rotational mixing, dominated by Eddington-Sweet circulation but also including secular and dynamical instabilities and the Goldreich–Schubert–Fricke instability, as described by Heger et al. (2000a). They evolve chemically homogeneously and have rotational mixing coefficients enhanced by a factor 10 compared to Brott et al. (2011b). This choice is made, similarly to ALMS18, to both decrease the amount of helium in the surface of our models at core collapse, and to extend the parameter space where chemically homogeneous evolution occurs into lower masses. While introduced as an ansatz, we justify this choice by the fact that these coefficients are not well parametrized in the case of near-critical rotation, as well as by the fact that, through this choice, we are able to reproduce features that are expected in SLSN and GRB progenitors. These include not only the rotation rates, enough to power the two energetic explosions, but the lower limit in ejecta masses of SLSNe found by Blanchard et al. (2020), which is of the order of a few $M_{\odot}$, and the peculiar surface composition implied by the observed spectra.

Convection is applied according to the Ledoux criterion, and standard mixing length theory (Böhm-Vitense, 1958) with $\alpha_{MLT} = 1.5$ is employed. Step convective overshooting during hydrogen burning with $\alpha_{OV} = 0.335$ and semiconvection with $\alpha_{SC} = 0.01$ are applied, and we employ MESA's `approx21` nuclear network (Paxton et al., 2011). We use Type 2 OPAL opacities to take into account the chemical enrichment of the surface (Iglesias et al., 1996) and implement the empirical mass loss rates from (Vink et al., 2001) and (Hamann et al., 1995) for hydrogen rich ($X_S > 0.7$) and hydrogen poor stars ($X_S < 0.4$), respectively; the latter multiplied by a factor of 1/10. In the regime in between we linearly interpolate between the two, and we employ a metallicity dependence of $\dot{M} \propto (Z/Z_{\odot})^{0.85}$. Mass loss is, however, domina ted by the effect of rotation. We implement the enhancement of rotational mass loss rates due to rotation (Bjorkman et al., 1993), and impose that the ratio $\Omega/\Omega_{\rm crit} < 0.98$, which has a larger effect than the prescriptions employed. Limiting $\Omega/\Omega_{\rm crit}$ to be smaller than 1 has the effect of avoiding models that rotate above the critical limit, which has been observed in previous calculations of chemically homogeneoously evolving stars, that have used rotationally enhanced mass loss rates, but with an upper limit given by the thermal mass loss rate. The value of 0.98 is arbitrary, but varying it by a few percent was not observed to have an effect on our results.

Some changes were applied both to the numerical treatment and the employed physics to improve on the results of ALMS18 by reaching core collapse (infall velocity larger than 1000 km s^{-1} in the core) in our evolutionary calculations, and to more accurately capture the effects of rotation. We include the treatment of the hydrodynamical structure of the star, but exclude the outer layers from this treatment when time steps are small (i.e. the velocity is set to 0 where $\log(T/K) < 8$ if the time steps are smaller than 0.1 yr; which corresponds to the envelope during the last phases of evolution). We neglect mass loss during the last years of evolution when the central temperature exceeds 2.5×10^{9} K; and we include the predictive mixing scheme in MESA to avoid glitches in the structure of convective regions during helium burning. For models with initial mass between 40 and 45 $M_{\odot}$, we remove the condition that $\Omega/\Omega_{\rm crit} < 0.98$ at the end of carbon burning, which is only broken for a few timesteps and then recovered through rotationally enhanced mass loss.

We change the treatment of angular momentum loss, which has been modified in the most recent releases of MESA. Angular momentum loss was originally associated to the integrated amount of angular momentum contained in a layer of mass equivalent to the mass lost at each timestep. The current employed mechanism defines $\dot{J}$ as the product of the mass loss rate at each timestep and the specific angular momentum at the surface. This is equivalent to removing angular momentum from a layer closer to the surface, which has higher specific angular momentum than the average over a larger volume. This affects the final masses and compositions of these models with respect to the previously published ones. This corresponds to setting the variable do_adjust_J_lost = .true. option, which is set by default in version 10398.

The uncertainties in the prescription of the specific angular momentum loss, i.e., the angular momentum lost per lost gram of matter, affect mostly the total amount of matter lost in the phases near critical rotation, since the required amount of angular momentum loss is simply dictated by the decrease in the moment of inertia during the contraction stages. An estimate of the inherent uncertainty can be obtained by comparing the results presented below with those of ALMS18 (cf. Section 3.2.2).

The changes in the treatment of angular momentum losses likely represent an improvement in the calculations, but it is important to note that, even though angular momentum losses are treated in a more physically consistent way, the true angular momentum losses that a critically rotating star experiences are uncertain. The description of stellar structure is only accurate only up to a certain point, but assumptions that go into the calculations of rapidly rotating stars might break down above a certain threshold value of $v_{\rm rot}/v_{\rm crit}$, and the models presented here are certainly above that value as they are at critical rotation for a significant portion of their evolution.

Furthermore, fast rotation induces a latitude dependent temperature structure, which may lead to a latitude dependent mass and angular momentum loss rates, and the mass close to the surface of the star might interact with the magnetic field and the decretion disk, making this a highly non trivial problem. Therefore, although we have improved the physical treatment of angular momentum loss, our results are subject to the uncertainties that plague all rapidly rotating stellar evolution calculations, and should be taken with caution.

3.2.2 Comparison with ALMS18

Differences in the evolutionary sequences in ALMS18 and the current work (see Section 3.2.1) are mainly due to the different treatment of the angular momentum loss. Having a more efficient angular momentum loss per unit mass implies that an almost critically rotating star will have to lose less mass as it contracts for its surface to remain under the break-up limit. Differences in angular momentum loss rate can be up to about 50%, and they are especially significant during core helium burning, but remain important until a few decades before core collapse.

This is reflected in the top panel of Figure 3.1, where we compare the final masses of previous models to those presented here. Note that, although the current models are precisely at core collapse, whereas the previous ones are calculated at a time shortly before, the remaining lifetime before of previous models is of the order of a few seconds, such that the final masses are well defined. Differences in final masses will become important for the explosive event that follows from this evolutionary channel, since they will determine the ejecta mass, the boundary between core collapse and the onset of pulsational pair instability, as well as the amount of radiation produced by CSM interaction. This is further discussed in Section 3.4.

The middle panel of Figure 3.1 reflects the difference in final total helium mass in the envelope. The helium content in the envelope is higher in most cases in the current work due to the higher final masses retained by the models at core collapse. Despite the considerable difference in final mass, reaching up to 25% in some cases, particularly at higher initial masses, all of these models retain less than 0.013 $M_\odot$ of helium in their envelopes. We do not expect helium lines to form in these progenitors since they retain very little helium, and all of the remaining helium is located in a carbon/oxygen rich layer which will lower the probability of exciting helium lines, as opposed to the case of a Ib progenitor that has a pure helium and nitrogen layer (Dessart et al., 2017; Dessart et al., 2015). Furthermore, excitation of helium lines depends on the mixing of ^{56}Ni, which may be differently distributed in the ejecta in case of a successful explosion coming from one of our progenitors, likely resulting in a type Ic SN in any case (Yoon et al., 2019).

As can be seen in the bottom panel of Figure 3.1, final radii are not significantly affected by the additional mass, except for the cases below about 8 $M_\odot$. This is not unexpected since the radius is determined by a competition of the the increasingly stronger neutrino losses stars experience during the late evolutionary stages, and the formation of a helium burning shell. In lower mass models, the relatively larger helium content in the envelope ignites earlier than in the ALMS18 models, and due to the larger lifetime, the helium burning shell manages not only to halt the neutrino-driven contraction, but to produce an expansion of the envelope.

Another important consequence of a more efficient angular momentum loss is that the immediate CSM mass –produced in the final $\approx$ 1000 years by the combined effect of neutrino-driven contraction and fast rotation– will be smaller, and the ejecta more massive. The CSM mass, quantified by $\Delta M_{\mathrm{He}\rightarrow\mathrm{final}}$, the mass lost from core helium depletion until core collapse, as discussed in detail by ALMS18, has to remain close to the star since it is lost by centrifugal acceleration, which decays quickly as the mass moves away from the star, and cannot be accelerated by radiation. A comparison between these quantities is shown in Figure 3.2. It is striking that some of these CSM masses are reduced by about half by the different treatment of angular momentum losses, but they will still play a significant role in some of the expected transients (see Section 3.4).

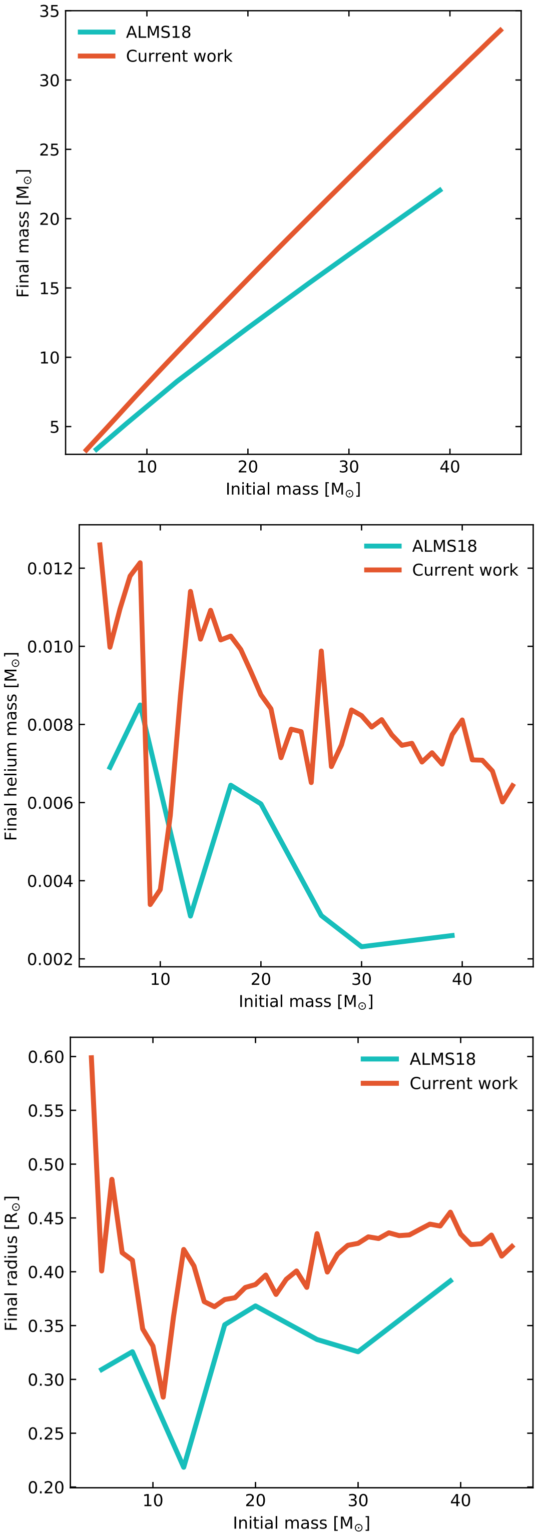

Figure 3.1: Panels show a comparison of different key properties of core collapse models in this study (represented in orange), with the final models from ALMS18 (represented in blue). Panels show the final masses (top), final helium masses in the envelope (excluding the helium formed in the core due to photodisintegration of iron, middle), and final radii (bottom), as a function of initial mass.

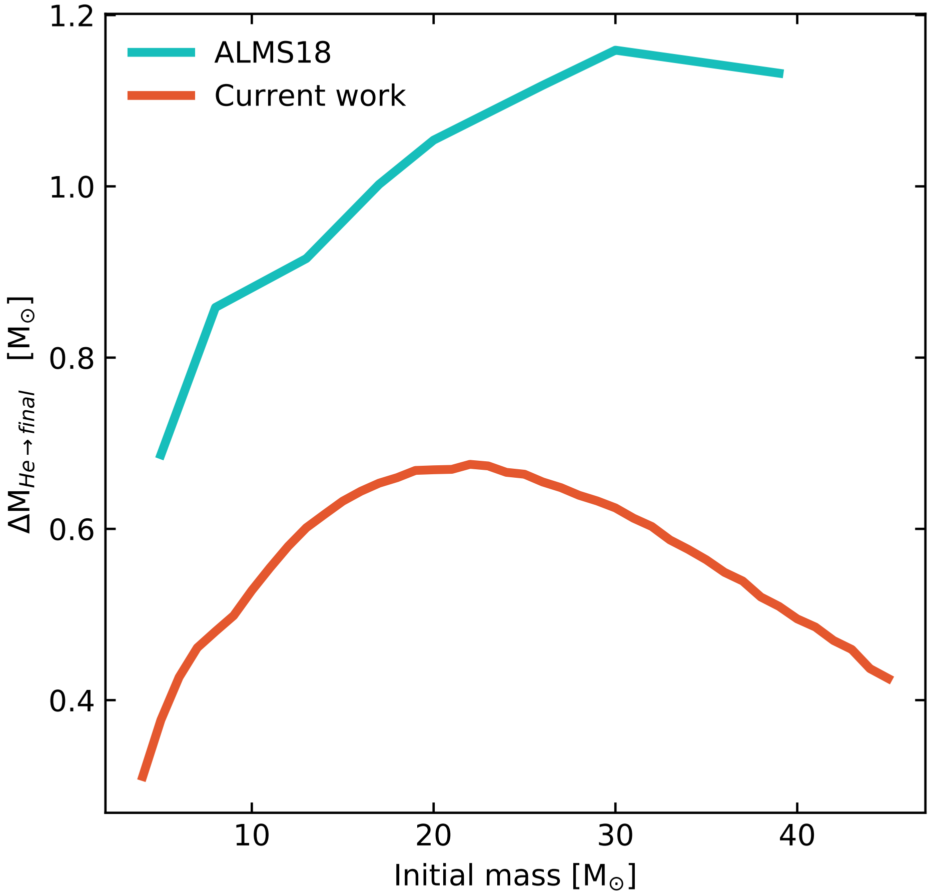

Figure 3.2: Mass lost between core helium depletion and core collapse ($\Delta M_{\mathrm{He}\rightarrow\mathrm{final}}$), representative of the CSM mass immediately close to the progenitors at core collapse, as a function of initial mass. Comparison between core collapse models from this study (orange) and the final models from ALMS18 (blue).

3.3 Results

As detailed in Section 3.2.1, the global properties and conclusions from ALMS18 remain valid after re-performing the simulations with the changes described in Section 3.2.2. The main parameters of our pre-SN models are summarized in Table 3.1. This Section is divided as follows: In Section 3.3.1 we discuss the general evolution from ZAMS to core collapse of our models, and in Section 3.3.2 we discuss the pre-collapse core properties and explodability of fast rotating stars.

3.3.1 Pre-collapse evolution

Similar to the simulations in ALMS18, we find that the evolution of fast rotating stars at low metallicity is well described by previous works of quasi-chemically homogeneous stars (e.g. Brott et al., 2011b) during the main sequence, but late evolution differs significantly from previous studies in a number of ways. The most notorious difference is that rotational mixing and mass loss work together to leave no hydrogen on the surface at the end of the main sequence, and only a small amount of helium in the envelope at the end of core helium burning.

This causes the helium shell that is left to ignite later and be weaker, thus preventing expansion of the stellar radius due to the so-called *mirror principle* (Kippenhahn et al., 1990), and leading to a continuous contraction from ZAMS to core collapse. This contraction proceeds in a thermal time scale, and it becomes accelerated from the end of helium burning by neutrino cooling in the core.

Contraction in these models leads to an increase in surface rotational velocity, which is limited by the critical value, which in turn leads to intense mass loss. In particular during the last few thousand years these stars experience the loss of about 0.5 $M_\odot$ (see Figure 3.2, Table 3.1), which cannot be accelerated far from the star and will thus likely interact with the SLSN/lGRB ejecta.

Due to the strong rotational mixing, helium core masses and carbon-oxygen core masses are determined almost exclusively by the mass of the entire star at the end of hydrogen and helium burning, respectively, since no strong composition gradient is present at these times. Only after, during core carbon burning, a distinct core-envelope structure is formed, inhibiting mixing through regions with newly formed composition gradients. This, together with the remaining mass at carbon ignition, determines the core structure in the remainder of the stellar life. This is illustrated in Figure 3.3, where the evolution of the diffusion coefficient for rotational mixing of our 9 $M_\odot$ model (sum of all effects included in the calculations, but dominated by Eddington-Sweet circulation) is compared to the locations of the convective and overshooting regions during the evolution. It illustrates how the strength of rotational mixing is reduced by the composition gradient established by carbon burning, but it still has a role in shaping the chemical gradient and size of the subsequent carbon, neon and oxygen burning shells in and close to the core by mixing the otherwise static radiative regions between the convective shells.

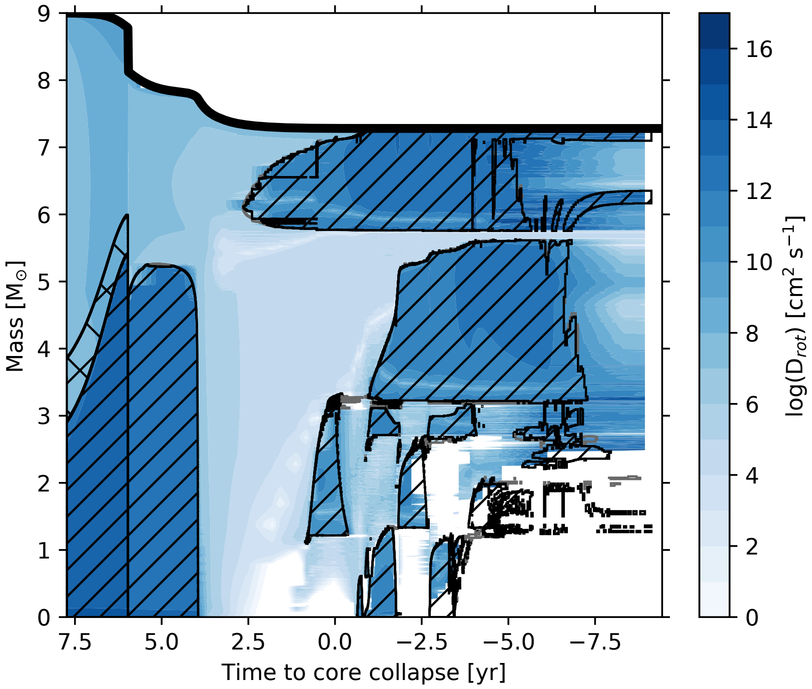

Figure 3.3: Kippenhahn diagram following the efficiency of rotational mixing, and the structure of convective and overshooting regions of the 9 M$_\odot$ evolutionary calculation from ZAMS to core collapse, as a function of the time remaining before core collapse. Color denotes the diffusion coefficient due to rotational mixing (dominated by Eddington-Sweet circulation). Regions hatched with diagonals denote convective regions, whereas the region hatched with perpendicular lines, above the hydrogen burning core, denotes an overshooting region.

Table 3.1: Initial mass, final mass, mass lost between ZAMS and the onset of core helium burning, mass lost between the end of helium burning and core collapse of evolutionary sequences in this work, and key parameters of their respective core collapse models. The compactness parameter $\xi_{2.5}$, and the values of M_4 and μ_4 as defined by Equations 3.1, 3.2 and 3.3 respectively.

M_{init} $[M_\odot]$	M_{fin} $[M_\odot]$	$\Delta M^{a}_{H\rightarrow He}$ $[M_\odot]$	$\Delta M^{b}_{He\rightarrow final}$ $[M_\odot]$	He mass^{c} $[M_\odot]$	Y_{surf} asfsdf	$\bar{j}_{1.5M_\odot}$ $[10^{15}$ cm^2 s$^{-1}]$	$\bar{j}_{2M_\odot}$ $[10^{15}$ cm^2 s$^{-1}]$	$\bar{j}_{5M_\odot}$ $[10^{15}$ cm^2 s$^{-1}]$	$\xi_{2.5}$ ssdfsdf	M_4 sadfsadfsdf	μ_4
4	3.31	0.20	0.32	0.013	0.10	0.51	0.91	9.07	0.13	1.77	0.063
5	4.10	0.22	0.40	0.010	0.09	0.50	1.65	20.9	0.20	1.54	0.136
6	4.89	0.25	0.46	0.011	0.09	1.22	2.07	38.1	0.19	1.82	0.075
7	5.68	0.30	0.49	0.012	0.08	1.07	2.13	25.1	0.13	1.57	0.062
8	6.48	0.36	0.52	0.012	0.08	1.11	2.20	20.6	0.14	1.65	0.058
9	7.28	0.42	0.54	0.003	0.08	1.22	2.30	11.5	0.68	2.36	0.183
10	8.06	0.49	0.56	0.004	0.08	3.01	4.05	20.0	0.50	2.24	0.152
11	8.84	0.56	0.58	0.006	0.08	2.42	3.39	15.6	0.42	2.12	0.123
12	9.61	0.63	0.60	0.009	0.08	2.20	3.31	14.1	0.23	1.88	0.068
13	10.37	0.71	0.62	0.011	0.08	1.24	2.76	12.6	0.21	1.86	0.073
14	11.13	0.78	0.63	0.010	0.08	1.12	2.46	11.0	0.31	2.07	0.092
15	11.89	0.87	0.65	0.011	0.08	1.36	2.76	11.1	0.37	2.15	0.107
16	12.64	0.95	0.66	0.010	0.08	1.46	2.86	9.73	0.54	2.34	0.197
17	13.39	1.04	0.67	0.010	0.08	1.33	2.58	8.96	0.59	2.45	0.163
18	14.15	1.12	0.68	0.010	0.08	1.34	2.64	8.62	0.62	2.49	0.169
19	14.89	1.21	0.69	0.010	0.08	1.19	2.29	8.22	0.65	2.27	0.262
20	15.64	1.29	0.69	0.009	0.09	0.98	1.95	7.93	0.66	2.28	0.278
21	16.39	1.38	0.69	0.008	0.09	1.07	2.17	7.95	0.66	2.15	0.304
22	17.12	1.47	0.70	0.007	0.09	1.06	2.02	8.24	0.63	2.01	0.277
23	17.86	1.56	0.70	0.008	0.09	1.26	2.46	8.88	0.54	2.04	0.285
24	18.60	1.65	0.69	0.008	0.09	0.43	0.93	8.66	0.53	1.71	0.259
25	19.33	1.76	0.69	0.007	0.09	0.33	0.68	8.88	0.47	1.75	0.186
26	20.05	1.87	0.68	0.010	0.09	1.75	3.19	9.29	0.36	1.93	0.115
27	20.78	1.98	0.67	0.007	0.09	1.30	2.46	9.52	0.43	1.85	0.153
28	21.50	2.10	0.66	0.007	0.09	1.56	2.95	9.70	0.40	1.92	0.133
29	22.22	2.24	0.66	0.008	0.09	1.77	3.43	10.4	0.43	2.07	0.124
30	22.95	2.36	0.65	0.008	0.09	1.34	2.63	9.54	0.43	2.08	0.129

31	23.66	2.48	0.64	0.008	0.09	1.17	2.46	9.51	0.43	2.04	0.134
32	24.38	2.62	0.63	0.008	0.09	2.01	3.73	10.5	0.52	2.26	0.137
33	25.10	2.75	0.61	0.008	0.09	2.07	3.75	9.97	0.55	2.28	0.138
34	25.82	2.90	0.60	0.007	0.10	1.97	3.55	10.0	0.60	2.35	0.153
35	26.53	3.04	0.59	0.008	0.10	1.57	2.95	9.44	0.57	2.33	0.149
36	27.24	3.18	0.58	0.007	0.10	1.55	2.82	8.84	0.62	2.37	0.154
37	27.95	3.33	0.57	0.007	0.10	1.86	3.23	9.35	0.68	2.43	0.159
38	28.67	3.49	0.55	0.007	0.10	1.65	2.88	9.01	0.75	2.50	0.178
39	29.37	3.64	0.54	0.008	0.10	2.28	3.78	9.44	0.75	2.54	0.183
40	30.08	3.8	0.53	0.008	0.10	2.08	3.32	9.92	0.78	2.56	0.184
41	30.78	3.97	0.52	0.007	0.10	1.49	2.47	8.33	0.77	2.6	0.173
42	31.49	4.14	0.5	0.007	0.10	2.24	3.50	8.81	0.83	2.63	0.209
43	32.18	4.3	0.49	0.007	0.10	2.06	3.25	9.22	0.84	2.71	0.219
44	32.89	4.49	0.47	0.007	0.10	2.31	3.56	9.05	0.85	2.78	0.238
45	33.59	4.67	0.46	0.006	0.10	1.95	3.01	8.54	0.85	2.84	0.215

[a] Mass lost from between H and He burning, defined as $\Delta M_{H\rightarrow He} = \int_{T8_c>0.5}^{T8_c<1.2} \dot{M}\,dt$

[b] Mass lost from He core depletion to the end of the simulation

[c] In the envelope

3.3.2 Properties at core collapse

With an increased resolution in mass we are able to set a limit to the onset of pulsational pair instability between initial masses of 45 and 46 $M_\odot$, and to determine with higher accuracy the fate of these evolutionary sequences at and after core collapse. This, however, depends on the mass of the star at the onset of carbon burning (S. E. Woosley, 2017), and on the amount of carbon at the end of helium burning (Farmer et al., 2019), and therefore is uncertain inasmuch as the loss of angular momentum, and reaction rates remain uncertain.

The amount of angular momentum that is retained in the interior of the modelled stars leads to the expectation that they could form a collapsar, resulting in a lGRB, in the case that core collapse leads to BH formation. Otherwise, if core collapse leads to the formation of a NS, its spin and magnetic field will be consistent with those expected from SLSNe.

To assess which parts of the parameter space correspond to each of these possible fates, we make the ansatz that those models that we predict successfully explode as neutrino-driven SNe, would produce a SLSN, since this NS would be very fast rotating and highly magnetized, comparable to the magnetars required to produce SLSNe. On the other hand, we assume that explosions that we predict would not successfully explode, but instead form BHs, would produce collapsars due to the high content of angular momentum in our models. This would in turn power both a lGRB and its accompanying type Ic-BL SN. To determine this, we make use of results obtained for neutrino-driven core collapse of non-rotating SN progenitors. Applying explosion criteria for neutrino-driven SNe is evidently an oversimplification, but can nonetheless be justified as a first estimate. One concern is that the mechanism for shock revival in SLSNe may rely on magnetohydrodynamic effects to begin with, so that success and failure are determined by different criteria. However, this is by no means certain. Recent SN simulations suggest that neutrino-driven explosions can occur quite readily in rapidly rotating massive progenitors (Takiwaki et al., 2016; Summa et al., 2018; Obergaulinger et al., 2020) thanks to support by centrifugal forces and possibly a corotation instability. Even if part or most of the explosion energy is ultimately delivered by magnetohydrodynamic effects in SLSNe, there may well be a neutrino-driven “precursor” explosion, whose occurrence will be governed by similar explodability criteria as in the non-rotating case, though the criteria will be relaxed (Summa et al., 2018) due to rotational support. Moreover, regardless of the nature of the SN mechanism, explosions will be inhibited or cut off by similar factors, e.g., high pre-shock ram pressure, a high binding energy of the shells surrounding the core, and an unduly high core mass that leaves little time for a successful explosion to develop before ongoing accretion onto the NS results in collapse to a BH. Hence we expect that common explodability criteria for non-rotating progenitors will remain qualitatively useful even for magnetorotational SNe.

The importance of the core compactness in SN models –a measure of the gravitational binding energy near the core of pre-SN stars– in determining the final fate of a stellar model, has been pointed out as a possible tool to determine whether they will successfully explode (O’Connor et al., 2011; Ugliano et al., 2012; Sukhbold et al., 2014; B. Müller et al., 2016; Sukhbold et al., 2018). The core compactness was defined by O’Connor et al. (2011) as

$$\xi_\mathrm{M} = \frac{\mathrm{M}/\mathrm{M}_\odot}{\mathrm{R}(\mathrm{M}_\mathrm{bary} = \mathrm{M})/1000\,\mathrm{km}}, \tag{3.1}$$

and it was recognized as an indicator of whether the collapse of a non-rotating stellar core leads to a successful explosion (where neutrino winds are the cause of the explosion), or conversely ends up with the formation of a BH. It was found by Sukhbold et al. (2014) that ξ_M is well determined when measured at a mass coordinate of 2.5 $M_\odot$, and at core collapse, which is defined as the point where the

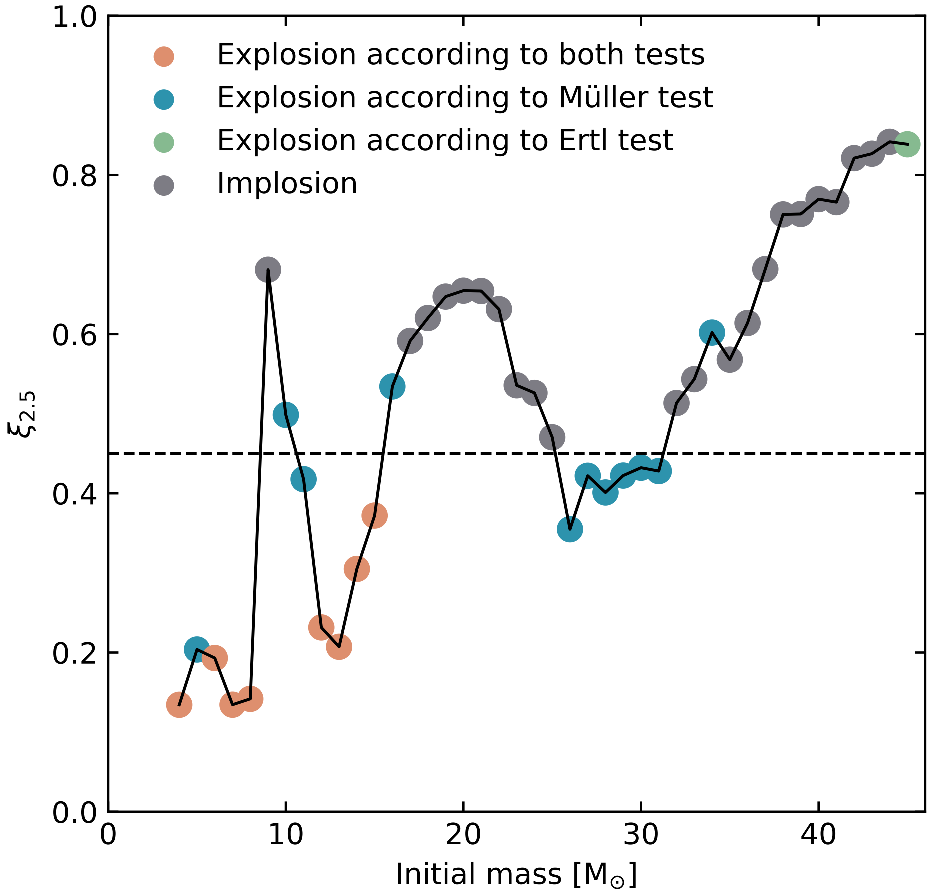

Figure 3.4: Compactness parameter measured at 2.5 $M_\odot$ of the core collapse models in this study, as a function of their initial mass. The dotted line at $\xi_{2.5}$ = 0.45 separates models that might explode (below the line) or implode (above the line) according to O'Connor et al. (2011), orange points indicate models that are predicted to explode according to the explodability the B. Müller et al. (2016) and Ertl et al. (2016) tests, blue points are models that are predicted to explode according the B. Müller et al. (2016) test, but not by the Ertl et al. (2016) test, the green point is a model that is predicted to explode according to the Ertl et al. (2016) test but not the B. Müller et al. (2016) test, and grey points are models that would not successfully explode according to both tests.

infall velocity in the core reaches 1000 km s^{-1}. The fate of a core collapse event is then approximately determined by whether $\xi_{2.5}$ is smaller than 4.5, which leads to a successful neutrino-driven explosion; or larger, which leads to the formation of a BH. The compactness parameter of our models at core collapse is illustrated in Figure 4.11. Although this test is not sufficient to accurately predict whether a stellar model will explode or not (Ertl et al., 2016; B. Müller et al., 2016), more so for fast rotators that have additional sources of energy that could help a successful explosion, it still provides useful information of the structure of a stellar core in the pre-SN stage.

To improve on the predictions of Equation 3.1, Ertl et al. (2016) propose a method to determine the fate of a core-collapse event with a two parameter test. They define the parameters

$$M_4 = m(s = 4)/M_\odot, \tag{3.2}$$

where m is the Lagrangian mass coordinate and s is the specific entropy in units of k_B, and

$$\mu_4 = \left.\frac{\mathrm{dm}/\mathrm{M}_\odot}{\mathrm{dr}/1000\ \mathrm{km}}\right|_{\mathrm{s}=4}, \tag{3.3}$$

the mass gradient evaluated at M_4, evaluated in practice by setting $dm = 0.3\mathrm{M}_\odot$ and dividing by the change in radius between M_4 and $M_4 + dm$. Ertl et al. (2016) provide a calibration of the two parameters where they found the boundary between successful and failed explosions. We evaluate these parameters in our models with the default parameters in Ertl et al. (2016), showing the exploding models according to this test as orange dots in Figure 4.11.

A more sophisticated method to determine explodability was provided by B. Müller et al. (2016), who created a semi-analytic model of the formation of a proto-NS and how it grows by accreting material from its surroundings, and injects a fraction of its neutrino luminosity into the outflowing layers above it, parametrizing the onset of the explosion with mass, radius, density and entropy distribution as inputs from the stellar model at core-collapse, and yielding not only the explodability of a certain model, but also providing other parameters of the explosion.

Since we expect that rotation and magnetic fields increase the likelihood for a successful explosion, we adopted slightly more optimistic values for some of the model parameters. In particular, we employed a smaller value for the efficiency factor for conversion of accretion energy into ν luminosity, setting $\zeta = 0.7$ instead of 0.8, and a longer cooling time-scale for 1.5 $\mathrm{M}_\odot$ NS, setting it to $\tau_{1.5} = 1.5$ s instead of 1.2 s. We found that the dominating effect is to set a shorter $\tau_{1.5}$, which corresponds to injecting energy more quickly into the layers above the collapsing core. These choices correspond to reducing the importance of accretion power in delivering the energy to the gain region, which was done to mimic an energy source that depends on the NS binding energy rather than on the accretion rate, similar to the case we would expect in a magnetorotational mechanism that taps energy from rotation rather than from neutrino emission.

Figure 4.11 shows also the results of this test, pointing out the exploding models with orange and blue dots. With few exceptions, the semi-analytic model is compatible with a dividing line at $\xi_{2.5} \approx 0.45$ between NS and BH formation, which is somewhat higher than the threshold of $\xi_{2.5} \approx 0.3$–0.35 for the standard case of B. Müller et al. (2016), as intended.

The non-monotonic behavior of the compactness parameter as a function of initial mass, as well as the presence of a few cases of mismatching predictions between different tests, also present in previous studies, can be observed to persist in our fast rotating and efficiently mixed evolutionary sequences. This suggests that if stars undergo quasi-chemically homogeneous evolution and rotational mixing is efficient, they may result in a variety of transient events depending on their core properties, and that the outcome of their explosions is not a monotonic function of the progenitor mass. However, it must be reiterated that these results are approximate and are not calibrated to work with fast rotating stars. Recently, Powell et al. (2020) performed a 3D hydrodynamical, neutrino-driven simulation of the core-collapse SN resulting from a 39 $\mathrm{M}_\odot$ model similar to those in ALMS18. This resulted in a successful SN explosion that produced a massive NS instead of a BH. Burrows et al. (2020) also expressed doubts about the anticorrelation of the compactness parameter with explodability based on a large set of 3D SN simulations. On the other hand, these simulation results are also beset with uncertainties and will not necessarily be closer to reality than the phenomenological explosion criteria. Especially explosions for very high compactness would be difficult to reconcile with the lack of high-mass stars among observationally identified SN progenitors (Smartt, 2015).

Compactness (and therefore explodability) seems to correlate closest with iron core mass, which is also a non-monotonic function of initial mass. As seen in Figure 3.5, the distribution of iron core masses

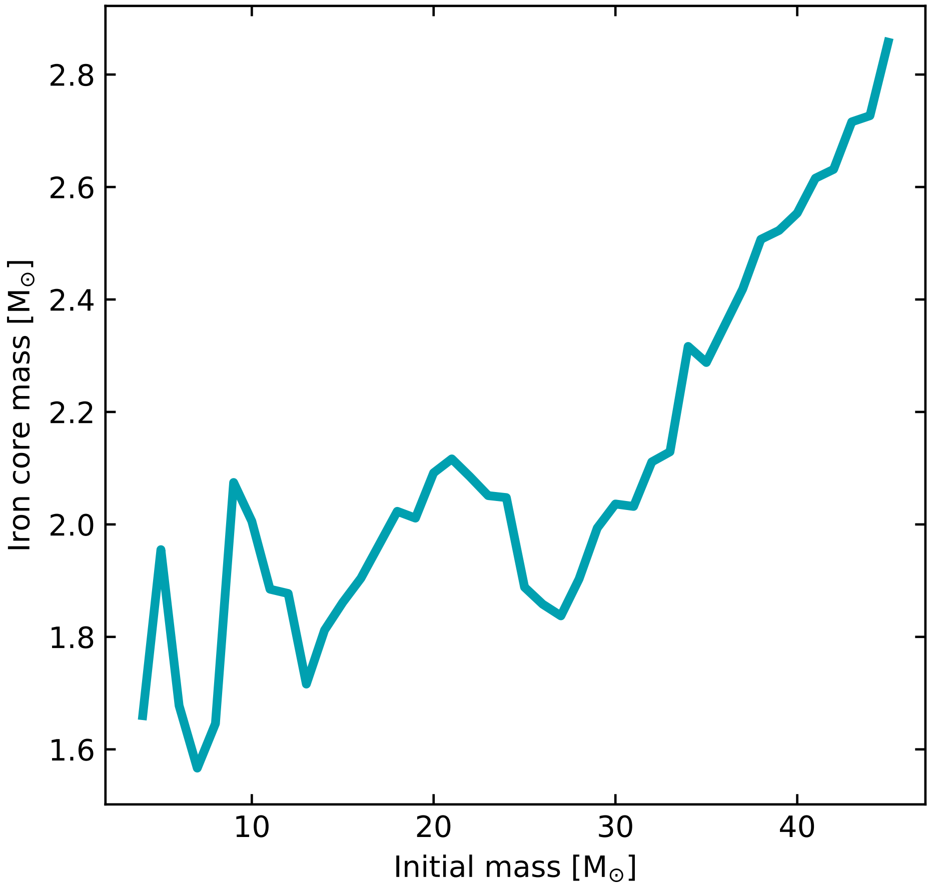

Figure 3.5: Iron core mass of the core collapse models in this study, as a function of initial mass.

resembles closely that of $\xi_{2.5}$. This is also reflected in Figure 3.6, where the correlation between $\xi_{2.5}$ and iron core mass is explicitly demonstrated. Figure 3.6 also shows that models where convective carbon burning occurs tend to have a lower overall compactness, as found by Sukhbold et al. 2018.

We can infer from these results that BH formation may be favorable in the mass range from 9 to 11 M$_\odot$, and in those exceeding around 15 M$_\odot$, excluding perhaps a window around 25-31 M$_\odot$, where explosions are not predicted by the Ertl et al. (2016) method, but are predicted to explode by the B. Müller et al. (2016) method and have relatively low compactness. Furthermore, these models might be affected by centrifugal acceleration, rotationally induced instabilities and the evolution of their magnetic field during collapse, which might result in a different number of explosions in a given mass range.

This suggests that the parameter space where we expect to form SLSNe powered by a magnetar or lGRBs powered by a collapsar is a non-monotonic function of mass, and windows of explodibility exist in the case of chemically homogeneously evolving stars as well, even if rotational mixing is efficient. However, it is important to reiterate that this threshold for explodibility are calibrated with explosion models powered by neutrino heaeting, and detailed numerical calculations are still required to study the effect of energy deposition by the central engine itself, the evolution of the magnetic fields, and other 3D effects that might become important during the collapse.

Although the non-monotonic behavior of $\xi_{2.5}$ is present in all pre-SN models, some of the differences between the canonical evolutionary channel of single massive stars and chemically homogeneous stars are

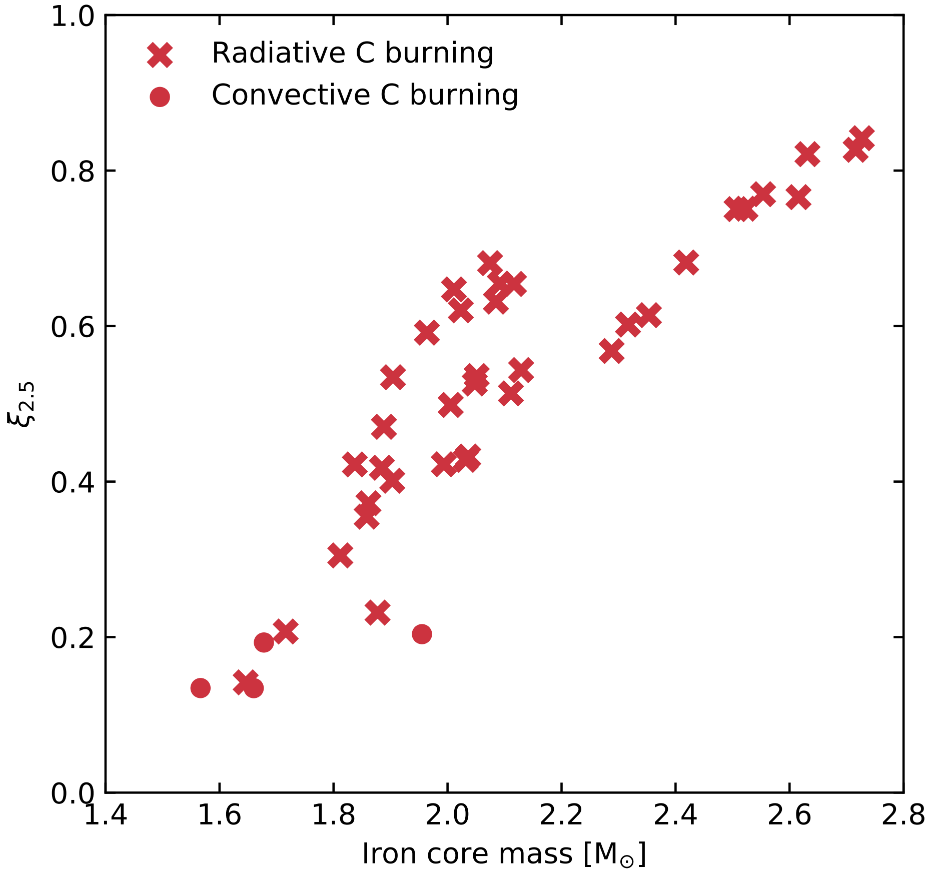

Figure 3.6: Compactness parameter measured at 2.5 M$_\odot$ of the core collapse models in this study, as a function of iron core mass at the moment of core collapse. Crosses indicate models where core carbon burning occurred radiatively, whereas points indicate convective core carbon burning.

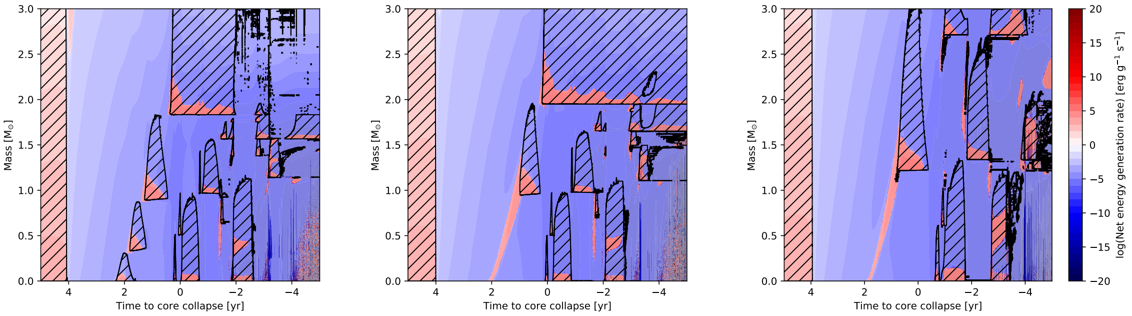

Figure 3.7: Kippenhahn diagrams following the energy generation/loss rate, and the structure of convective regions as a funciton of time remaining until core collapse, from core helium burning until minutes before core collapse. Represented are the evolutionary sequences with initial masses of 7 (left), 8 (middle) and 9 M$_\odot$ (right). Color denotes the intensity of energy generation rate (red), and the energy loss rate (blue). Regions hatched with diagonals denote convective regions.

reflected in the behavior of $\xi_{2.5}$. Despite the low metalicity, rotation and neutrino-driven contraction cause a very strong rotationally enhanced mass loss rate, which ends up accounting for around 0.5 – 0.7 $M_{\odot}$ of material in the last 1000 years of evolution (depending on the loss of angular momentum, see Section 3.2.2), as well as a large fraction of the initial mass during the rest of its evolution, particularly during the contraction after hydrogen and helium burning. Mass loss is already known to have an important effect (Renzo et al., 2017; Sukhbold et al., 2018) in the behavior of $\xi_{2.5}$, since it sets the relation between initial mass and carbon/oxygen core mass, which in turn fixes the boundaries between different behaviors during carbon and oxygen burning.

Models with ZAMS masses between 7 and 14 $M_{\odot}$ are expected to have more variations than we currently trace with the resolution in initial mass in our models. As was shown by Sukhbold et al. (2014) and Sukhbold et al. (2018), solutions to the equations of stellar structure vary significantly with small changes in mass in this regime, due to the transition that occurs between radiative and convective core carbon burning, which is shown in Figure 3.7 to occur in this mass regime, and which was found to have a very strong effect on $\xi_{2.5}$. In our simulations, this transition is found between 7 and 8 $M_{\odot}$, but a strong variation of $\xi_{2.5}$ was resolved between 8 and 9 $M_{\odot}$ and beyond. The first and second carbon shells disappear between 7 and 8 $M_{\odot}$, but between 8 and 9 $M_{\odot}$ the third carbon burning shell (following the notation from Sukhbold et al. (2014)) ignites much more intensely, resulting in a convective region that spans almost all of the carbon/oxygen shell, and that burns strongly until the core collapses, as opposed to lower mass models which develop a number of smaller carbon burning shells through their evolution. This, in turn, results in a later ignition of neon/oxygen, allowing the innermost part of the core to contract for a longer time, resulting in a higher value of $\xi_{2.5}$.

Once the core exceeds around 15 $M_{\odot}$, however, the core structure becomes more regular: Radiative carbon burning followed by convective neon and oxygen burning shells, a convective region that encompasses the silicon core and the oxygen shell, and a strong carbon burning shell on top that remains on until the end of the evolution, and that is active from the edge of the core to the helium burning shell close to the surface. As each of these regions grows in mass with the total mass of the star, the factors that then determine the compactness are the size of the core, which determines the relative location of the 2.5 $M_{\odot}$ mass coordinate where we define the compactness, and the behavior of the silicon burning region and oxygen shells only minutes before core collapse.

Using the B. Müller et al. (2016) analytical model to determine explodability of these models also yields a number of other interesting parameters. These are summarized in Figure 3.8 and in Table 3.2.As expected from the relatively high compactness and high core masses. these models will –on average– lead to a large amount of energy deposited by neutrinos into the ejecta, as well as producing massive NSs, and large amounts of ^{56}Ni during the explosion. Strictly speaking, this only means that we expect a large energy and ejected nickel mass of a neutrino-driven “precursor” to the millisecond magnetar phase, or a significant auxiliary contribution of neutrino heating to the explosion energy in a magnetorotational SN. For this reason, we also list the rotational energy $E_{\mathrm{rot,NS}}$ of the NS in Table 3.2 as a rough estimate for the energy attainable in a magnetorotational explosion.

Table 3.2: Explosion parameters inferred from core collapse models in this work analyzed with the B. Müller et al. (2016) model, and rotational energy of the resulting NS, total rotational and absolute value of their total energies (sum of gravitational, internal, kinetic and rotational energies) at core collapse.

M_{init} [$M_{\odot}$]	E^{a}_{exp} [10^{51} erg]	M(^{56}Ni) ^{a} [$M_{\odot}$]	$M^{a}_{\mathrm{grav,NS}}$ [$M_{\odot}$]	M^{a}_{ejecta} [$M_{\odot}$]	$E^{b}_{\mathrm{rot,NS}}$ [10^{51} erg]	E^{c}_{rot} [10^{51} erg]	$\lvert E_{\mathrm{tot}}\rvert^{c}$ [10^{51} erg]
4	1.64	0.12	1.34	1.83	0.69	0.0004	0.97
5	2.75	0.22	1.21	2.76	0.38	0.0009	1.06

6	1.33	0.12	1.38	3.35	4.77	0.0021	1.10
7	0.65	0.07	1.26	4.3	1.97	0.0021	1.04
8	0.83	0.09	1.28	5.07	2.40	0.0030	1.12
9	–	–	–	–	21.5	0.0077	1.71
10	4.45	0.11	1.75	6.07	24.8	0.0092	1.64
11	2.64	0.13	1.64	6.98	20.1	0.0128	1.71
12	1.41	0.09	1.46	7.98	8.52	0.0089	1.48
13	2.47	0.15	1.39	8.82	5.17	0.0073	1.48
14	3.84	0.21	1.49	9.47	6.10	0.0091	1.66
15	4.28	0.20	1.59	10.1	13.2	0.0116	1.78
16	5.09	0.09	1.79	10.6	30.2	0.0138	1.96
17	–	–	–	–	–	0.0151	2.08
18	–	–	–	–	–	0.0166	2.19
19	–	–	–	–	–	0.0183	2.31
20	–	–	–	–	–	0.0120	2.44
21	–	–	–	–	–	0.0227	2.56
22	–	–	–	–	–	0.0267	2.71
23	–	–	–	–	–	0.0267	2.71
24	–	–	–	–	–	0.0259	2.75
25	–	–	–	–	–	0.0295	2.79
26	2.99	0.098	1.53	18.3	17.1	0.0245	2.61
27	4.97	0.170	1.48	19.1	7.51	0.03[a]12	2.86
28	3.50	0.142	1.55	19.8	15.8	0.0307	2.87
29	3.85	0.095	1.65	20.4	26.2	0.0311	2.95
30	4.07	0.096	1.66	21.1	16.2	0.0318	3.04
31	4.29	0.096	1.65	21.8	12.6	0.0328	3.12
32	–	–	–	–	–	0.0376	3.26
33	–	–	–	–	–	0.0389	3.35
34	1.17	0.003	2.01	23.5	98.6	0.0421	3.46
35	–	–	–	–	–	0.0420	3.53
36	–	–	–	–	–	0.0434	3.64
37	–	–	–	–	–	0.0457	3.73
38	–	–	–	–	–	0.0479	3.84
39	–	–	–	–	–	0.0501	3.90
40	–	–	–	–	–	0.0487	3.99
41	–	–	–	–	–	0.0505	4.05
42	–	–	–	–	–	0.0556	4.18
43	–	–	–	–	–	0.0565	4.30
44	–	–	–	–	–	0.0630	4.38
45	–	–	–	–	–	0.0608	4.42

[a] Resulting from applying the B. Müller et al. (2016) model

[b] Considering the mass of the NS from the B. Müller et al. (2016) model, moment of inertia from Worley et al. (2008), assuming conservation of angular momentum during core collapse and a NS radius of 15 km

[c] At core collapse

In the context of magnetorotational explosions it is also interesting to consider the initial magnetic

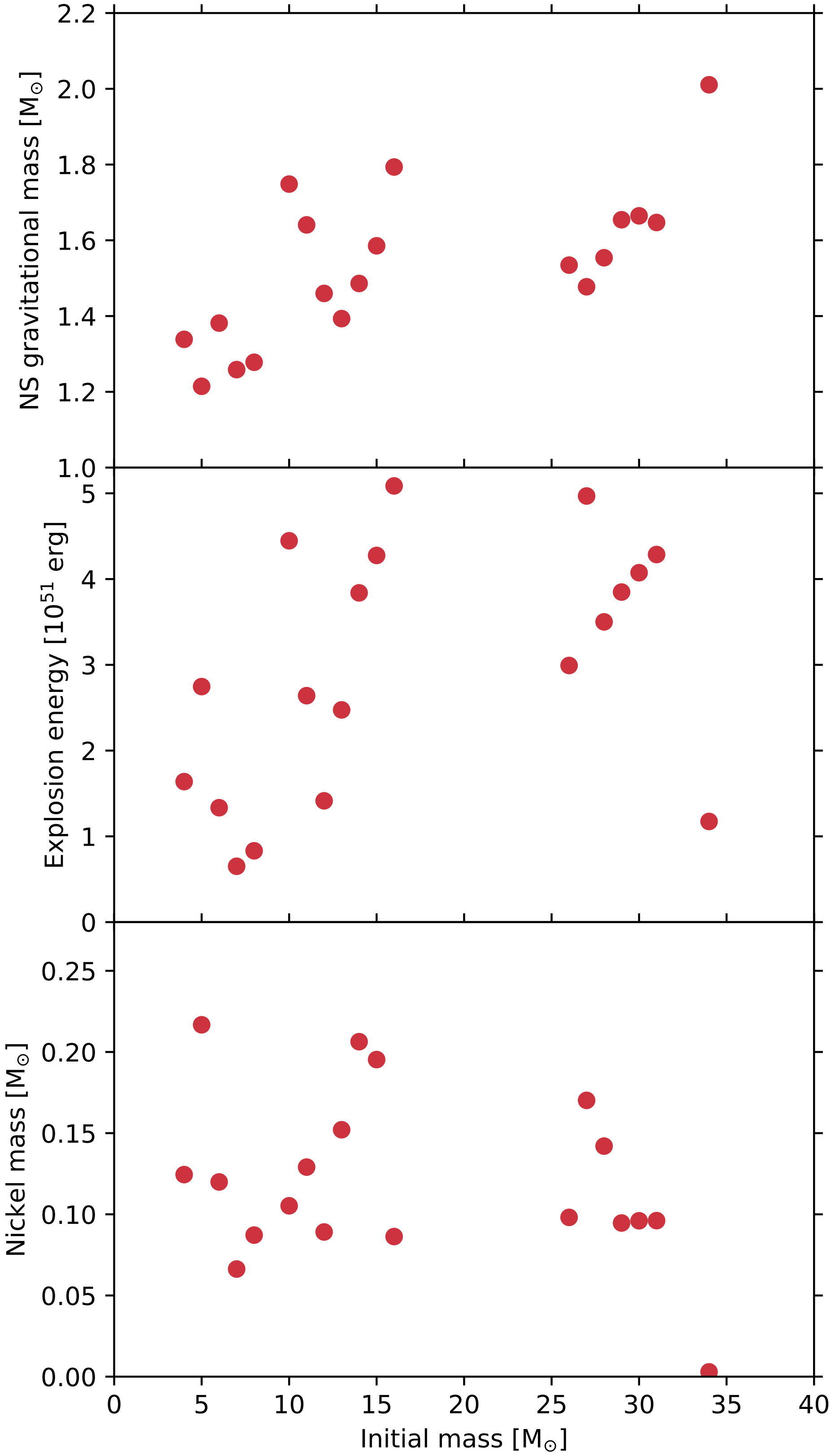

Figure 3.8: NS gravitational mass, explosion energy and ^{56}Ni mass resulting from SN explosions produced from our core collapse models, as predicted by the B. Müller et al. (2016) model, as a function of initial mass.

field strength in the core. Figure 3.9, shows the strength of dynamo-generated magnetic fields averaged inside the innermost 1.5 $M_\odot$; namely

$$\langle B_\phi \rangle = \frac{\int_0^{1.5M_\odot} B_\phi(m)\mathrm{d}m}{\int_0^{1.5M_\odot} \mathrm{d}m}, \tag{3.4}$$

at core collapse in blue, and assuming that the core contracted homologously to a radius of 15 km and that contraction was flux conserving after core collapse in orange. Magnetic fields generated by the Spruit-Tayler dynamo alone are of the order of 10^{10} Gauss in the stellar cores. Despite this large strength, these fields are unlikely to be dynamically important (as opposed to rotation), since the plasma parameter β inside the core never goes below around 10^2 in any of our models at core collapse (or at any other evolutionary stage).

Magnetic field strengths calculated assuming homologous contraction and flux conservation yield values that are in similar orders of magnitude than those inferred for magnetar driven SLSNe by observations (Nicholl et al., 2017; Villar et al., 2018; Blanchard et al., 2018; Blanchard et al., 2019; Blanchard et al., 2020). However, magnetic field values at core collapse are not simply scaled to their flux-conserving value at NS radius, but are rather amplified by a dynamo during the formation of the proto-NS, either driven by convection (e.g. Thompson et al. 1993; Raynaud et al. 2020), or the magnetorotational instability (MRI, e.g., Akiyama et al. 2003; Masada et al. 2015; Guilet et al. 2015; Mösta et al. 2015; Masada et al. 2012; Obergaulinger et al. 2018). These amplification mechanisms may not guarantee fast magnetorotational explosions independent of the seed fields. In the case of the MRI, the amplification factor may be limited (Rembiasz et al., 2016) or it may not immediately produce strong dipole fields . Furthermore, strong dipole fields created by dynamo action inside the proto-SN may not affect SN dynamics on short time scales, before they break out through the NS surface. It is therefore noteworthy that the magnetic field strengths we predict are already very high, and little amplification is needed to match the observationally inferred values.

3.4 Observable properties

The final fate of our evolutionary sequences will be determined to first order by whether a BH or a fast spinning magnetar is predicted to be formed by their core collapse model. BH forming fast rotators are likely to form collapsars, whereas magnetar-forming stars may produce magnetar-driven SLSNe, magnetar driven lGRBs, or perhaps both.

Taking the results from Table 3.2 at face value also implies that, given the high values for ejecta masses, nickel masses and explosion energies provided by the neutrinos alone, we could already expect the transients coming from progenitors that are predicted to successfuly explode solely powered by neutrinos to have longer lifetimes and slower rise times than typical stripped-envelope SNe, following simply from the model of Arnett (1982), but the energies and nickel masses alone are not able to explain the high luminosities of SLSNe.

Assuming that our evolutionary sequences result in magnetar formation yields consistent results with the observed properties of SLSNe inferred by the samples analyzed by Nicholl et al. (2017), Villar et al. (2018) and Blanchard et al. (2020). Figure 3.10 shows the expected ejecta masses (taken from Table 3.2) and spin periods expected from the evolutionary sequences that explode as SLSNe. The spin period is calculated assuming that the NS formed after collapse contains the angular momentum remaining on the mass that is not ejected, and that angular momentum is conserved and reconfigured into a radius of 15 km. The moment of inertia of the newly-formed NS is taken from Worley et al. (2008). These values

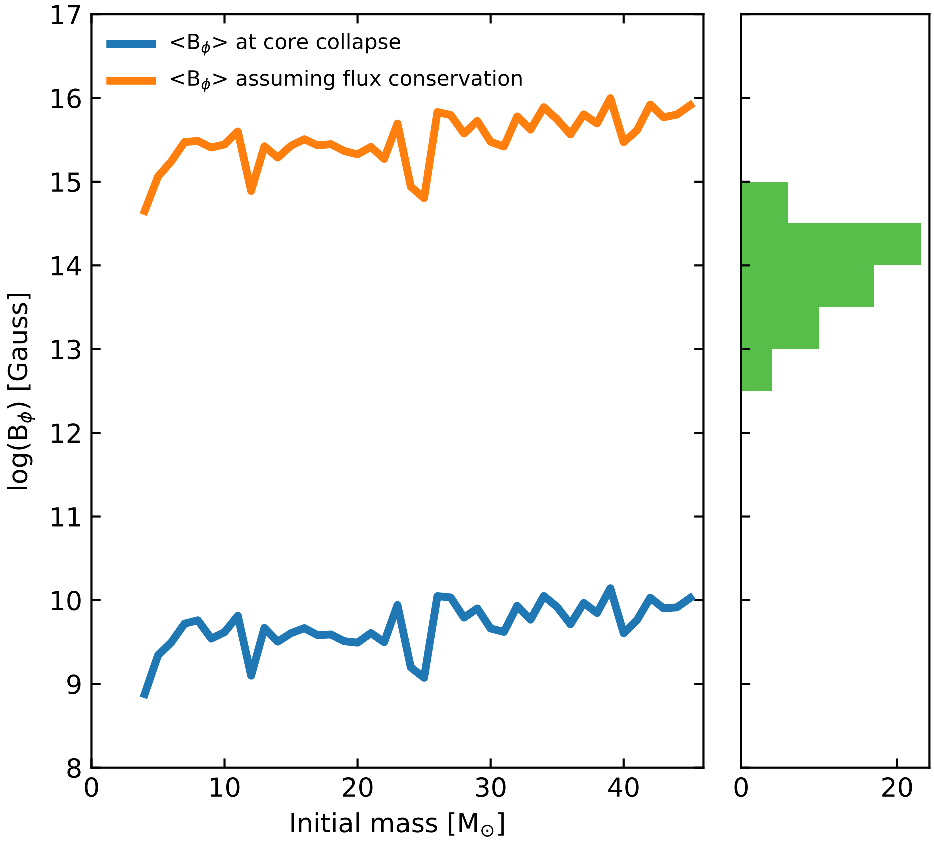

Figure 3.9: Azimuthal component of the magnetic field, averaged over the innermost $1.5M_\odot$ of our core collapse models (blue), and assuming this region contracts homologously to a radius of 15 km, and that magnetic flux is conserved during the contraction (orange), as a funciton of initial mass. Compared to the inferred values for the SLSN samples analyzed by Nicholl et al. (2017), Villar et al. (2018) and Blanchard et al. (2018) and and Blanchard et al. (2019) in the context of the magnetar model (histogram on the right).

seem to be consistent with those inferred from observations, and match correlation between spin period and ejecta mass found by Blanchard et al. (2020). In our models, this correlation is caused to first order by the different life times that stars have as a function of initial mass: Less massive stars live longer, and thus have more time to transport angular momentum outside of their contracting iron core.

Another feature that will become important, particularly for lower mass progenitors, is how the ejecta will interact with the CSM. Even with lower mass loss rates than in ALMS18, it is expected that the ejecta will encounter a massive CSM in a non-trivial geometry, given the fact that the mass loss rates increase steeply during the last 1000 years before core collapse, and a non-spherical structure of around 0.5 $M_\odot$ will be located in a likely toroidal configuration around the star.Determining the exact location and density profile of this structure requires, at least, 2D numerical simulations of the flow, which will be concentrated in the equatorial plane, and which will likely have low velocities, since it is accelerated by the centrifugal force of material at the surface, and not by the radiation field of the star, as is the case in a Wolf-Rayet wind (see van Marle et al. (2008) for simulations of similar structures, and ALMS18 for a detailed discussion). However, as shown with the red and orange lines in Figure 3.11, the mass contained in this region can convert a fraction f_M of the kinetic energy of the ejecta into radiation, that goes up to 15% in the lowest mass models. This could possibly help in explaining bumps in SLSNe light curves, or

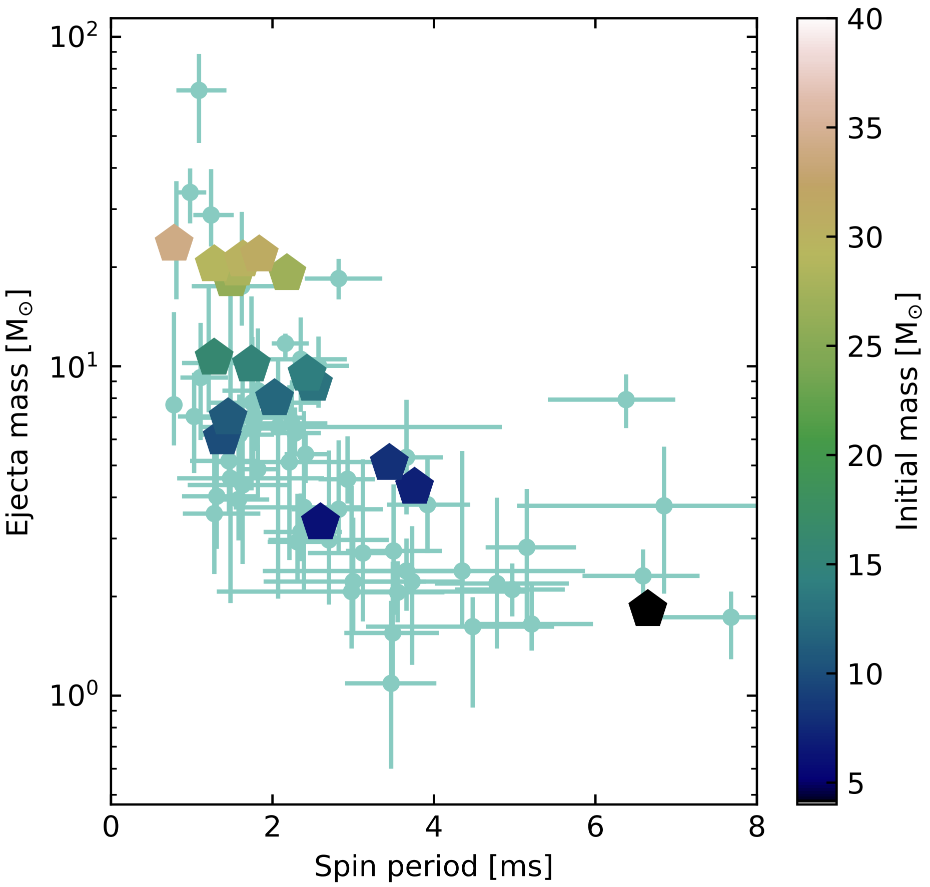

Figure 3.10: Pentagons represent the ejecta masses produced by SN explosions produced from the our core collapse models –as predicted by the B. Müller et al. (2016) model– as a function of the spin periods calculated for their remnants, and colored by their initial mass. Spin periods are calculated assuming homologous contraction of the collapsing core to a radius of 15 km, conservation of angular momentum, and NS moment of inertia as prescribed by Worley et al. (2008). Light blue points correspond to the inferred values from observations obtained for observed SLSNe obtained by Nicholl et al. (2017), Villar et al. (2018) and Blanchard et al. (2018) and and Blanchard et al. (2019).

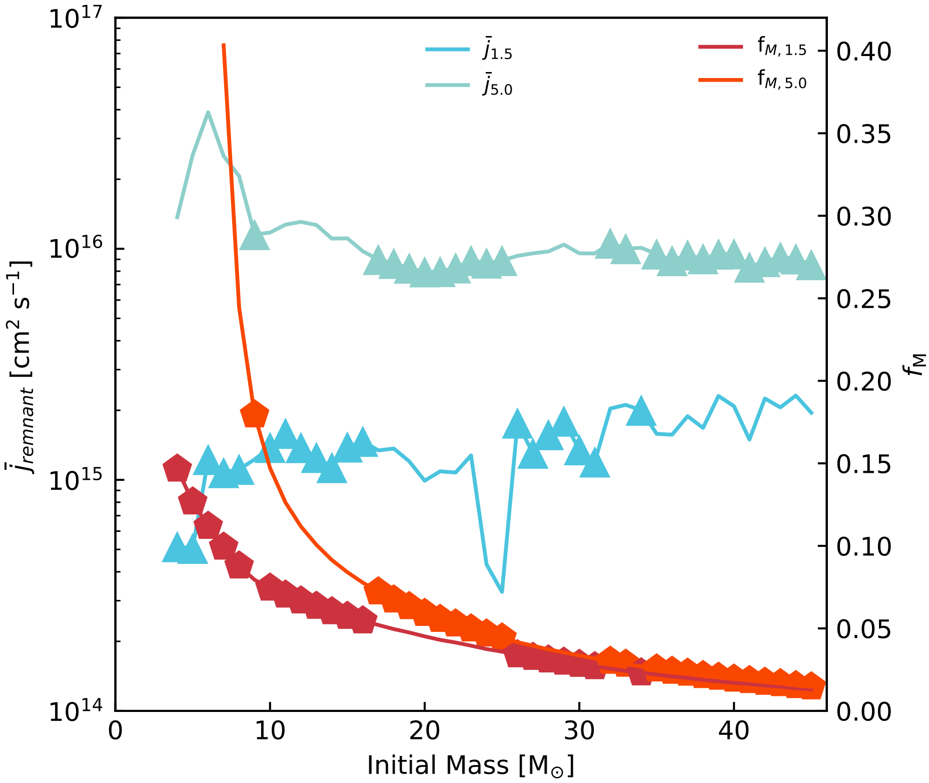

Figure 3.11: The left y-axis shows the average specific angular momentum in the innermost 1.5 $M_\odot$ (blue) and 5 $M_\odot$ (orange) of core collapse models, chosen as mass coordinates representative of NS and collapsar forming models, respectively.On the right y-axis, the fraction of the kinetic energy that can be converted into radiation by CSM interaction, f_M, is shown. This is calculated assuming that the explosions leave behind a 1.5 $M_\odot$ remnant (red) and a 5 $M_\odot$ remnant (orange), and that the ejected mass interacts with the CSM mass given by $\Delta M_{\mathrm{He}\rightarrow\mathrm{final}}$. Hexagons in the plot correspond to core collapse models that explode as a SLSN according to the Marchant et al. (2016b) model, triangles correspond to models that are expected to form a BH. All quantities shown as a function of initial mass.

possibly becoming important several days after maximum, depending on the geometry of the CSM (see Figure 12 of ALMS18).

Figure 3.11 also shows average specific angular momentum in the innermost 1.5 $M_\odot$, corresponding to a case that forms a NS, and 5 $M_\odot$, taken as a fiducial mass for a BH, indicating which progenitor models we expect to successfully explode, and which ones we expect to form a BH with a triangle in models with $\xi_{2.5}$ larger or smaller than 4.5. Those that we expect to form BHs are going to have enough angular momentum to form collapsars, whereas those that form NSs have angular momenta consistent with magnetars (also seen in Figure 3.10).

3.5 Conclusions

We computed a grid of evolutionary models for fast rotating, low metallicity stars with enhanced rotational mixing, and found that changing the way that angular momentum is lost in response to mass loss changed the expected outcome with respect to ALMS18. We found larger final masses, a higher helium content and less massive CSM. However, we still expect them to be viable progenitors for Type Ic SLSNe and lGRBs, and we expect that interaction with the nearby CSM will manifest itself in the lightcurve in an observable way, particularly in models with low ejecta mass, which will be closer to the expected CSM mass.

We studied the explodability of our core collapse models through their compactness parameter $\xi_{2.5}$ (O'Connor et al., 2011), the parameters M_4 and μ_4 (Ertl et al., 2016), and an analytical test proposed by B. Müller et al. (2016). These three tests have been used to estimate the likelihood of non-rotating stellar evolutionary sequences during core collapse to form either a NS –and a successful SN explosion– or formation of a BH, in the neutrino driven SN scenario. Given their angular momenta and magnetic field strengths, these progenitors might correspond to progenitors of either lGRBs or SLSNe, depending on the result of the collapse. We find that the behavior of these tests is similar to non-rotating stars, presenting a non-linear behavior as a function of initial mass, but rotational mixing can affect the exact evolution of the stellar core by changing the relation between initial mass and subsequent core masses, and also smoothing composition gradients throughout the evolution, therefore affecting the explodability of these stars.

We found that, taking $\xi_{2.5}$ as an indicator of the likelihood of forming either NSs or BHs during core collapse, it is possible that the initial mass is not enough to determine the fate of a quasi-chemically homogeneous massive star. This may result in either the explosion forming a SLSN or a lGRB, depending on whether a magnetar or a BH is formed.

However, a significant amount of rotational energy can be released by the contracting proto-NS during collapse, and the explosion should also be promoted by rotationally and magnetically driven instabilities, which might relax the value of the compactness parameter that separates exploding and imploding cores. (see Summa et al. 2018 for the beneficial influence of rapid rotation in the explosion mechanism). Nevertheless, only detailed simulations of the explosion could give a definite answer. Regardless of the initial mass of the progenitor, our core collapse models resemble the observed ejecta masses and rotation periods inferred for SLSNe, if indeed magnetars are the main source of energy during the explosion, even when considering more efficient angular momentum loss.

We also found that fast rotating stars at low metallicity are consistently strongly magnetic in their cores, which might lead to the magnetic fields being important during the process of collapse, although not dynamically during the evolution of the star.

We found that the evolutionary channel experienced by the evolutionary sequences presented in this work will produce lGRBs and SLSNe, consistent with the inferred properties of their progenitors, and likely as a non-monotonic function of initial mass. In particular, our models reproduce the range of ejecta masses, magnetar spin periods and magnetic fields inferred for SLSNe (Blanchard et al., 2020). A more detailed study of this channel in different metallicities and with different rotational velocities is required, however, to compare with the SLSN and lGRB rates, and with the ejecta mass distribution inferred by Blanchard et al. (2020). These transients might have important CSM interaction, particularly if observed close to their plane of rotation.

Acknowledgements. DRAD would like to acknowledge valuable discussions with Matteo Bugli, Luc Dessart, Eva Laplace, Abel Schootemeijer and Alejandro Vigna-Gomez. BM was supported by the Australian Research Council (ARC) through Future Fellowship FT160100035 and as an associate investigator of the ARC CoE for Gravitational Wave Discovery *OzGrav* (CE170100004).

CHAPTER 4

Type Ibc Supernovae Progenitors and Wolf-Rayet Stars Evolving from Helium Stars in Different Metallicities

David R. Aguilera-Dena[1,2], Norbert Langer[1,2], John Antoniadis[2,1,3], Daniel Pauli[1], Bernhard Müller[4], Luc Dessart[5], Alejandro Vigna-Gómez[6], Götz Gräfener[1] & Sung-Chul Yoon[7]
[1]Argelander-Institüt für Astronomie, Universität Bonn, Auf dem Hügel 71, 53121 Bonn, Germany
[2]Max-Planck-Institut für Radioastronomie, Auf dem Hügel 69, 53121 Bonn, Germany
[3]Institute of Astrophysics, FORTH, Dept. of Physics, University of Crete, Voutes, University Campus, GR-71003 Heraklion, Greece
[4]School of Physics and Astronomy, Monash University, VIC 3800, Australia
[5]Institut d'Astrophysique de Paris, CNRS-Sorbonne Université, 98 bis boulevard Arago, F-75014 Paris, France
[6]DARK, Niels Bohr Institute, University of Copenhagen, Blegdamsvej 17, 2100, Copenhagen,Denmark
[7]Department of Physics and Astronomy, Seoul National University, Gwanak-gu, Seoul, 151-742, Republic of Korea

To be submitted to *Astronomy & Astrophysics*

Abstract. Massive stars that have lost their hydrogen envelope, as a consequence of binary interaction or due to single star mass loss, can be observed as Wolf-Rayet (WR) stars, and are potential progenitors to Type I core-collapse supernovae (SNe). Approximating these systems through single helium stars, we studied the effects of metallicity during and after core helium burning, and in the transients they produce and the remnants left behind at the end of their stellar lives. We predict the fraction of the lifetimes these stars would spend as nitrogen-rich (WN) or carbon-rich (WC) WR stars, and their lower luminosity WN thresholds, both of which vary strongly as a function of metallicity. Combining these results, we estimate the number ratio of WC to hydrogen free WN stars as a function of metallicity in a stellar population produced by a constant star formation rate. We then analyze their surface properties at the time of core collapse, and derive how the number ratio of Ic to Ib SNe increases with metallicity. Using several methods to infer the explosion properties based on the pre-SN structure of our models, we find that not only the rates of different supernova types vary with metallicity, but also the neutron star (NS) and black hole (BH) mass distributions and the supernova ejecta masses. These variations can potentially have strong consequences for our understanding of binary BH and NS systems, including including then recently observed gravitational wave transients due to compact object mergers.

Key words. stars: massive – stars: Wolf-Rayet – supernovae:general

4.1 Introduction

Type I core-collapse supernovae (SNe) are relatively frequent in the local Universe. Most common among them are the "normal" Type Ib and Type Ic accounting for around 20 % of all core-collapse SNe (Cappellaro et al., 1999; van den Bergh et al., 2005; Prieto et al., 2008; Smartt et al., 2009; W. Li et al., 2011; Shivvers et al., 2017). The absence of prominent hydrogen lines in their spectra indicate that their progenitors have completely lost their hydrogen rich envelope by the time they reach core-collapse (Dessart et al., 2011; Hachinger et al., 2012). Their observed properties have been found to be reproduced by the explosion of relatively low mass helium stars (e.g. Dessart et al., 2011).

Since a significant fraction of massive stars evolve in binary systems that will interact before reaching core-collapse (Sana et al., 2011; Sana et al., 2012), binary interaction has been often proposed as a viable channel to produce hydrogen-deficient or hydrogen-free helium stars (e.g. Podsiadlowski et al., 1992; Yoon et al., 2010; Langer, 2012).

Several studies of evolutionary channels for interacting binaries as likely progenitors of Type I core-collapse SNe have been carried out in recent years. Several approaches have been taken, including detailed binary evolution (e.g. Yoon et al., 2010), rapid binary population synthesis (e.g. Kruckow et al., 2018), and detailed evolutionary calculations of single helium stars (e.g. Arnett, 1974; S. E. Woosley et al., 1995; McClelland et al., 2016; Yoon, 2017; S. E. Woosley, 2019; Ertl et al., 2020) and helium stars in binaries (e.g. Dewi et al., 2002; Dewi et al., 2003; Tauris et al., 2015). Evolutionary channels for Type I core-collapse SNe have been widely found in these studies, but explaining the rate, distribution of ejecta mass and of chemical composition remains challenging.

The distinction between the progenitors of Type Ib SNe, which have strong helium lines, to Type Ic SNe, which do not, has been widely discussed in the literature (e.g. Dessart et al., 2012; Dessart et al., 2020). They belong to a class of transients (known as stripped-envelope SNe, which includes Type Ibc SNe, but also Type IIb SNe) with properties that are distinct from the hydrogen-rich Type II SNe, as well as from other hydrogen and helium deficient transients of stellar origin that are more energetic, such as long gamma-ray bursts, Type I superluminous SNe and Type Ic-BL SNe (Modjaz et al., 2011; Modjaz et al., 2019); likely because their progenitors have a different evolutionary history, which in turn may influence their rate differently as a function of metallicity.

Massive helium stars are often observed as Wolf-Rayet (WR) stars. They are distinguished by emission lines in their spectra, consequence of their optically thick stellar winds. The observed mass loss rates of WR stars can be several orders of magnitude larger than stellar winds of main sequence and red supergiant stars, and they strongly influence the late evolution of massive, stripped-envelope stars (see, for example, Crowther, 2007, for a review).

In a recent study, Yoon (2017) found that an increase in the metallicity dependent mass loss rate that is observed to happen in WR stars of the WC subclass could account for the formation of the faintest WC and WO type stars in our Galaxy. The detailed SN light curve and spectral models of Dessart et al. (2020) confirm that an increase in the metallicity dependent mass loss rate of WR stars can lead to the production of Type Ic SNe, and results in a sharp dichotomy in the masses and compositions of progenitors of Type Ic and Type Ib SNe.

Since the metallicity dependent WR mass loss is so important for the observed properties of SNe that result from helium stars, in this paper we study the evolution of helium stars including wind mass loss, in a similar fashion to Yoon (2017) and S. E. Woosley (2019). We extend the initial conditions to cover different metallicity environments, focusing on high metallicity environments, which are not often addressed in the literature, but can account for changes in properties of populations of helium stars and Type I SNe.

We also pay particular attention to the empirical, metallicity-dependent lower luminosity limit of

WR stars (Götberg et al., 2018; Shenar et al., 2020), likely related to the drop of the mass loss rate for lower-luminosity helium stars (Vink, 2017; Sander et al., 2020).

We have subdivided our paper as follows: In Section 4.2 we describe the physical and numerical treatment we use in our simulations. In Section 4.3 we present our main results, subdividing them into a description of the time-dependent properties of helium stars in Section 4.3.1, and their properties at core-collapse and an analysis of the transients we expect from them in Section 4.4. We finalize our paper with a discussion in Section 4.5 and conclusions in Section 4.6.

4.2 Method

To study the effect of metallicity in the evolution of helium stars and the SNe they produce, we calculated grids of evolutionary sequences of non-rotating helium stars using version 10398 of the Modules for Experiments in Stellar Astrophysics (MESA) code (Paxton et al., 2011; Paxton et al., 2013; Paxton et al., 2015; Paxton et al., 2018), from the helium zero age main sequence (He-ZAMS) to the onset of core collapse, defined by the point where the infall velocity of the iron core is larger than 1000 km s^{-1}.

To test the effect of chemical composition in hydrogen depleted WR stars, we performed calculations for 7 different metallicities, from 0.01 to 0.04 in steps of 0.05, scaled from solar abundances found by Grevesse et al. (1996), and initial masses between 1.5 and 70 $M_\odot$ in steps of 0.5 $M_\odot$.

The initial models were generated taking hydrogen rich pre-main sequence models at the different metallicities, and evolving them chemically homogeneously and without mass loss until the end of hydrogen burning, but before core ignition of nitrogen, and further evolving them until they settled into thermal equilibrium from helium burning, relaxing the condition of homogeneity. This helped us guarantee that the abundances of CNO elements would correspond to those of the core of a massive star after helium burning (enhanced N, reduced C and O), and that their final helium content would be given by $Y = 1 - Z$.

Although binary evolution models find that some hydrogen remains in the surface of stars that have been stripped due to Roche lobe overflow (Gilkis et al., 2019; Laplace et al., 2020) we assume that the remaining hydrogen is small, and will be removed in a short time scale by winds or case B mass transfer, and thus does not significantly affect the evolution of helium stars.

Convection was modeled using the standard mixing length theory (Böhm-Vitense, 1958), using the standard MESA value of $\alpha_{MLT} = 2.0$, and adopting the Ledoux criterion for instability, and we employed efficient semiconvection, using $\alpha_{SC} = 1.0$, following the results of Schootemeijer et al. (2019). Convective overshooting was not included during helium burning, or during any of the later phases of evolution. We included thermohaline mixing as prescribed by Kippenhahn et al. (1980). To allow for the growth of the helium core in the case where no mass loss was present, we also employed MESA's predictive mixing in the helium burning regions Paxton et al. (2018). We calculated the energy generation rates and chemical composition changes using MESA's `approx21` nuclear network, from the initial model to core collapse.

Since pure helium stars often experience instabilities in their envelopes due to the proximity to the Eddington limit (e.g. Sanyal et al. 2015), we calculated these model using efficient energy transport through MESA's `mlt++`, and excluding radiative acceleration in the envelope by setting the velocity to 0 in layers with $T > 10^8$ K during the late evolution.

Models with masses below 15 $M_\odot$ use a finer temporal and spatial resolution than the default in MESA, achieved by setting the variables `varcontrol_target` to 10^{-5}, and `mesh_delta_coef` to 0.5. Models with initial helium mases above 15 $M_\odot$ were initially calculated with the same prescriptions, but if they failed to reach core collapse with this setup, they were calculated with `varcontrol_target` to 10^{-4}

(the default value), and `mesh_delta_coef` to 0.3, effectively increasing the number of grid points but also increasing the timesteps, and with the option `Pextra_factor` set to two, adding an extra pressure to avoid their envelopes from expanding. The options that were chosen to simplify the calculations in the envelope were done to focus our study in the core structure of helium stars as they approach core collapse, and we will address the detailed behavior of the envelope in a future paper.

We use the mass loss algorithm suggested by Yoon (2017), which prescribes different mass loss rates for WN and WC/WO stars. It is based on the work of Hainich et al. (2014) for WN stars and Tramper et al. (2016) for WC/WO stars. This mass loss algorithm has the form

$$\dot{\mathrm{M}}_{\mathrm{WN}} = f_{\mathrm{WR}} \left(\frac{\mathrm{L}}{\mathrm{L}_{\odot}}\right)^{1.18} \left(\frac{\mathrm{Z}}{\mathrm{Z}_{\odot}}\right)^{0.6} 10^{-11.32} \frac{\mathrm{M}_{\odot}}{\mathrm{yr}}, \tag{4.1}$$

for Y=1-$\mathrm{Z}_{\mathrm{init}}$, and for Y<0.9, it takes the form

$$\dot{\mathrm{M}}_{\mathrm{WC}} = f_{\mathrm{WR}} \left(\frac{\mathrm{L}}{\mathrm{L}_{\odot}}\right)^{0.85} \left(\frac{\mathrm{Z}}{\mathrm{Z}_{\odot}}\right)^{0.25} \mathrm{Y}^{0.85} 10^{-9.2} \frac{\mathrm{M}_{\odot}}{\mathrm{yr}}. \tag{4.2}$$

As suggested by Yoon (2017), we interpolate between them linearly in the regime between Y=1-$\mathrm{Z}_{\mathrm{init}}$ and Y<0.9 using

$$\dot{\mathrm{M}} = (1 - x)\dot{\mathrm{M}}_{\mathrm{WN}} + x\dot{\mathrm{M}}_{\mathrm{WC}}, \tag{4.3}$$

with $x = (1 - \mathrm{Z}_{\mathrm{init}} - \mathrm{Y})/(1 - \mathrm{Z}_{\mathrm{init}} - 0.9)$. We take the recommended value of f_{WR}=1.58, and scale these equations assuming $\mathrm{Z}_{\odot}$ =0.02. These wind mass loss algorithms for WR stars were determined empirically, and are likely to be improved in the future thanks to both modelling and observations of hydrogen poor stars. Furthermore, we model helium stars at lower luminosities than those used to derive these formulae, and it has been suggested that hydrogen deficient stars below a certain luminosity threshold no longer follow the observed relations for WR stars, but have lower mass loss rates instead (Vink, 2017). However, these assumptions are currently the best and we take them at face value, to try to determine statistical properties of the progenitors of Type I SNe.

4.3 Helium Star Evolution

In this Section we study the effect of metallicity on the evolution helium stars by analysing the grid of evolutionary calculations of helium stars with different metallicities, including mass loss via the algorithm prescribed by Yoon (2017), as described in Section 4.2. As discussed in Section 4.2, the mass loss algorithms employed in our helium star evolutionary calculations are adapted from empirical relations derived for WN type stars (Hainich et al., 2014) and WC and WO type stars (Tramper et al., 2016). Stars below the observed luminosity limit of WR stars are most likely observable as helium stars without optically thick winds. Stars below this luminosity limit –a quantity which also depends on metallicity (Shenar et al., 2020)– are believed to lose mass at a significantly lower rate than the one obtained from extrapolating the empirical relations observed for WR stars (e.g. Vink, 2017; Sander et al., 2020). However, currently there are no empirical mass loss rate algorithms for helium stars below this limit in the literature. For this reason, we extrapolate the mass loss rate algorithm for WR stars into the regime below the minimum luminosity limit of WR stars to study the transition between WR stars and helium stars with transparent winds.

Helium stars are candidate progenitors of Type I core collapse SNe. Since we focus on how core-collapse SN progenitors that come from stripped helium stars differ in environments of different metallicities, we ignore those stars that do not evolve to core collapse in the traditional way, where nuclear burning begins in the stellar centre, but instead form either electron capture SNe, WDs, or experience off-centre ignition before core-collapse. The evolution of these stars is studied has been studied in detail by S. E. Woosley (2019) and Antoniadis et al. (2020).

We have subdivided our results as follows: In Section 4.3.1 we review the evolution of helium stars of different masses and metallicities and characterize their lifetimes, surface abundances, wind optical depths and luminosities, and in Section 4.3.2 we discuss how these properties can impact stellar populations.

4.3.1 The Impact of Metallicity in Helium Stars

Helium stars that are massive enough to burn helium in their core through the triple alpha process begin their core helium burning lifetime with a convective core and a mostly radiative envelope. The radiative envelope of helium stars at this stage is mostly made up mostly of helium and nitrogen. The chemical composition of the envelope is set during hydrogen burning by CNO equilibrium. The core is also composed mostly of helium, but is enriched by neon and depleted of nitrogen, since nitrogen burning takes place before helium burning, and becomes increasingly rich in carbon and oxygen as helium burning takes place.

Depending on their mass, helium stars may evolve to become CO WDs, ONeMg WDs, or go through more advanced nuclear burning processes that either result in the formation of an electron capture SN or of an iron core that will eventually collapse. Their evolution has been studied in detail at solar metallicity (e.g. S. E. Woosley, 2019). With the physical and numerical choices we have taken, metallicity dependent mass loss rates are the factor that most drastically affects the evolution of helium stars in different metallicities. Other consequences of changes in metallicity, such as its effect on envelope inflation, are not captured by our treatment using MESA's `mlt++`.

Some helium stars will lose enough mass to expose the layers where nitrogen is depleted and carbon and oxygen are enhanced. At this point, they will experience an increase in mass loss rate, due to the fact that they will reach the WC/WO stage. This creates a dichotomy in the mass and chemical composition of helium star models at core collapse. Since the convective core of mass-losing helium stars constantly shrinks due to mass loss, no semiconvective layers are formed in regions with chemical composition gradients, excluding systems that could be observable as WN/WC type stars, with surface layers rich in both carbon and nitrogen (Langer, 1991b).

All models evolve early on losing mass with a mass loss rate consistent with the observed WN stars, but more massive ones will spend a fraction of their lifetime losing mass at a higher rate during the WC/WO phase. The enhanced mass loss rates for both WN and WC/WO winds included in the mass loss algorithm of Yoon et al. (2017) explain the presence of WC stars that have a lower luminosity than that achievable through both single and binary star evolution using other WR wind mass loss recipes (e.g Nugis et al., 2000).

The effect of increasing mass and metallicity is illustrated by the Kippenhahn diagrams of four example evolutionary calculations in Figure 4.1. The evolutionary calculation corresponding to an 8 $M_\odot$ star with metallicity of 0.01 has a convective core that initially spans ~4.8 $M_\odot$, and which gradually decreases in mass as the total mass of the star decreases due to mass loss. This continues until the end of core helium burning, when core convection is stopped. At the end of core helium burning, helium burning is ignited in a shell above the core. Afterwards, this particular evolutionary sequence goes through carbon burning in a series of convective flames that appear at subsequently higher masses before igniting neon in the core. The layers enriched by helium burning ashes are never exposed by mass loss, and thus this model has $Y_{\rm surf} = 1 - Z_{\rm init}$ and a high nitrogen abundance in its surface throughout its entire evolution, observable always as a WN type star, and ending with a Type Ib SN explosion.

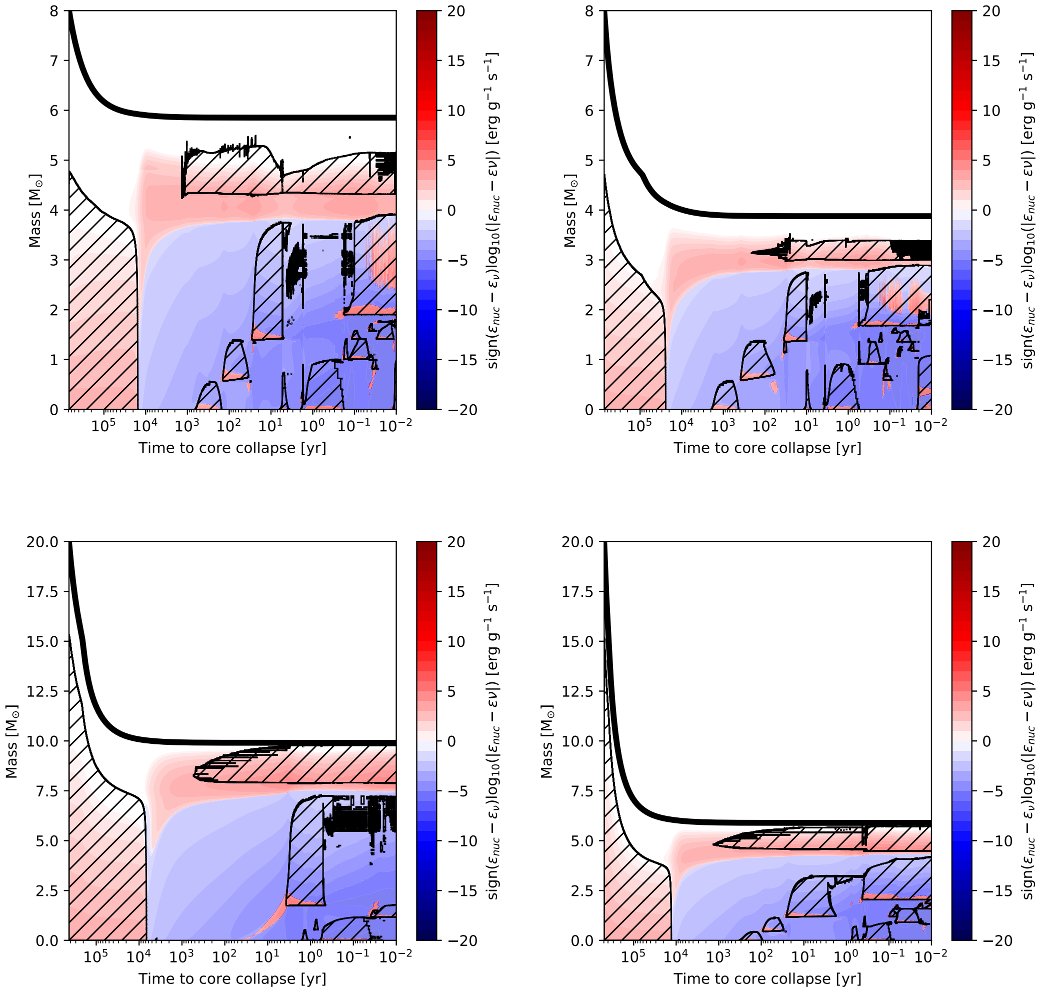

Figure 4.1: Kippenhahn diagrams following the energy generation/loss rate and the structure of convective regions as a function of time remaining until core collapse, from core helium burning until a few days before core collapse. Represented are the evolutionary calculations with initial helium star masses of 8 (left) and 20 (right) M$_\odot$, with metallicities of Z=0.01 (top) and Z=0.04 (bottom). Color denotes the intensity of the energy generation (red) and loss (blue) rate. Hatched regions denote convective regions.

In comparison, the sequence with same initial mass and higher metallicity loses mass at a higher rate, and thus its convective core also decreases its mass at a higher rate. During core helium burning, the layers depleted of nitrogen and enriched in carbon and oxygen are exposed. At this point, the mass loss rate transitions from the algorithm for WN type stars, to the algorithm for WC and WO type stars, resulting in an increase in mass loss rate which also accelerates the retreat of the convective core. Subsequent episodes of nuclear burning in the core occur similarly, but the final mass is considerably smaller, and the final surface composition is considerably different, having a lower helium content, and with the ashes of helium burning also present in the surface.

The 20 $M_{\odot}$ sequence with metallicity of 0.01 experiences the transition between mass loss algorithms early in its evolution, similar to the 8 $M_{\odot}$ sequence at a metallicity of 0.04, but has a different core evolution due to its higher mass. Carbon burning in the core occurs radiatively in a flame that moves to higher layers of the star, until it settles at the base of a convective zone that encompasses almost all of the remainder of the carbon-oxygen core. This is common for stars of high mass, and affects the core structure, likely leading to a direct collapse into a BH instead of a SN explosion (Sukhbold et al., 2014).

The 20 $M_{\odot}$ sequence with metallicity of 0.04 has a stronger mass loss and experiences the transition in mass loss earlier in its evolution. Due to its smaller mass at the end of core helium burning, it experiences carbon burning in a series of convective flames like the lower mass examples, linked to a higher probability of ending in a successful explosion at the end of its evolution.

The life time of helium burning stars is mostly determined by their initial mass, and is only weakly dependent on metallicity. As shown in Figure 4.2, lifetimes are a monotonically decreasing function of initial mass. Models at lower metallicity have slightly shorter lifetimes, since they retain a larger amount of mass at any given evolutionary stage, but the difference is limited to a few percent.

Surface composition affects how helium stars evolve, and the properties they will have when they are observed (both as stars and as SNe). We characterize the evolution of their surface composition by presenting the fraction of their lifetimes they spend with an envelope that is nitrogen rich (likely observable as a WN if massive enough, top panel of Figure 4.3), and the ratio of nitrogen rich to WC lifetimes (bottom panel of Figure 4.3), as a function of initial mass and metallicity.

Helium stars below a certain mass spend their entire lifetime as WN stars without ever exposing their nitrogen depleted interior. This minimum mass decreases with increasing metallicity, due to the increase in mass loss rates in the WN stage. Since the mass loss rates also increase with increasing luminosity, which is a proxy of mass (e.g. Langer, 1989; Gräfener et al., 2011), helium stars that are massive enough to expose layers of their formerly convective core will spend a fraction of their lifetime as WC stars, and this fraction will increase the more massive they are. Therefore, for a fixed initial mass, the fraction of stellar lifetime spent as a WC/WO increases as a function of metallicity. This implies that WC/WO stars ought to be more common in environments of higher metallicity.

The top panel of Figure 4.3 also shows that stars with an enhanced carbon and oxygen surface abundance will typically have larger initial masses than their nitrogen rich counterparts, and will therefore be found at preferentially higher luminosities. This is exemplified in Figure 4.4, where the evolution of luminosity and surface helium mass fraction Y_{surf} are shown as a function of age since core helium ignition. WN stars exist throughout the entire luminosity range present in our simulations, but WC stars have a minimum luminosity that depends on metallicity, since stronger winds are required to expose the formerly convective zones of a star.

As shown in Figure 4.1, massive helium stars will lose mass at a rate large enough that their convective core will decrease in size. This leads to a continuous luminosity drop during helium burning, as shown in Figure 4.4. The drop in luminosity as a function of time will consequently be larger at higher metallicities, and it will become faster for stars with decreasing helium in their surface due to the transition to WC/WO mass loss rates. Stars with lower masses, however, that have lower mass loss rates during helium burning,

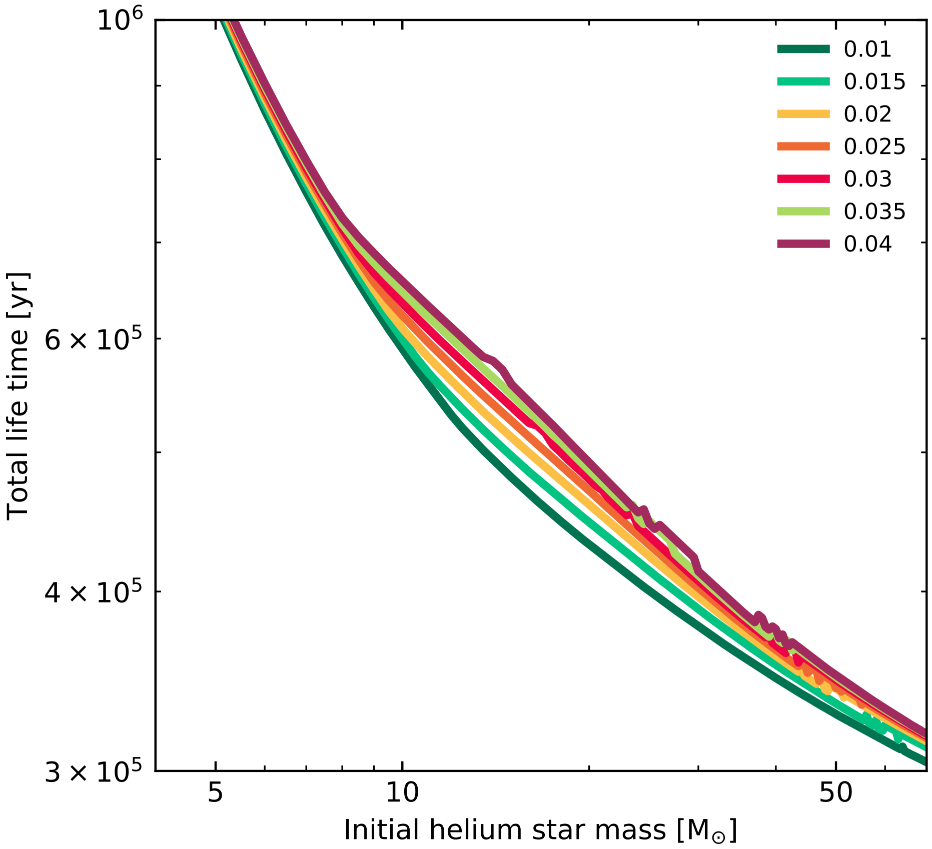

Figure 4.2: Total life time of helium stars of different initial masses, from the start of helium core burning to core-collapse, as a function of initial helium star mass, for helium stars of different metallicities.

will experience a steady or increasing luminosity as they evolve, as their winds are not strong enough to decrease their core size.

Much like stars with hydrogen rich envelopes, helium stars will experience an increase in luminosity close to the end of their evolution, caused by the ignition of helium shell burning when helium is depleted in their core.

Below a certain mass, which corresponds to the minimum mass that a WC/WO star can be produced by winds at a given metallicity, the final surface helium abundance in our models will correspond to the initial one, of 1-Z. Above this limit, the final helium surface abundance decreases quickly, reaching a saturation value. of around 0.3. This transition takes place when the layers of the helium burning shell are reached exposed by the stellar wind. Since these layers were convective before being exposed, the helium abundance in them is roughly constant and does not significantly decrease until the layers below the shell are reached, but these layers are never exposed in our simulations.

As previously mentioned, not every helium star will be observable as a classical WR. There is a lower limit on the luminosity of WRs, which corresponds to a lower mass limit (Shenar et al., 2020), below which stripped-envelope stars will not have the observational properties of a WR star; namely emission lines due to an optically thick wind. This limit is observed to be strongly dependent on metallicity, and Shenar et al. (2020) offer a relation for $L_{min,WR}$ as a function of Z. They find this relation by means of the so-called transformed radius R_t (Schmutz et al., 1989), which depends on the stellar radius R_*,

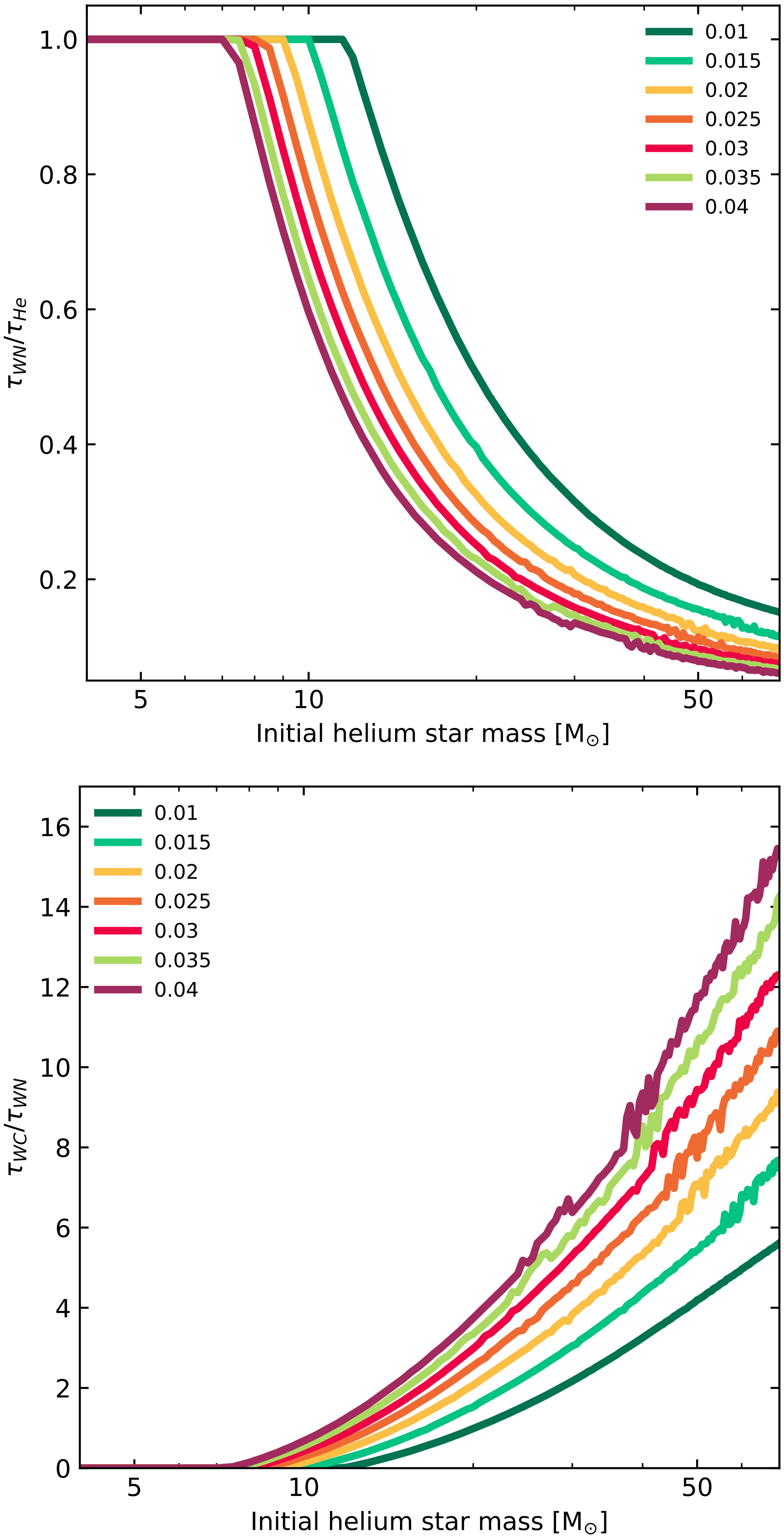

Figure 4.3: Fraction of the total life time of our helium star models spent as WN stars (helium/nitrogen rich envelope, top), and ratio between WC (carbon/oxygen rich envelope) and WN life times (bottom), as a function of initial mass, for helium stars of different metallicities.

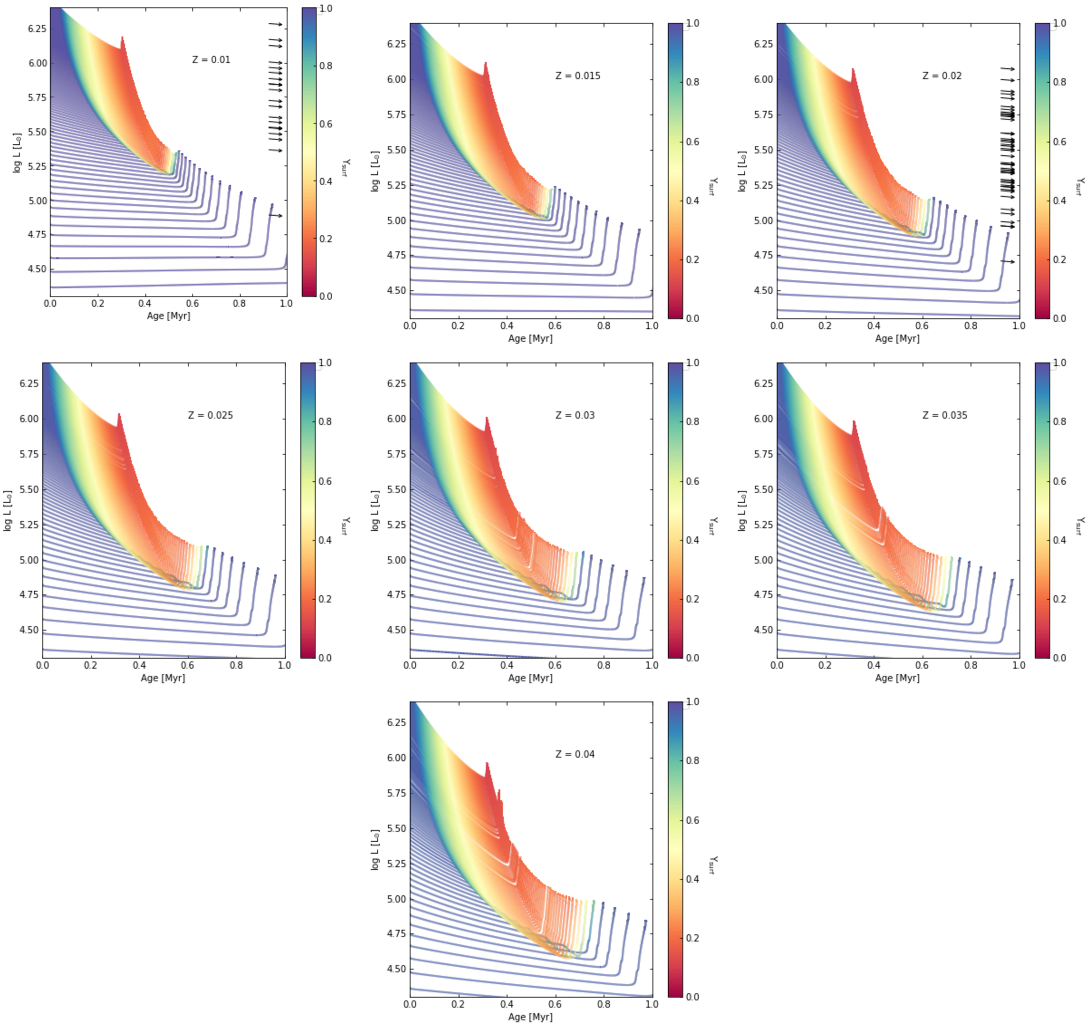

Figure 4.4: Evolution of surface luminosity as a function of age, between the He-ZAMS and core carbon depletion, for helium star models with different initial masses, colored by surface helium abundance. Each panel represents a set of models with different metallicity, going from 0.01 (top left) to 0.04 (bottom). Arrows on the right hand side represent the luminosities of observed WC stars in the LMC, in the case of Z=0.01, and the known Galactic WC stars in the case of Z=0.02.

terminal wind velocity v_∞, mass loss rate $\dot{M}$ and wind clumping factor D. Assuming that the mass loss rate depends on luminosity and metallicity with a functional form given by $\dot{M} \propto L^{\alpha}Z^{\beta}$, and all other quantities are independent of either L or Z, and further assuming that there is a fixed value of R_t above which helium stars will have WR spectra, they arrive at a proportionality of the form $L_{min,WR} \propto Z^{4\alpha/(3-4\beta)}$. Using values for α and β derived by Vink (2017) in the context of low mass helium stars, below the WR limit, they find that the exponent is roughly equal to -1, which provides a reasonable fit to the observed values of $L_{min,WR}$ in the SMC, LMC and our Galaxy.

Here, we take a similar approach, but instead calculate the optical depth at the base of the winds of WR stars, $\tau(R)$, using the analytical approach of Langer (1989). In this model, for a wind velocity law with $\beta = 1$ (Equation 8 in Langer, 1989), the optical depth at the base of the wind is given by

$$\tau(R) = \frac{\kappa|\dot{M}|}{4\pi R(v_\infty - v_0)} \ln \frac{v_\infty}{v_0}, \tag{4.4}$$

where κ is the opacity, R the stellar radius, and v_∞ and v_0 are the terminal wind velocity and the velocity at the base of the wind, respectively. We combine this with the metallicity and luminosity dependent wind mass loss rates for WN type stars from Yoon (2017), and assume that the terminal wind velocity is given by the escape velocity at the surface, multiplied by a factor K (Gräfener et al., 2017); namely

$$v_\infty = K v_{esc} = K \sqrt{\frac{2GM}{R}(1 - \Gamma)}, \tag{4.5}$$

where Γ is the Eddington factor. Substituting these values in Equation 4.4 yields

$$\begin{aligned} \tau(R) = \quad & \tfrac{\kappa|\dot{M}(L,Z)|}{4\pi R(L)} \left(1.3 \sqrt{\tfrac{2GM}{R(L)}(1 - \tfrac{\kappa L}{4\pi G c M(L)})} - v_0\right)^{-1} \\ & \times \ln\left(\frac{1.3 \sqrt{\frac{2GM}{R(L)}(1 - \frac{\kappa L}{4\pi G c M(L)})}}{v_0}\right). \end{aligned} \tag{4.6}$$

Adopting $\kappa = 0.2\,\mathrm{cm^2 g^{-1}}$, and using the relations of Langer (1989) for $M(L)$ and $R(L)$ means that the optical depth at the base of the wind is only a function of luminosity and metallicity, and the exact dependence of $\tau(R)$ on L and Z depends on the choice of mass loss rate algorithm. The result of this calculation for a WN wind (using K=1.3 and Equation 4.1, following Gräfener et al. (2011)) is presented in Figure 4.5, along with a value for the transition between optically thick and thin at $\tau = 1$, and a line for $\tau = 2$, found from Equation 4.6 obtained by solving Equation 4.6 using the secant method. These values are also compared to the observed WR luminosity thresholds from Shenar et al. (2020).

As seen in Figure 4.4, there is also a minimum luminosity below which WC stars are not observed, $L_{min,WC}$, and this value is also metallicity dependant. For our models, this is dictated only by the strength of the mass loss rate, but the question of whether or not these stars will be observable as WR stars or not is not clear from the models alone. Therefore, we reproduce the analysis of $\tau(R)$, this time substituting Equation 4.2 in Equation 4.6, and adopting a value of K=1.6 (Gräfener et al., 2017). This is presented in Figure 4.6, along with the least luminous WC stars observed in the SMC, LMC and in our Galaxy, and the minimum luminosity that we find for WC stars in our models.

Figures 4.5 and 4.6 show that despite the complicated form of Equation 4.6, the condition $\tau(L, Z) = \tau_0$ is well described by a power law of the form

$$L_{min,WR} = A(\tau_0)\left(\frac{Z}{Z_\odot}\right)^b. \tag{4.7}$$

Fitting a power law to the solution to $\tau(L, Z) = 1$ for WN stars, we find that $b \approx -0.71$ and $A(\tau = 1) \approx 10^{3.4}$. We also find, by fitting a power law with the same slope to the observed data, that $A \approx 10^{3.6}$ is the value that best fits the observations, which have values of τ ranging between 1.3 and 1.6.

Similarly, fitting a power law solution to $\tau(L, Z) = 1$ for WC stars yields a much steeper slope of $b = -1.51$, and a value of $A \approx 10^{1.0}$. The lowest luminosity WC stars in our sample seem to fall along the $\tau = 3$ line, however. Here, we found that taking $b = -1.59$, and $A \approx 10^{1.7}$ reproduce the solution to Equation 4.6 in this case, and fits the observations.

It becomes clear from this analysis that $L_{min,WR}$ and $L_{min,WC}$ (and therefore $M_{min,WR}$ and $M_{min,WC}$

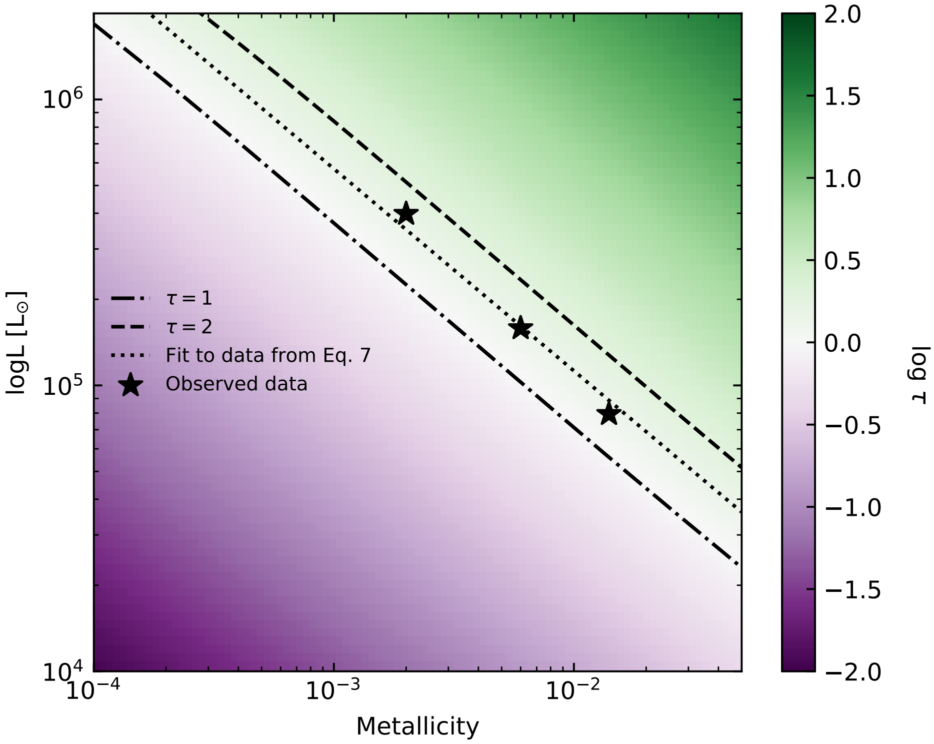

Figure 4.5: Optical depth at the base of a WR wind, as a function of metallicity and luminosity, obtained from Equation 4.6. It is assumed that the wind depends on metallicity and luminosity as in Equation 4.1. The lines represent the solutions for $\tau = 1$ and $\tau = 2$, and the fit to observations obtained with Equation 7. Star shaped symbols represent the threshold luminosity for observed WR stars in the SMC, LMC and in the Galaxy, as inferred by Shenar et al. (2020).

decrease with increasing metallicity due to the increase in density of the stellar wind. We also conclude that the minimum value in an environment of a given metallicity is well described by stars with a wind optical depth of roughly 1. Furthermore, we find that, at least with the wind mass loss algorithm of Yoon (2017), no carbon and oxygen rich helium stars are produced below $L_{min,WC}$ in the metallicity range of our models.

However, due to the fact that the slopes for τ = const. are different for WN and WC/WO stars, there is a region where $L_{min,WC} < L_{min,WR}$. This suggests that, below a certain metallicity, some stars that evolve as WN and lose their helium/nitrogen envelope might subsequently have transparent winds and stop being WR stars. If we extrapolate the values of $L_{min,WC}$ that we obtain from our simulations down to lower metallicities, we infer that this might occur already in environments such as the SMC.

4.3.2 Helium Star Populations

Using the value of $L_{min,WR}$ obtained in Section 4.3 we can infer which helium stars in our sample are observable as WR stars, and which ones are below the luminosity limit, and would therefore not have emission lines. We use this to estimate how the average number ratio of WC to WN stars $\langle N_{WC}/N_{WN} \rangle$ varies as a function of metallicity from our grids of simulations. We estimate this quantity assuming that the ZAMS mass of a star that produces a helium star of a given mass (i.e. the helium core mass of a main sequence star) is not a function of metallicity, but only of the initial helium star mass. We employ the

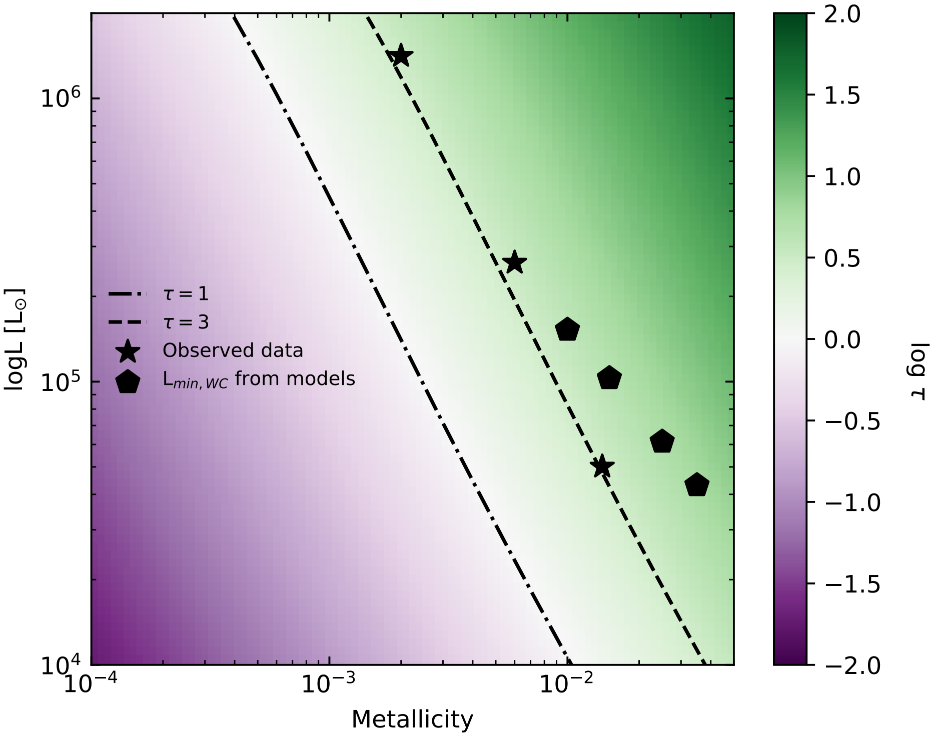

Figure 4.6: Optical depth at the base of a WC/WO wind, as a function of metallicity and luminosity, obtained from Equation 4.6. It is assumed that the wind depends on metallicity and luminosity as in Equation 4.2. The lines represent the solutions for $\tau = 1$ and $\tau = 3$. The red line represents the minimum luminosity of WC/WO stars found in our models. Star shaped symbols represent the minimum luminosity of observed WC/WO stars in the SMC, LMC and in the Galaxy. Pentagons represent the minimum luminosity of a WC attained in our models.

formula of S. E. Woosley (2019), given by

$$M_{\rm He,ini} \approx \begin{cases} 0.0385 M_{\rm ZAMS}^{1.603} M_\odot & {\rm if} M_{\rm ZAMS} < 30 M_\odot \\ 0.5 M_{\rm ZAMS} - 5.87 M_\odot & {\rm if} M_{\rm ZAMS} \geq 30 M_\odot \end{cases}, \tag{4.8}$$

and we assume that all stars are immediately stripped at the beginning of core helium burning, and evolve as single helium stars. This leads to

$$\left\langle \frac{N_{\rm WC}}{N_{\rm WN}} \right\rangle = \frac{\int_{M_{\rm min}}^{M_{\rm max}} \xi(M_{\rm ZAMS}) \tau_{\rm WC} dM}{\int_{M_{\rm min}}^{M_{\rm max}} \xi(M_{\rm ZAMS}) \tau_{\rm WN} dM}, \tag{4.9}$$

where we have taken the initial mass function $\xi(M_{\rm ZAMS}) \propto M_{\rm ZAMS}^{-2.35}$ from Salpeter (1955). Here, $\tau_{\rm He}$ is the total helium burning life time, $\tau_{\rm WC}$ the time spent as a WC star and $\tau_{\rm WN}$ the time spent as a WN, all of which depend on the helium star mass. $M_{\rm min}$ and $M_{\rm max}$ are the minimum and maximum masses of WR stars, respectively, the first of which is dependent on metallicity.

The value of $M_{\rm max}$ is taken as 151.74 $M_\odot$, corresponding to the ZAMS mass of our most massive helium star model, with 70 $M_\odot$. The result is not sensitive to the exact value of $M_{\rm max}$, as long as it is large. It is, however, sensitive to the value of $M_{\rm min}$. To show this, we present this calculation range of minimum masses that corresponds to the values of luminosities between $\tau = 1$ and $\tau = 2$ according to Equation 4.6, and those that come from fitting Equation 4.7 to the observed data, related to each other through the mass-luminosity relation of Langer (1989), to give a range of possible values for $\langle N_{WC}/N_{WN} \rangle$.

This calculation is a crude approximation, since not all stars will become stripped, many WRs will likely have evolved from single stars that perhaps retain a hydrogen envelope during a substantial fraction of their helium burning lifetime, and WRs that evolve from binaries are neither always stripped exactly at the beginning of helium burning, nor completely stripped. However, we can gain understanding of how varying strengths of WR winds can influence the components of a stellar population.

The result of this calculation as a function of metallicity is shown in Figure 4.7 for choices of M_{min}. The lower limit corresponds to setting M_{min} to correspond to $\tau = 1$ in Equation 4.6, and the upper limit corresponds to $\tau = 2$. The intermediate value corresponds to the minimum masses predicted by Equation 4.7, using the observed values in the SMC, LMC and the Galaxy. For all three choices $\langle N_{WC}/N_{WN} \rangle$ increases as a function of metallicity. This behavior qualitatively reproduces what has been observed in WRs in different environments Neugent et al. (e.g. 2011) and and Neugent et al. (2012), although our estimation only encompasses the number of hydrogen-free WN stars, and excludes the rest of the population.

As can be seen from Figures 4.2 and 4.7, a large fraction of helium stars will become WC, particularly at higher metallicities, and the lowest mass at which a star can be observed as a WC is also strongly dependent of the metallicity. Figure 4.4 shows the luminosity evolution of our evolutionary tracks as a function of age, colored by the surface helium abundance. As discussed earlier, anything with a helium surface abundance of less than approximately 1 will not be observable as a WN, since immediately as soon as the former convective core is exposed, nitrogen will be depleted at the surface, and carbon and oxygen abundances will increase instead.

The increase in $\langle N_{WC}/N_{WN} \rangle$ as a function of metallicity is a consequence of two effects. One of these is the increase in (τ_{WC}/τ_{He}), for a fixed initial helium mass, as a function of metallicity. The second cause is the decrease of $M_{min,WC}$ that is experienced in the evolutionary tracks (see Figure 4.6). The dependence on the choice of M_{min} is also steep due to the steepness of the initial mass function. Increasing the value of M_{min} excludes lower mass stars, favored by the initial mass function, and more likely to spend time as WN stars than WC stars. Therefore, this choice will increase the number of WC stars at any given metallicity.

In the metallicity range that our simulations cover, the behaviour of $\langle N_{WC}/N_{WN} \rangle$ is limited to the changes in on M_{min} for WN stars, since in our models, every time a star has its carbon and oxygen rich layers exposed by a WN wind, it will also be luminous enough to appear as a WC star. However, below a certain threshold metallicity, it is likely that some stars evolve as WN stars and expose their previously convective cores, but not be observed as WC stars, as they may lie below the threshold value shown in Figure 4.6. However, we do not know with certainty that this transition occurs at lower metallicity, and they should be modelled in detail independently.

4.4 Properties of Helium Stellar Models at Core Collapse

4.4.1 Final Masses and Chemical Compositions

The properties of the expected transients (if any occur) and of the remnants that the helium star models we presented in Section 4.3 produce can be inferred from their mass, composition and structure at core-collapse. As discussed in Section 4.3.1, lifetimes of helium stars are mostly independent of their metallicity and depend mostly on initial mass. Therefore, the final mass, which will translate into ejecta

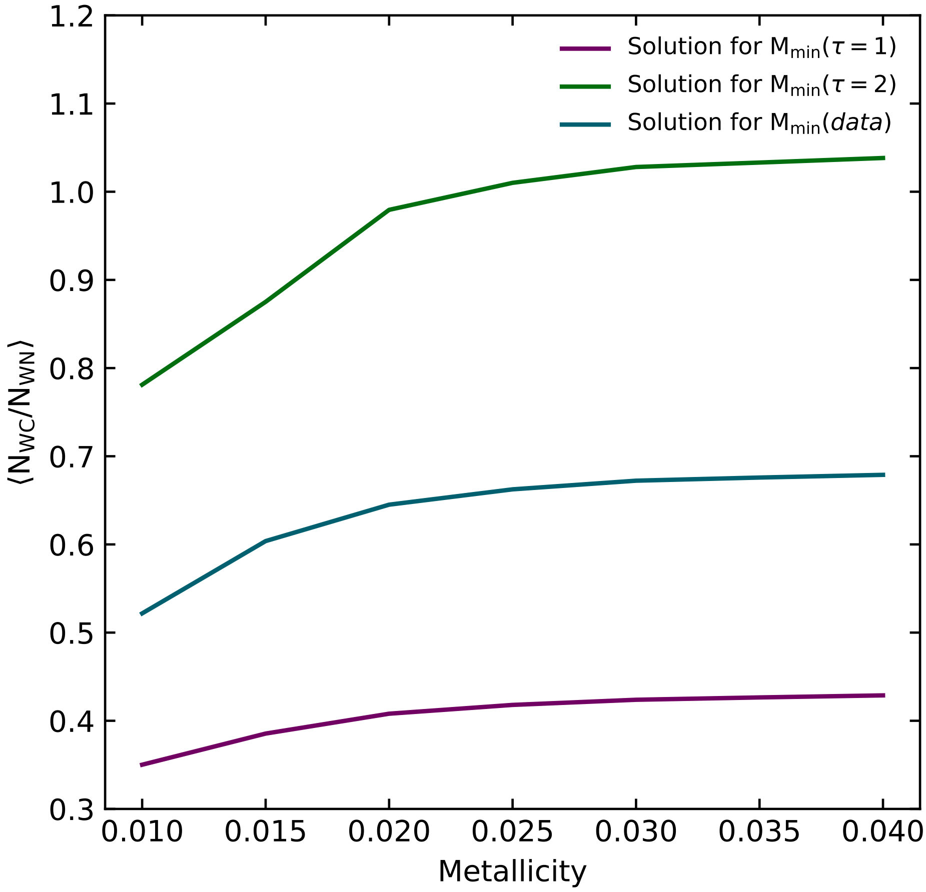

Figure 4.7: Average number ratio of WC to WN stars as a function of metallicity, as estimated by Equation 4.9. This quantity strongly depends on the minimum mass for a star to be observable as a WR. Different lines in this figure correspond to assuming that the minimum mass corresponds to setting the WR wind optical depth in Equation 4.6 to $\tau = 1$ (purple), $\tau = 2$ (green) and the fit to observations in Equation 4.7 (blue).

mass should such stars produce SNe, is expected to be lower at higher metallicities. Figure 4.8 shows the effect of metallicity on the final mass (defined as the mass at core collapse, see Section 4.2).

A change in the trend of final mass occurs between around 11 and 7 $M_\odot$, depending on the metallicity, and it is also observed in the models of Yoon (2017) and S. E. Woosley (2019). It corresponds to the transition between the stars that lose mass as WNs for most of their lives, and those that spend a significant time as WC/WO stars with stronger mass loss rates (see Figure 4.2). The ejecta mass of successful SNe can be estimated from Figure 4.8, but a more thorough analysis is presented in Section 4.4.2.

Low mass helium stars, in particular those below $M_{min,WR}$, will likely evolve with significantly lower mass loss rates. Their final masses are expected to be closer to their initial mass. They are also likely to become large due to envelope inflation, and go through an episode of case BB mass transfer, likely also reducing their final masses significantly, and producing ultra-stripped SNe (Tauris et al., 2013). Such considerations are beyond the scope of this paper, but should be kept in mind, particularly in the regime below $M_{min,WR}$.

The type of SN that helium stars could explode as does not only depend on the final or ejecta mass, but

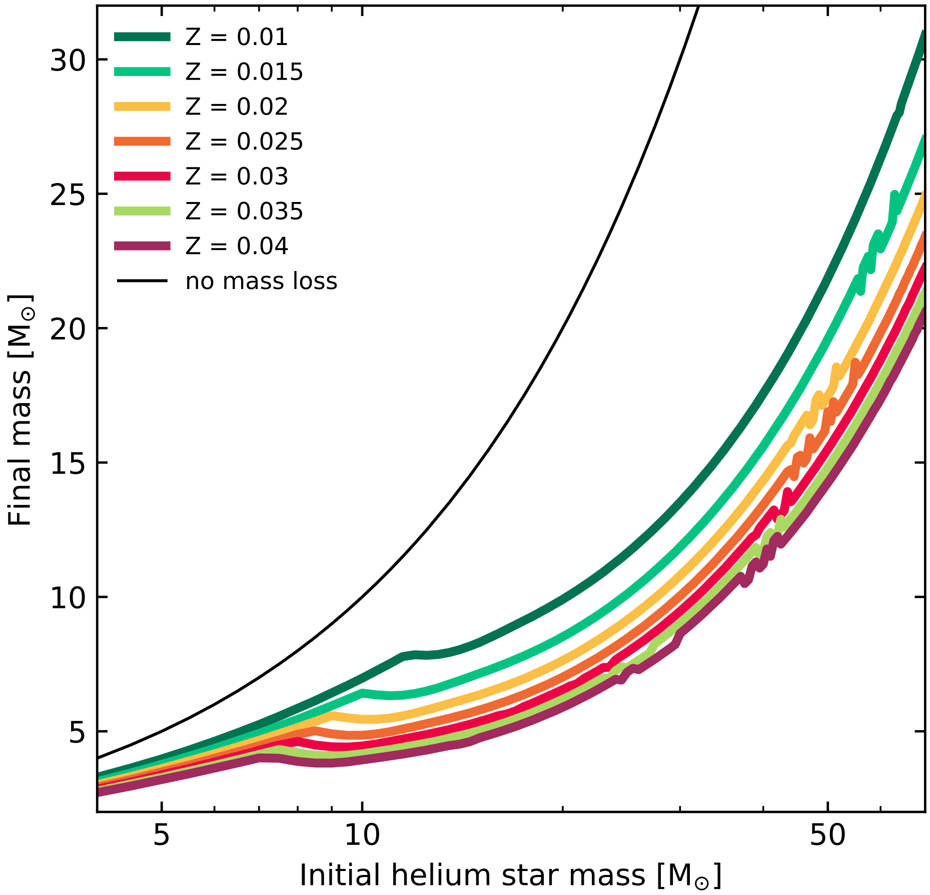

Figure 4.8: Final mass (at core-collapse) as a function of initial mass for helium stars of different metallicities.

also on the composition of their envelope (Dessart et al., 2020). Figure 4.9 shows the remaining mass of helium in the envelope as a function of initial mass. We calculate it as

$$M_{He} = \int_{T<10^8\ \mathrm{K}} Y(m)\, dm, \tag{4.10}$$

where, by only considering the regions with temperature smaller than 10^8 K, we exclude the helium formed in the core during collapse, and only include the envelope content. Note that this is different from the envelope mass (i.e. the total mass above the carbon-oxygen core), since only the mass in the form of helium is accounted for.

According to Hachinger et al. (2012), approximately only 0.01 $\mathrm{M}_{\odot}$ of helium in the envelope of a hydrogen poor star at core collapse is enough to produce detectable helium lines lines in the SN spectrum. This would render all of our models as possible Type Ib SNe progenitors. However, Dessart et al. (2011) and and Dessart et al. (2012) determined that the difference in spectral properties corresponds not only to the total helium mass, but also to the envelope composition at core-collapse and the mixing that takes place during the SN explosion. Furthermore, the model spectra of Dessart et al. (2020), produced by progenitors similar to the ones presented in this work, show that Type Ic SNe spectra can be produced by helium stars if their mass loss is strong enough to remove the helium envelope. Thus, there is a sharp

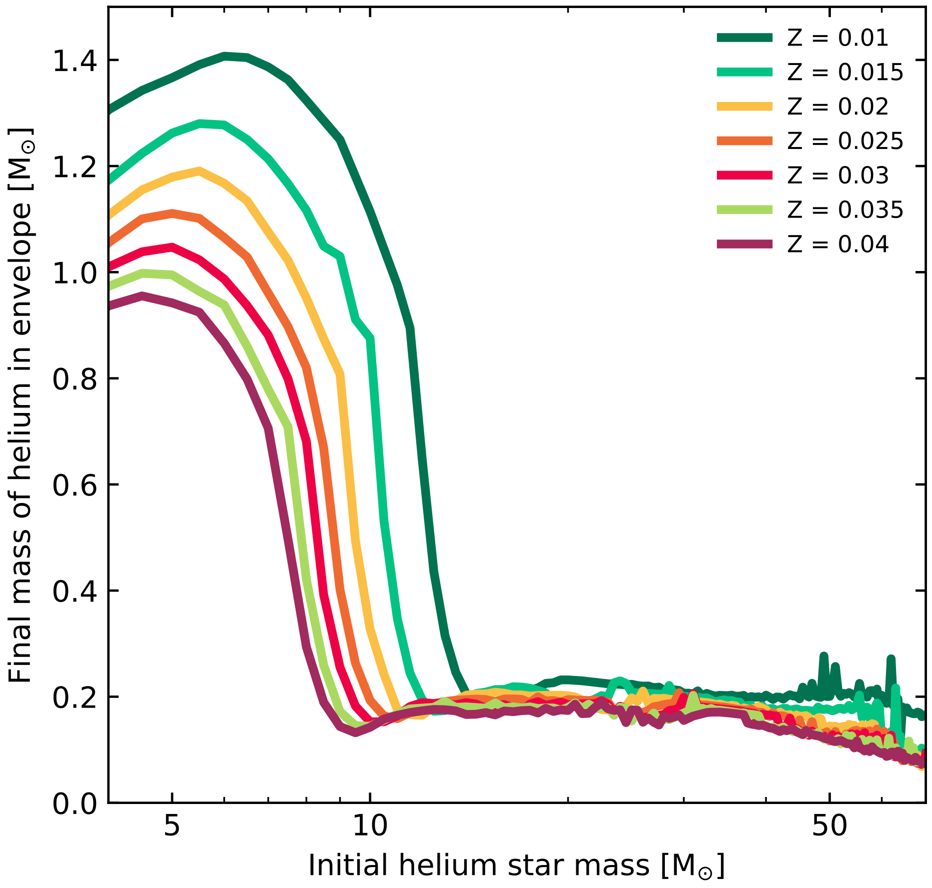

Figure 4.9: Final mass of helium in the envelope, as calculated by Equation 4.10, as a function of initial mass for helium stars of different metallicities.

transition between the evolution of progenitors of Type of Ib and Ic SNe, and it roughly corresponds to the transition between WN and WC/WO type stars.

As shown in Figure 4.9, helium stars transition from having abundant helium in their envelope, to having only very little, and the transition but the transition is relatively smooth. Most models that lose mass as WN stars throughout their evolution have between 0.8 and 1.4 $M_{\odot}$ of helium in their envelopes. On the other hand, the amount of helium in the envelope of massive helium stars converges at a value of around 0.2 $M_{\odot}$, and very few models reach core collapse in between this two regimes. The position where this transition occurs depends on metallicity, but models with intermediate helium masses occur at all metallicities.

Contrary to the helium cores of hydrogen rich stars, the convective cores of helium stars shrink in size as they evolve. As their convective cores decrease in mass, a smooth composition gradient develops in the formerly convective region, followed by a sharp transition between the helium/nitrogen envelope and the layers enriched with carbon and oxygen. The layers directly above the helium free core will later be part of a convective burning shell, which can grow in mass due to the smooth composition gradient left behind by the gradual retreat of the convective helium core. This means that most of the helium will be stored in the nitrogen reach envelope, and stars that lose this layers will have a similarly low amounts of helium at core collapse.

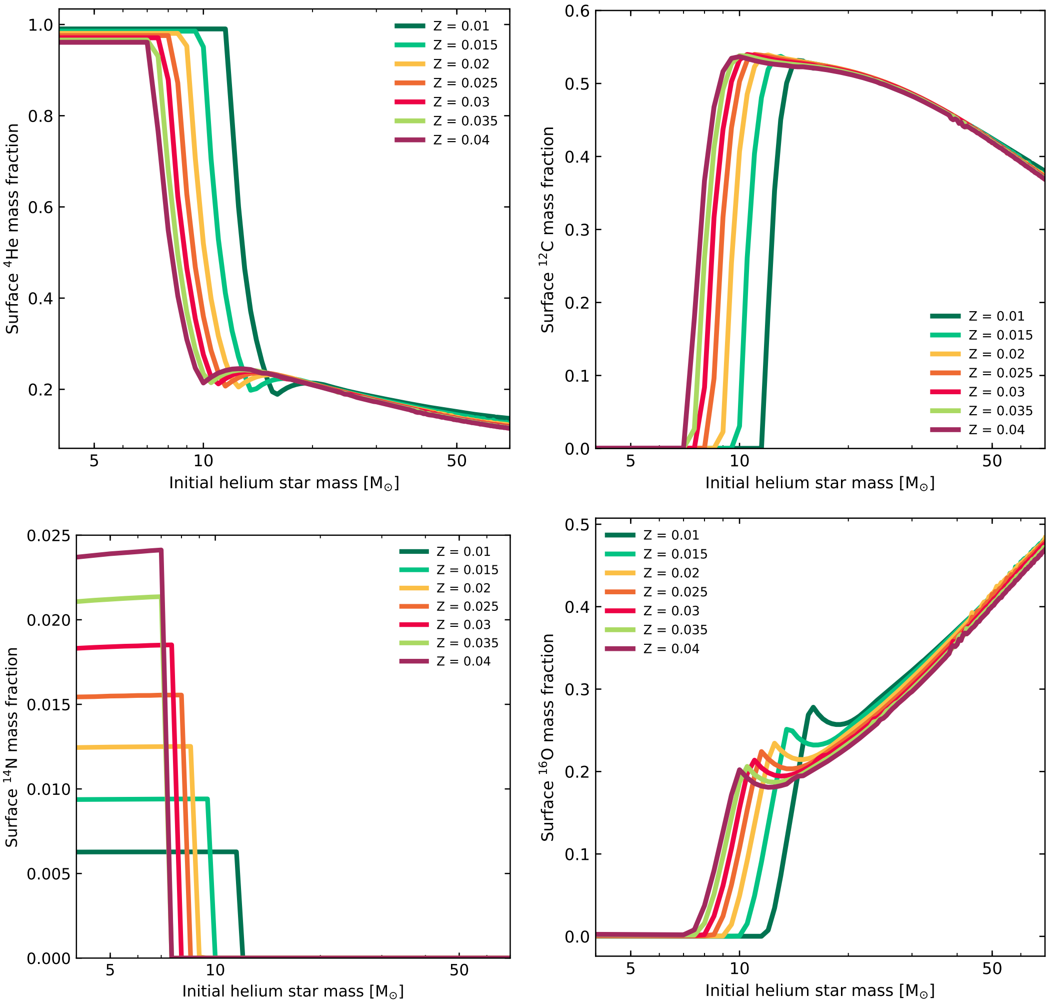

Figure 4.10: Surface mass fractions of ^{4}He, ^{12}C, ^{14}N and ^{16}O of helium stars at core-collapse, as a function of initial mass, for different metallicities.

Total helium mass is, however, not the only determining factor in whether the star will explode as a Type Ib or a Type Ic SN. Figure 4.10 shows the behavior of the surface abundances of He, C, N and O as a function of initial mass. There is a clear dichotomy in surface chemical composition, particularly steep change in N abundance; but also gradual reduction of He and increase of C and O as a function of initial mass, transitioning from CNO equilibrium abundances to the equilibrium abundances that result from helium burning. Our models have a sharp divide between these two populations of helium stars, with no intermediate cases. Surface nitrogen abundance has the sharpest drop since it burns at a lower temperature than helium, leading to a sharp transition in its abundance between the initially convective region and the envelope. The absence of nitrogen rich layers corresponds with the transition between Type Ib and the hybrid Type Ibc and Type Ic spectra in Dessart et al. (2020), and we therefore use that as the dividing line between the two cases in the following sections.

The transition between nitrogen/helium envelopes to those enriched with carbon and coincides with the transition between WN and WC/WO mass loss rates. As initial mass increases, there is a trend for the carbon abundance to increase as a function of initial mass, and then decreases again. A similar trend is observed in surface oxygen, except the trend has a local maximum and minimum before continuing to increase for the highest final masses. Above ~20 $M_\odot$, final surface abundances seem to depend mostly on initial mass. This implies that this quantity is determined early in the evolution, and leads to smalls variations in the surface abundances for models of similar final mass, independent of the metallicity.

4.4.2 Supernova Explosions from Helium Stars

The relative rate of different SN types coming from helium stars changes as a function of metallicity. This is due to changes in final chemical composition of helium stars (Dessart et al., 2020), but the rates also depend on the number of stars that actually become SNe, instead of collapsing into a black hole directly. The change in chemical composition has been addressed in Section 4.4.1. The latter issue is discussed here. To gauge the explodability of our core collapse models, we employ three methods: we analyse our models through their the compactness parameter $\xi_{2.5}$ proposed by O'Connor et al. (2011), we employ the two-parameter approach proposed by Ertl et al. (2016), and the model proposed by B. Müller et al. (2016).

As shown by S. E. Woosley (2019), contrary to the helium cores of hydrogen rich massive stars, which grow in mass as they are fed by their neighboring hydrogen burning shell, stripped helium stars lose mass, leading to a shrinking of their convective core during helium burning. This, in turn, implies that a helium star of a given initial mass will often have a lower compactness than a hydrogen rich whose ZAMS mass correspond to the same helium core mass at the beginning of core helium burning, and the first sharp increase in the value of $\xi_{2.5}$ will occur at lower ZAMS mass than for stars with a hydrogen envelope.

Figure 4.11 shows the compactness parameters of our models, as a function of both initial helium star mass and final mass. We obtain a general trend for features in the behaviour of compactness as a function of initial helium star mass, such as peaks and valleys, to be displaced to higher initial helium star masses with metallicity, correlated with the drop in final mass for similar initial masses, as shown in the bottom panel of Figure 4.11.

Although the compactness parameter alone is not enough to determine whether a stellar model at core collapse will lead to a successful neutrino-driven SN explosion or not, we find that most cases with $\xi_{2.5} < 0.35$ are predicted to explode according to the (Ertl et al., 2016) test, as well as with the B. Müller et al. (2016) test with their standard parameters. At every metallicity, we find that most helium stars with initial mass below ~40 $M_\odot$ will produce successful explosions, with a few exceptions located mostly at the peak in $\xi_{2.5}$ found at a final mass of around 8 $M_\odot$. The similarity in $\xi_{2.5}$ for models with similar final masses is due to the fact that the final mass is roughly determined before the beginning of carbon burning (see Figure 4.1. The remaining lifetime is too short for stars to lose a significant amount of mass, and since core structure is determined by the mass of the carbon oxygen core, features such as the transition between models with convective and radiative core carbon burning occur at similar final masses, correlated to the first peak in $\xi_{2.5}$ (Sukhbold et al., 2014).

An interesting feature in the behaviour of $\xi_{2.5}$ appears at final masses above 15 $M_\odot$, where we find a region in which two solutions to the compactness parameter appear. This feature has not been reported in previous analyses of helium star models (e.g. S. E. Woosley, 2019; Ertl et al., 2020). The two branches of values of the compactness parameter models in this region correspond to values of $\xi_{2.5}$ between 0.4 - 0.6 and 0.6 - 0.8. All values are above the limit of $\xi_{2.5} \sim 0.35$ where we expect to find exploding models, and all models are predicted to not form SNe according to both the Ertl et al. (2016) and the B. Müller et al. (2016) tests with standard parameters. However, small variations in the values of parameters in the B. Müller et al. (2016) model suffice to produce explosions in this case. Explosions could be facilitated in this regime by the presence of strong rotation, which has been found to contribute to the success of neutrino-driven SN explosions (e.g. Summa et al., 2018), and could arise from the high fraction of

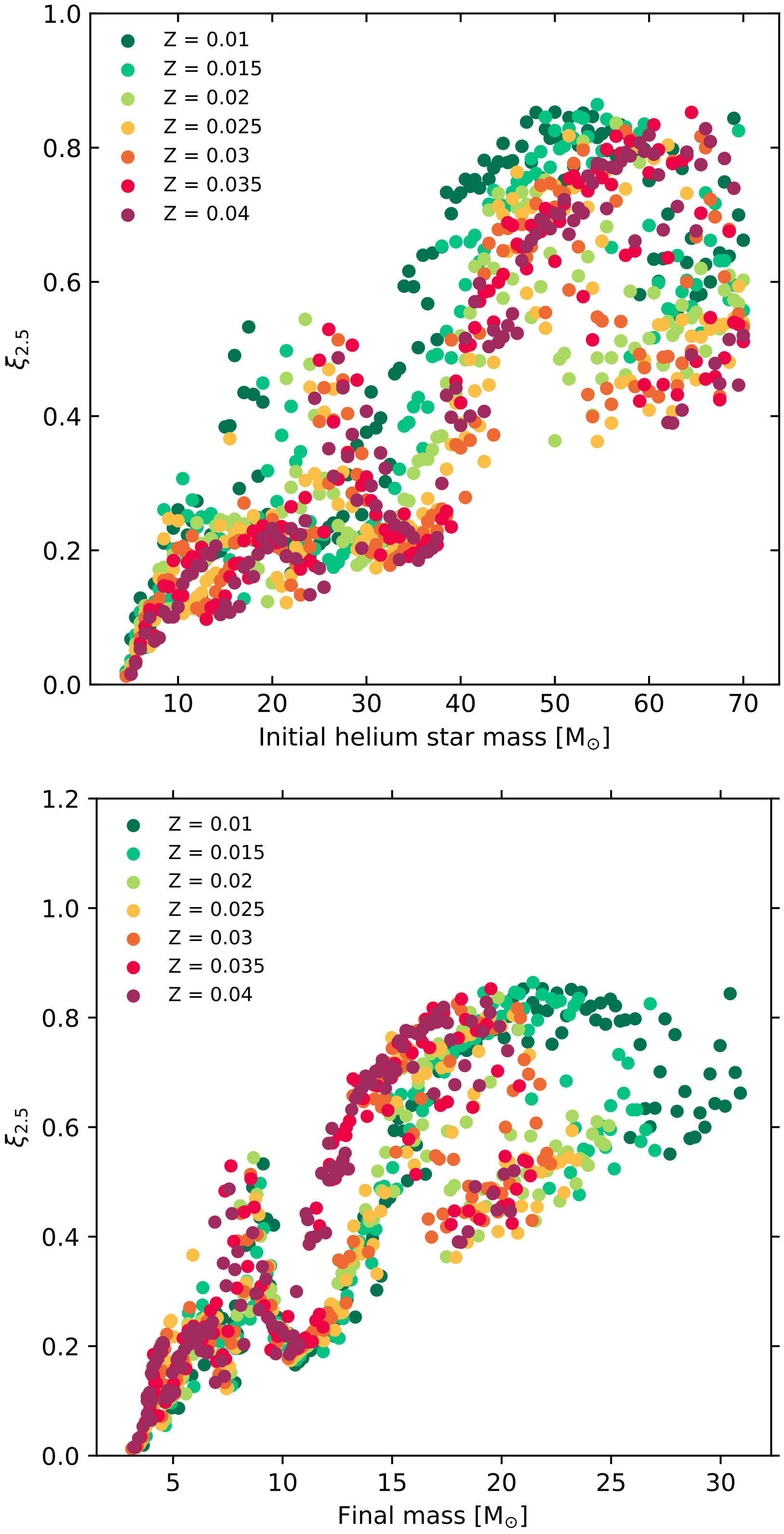

Figure 4.11: Compactness parameter as a function of initial mass (top) and final mass (bottom) for helium stars of different metallicities.

binarity in stars in massive stars (Sana et al., 2012).

Analysing our models with the B. Müller et al. (2016) explodability test also yields estimates of explosion energies, neutron star gravitational masses and nickel masses, which we can directly compare to Type Ibc SN observations. Some of these parameters are summarized in Figure 4.12.

As Ertl et al. (2020) had already found with their 1.5 $\dot{M}$ models, the so called "islands of explodability" become displaced if wind mass loss rates are different. However, as Figure 4.12 suggests, final mass is not the only defining factor that determines the explodability of a model and the properties it will have upon explosion. A region at around final masses of ~8 $M_\odot$ where low mass BHs can form exists for all metallicities, but there is a tendency for the highest final mass where explosions take place to increase with decreasing metallicity. This implies that explosions with high ejecta masses are more likely to occur in low metallicity environments. Such explosions also tend to be more energetic. However, the exact morphology and location of these regions depends on the choice of parameters in the B. Müller et al. (2016) model.

The trend for more models exploding as Type Ic instead of Type Ib can also be observed by the displacement of the red line in Figure 4.12.

To have a better idea of how these measurable parameters of SN explosions evolve as a function of metallicity, we have convolved them with a Salpeter IMF Salpeter (1955), using the same ZAMS to helium mass relation in Equation 4.8. This yields the normalized cumulative distribution functions presented in Figure 4.13, and the mean values and standard deviations of the same quantities presented in 4.14.

This estimates allow us to assess similarities and differences in the SN explosions resulting from populations of helium stars in different metallicity environments. The populations of NSs they produce will have similar masses, averaging at around 1.37 $M_\odot$. There is a weak trend for NS mass to decrease with metallicity, but it is well within the standard deviation at any given metallicity.

BH masses have a tendency to be more massive in lower metallicity environments. The largest mass BH produced in our models is at ~31 $M_\odot$, which corresponds to our largest final mass at Z=0.01. More massive BHs can be formed exist but will likely follow a similar pattern, and are proportionately more unusual. The BH distribution is double-peaked, with a peak around 8 $M_\odot$ (see also Figure 4.12), and a second peak at higher masses. The low mass peak tends to be more populated in lower metallicities, owing to the fact that they are produced by lower initial mass helium stars, which will be favored by the IMF. The second peak is displaced to lower masses in higher metallicity environments, peaking around 14 $M_\odot$ in Z=0.04, and at around 16 $M_\odot$ in Z=0.01. These two effects combined increase the average masses of BHs with decreasing metallicity.

Ejecta mass is the quantity that changes most dramatically as a function of metallicity. As one could naively expect, higher metallicity environments produce, on average, explosions with lower ejecta mass. This is true for both Type Ib and Type Ic supernovae. Type Ib SNe also tend to have significantly more massive ejecta than Type Ic SNe. Furthermore, while the spread in mass tends to be similar for Type Ic SNe, regardless of their metallicity, the spread in ejecta mass also decreases significantly for Type Ib SNe at high metallicity, owing to the reduction of the window in initial helium star mass from which they originate.

The amount of ^{56}Ni synthesized during the explosion and the kick velocity that it imparts to its remnant are also similar, regardless of the environment of the progenitor. The distributions of ^{56}Ni mass peak at around 0.05 $M_\odot$ and few cases are observed 0.08 $M_\odot$. There is no clear trend for this to be significantly different depending on the composition. Kick velocity distributions peak between 100 and 200 km s^{-1}, and appear to have a weak tendency to become lower at higher metallicity.

Another immediate consequence of the metallicity dependence of stellar winds is an increase of rates of SNe Type Ic with respect to SNe Type Ib as for higher metallicity. We quantify this increase by

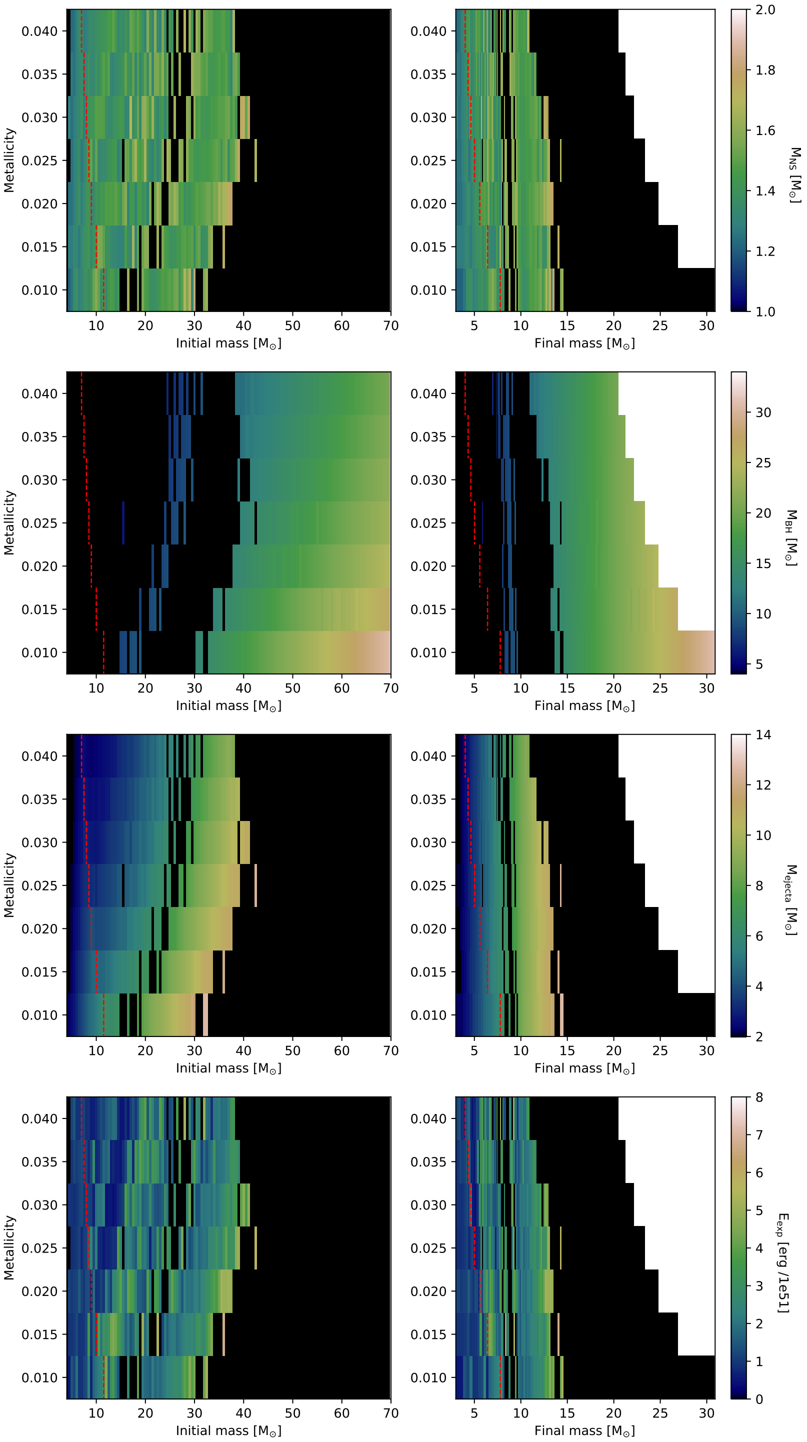

Figure 4.12: Summary of the key parameters obtained from the core collapse models of helium stars through the explosion model of B. Müller et al. (2016), as a function of initial mass (left) and final mass. We include the NS gravitational mass for core collapse models that successfully explode, the BH mass for models that directly collapse (which corresponds to their final mass), the ejecta mass and explosion energy. Dashed lines indicate the division between Type Ib and Type Ic progenitors.

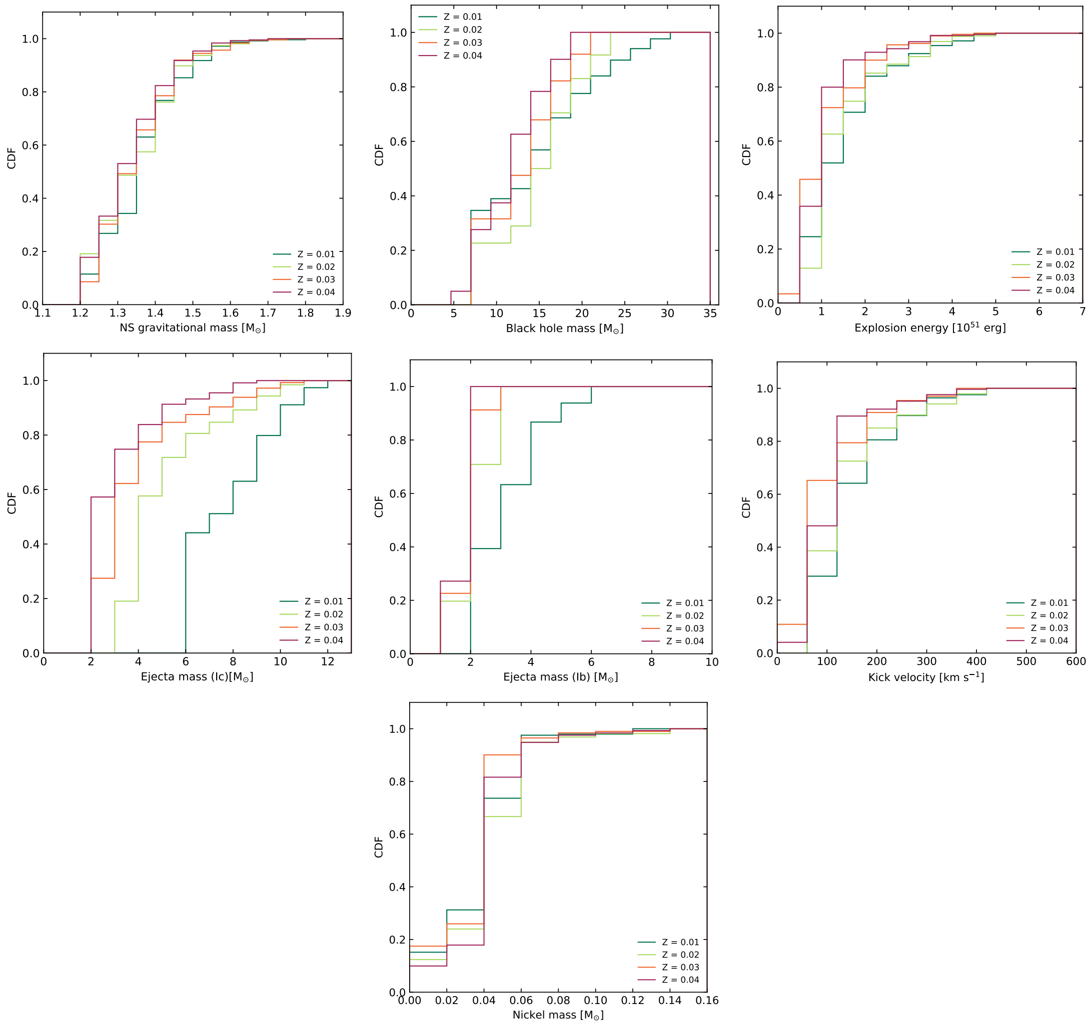

Figure 4.13: Cumulative distribution functions of NS gravitational masses, BH masses, explosion energies, ejecta masses for both Type Ib and Ic SNe, kick velocities and nickel masses that result from analyzing our core-collapse models with the B. Müller et al. (2016) model, using the standard parameters, weighted by the IMF from Salpeter (1955). Different color lines represent different metallicities.

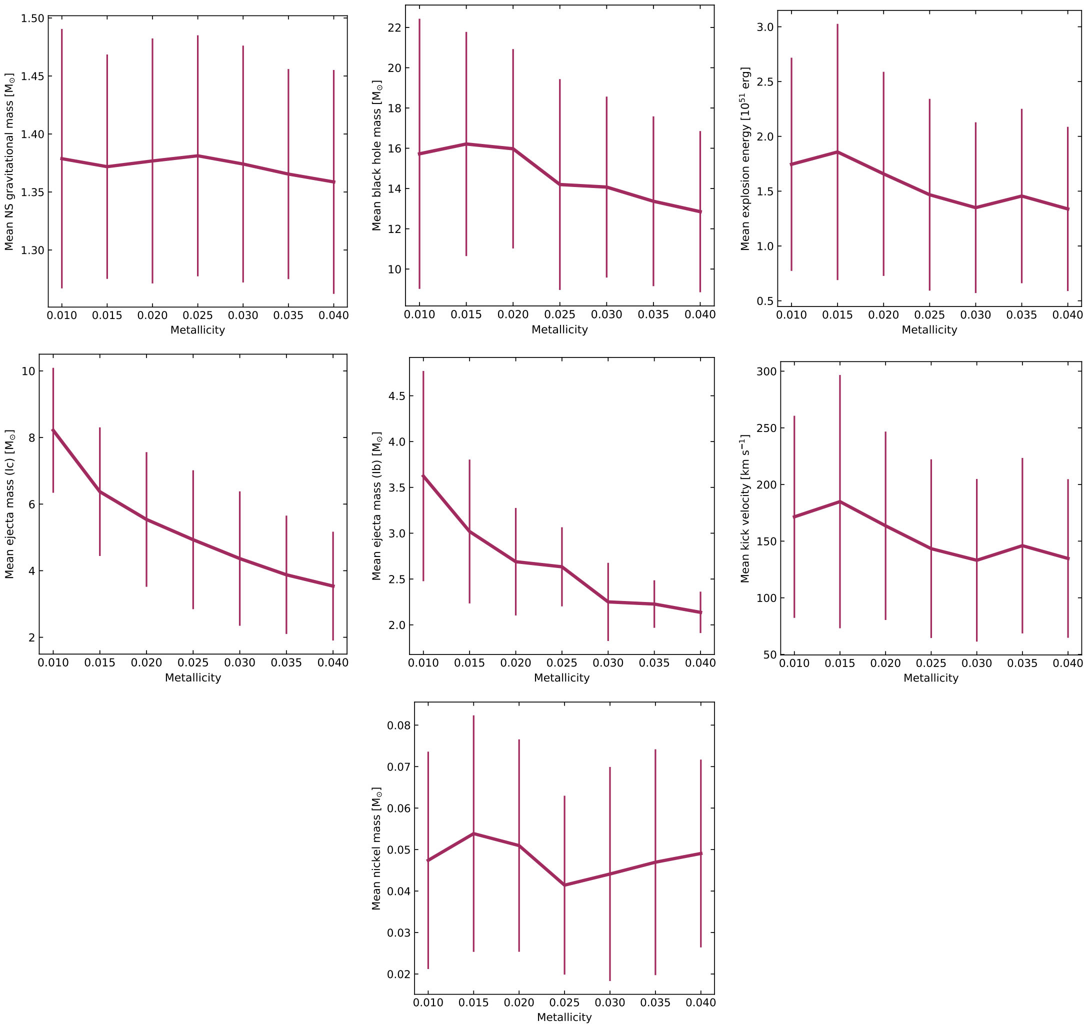

Figure 4.14: Mean values and standard deviation of NS gravitational masses, BH masses, explosion energies, ejecta masses for both Type Ib and Ic SNe, kick velocities and nickel masses at different metallicities, that result from analyzing our core-collapse models with the B. Müller et al. (2016) model, using the standard parameters, weighted by the IMF from Salpeter (1955).

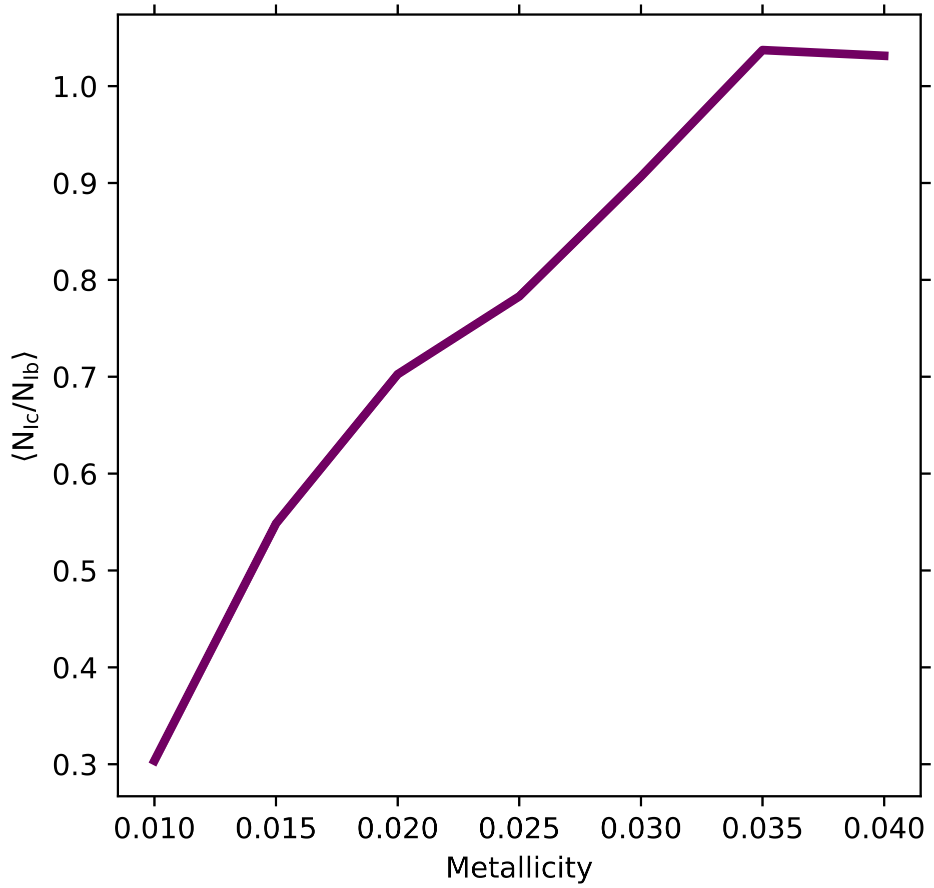

Figure 4.15: Expected number ratio of Type Ib and Type Ic SNe as a function of metallicity, as estimated by Equation 4.11.

convolving the expected outcome of core-collapse with the IMF. We consider the boundary between models that explode as Type Ib and Type Ic SNe to take coincide with the transition between models with helium/nitrogen envelopes and those enriched with carbon and oxygen discussed in Section 4.4.1. This leads to the number ratio to take the form

$$\left\langle \frac{\mathrm{N_{Ic}}}{\mathrm{N_{Ib}}} \right\rangle = \frac{\int_{\mathrm{M_{min}}}^{\mathrm{M_{max}}} \xi(\mathrm{M_{ZAMS}}) f_{\mathrm{Ic}}(\mathrm{M})\mathrm{dM}}{\int_{\mathrm{M_{max}}}^{\mathrm{M_{max}}} \xi(\mathrm{M_{ZAMS}}) f_{\mathrm{Ib}}(\mathrm{M})\mathrm{dM}}, \tag{4.11}$$

similar to Equation 4.9. Here, the function $f_{\mathrm{Ic}}(\mathrm{M})$ takes a value of either 1 or 0, depending on whether the closest mass model in our grid is expected to explode as a Type Ic SN or not, respectively, and $f_{\mathrm{Ic}}(\mathrm{M})$ behaves similarly for mass ranges where Type Ib SNe are expected. Here, the value of $\mathrm{M_{min}}$ is the smallest mass that produces a core collapse SN in our models at a given metallicity, and $\mathrm{M_{max}}$ is again our highest model mass. The result of this calculation is presented in Figure 4.15.

According to this calculation, the number ratio of Type Ic to Type Ib SNe should increase as a function of metallicity, starting from approximately 0.3 at a metallicity of 0.01, to above 1 at a metallicity of 0.04. This rising trend is mainly due to the fact the initial helium mass threshold for the production of a Type Ic supernova decreases with increasing metallicity.

According to our analysis in Section 4.3.2, stars in our sample that evolve to become progenitors of Type Ic SNe will be luminous enough to be observable as WR type stars, meaning that they are unaffected by the uncertainty in the mass loss rates of low luminosity helium stars. Furthermore, the number of SNe coming from low luminosity helium stars is not expected to be affected by a reduction in the mass loss rate of their progenitor, since their lower initial mass also implies a low value of $\xi_{2.5}$. Therefore, we argue that this calculation is not dependent on the effect of decreasing winds for helium stars with luminosities below the $L_{min,WR}$. However, we note that a caveat to this calculation lies in the fact that we do not account for SNe that come from progenitors in which off-centre burning occurs above a degenerate core at any time, which might add to the number of Type Ib SNe. However, the SNe that result from the evolution of such stars might have different observational properties, due to the different mechanism that produces them, as well as to the likely much larger radius they have compared to higher mass progenitors.

4.5 Discussion

The effect of metallicity in helium stars that is discussed in this paper was obtained by varying the composition of initially homogeneous stellar models, with compositions consistent to what they would have at formation due to CNO equilibrium. The main effect of changing metallicity in models of equal initial mass, given the physical treatment that we employ, is due to the metallicity dependent winds, which were adapted from Yoon (2017). These were obtained from separate studies on WN stars (Hainich et al., 2014) and WC stars (Tramper et al., 2016), and calibrated to have matching clumping factors, which Yoon (2017) found would help reconcile the lowest luminosity WC stars observed to our understanding of WR mass loss. Other phenomena that are affected by metallicity cannot be captured in our simulations due to our use of MESA's `mlt++`.

Approximating the late evolution of hydrogen-deficient stars through helium stars provides a powerful tool to understand the late evolution of massive stars. Stars similar to those in our models might be the result of binary interactions or mass loss. However, binary models where stripping due to mass transfer occurs do not generally predict that the entire hydrogen envelope will be removed by this interactions (e.g. Gilkis et al., 2019; Laplace et al., 2020). Furthermore, stars that lose their hydrogen envelopes before the beginning of core helium burning cannot reproduce phenomena such as WN/WC stars, which are observed to be rich in both nitrogen and carbon, and require a mixing mechanism that likely arises from helium gradients that only occur in helium cores that grow in mass (Langer, 1991b).

The mass loss rates we employed (Yoon, 2017) capture more phenomenology of WR stars than those employed in previous studies of helium stars (e.g. Hamann et al., 1995; Nugis et al., 2000), such as the higher intensity and less steep luminosity and metallicity dependences for WC stars. However, they are still far from the final word. Stripped stars below the local minimum WR luminosity experience weaker winds than their classical WR counterparts Vink (2017) and and Sander et al. (2020). This implies that low mass helium stars have larger lifetimes, final masses and average luminosities than those obtained with our models.

Furthermore, the final masses of helium stars might not only be determined by their mass loss rates, as in the case of our models. Such stars may be subject to instabilities in their surface layers due to their proximity to the Eddington limit, which are not captured with our modelling scheme (particularly due to the use of MESA's `mlt++`), and as such, correspond to an upper limit to the masses of helium stars at core collapse. However, stars with masses below $M_{min,WR}$ experience lower mass loss rates than WR stars (Vink, 2017; Sander et al., 2020), and thus their final masses are most likely underestimated.

The core evolution of helium stars will be similar across different metallicities, but the masses at which effects start taking place, such as the transition from convective to radiative carbon burning, and the mass at which stars start evolving as WCs, will be displaced as a function of metallicity. S. E. Woosley (2019) compared the evolution of massive helium stars to quasi-chemically homogeneously evolving stars. Even at the lowest metallicities, however, the evoltuion of WRs is mainly dictated by their mass and metallicity. We expect that their winds will be approximately spherical, creating a relatively spherical CSM, as is inferred from several observations (Bartel et al., 2017). Furthermore, their winds will be relatively static over long periods of time, consistent to the fairly regular radio emission of Type Ibc SNe, which rises from the interaction between the fastest ejecta and the CSM (Chevalier, 1998). Stars that evolve quasi-chemically homogeneously display a very different behaviour, which is mediated by their rotation and their neutrino losses, particularly after helium core depletion (Aguilera-Dena et al., 2018). Regardless of whether they develop a helium envelope or not, we expect very different evolution and transients from these two channels, and warn the reader against comparing the two channels of stellar evolution.

Our evolutionary calculations are extended to several metallicities, but our results are generally consistent with previous works on helium star evolution. The final masses of models Z=0.02 are in agreement with the final masses of the models from Yoon (2017), and those at Z=0.015 are also consistent with S. E. Woosley (2019) (who use Z=0.0145) at masses where the WC/WO wind is unimportant. However, we observe systematically lower final masses for WC/WO progenitors than what is found from the KEPLER code, at similar metallicity.

The average ratios of WC/WN and Ic/Ib that we calculated in Figures 4.7 and 4.15 are subject to some caveats. We use the ZAMS mass to helium mass relation from S. E. Woosley (2019), but it might depend on metallicity, which has not been taken into account. Another caveat is that we do not consider that binary fractions and stripping probabilities might depend on mass and metallicity. Finally, stripping processes might depend strongly on metallicity and in the detailed binary evolution that we overlook in this paper, as was shown by Götberg et al. (2018), Laplace et al. (2020) and Shenar et al. (2020). However, they do reveal certain trends that will likely hold up, even after all our simplifications. More stars will become WC stars at higher metallicity, the lowest luminosity WR will decrease with increasing metallicity, and more Type Ic SNe will be observed coming from such environments.

4.6 Conclusions

We have modelled massive helium stars, similar to those that are likely formed in real stellar systems of all initial masses through binary interactions (including stable mass transfer and common envelope ejections), or by strong stellar winds during the main sequence for stars with the highest initial masses, particularly in larger metallicity environments. We have covered the range of initial helium masses between 3.5 and 70 , and metallicities between 0.01, similar to that observed in the LMC, to 0.04, similar to the highest metallicitiy environments like near the center of our Galaxy, or in nearby massive galaxies. We find that the life time of helium stars is only very weakly dependent in metallicity. Their core evolution, observable properties and their fates after core-collapse, however, are strongly dependent on metallicity.

Owing to the fact that nitrogen will burn at a lower temperature than helium, helium stars will have a very strong chemical composition gradient set at the beginning of helium burning. Layers initially outside the convective helium burning core will have $Y = 1 - Z$, and will mostly be abundant in nitrogen, enhanced during hydrogen burning due to CNO equilibrium. The inside of the core, on the other hand, will have a progressively decreasing amount of helium, and will instead be enriched in carbon and oxygen. This will give rise to the observational dichotomy between WNE and WC/WO stars. The change in mass loss rates that accompanies the sudden change in surface composition in our models translates to the observed dichotomy between spectral properties and ejecta masses Type Ib and Type Ic SNe.

We have found that the minimum luminosity of WR stars, for both WN and WC, is well described by a combination of the wind parameters from Yoon (2017) and the wind opacity, as derived by Langer (1989). We provide a quantitative way to determine this limit in different environments.

We also find that the ratio of WC to WN type stars should increase as a function of increasing luminosity, owing to the fact that stars at higher metallicities spend a longer fraction of their life as WCs, even after taking into account that the number of WNs might increase due to the decrease in the luminosity limit. However, this increase is not dramatic and stalls at Z~0.03 due to the shorter life time of WC stars, compared to WN stars.

We find that helium stars with carbon and oxygen in their surface will be observed as WR stars at the metallicities that we cover in our models. Our models reproduce the areas where WC stars are more numerous in the LMC and our Galaxy, but stars below this limit are also observed. They are close to the transition between optically thin and optically thick winds, and are likely not only a product of single helium star evolution.

The use of stronger mass loss rates was motivated by the mismatch between the theoretical predictions of luminostites of WC stars and their observed values (Yoon, 2017). We reproduce these findings, and have found that a combination of the wind mass loss rates and the difference in metallicity will be able to reproduce both the decreasing minimum luminosity for observed WRs in increasing metallicity environments, as well as the increasing rate of WC stars with respect to the amount of WNs.

Finally, we find that properties of Type Ib and Type Ic SNe, and compact remnants resulting from helium stars will vary across different metallicity environments. BHs with masses around 8 $M_{\odot}$ are produced at every metallicity, but the mass distribution of BHs has a second peak which is moved to lower masses as metallicity increases. On the other hand, this implies that explosions with more massive ejecta and higher energies are expected at low metallicity. Distributions of NS masses, kick velocities and nickel masses of both Type Ib and Type Ic progenitors have only weak variations across different metallicities, but distributions of ejecta mass, and the relative rate of Ic SNe with respect to Ib SNe are strongly dependent in metallicity as well.

CHAPTER 5

Outlook

The work presented in this thesis is an exploration of possible pathways in the evolution of massive stars that could explain the observed phenomenology of a few types of astrophysical transients. This study focuses on Type I superluminous supernovae, Type Ic-BL supernovae, gamma-ray bursts and the ordinary Type Ib and Type Ic supernovae; only a few of the many families of transients that have been discovered and studied so far. It required the effort to combine the knowledge of theoretical stellar physics through state of the art numerical simulations of stellar evolution, along with insights obtained through continued discovery and follow-up of astronomical transients, and from observations of populations of massive stars.

The serendipitous discovery of gamma-ray bursts in the 1970s (Klebesadel et al., 1973) led to many works speculating about their origin, distribution, and an explanation for the mechanism that created their highly energetic emission. As the number of observations of these events increased, it was suggested that the majority of these explosions originate in massive stars (e.g. Paczyński, 1998). The connection between long gamma-ray bursts and massive stars today is clear, but the pathways of stellar evolution that could turn massive stars into gamma-ray bursts is still debated, and more work is required to fully understand the origin of these events.

The discovery of superluminous supernovae occurred much more recently (Quimby et al., 2007). Since their discovery, these objects have been routinely discovered and analyzed. However, their discovery posed severe challenges to theoretical astrophysics. Explaining the energy released by the decay of ^{56}Ni, the mechanism that was found to power the light curves of other types of supernovae (i.e. Arnett, 1982), seemed to be in opposition to the inferred ejecta masses (e.g. Smith et al., 2007), and several ideas emerged for engines that could possibly provide the energy required. Stellar evolution follows, trying to find different ways that these engines could be formed inside massive stars, taking into account the constraints found in observations, as well as the rate of occurrence and the environments of the transients.

Even observations of the most common types of supernovae, which were initially found in large numbers during the 1930s (Baade et al., 1934b), still pose questions about stellar evolution, and put constraints on topics that are currently debated in stellar astrophysics, such as the influence of binary and multiple systems in stellar populations, the effect of rotation, the internal mixing and angular momentum transport mechanisms, the effect of stellar winds.

In this thesis, we have tackled the problem of how to explain the origin of superluminous supernovae, gamma-ray bursts, and stripped-envelope supernovae through simulations of massive star evolution. We proposed an evolutionary channel that could naturally explain the ejecta masses and spin periods of superluminous supernovae, as well as attain enough angular momentum to produce long gamma-ray bursts. We analysed the core structure attained in our progenitor models to find the ranges of initial mass where each of these events could take place. Finally, we modelled the influence of metallicity dependent winds on helium stars to study its influence on the known populations of Wolf-Rayet stars, and Type Ib and Type Ic supernovae.

The transient events that we covered in this study are but a small sample of the astrophysical transients that are known today. Recent and ongoing observational efforts such as the Palomar Transient Factory, the Lick Observatory Supernova Search, the Neil Gehrels Swift Observatory, the Zwicky Transient Factory, the Panoramic Survey Telescope and Rapid Response System, the Public ESO Spectroscopic Survey of Transient Objects, and several others are revolutionizing the field by observing and classifying new types of transients every day. New types of transients keep being discovered, such as the recent discovery of gravitational wave events by the LIGO/Virgo collaboration, or the discovery of fast radio bursts at Parkes Observatory have created entirely new fields of study in transient astrophysics.

And the plot is bound to thicken even more. The upcoming Vera C. Rubin Observatory will likely discover about ten times more transients than our current best facilities. The Laser Interferometer Space Antenna and the Einstein Telescope will broaden the frequency range where we can discover gravitational wave events. The Space Variable Objects Monitor will discover and locate hundreds of gamma-ray bursts. The James Webb Space Telescope will be able to look at the most distant transients, that occurred shortly after the Big Bang. Synergy between observatories will allow to study transients not only across the electromagnetic spectrum, but also through gravitational waves, neutrino detections and cosmic ray observations. We are at the dawn of the era of multi-messenger astrophysics, and the study of transients coming from massive stars is at the heart of it all.

It is not clear whether the evolutionary channel we proposed for possible progenitors of superluminous supernovae and gamma-ray bursts in Chapters 2 and 3 is pursued by stars in nature. Solid evidence for the existence of chemically homogeneously evolving stars has not been found within the stellar populations that have been studied up to now. Detecting these objects might be difficult. If they exist, they will be more prominent in the low metallicity environments of distant galaxies, where stars cannot be resolved individually with current telescopes. However, with the increasing number of observations of of superluminous supernovae and gamma-ray bursts, a better constraint on the rate of these events as a function of metallicity will be available. With the production of a larger grid of chemically homogeneous stars, we may be able to set theoretical constraints to the rate of occurrence of these events, which is correlated with the rate of occurrence of chemically homogeneously evolving stars, and therefore with the efficiency of rotational mixing.

Another issue that remains unclear is the influence of fast rotation on supernova explosions. Instabilities that grow in the cores of massive stars shortly before they explode as supernovae have been found to produce an aspherical structures that can increase the likelihood of producing neutrino-driven explosions of massive stars (e.g. Couch, 2017; Yoshida et al., 2019). The influence of a realistic rotation profile on such structures is unknown, but the models provided in Chapters 2 and 3 could provide useful initial conditions for multidimensional simulations of the onset of core collapse.

The field of 2D and 3D hydrodynamic simulations of supernova explosions is complex, but fast growing. Hydrodynamic effects (e.g. H. .-.-T. Janka et al., 1996; Blondin et al., 2003; Hanke et al., 2013), magnetic effects (e.g. Kotake et al., 2004; Obergaulinger et al., 2006; Obergaulinger et al., 2018) and effects of rotation (e.g. Ott et al., 2005; Takiwaki et al., 2016) have also been found to influence the onset of supernova explosion. Our models can potentially provide realistic initial conditions to such simulations, to study the effects of rotation and seed magnetic fields during core collapse. Recently, Powell et al. (2020) found that fast rotation can influence the gravitational wave emission expected from core collapse supernovae by performing 3D core collapse simulations using one of the models discussed in this thesis as an initial condition.

Regarding the more typical supernovae, our results from Chapter 4 set constraints on the properties of their progenitors in several metallicity environments. Our results extend the applicability of population synthesis studies that include stripped-envelope stars (e.g. Kruckow et al., 2018) to better constrain the properties of supernovae, as well as compact object mergers as sources of gravitational waves. Furthermore, it is a step forward into our understanding of Wolf-Rayet stars, and can potentially be extended into regimes of low metallicity, where the ionizing radiation of massive helium stars is believed to play a role in the epoch of reionization (Götberg et al., 2017).

In conclusion, the fields of massive stellar evolution and transient astrophysics are deeply intertwined, and the contributions of this thesis can have implications in our understanding of their connection. Many prospects and open questions lie ahead, and the incoming wave of new transient discoveries will likely lead to many more mysteries, as they have in the past, and will allow for many new avenues to deepen our understanding of massive stars and their influence in shaping the Universe.

Bibliography

Abbott, B. P., R. Abbott, T. D. Abbott, F. Acernese, K. Ackley, C. Adams, T. Adams, P. Addesso, R. X. Adhikari, V. B. Adya, C. Affeldt, M. Afrough, B. Agarwal, M. Agathos, K. Agatsuma, N. Aggarwal, O. D. Aguiar, L. Aiello, A. Ain, P. Ajith, B. Allen, G. Allen, A. Allocca, P. A. Altin, A. Amato, A. Ananyeva, S. B. Anderson, W. G. Anderson, S. V. Angelova, S. Antier, S. Appert, K. Arai, M. C. Araya, J. S. Areeda, N. Arnaud, K. G. Arun, S. Ascenzi, G. Ashton, M. Ast, S. M. Aston, P. Astone, D. V. Atallah, P. Aufmuth, C. Aulbert, K. AultONeal, C. Austin, A. Avila-Alvarez, S. Babak, P. Bacon, M. K. M. Bader, S. Bae, M. Bailes et al. (2017). *GW170817: Observation of Gravitational Waves from a Binary Neutron Star Inspiral*. Physical Review Letters **119** 161101. arXiv: `1710.05832 [gr-qc]` (cit. on p. 15).

Abbott, B. P., R. Abbott, T. D. Abbott, F. Acernese, K. Ackley, C. Adams, T. Adams, P. Addesso, R. X. Adhikari, V. B. Adya, C. Affeldt, M. Afrough, B. Agarwal, M. Agathos, K. Agatsuma, N. Aggarwal, O. D. Aguiar, L. Aiello, A. Ain, P. Ajith, B. Allen, G. Allen, A. Allocca, P. A. Altin, A. Amato, A. Ananyeva, S. B. Anderson, W. G. Anderson, S. V. Angelova, S. Antier, S. Appert, K. Arai, M. C. Araya, J. S. Areeda, N. Arnaud, K. G. Arun, S. Ascenzi, G. Ashton, M. Ast, S. M. Aston, P. Astone, D. V. Atallah, P. Aufmuth, C. Aulbert, K. AultONeal, C. Austin, A. Avila-Alvarez, S. Babak, P. Bacon, M. K. M. Bader, S. Bae, P. T. Baker et al. (2017). *Multi-messenger Observations of a Binary Neutron Star Merger*. Astrophysical Journal, Letters **848** L12. arXiv: `1710.05833 [astro-ph.HE]` (cit. on p. 14).

Abbott, B. P. et al. (2016). *Observation of Gravitational Waves from a Binary Black Hole Merger*. Phys. Rev. Lett. **116** (6) 061102. URL: `https://link.aps.org/doi/10.1103/PhysRevLett.116.061102` (cit. on pp. 15, 16).

Adams, S. M. et al. (2017). *The search for failed supernovae with the Large Binocular Telescope: confirmation of a disappearing star*. Monthly Notices of the RAS **468** 4968. arXiv: `1609.01283 [astro-ph.SR]` (cit. on p. 16).

Aguilera Dena, D. R. (2017). *Pre-supernova Evolution of Rapidly RotatingMassive Stars at Low Metallicity*. Master Thesis: University of Bonn. URL: `https://astro.uni-bonn.de/~nlanger/thesis/david_master.pdf` (cit. on pp. 22–25, 27, 31, 32, 35, 38, 44).

Aguilera-Dena, D. R. et al. (2018). *Related Progenitor Models for Long-duration Gamma-Ray Bursts and Type Ic Superluminous Supernovae*. Astrophysical Journal **858** 115. arXiv: `1804.07317 [astro-ph.SR]` (cit. on pp. 25, 27, 29–40, 42–44, 49, 99).

Akiyama, S. et al. (2003). *The Magnetorotational Instability in Core-Collapse Supernova Explosions*. Astrophysical Journal **584** 954. arXiv: `astro-ph/0208128 [astro-ph]` (cit. on pp. 37, 67).

Aldering, G., R. M. Humphreys and M. Richmond (1994). *SN 1993J: The Optical Properties of its Progenitor*. Astronomical Journal **107** 662 (cit. on p. 15).

Allan, A. P. et al. (2020). *The possible disappearance of a massive star in the low-metallicity galaxy PHL 293B*. Monthly Notices of the RAS **496** 1902. arXiv: `2003.02242 [astro-ph.SR]` (cit. on p. 16).

Angus, C. R. et al. (2016). *A Hubble Space Telescope survey of the host galaxies of Superluminous Supernovae*. Monthly Notices of the RAS **458** 84. arXiv: `1601.01874 [astro-ph.GA]` (cit. on p. 48).

Antoniadis, J. et al. (2020). *Type Ia supernovae from non-accreting progenitors*. Astronomy and Astrophysics **635** A72. arXiv: `1912.07608 [astro-ph.SR]` (cit. on p. 77).

Arnett, W. D. (1974). *Advanced evolution of massive stars. VI. Oxygen burning.* Astrophysical Journal **194** 373 (cit. on p. 74).

– (1982). *Type I supernovae. I - Analytic solutions for the early part of the light curve*. Astrophysical Journal **253** 785 (cit. on pp. 67, 101).

Baade, W. and F. Zwicky (1934a). *Cosmic Rays from Super-novae*. Proceedings of the National Academy of Science **20** 259 (cit. on pp. 4, 13, 15).

– (1934b). *On Super-novae*. Proceedings of the National Academy of Science **20** 254 (cit. on pp. 3, 101).

Balberg, S. and A. Loeb (2011). *Supernova shock breakout through a wind*. Monthly Notices of the RAS **414** 1715. arXiv: `1101.1489 [astro-ph.HE]` (cit. on p. 38).

Bartel, N., B. Karimi and M. F. Bietenholz (2017). *VLBI of supernovae and gamma-ray bursts*. Astronomy Reports **61** 299 (cit. on p. 99).

Bjorkman, J. E. and J. P. Cassinelli (1993). *Equatorial Disk Formation around Rotating Stars Due to Ram Pressure Confinement by the Stellar Wind*. Astrophysical Journal **409** 429 (cit. on pp. 28, 51).

Blanchard, P. K., M. Nicholl, E. Berger, R. Chornock, R. Margutti et al. (2018). *The Type I Superluminous Supernova PS16aqv: Lightcurve Complexity and Deep Limits on Radioactive Ejecta in a Fast Event*. Astrophysical Journal **865** 9. arXiv: `1805.07372 [astro-ph.HE]` (cit. on pp. 42, 48, 67–69).

Blanchard, P. K., M. Nicholl, E. Berger, R. Chornock, D. Milisavljevic et al. (2019). *A Hydrogen-poor Superluminous Supernova with Enhanced Iron-group Absorption: A New Link between SLSNe and Broad-lined Type Ic SNe*. Astrophysical Journal **872** 90. arXiv: `1810.11051 [astro-ph.HE]` (cit. on pp. 42, 48, 67–69).

Blanchard, P. K., E. Berger et al. (2020). *The Pre-Explosion Mass Distribution of Hydrogen-Poor Superluminous Supernova Progenitors and New Evidence for a Mass-Spin Correlation*. arXiv e-prints arXiv:2002.09508. arXiv: `2002.09508 [astro-ph.HE]` (cit. on pp. 37, 42, 48–50, 67, 68, 71).

Blondin, J. M., A. Mezzacappa and C. DeMarino (2003). *Stability of Standing Accretion Shocks, with an Eye toward Core-Collapse Supernovae*. Astrophysical Journal **584** 971. arXiv: `astro-ph/0210634 [astro-ph]` (cit. on p. 102).

Böhm-Vitense, E. (1958). *Über die Wasserstoffkonvektionszone in Sternen verschiedener Effektivtemperaturen und Leuchtkräfte. Mit 5 Textabbildungen*. Zeitschrift fuer Astrophysik **46** 108 (cit. on pp. 50, 75).

Brott, I. et al. (2011a). *Rotating massive main-sequence stars. I. Grids of evolutionary models and isochrones*. Astronomy and Astrophysics **530** A115. arXiv: `1102.0530 [astro-ph.SR]` (cit. on pp. 22, 28).

– (2011b). *Rotating massive main-sequence stars. I. Grids of evolutionary models and isochrones*. Astronomy and Astrophysics **530** A115. arXiv: `1102.0530 [astro-ph.SR]` (cit. on pp. 49, 50, 54).

Bugli, M. et al. (2020). *The impact of non-dipolar magnetic fields in core-collapse supernovae*. Monthly Notices of the RAS **492** 58. arXiv: `1909.02824 [astro-ph.HE]` (cit. on p. 38).

Burrows, A. et al. (2020). *The overarching framework of core-collapse supernova explosions as revealed by 3D FORNAX simulations*. Monthly Notices of the RAS **491** 2715. arXiv: `1909.04152 [astro-ph.HE]` (cit. on p. 61).

Cantiello, M. et al. (2007). *Binary star progenitors of long gamma-ray bursts*. Astronomy and Astrophysics **465** L29. arXiv: `astro-ph/0702540 [astro-ph]` (cit. on p. 49).

Cao, Y. et al. (2013). *Discovery, Progenitor and Early Evolution of a Stripped Envelope Supernova iPTF13bvn*. Astrophysical Journal, Letters **775** L7. arXiv: `1307.1470 [astro-ph.SR]` (cit. on p. 15).

Cappellaro, E., R. Evans and M. Turatto (1999). *A new determination of supernova rates and a comparison with indicators for galactic star formation*. Astronomy and Astrophysics **351** 459. eprint: `astro-ph/9904225` (cit. on p. 74).

Cardona, Á. R. (2013). *Breve historia de la astronomía*. Tombooktu México (cit. on p. 1).

Carroll, B. W. and D. A. Ostlie (1996). *An Introduction to Modern Astrophysics* (cit. on p. 4).

Chaisson, E. and S. McMillan (2005). *Astronomy Today* (cit. on p. 10).

Chatzopoulos, E., J. C. Wheeler and J. Vinko (2012). *Generalized Semi-analytical Models of Supernova Light Curves*. Astrophysical Journal **746** 121. arXiv: `1111.5237 [astro-ph.HE]` (cit. on p. 48).

Chen, T. .-.-W. et al. (2017). *The evolution of superluminous supernova LSQ14mo and its interacting host galaxy system*. Astronomy and Astrophysics **602** A9. arXiv: `1611.09910 [astro-ph.SR]` (cit. on p. 21).

Chen, T.-W. et al. (2017). *The evolution of superluminous supernova LSQ14mo and its interacting host galaxy system*. Astronomy and Astrophysics **602** A9. arXiv: `1611.09910 [astro-ph.SR]` (cit. on p. 43).

Chevalier, R. A. (1998). *Synchrotron Self-Absorption in Radio Supernovae*. Astrophysical Journal **499** 810 (cit. on p. 99).

Chevalier, R. A. and C. M. Irwin (2011). *Shock Breakout in Dense Mass Loss: Luminous Supernovae*. Astrophysical Journal, Letters **729** L6. arXiv: `1101.1111 [astro-ph.HE]` (cit. on p. 21).

Clark, D. H. and F. R. Stephenson (1977). *The historical supernovae* (cit. on p. 3).

Colgate, S. A. (1974). *Early Gamma Rays from Supernovae*. Astrophysical Journal **187** 333 (cit. on p. 38).

Couch, S. M. (2017). “Influence of Non-spherical Initial Stellar Structure on the Core-Collapse Supernova Mechanism”. *Handbook of Supernovae*. Ed. by A. W. Alsabti and P. Murdin 1791 (cit. on p. 102).

Crowther, P. A. (2007). *Physical Properties of Wolf-Rayet Stars*. Annual Review of Astronomy and Astrophysics **45** 177. arXiv: `astro-ph/0610356 [astro-ph]` (cit. on pp. 16, 74).

Davies, B. and E. R. Beasor (2020). *The ‘red supergiant problem’: the upper luminosity boundary of Type II supernova progenitors*. Monthly Notices of the RAS **493** 468. arXiv: `2001.06020 [astro-ph.SR]` (cit. on pp. 15, 20).

de Mink, S. E. et al. (2009). *Rotational mixing in massive binaries. Detached short-period systems*. Astronomy and Astrophysics **497** 243. arXiv: `0902.1751 [astro-ph.SR]` (cit. on p. 49).

Dessart, L., D. J. Hillier, C. Li et al. (2012). *On the nature of supernovae Ib and Ic*. Monthly Notices of the RAS **424** 2139. arXiv: `1205.5349 [astro-ph.SR]` (cit. on pp. 74, 88).

Dessart, L., D. J. Hillier, E. Livne et al. (2011). *Core-collapse explosions of Wolf-Rayet stars and the connection to Type IIb/Ib/Ic supernovae*. Monthly Notices of the RAS **414** 2985. arXiv: `1102.5160 [astro-ph.SR]` (cit. on pp. 74, 88).

Dessart, L., D. J. Hillier, S. Woosley et al. (2015). *Radiative-transfer models for supernovae IIb/Ib/Ic from binary-star progenitors*. Monthly Notices of the RAS **453** 2189. arXiv: `1507.07783 [astro-ph.SR]` (cit. on pp. 48, 52).

Dessart, L., D. John Hillier et al. (2017). *Radiative-transfer models for explosions from rotating and non-rotating single WC stars. Implications for SN 1998bw and LGRB/SNe*. Astronomy and Astrophysics **603** A51. arXiv: `1703.08932 [astro-ph.SR]` (cit. on p. 52).

Dessart, L., S.-C. Yoon et al. (2020). *Supernovae Ib and Ic from the explosion of helium stars*. arXiv e-prints arXiv:2008.07601. arXiv: `2008.07601 [astro-ph.SR]` (cit. on pp. 26, 74, 88, 90, 91).

Detmers, R. G. et al. (2008). *Gamma-ray bursts from tidally spun-up Wolf-Rayet stars?* Astronomy and Astrophysics **484** 831. arXiv: `0804.0014 [astro-ph]` (cit. on p. 49).

Dewi, J. D. M. and O. R. Pols (2003). *The late stages of evolution of helium star-neutron star binaries and the formation of double neutron star systems*. Monthly Notices of the RAS **344** 629. arXiv: `astro-ph/0306066 [astro-ph]` (cit. on p. 74).

Dewi, J. D. M., O. R. Pols et al. (2002). *The evolution of naked helium stars with a neutron star companion in close binary systems*. Monthly Notices of the RAS **331** 1027. arXiv: `astro-ph/0201239 [astro-ph]` (cit. on p. 74).

Dexter, J. and D. Kasen (2013). *Supernova Light Curves Powered by Fallback Accretion*. Astrophysical Journal **772** 30. arXiv: `1210.7240 [astro-ph.HE]` (cit. on p. 21).

Diehl, R. et al. (2006). *Radioactive* ^{26}*Al from massive stars in the Galaxy*. Nature **439** 45. arXiv: `astro-ph/0601015 [astro-ph]` (cit. on p. 16).

Dong, S. et al. (2016). *ASASSN-15lh: A highly super-luminous supernova*. Science **351** 257. arXiv: `1507.03010 [astro-ph.HE]` (cit. on p. 2).

Drout, M. R. et al. (2011). *The First Systematic Study of Type Ibc Supernova Multi-band Light Curves*. Astrophysical Journal **741** 97. arXiv: `1011.4959 [astro-ph.CO]` (cit. on p. 12).

Endal, A. S. and S. Sofia (1976). *The evolution of rotating stars. I. Method and exploratory calculations for a 7 M sun star.* Astrophysical Journal **210** 184 (cit. on p. 18).

Ertl, T., H.-T. Janka et al. (2016). *A Two-parameter Criterion for Classifying the Explodability of Massive Stars by the Neutrino-driven Mechanism*. Astrophysical Journal **818** 124. arXiv: `1503.07522 [astro-ph.SR]` (cit. on pp. 20, 49, 60–62, 71, 91).

Ertl, T., S. E. Woosley et al. (2020). *The Explosion of Helium Stars Evolved with Mass Loss*. Astrophysical Journal **890** 51. arXiv: `1910.01641 [astro-ph.HE]` (cit. on pp. 26, 74, 91, 93).

Farmer, R. et al. (2019). *Mind the Gap: The Location of the Lower Edge of the Pair-instability Supernova Black Hole Mass Gap*. Astrophysical Journal **887** 53. arXiv: `1910.12874 [astro-ph.SR]` (cit. on p. 59).

Filippenko, A. V. (1997). *Optical Spectra of Supernovae*. Annual Review of Astronomy and Astrophysics **35** 309 (cit. on pp. 11–13).

Folatelli, G. et al. (2016). *Disappearance of the Progenitor of Supernova iPTF13bvn*. Astrophysical Journal, Letters **825** L22. arXiv: `1604.06821 [astro-ph.SR]` (cit. on p. 15).

Friend, D. B. and D. C. Abbott (1986). *The Theory of Radiatively Driven Stellar Winds. III. Wind Models with Finite Disk Correction and Rotation*. Astrophysical Journal **311** 701 (cit. on pp. 18, 28).

Gal-Yam, A. (2012). *Luminous Supernovae*. Science **337** 927. arXiv: `1208.3217` (cit. on pp. 14, 48).

Gal-Yam, A. (2019). *A Simple Analysis of Type I Superluminous Supernova Peak Spectra: Composition, Expansion Velocities, and Dynamics*. Astrophysical Journal **882** 102. arXiv: `1806.08224 [astro-ph.HE]` (cit. on p. 48).

Gal-Yam, A. et al. (2009). *Supernova 2007bi as a pair-instability explosion*. Nature **462** 624. arXiv: `1001.1156` (cit. on pp. 20, 21, 48).

Gerke, J. R., C. S. Kochanek and K. Z. Stanek (2015). *The search for failed supernovae with the Large Binocular Telescope: first candidates*. Monthly Notices of the RAS **450** 3289. arXiv: `1411.1761 [astro-ph.SR]` (cit. on p. 16).

Gilkis, A. et al. (2019). *Effects of winds on the leftover hydrogen in massive stars following Roche lobe overflow*. Monthly Notices of the RAS **486** 4451. arXiv: `1904.09221 [astro-ph.SR]` (cit. on pp. 75, 98).

Gliese, W. (1957). *Katalog der Sterne näher ALS 20 Parsek für 1950.0*. Astronomisches Rechen-Institut Heidelberg Mitteilungen Serie A **8** 1 (cit. on p. 6).

Gomez, S. et al. (2019). *SN 2016iet: The Pulsational or Pair Instability Explosion of a Low-metallicity Massive CO Core Embedded in a Dense Hydrogen-poor Circumstellar Medium*. Astrophysical Journal **881** 87. arXiv: `1904.07259 [astro-ph.HE]` (cit. on p. 44).

Götberg, Y., S. E. de Mink and J. H. Groh (2017). *Ionizing spectra of stars that lose their envelope through interaction with a binary companion: role of metallicity*. Astronomy and Astrophysics **608** A11. arXiv: `1701.07439 [astro-ph.SR]` (cit. on pp. 18, 103).

Götberg, Y., S. E. de Mink, J. H. Groh et al. (2018). *Spectral models for binary products: Unifying subdwarfs and Wolf-Rayet stars as a sequence of stripped-envelope stars*. Astronomy and Astrophysics **615** A78. arXiv: `1802.03018 [astro-ph.SR]` (cit. on pp. 75, 99).

Gräfener, G., S. P. Owocki et al. (2017). *On the optically thick winds of Wolf-Rayet stars*. Astronomy and Astrophysics **608** A34. arXiv: `1710.04543 [astro-ph.SR]` (cit. on p. 83).

Gräfener, G., J. S. Vink et al. (2011). *The Eddington factor as the key to understand the winds of the most massive stars. Evidence for a* Γ*-dependence of Wolf-Rayet type mass loss*. Astronomy and Astrophysics **535** A56. arXiv: `1106.5361 [astro-ph.SR]` (cit. on pp. 79, 83).

Grafener, G. et al. (1998). *Spectral analyses of WC stars in the LMC*. Astronomy and Astrophysics **329** 190 (cit. on p. 35).

Green, D. A. and F. R. Stephenson (2017). "Possible and Suggested Historical Supernovae in the Galaxy". *Handbook of Supernovae*. Ed. by A. W. Alsabti and P. Murdin 179 (cit. on p. 3).

Grevesse, N., A. Noels and A. J. Sauval (1996). "Standard Abundances". *Cosmic Abundances*. Ed. by S. S. Holt and G. Sonneborn. Vol. 99. Astronomical Society of the Pacific Conference Series 117 (cit. on pp. 22, 27, 50, 75).

Guilet, J. and E. Müller (2015). *Numerical simulations of the magnetorotational instability in protoneutron stars - I. Influence of buoyancy*. Monthly Notices of the RAS **450** 2153. arXiv: `1501.07636 [astro-ph.HE]` (cit. on pp. 37, 67).

Hachinger, S. et al. (2012). *How much H and He is 'hidden' in SNe Ib/c? - I. Low-mass objects*. Monthly Notices of the RAS **422** 70. arXiv: `1201.1506 [astro-ph.SR]` (cit. on pp. 48, 74, 88).

Hainich, R. et al. (2014). *The Wolf-Rayet stars in the Large Magellanic Cloud. A comprehensive analysis of the WN class*. Astronomy and Astrophysics **565** A27. arXiv: `1401.5474 [astro-ph.SR]` (cit. on pp. 76, 98).

Hamann, W. .-.-R., L. Koesterke and U. Wessolowski (1995). *Spectral analyses of the Galactic Wolf-Rayet stars: hydrogen-helium abundances and improved stellar parameters for the WN class*. Astronomy and Astrophysics **299** 151 (cit. on pp. 50, 98).

Hanke, F. et al. (2013). *SASI Activity in Three-dimensional Neutrino-hydrodynamics Simulations of Supernova Cores*. Astrophysical Journal **770** 66. arXiv: `1303.6269 [astro-ph.SR]` (cit. on p. 102).

Hastings, B., N. Langer and G. Koenigsberger (2020). *Internal circulation in tidally locked massive binary stars – Consequences for double black hole formation*. arXiv e-prints arXiv:2007.11299. arXiv: `2007.11299 [astro-ph.SR]` (cit. on p. 49).

Heger, A. and N. Langer (1996). *Stationary hydrodynamic models of Wolf-Rayet stars with optically thick winds.* Astronomy and Astrophysics **315** 421 (cit. on p. 35).

– (2000). *Presupernova Evolution of Rotating Massive Stars. II. Evolution of the Surface Properties*. Astrophysical Journal **544** 1016. arXiv: `astro-ph/0005110 [astro-ph]` (cit. on p. 49).

Heger, A., N. Langer and S. E. Woosley (2000a). *Presupernova Evolution of Rotating Massive Stars. I. Numerical Method and Evolution of the Internal Stellar Structure*. Astrophysical Journal **528** 368. arXiv: `astro-ph/9904132 [astro-ph]` (cit. on pp. 18, 50).

– (2000b). *Presupernova Evolution of Rotating Massive Stars. I. Numerical Method and Evolution of the Internal Stellar Structure*. Astrophysical Journal **528** 368. eprint: `astro-ph/9904132` (cit. on pp. 28, 31, 44).

Heger, A., S. E. Woosley and H. C. Spruit (2005). *Presupernova Evolution of Differentially Rotating Massive Stars Including Magnetic Fields*. Astrophysical Journal **626** 350. eprint: `astro-ph/0409422` (cit. on pp. 33, 35, 37).

Hjorth, J. and J. S. Bloom (2012). “The Gamma-Ray Burst - Supernova Connection”. *Chapter 9 in ”Gamma-Ray Bursts* 169 (cit. on p. 48).

Howell, D. A. (2017). “Superluminous Supernovae”. *Handbook of Supernovae, ISBN 978-3-319-21845-8. Springer International Publishing AG, 2017, p. 431*. Ed. by A. W. Alsabti and P. Murdin 431 (cit. on p. 48).

Iglesias, C. A. and F. J. Rogers (1996). *Updated Opal Opacities*. Astrophysical Journal **464** 943 (cit. on p. 50).

Inserra, C. (2019). *Observational properties of extreme supernovae*. Nature Astronomy **3** 697. arXiv: `1908.02314 [astro-ph.HE]` (cit. on p. 48).

Inserra, C. et al. (2017). *Complexity in the light curves and spectra of slow-evolving superluminous supernovae*. Monthly Notices of the RAS **468** 4642. arXiv: `1701.00941 [astro-ph.HE]` (cit. on p. 43).

Irwin, C. M. and R. A. Chevalier (2016). *Jet or shock breakout? The low-luminosity GRB 060218*. Monthly Notices of the RAS **460** 1680. arXiv: `1511.00336 [astro-ph.HE]` (cit. on p. 44).

Ivanova, N. et al. (2013). *Common envelope evolution: where we stand and how we can move forward*. Astronomy and Astrophysics Reviews **21** 59. arXiv: `1209.4302 [astro-ph.HE]` (cit. on p. 18).

Janka, H. .-.-T. and E. Mueller (1996). *Neutrino heating, convection, and the mechanism of Type-II supernova explosions*. Astronomy and Astrophysics **306** 167 (cit. on p. 102).

Japelj, J. et al. (2016). *Taking stock of superluminous supernovae and long gamma-ray burst host galaxy comparison using a complete sample of LGRBs*. Astronomy and Astrophysics **593** A115. arXiv: `1607.01045 [astro-ph.HE]` (cit. on p. 48).

Joglekar, H. et al. (2011). *Oldest sky-chart with Supernova record*. Puratattva-Bulletin of the Indian Archaeological Society **41** 207 (cit. on pp. 2, 3).

Kasen, D. and L. Bildsten (2010a). *Supernova Light Curves Powered by Young Magnetars*. Astrophysical Journal **717** 245. arXiv: `0911.0680 [astro-ph.HE]` (cit. on p. 42).

Kasen, D., S. E. Woosley and A. Heger (2011). *Pair Instability Supernovae: Light Curves, Spectra, and Shock Breakout*. Astrophysical Journal **734** 102. arXiv: `1101.3336 [astro-ph.HE]` (cit. on p. 20).

Kasen, D. and L. Bildsten (2010b). *Supernova Light Curves Powered by Young Magnetars*. Astrophysical Journal **717** 245. arXiv: `0911.0680 [astro-ph.HE]` (cit. on pp. 20, 48, 49).

Kilpatrick, C. D., R. J. Foley et al. (2017). *On the progenitor of the Type IIb supernova 2016gkg*. Monthly Notices of the RAS **465** 4650. arXiv: `1610.04587 [astro-ph.SR]` (cit. on p. 15).

Kilpatrick, C. D., T. Takaro et al. (2018). *A potential progenitor for the Type Ic supernova 2017ein*. Monthly Notices of the RAS **480** 2072. arXiv: `1808.02989 [astro-ph.SR]` (cit. on p. 15).

Kippenhahn, R., G. Ruschenplatt and H. .-.-C. Thomas (1980). *The time scale of thermohaline mixing in stars*. Astronomy and Astrophysics **91** 175 (cit. on p. 75).

Kippenhahn, R. and A. Weigert (1990). *Stellar Structure and Evolution* (cit. on pp. 4, 5, 13, 55).

Klebesadel, R. W., I. B. Strong and R. A. Olson (1973). *Observations of Gamma-Ray Bursts of Cosmic Origin*. Astrophysical Journal, Letters **182** L85 (cit. on p. 101).

Kochanek, C. S. et al. (2008). *A Survey About Nothing: Monitoring a Million Supergiants for Failed Supernovae*. Astrophysical Journal **684** 1336. arXiv: `0802.0456 [astro-ph]` (cit. on p. 20).

Kotake, K. et al. (2004). *Magnetorotational Effects on Anisotropic Neutrino Emission and Convection in Core-Collapse Supernovae*. Astrophysical Journal **608** 391 (cit. on p. 102).

Kruckow, M. U. et al. (2018). *Progenitors of gravitational wave mergers: binary evolution with the stellar grid-based code COMBINE*. Monthly Notices of the RAS **481** 1908. arXiv: `1801.05433 [astro-ph.SR]` (cit. on pp. 74, 103).

Langer, N. (1989). *Standard models of Wolf-Rayet stars*. Astronomy and Astrophysics **210** 93 (cit. on pp. 79, 82, 83, 86, 100).

– (1991a). *Evolution of massive stars in the Large Magellanic Cloud : models with semiconvection.* Astronomy and Astrophysics **252** 669 (cit. on p. 28).

– (1991b). *Wolf-Rayet stars of type WN/WC and mixing processes during core helium burning of massive stars?* Astronomy and Astrophysics **248** 531 (cit. on pp. 77, 98).

– (1992). *Helium enrichment in massive early type stars.* Astronomy and Astrophysics **265** L17 (cit. on p. 49).

– (2012). *Presupernova Evolution of Massive Single and Binary Stars*. Annual Review of Astronomy and Astrophysics **50** 107. arXiv: `1206.5443 [astro-ph.SR]` (cit. on pp. 18, 21, 74).

Laplace, E. et al. (2020). *The expansion of stripped-envelope stars: Consequences for supernovae and gravitational-wave progenitors*. Astronomy and Astrophysics **637** A6. arXiv: `2003.01120 [astro-ph.SR]` (cit. on pp. 75, 98, 99).

Leloudas, G. et al. (2015). *Spectroscopy of superluminous supernova host galaxies. A preference of hydrogen-poor events for extreme emission line galaxies*. Monthly Notices of the RAS **449** 917. arXiv: `1409.8331 [astro-ph.GA]` (cit. on p. 48).

Li, W. et al. (2011). *Nearby supernova rates from the Lick Observatory Supernova Search - III. The rate-size relation, and the rates as a function of galaxy Hubble type and colour*. Monthly Notices of the RAS **412** 1473. arXiv: `1006.4613 [astro-ph.SR]` (cit. on p. 74).

Lunnan, R. et al. (2014). *Hydrogen-poor Superluminous Supernovae and Long-duration Gamma-Ray Bursts Have Similar Host Galaxies*. Astrophysical Journal **787** 138. arXiv: `1311.0026 [astro-ph.HE]` (cit. on pp. 15, 44, 48, 50).

Maeda, K. and Y. Terada (2016). *Progenitors of type Ia supernovae*. International Journal of Modern Physics D **25** 1630024. arXiv: `1609.03639 [astro-ph.SR]` (cit. on pp. 12, 13).

Maeder, A. (1987). *Evidences for a bifurcation in massive star evolution. The ON-blue stragglers.* Astronomy and Astrophysics **178** 159 (cit. on pp. 20, 49).

Maeder, A. (2009). *Physics, Formation and Evolution of Rotating Stars* (cit. on p. 18).

Marchant, P., N. Langer, P. Podsiadlowski, T. M. Tauris and T. J. Moriya (2016a). *A new route towards merging massive black holes*. Astronomy and Astrophysics **588** A50. arXiv: `1601.03718 [astro-ph.SR]` (cit. on p. 28).

Marchant, P., N. Langer, P. Podsiadlowski, T. M. Tauris, S. de Mink et al. (2017). *Ultra-luminous X-ray sources and neutron-star-black-hole mergers from very massive close binaries at low metallicity*. Astronomy and Astrophysics **604** A55. arXiv: `1705.04734 [astro-ph.HE]` (cit. on p. 49).

Marchant, P., N. Langer, P. Podsiadlowski, T. M. Tauris and T. J. Moriya (2016b). *A new route towards merging massive black holes*. Astronomy and Astrophysics **588** A50. arXiv: `1601.03718 [astro-ph.SR]` (cit. on pp. 49, 70).

Margalit, B. et al. (2018). *The GRB-SLSN connection: misaligned magnetars, weak jet emergence, and observational signatures*. Monthly Notices of the RAS **475** 2659. arXiv: `1705.01103 [astro-ph.HE]` (cit. on p. 48).

Masada, Y., T. Takiwaki and K. Kotake (2015). *Magnetohydrodynamic Turbulence Powered by Magnetorotational Instability in Nascent Protoneutron Stars*. Astrophysical Journal, Letters **798** L22. arXiv: `1411.6705 [astro-ph.HE]` (cit. on pp. 37, 67).

Masada, Y., T. Takiwaki, K. Kotake and T. Sano (2012). *Local Simulations of the Magnetorotational Instability in Core-collapse Supernovae*. Astrophysical Journal **759** 110. arXiv: `1209.2360 [astro-ph.SR]` (cit. on pp. 37, 67).

Mazzali, P. A. et al. (2016). *Spectrum formation in superluminous supernovae (Type I)*. Monthly Notices of the RAS **458** 3455. arXiv: `1603.00388 [astro-ph.HE]` (cit. on p. 48).

McClelland, L. A. S. and J. J. Eldridge (2016). *Helium stars: towards an understanding of Wolf-Rayet evolution*. Monthly Notices of the RAS **459** 1505. arXiv: `1602.06358 [astro-ph.SR]` (cit. on p. 74).

Metzger, B. D. et al. (2015). *The diversity of transients from magnetar birth in core collapse supernovae*. Monthly Notices of the RAS **454** 3311. arXiv: `1508.02712 [astro-ph.HE]` (cit. on p. 48).

Modjaz, M., L. Kewley et al. (2011). *Progenitor Diagnostics for Stripped Core-collapse Supernovae: Measured Metallicities at Explosion Sites*. Astrophysical Journal, Letters **731** L4. arXiv: `1007.0661 [astro-ph.CO]` (cit. on p. 74).

Modjaz, M., F. B. Bianco et al. (2019). *Host Galaxies of Type Ic and Broad-lined Type Ic Supernovae from the Palomar Transient Factory: Implication for Jet Production*. arXiv e-prints arXiv:1901.00872. arXiv: `1901.00872 [astro-ph.HE]` (cit. on p. 74).

Moriya, T. J., E. I. Sorokina and R. A. Chevalier (2018). *Superluminous Supernovae*. Space Science Reviews **214** 59. arXiv: `1803.01875 [astro-ph.HE]` (cit. on p. 48).

Moriya, T. J., M. Nicholl and J. Guillochon (2018). *Systematic Investigation of the Fallback Accretion-powered Model for Hydrogen-poor Superluminous Supernovae*. Astrophysical Journal **867** 113. arXiv: `1806.00090 [astro-ph.HE]` (cit. on p. 48).

Mösta, P. et al. (2015). *A large-scale dynamo and magnetoturbulence in rapidly rotating core-collapse supernovae*. Nature **528** 376. arXiv: `1512.00838 [astro-ph.HE]` (cit. on pp. 37, 67).

Müller, B. (2016). *The Status of Multi-Dimensional Core-Collapse Supernova Models*. Publications of the Astronomical Society of Australia **33** e048. arXiv: `1608.03274 [astro-ph.SR]` (cit. on p. 20).

Müller, B. et al. (2016). *A simple approach to the supernova progenitor-explosion connection*. Monthly Notices of the RAS **460** 742. arXiv: `1602.05956 [astro-ph.SR]` (cit. on pp. 20, 49, 59–62, 64–66, 69, 71, 91, 93–96).

Neugent, K. F. and P. Massey (2011). *The Wolf-Rayet Content of M33*. Astrophysical Journal **733** 123. arXiv: `1103.5549 [astro-ph.CO]` (cit. on p. 86).

Neugent, K. F., P. Massey and C. Georgy (2012). *The Wolf-Rayet Content of M31*. Astrophysical Journal **759** 11. arXiv: `1209.1177 [astro-ph.SR]` (cit. on p. 86).

Nicholl, M., J. Guillochon and E. Berger (2017). *The Magnetar Model for Type I Superluminous Supernovae. I. Bayesian Analysis of the Full Multicolor Light-curve Sample with MOSFiT*. Astrophysical Journal **850** 55. arXiv: `1706.00825 [astro-ph.HE]` (cit. on pp. 42, 48, 67–69).

Nicholl, M. and S. J. Smartt (2016). *Seeing double: the frequency and detectability of double-peaked superluminous supernova light curves*. Monthly Notices of the RAS **457** L79. arXiv: `1511.03740 [astro-ph.SR]` (cit. on p. 43).

Nugis, T. and H. J. G. L. M. Lamers (2000). *Mass-loss rates of Wolf-Rayet stars as a function of stellar parameters*. Astronomy and Astrophysics **360** 227 (cit. on pp. 77, 98).

Obergaulinger, M. and M. Á. Aloy (2020). *Magnetorotational core collapse of possible GRB progenitors - I. Explosion mechanisms*. Monthly Notices of the RAS **492** 4613. arXiv: `1909.01105 [astro-ph.HE]` (cit. on pp. 38, 59).

Obergaulinger, M., M. A. Aloy et al. (2006). *Axisymmetric simulations of magnetorotational core collapse: approximate inclusion of general relativistic effects*. Astronomy and Astrophysics **457** 209. arXiv: `astro-ph/0602187 [astro-ph]` (cit. on p. 102).

Obergaulinger, M., O. Just and M. A. Aloy (2018). *Core collapse with magnetic fields and rotation*. Journal of Physics G Nuclear Physics **45** 084001. arXiv: `1806.00393 [astro-ph.HE]` (cit. on pp. 37, 67, 102).

O'Connor, E. and C. D. Ott (2011). *Black Hole Formation in Failing Core-Collapse Supernovae*. Astrophysical Journal **730** 70. arXiv: `1010.5550 [astro-ph.HE]` (cit. on pp. 20, 49, 59, 60, 71, 91).

Ofek, E. O. et al. (2010). *Supernova PTF 09UJ: A Possible Shock Breakout from a Dense Circumstellar Wind*. Astrophysical Journal **724** 1396. arXiv: `1009.5378 [astro-ph.HE]` (cit. on p. 38).

Oppenheimer, J. R. and H. Snyder (1939). *On Continued Gravitational Contraction*. Phys. Rev. **56** (5) 455. URL: `https://link.aps.org/doi/10.1103/PhysRev.56.455` (cit. on p. 16).

Ott, C. D. et al. (2005). *One-armed Spiral Instability in a Low-T/|W| Postbounce Supernova Core*. Astrophysical Journal, Letters **625** L119. arXiv: `astro-ph/0503187 [astro-ph]` (cit. on p. 102).

Owocki, S. P. and K. G. Gayley (1997). “ThePhysics of Stellar Winds Near the Eddington Limit”. *Luminous Blue Variables: Massive Stars in Transition*. Ed. by A. Nota and H. Lamers. Vol. 120. Astronomical Society of the Pacific Conference Series 121 (cit. on p. 35).

Paczyński, B. (1998). *Are Gamma-Ray Bursts in Star-Forming Regions?* Astrophysical Journal, Letters **494** L45. arXiv: `astro-ph/9710086 [astro-ph]` (cit. on p. 101).

Palmerio, J. T. et al. (2019). *Are long gamma-ray bursts biased tracers of star formation? Clues from the host galaxies of the Swift/BAT6 complete sample of bright LGRBs. III. Stellar masses, star formation rates, and metallicities at z &gt; 1*. Astronomy and Astrophysics **623** A26. arXiv: `1901.02457 [astro-ph.HE]` (cit. on pp. 15, 22, 48).

Paxton, B., L. Bildsten et al. (2011). *Modules for Experiments in Stellar Astrophysics (MESA)*. Astrophysical Journal, Supplement **192** 3. arXiv: `1009.1622 [astro-ph.SR]` (cit. on pp. 22, 24, 27, 50, 75).

Paxton, B., M. Cantiello et al. (2013). *Modules for Experiments in Stellar Astrophysics (MESA): Planets, Oscillations, Rotation, and Massive Stars*. Astrophysical Journal, Supplement **208** 4. arXiv: `1301.0319 [astro-ph.SR]` (cit. on pp. 22, 24, 27, 50, 75).

Paxton, B., P. Marchant et al. (2015). *Modules for Experiments in Stellar Astrophysics (MESA): Binaries, Pulsations, and Explosions*. Astrophysical Journal, Supplement **220** 15. arXiv: `1506.03146 [astro-ph.SR]` (cit. on pp. 22, 24, 27, 50, 75).

Paxton, B., J. Schwab et al. (2018). *Modules for Experiments in Stellar Astrophysics (MESA): Convective Boundaries, Element Diffusion, and Massive Star Explosions*. Astrophysical Journal, Supplement **234** 34. arXiv: `1710.08424 [astro-ph.SR]` (cit. on pp. 24, 27, 50, 75).

Perley, D. A. et al. (2016). *Host-galaxy Properties of 32 Low-redshift Superluminous Supernovae from the Palomar Transient Factory*. Astrophysical Journal **830** 13. arXiv: `1604.08207 [astro-ph.HE]` (cit. on p. 48).

Perryman, M. A. C. et al. (1997). *The Hipparcos Catalogue.* Astronomy and Astrophysics **500** 501 (cit. on p. 6).

Phillips, M. M. (1993). *The Absolute Magnitudes of Type IA Supernovae*. Astrophysical Journal, Letters **413** L105 (cit. on p. 12).

Piran, T. (2004). *The physics of gamma-ray bursts*. Reviews of Modern Physics **76** 1143. arXiv: `astro-ph/0405503 [astro-ph]` (cit. on p. 15).

Podsiadlowski, P., P. C. Joss and J. J. L. Hsu (1992). *Presupernova evolution in massive interacting binaries*. Astrophysical Journal **391** 246 (cit. on p. 74).

Powell, J. and B. Müller (2020). *Three-dimensional core-collapse supernova simulations of massive and rotating progenitors*. arXiv e-prints arXiv:2002.10115. arXiv: `2002.10115 [astro-ph.HE]` (cit. on pp. 61, 102).

Prieto, J. L., K. Z. Stanek and J. F. Beacom (2008). *Characterizing Supernova Progenitors via the Metallicities of their Host Galaxies, from Poor Dwarfs to Rich Spirals*. Astrophysical Journal **673** 999. arXiv: `0707.0690` (cit. on p. 74).

Quimby, R. M. et al. (2007). *SN 2005ap: A Most Brilliant Explosion*. Astrophysical Journal, Letters **668** L99. arXiv: `0709.0302 [astro-ph]` (cit. on p. 101).

Ramírez-Agudelo, O. H. et al. (2013). *The VLT-FLAMES Tarantula Survey. XII. Rotational velocities of the single O-type stars*. Astronomy and Astrophysics **560** A29. arXiv: `1309.2929 [astro-ph.SR]` (cit. on pp. 18, 20, 50).

Raynaud, R. et al. (2020). *Magnetar formation through a convective dynamo in protoneutron stars*. arXiv e-prints arXiv:2003.06662. arXiv: `2003.06662 [astro-ph.HE]` (cit. on p. 67).

Rembiasz, T. et al. (2016). *On the maximum magnetic field amplification by the magnetorotational instability in core-collapse supernovae*. Monthly Notices of the RAS **460** 3316. arXiv: `1603.00466 [astro-ph.SR]` (cit. on pp. 38, 67).

Renzo, M. et al. (2017). *Systematic survey of the effects of wind mass loss algorithms on the evolution of single massive stars*. Astronomy and Astrophysics **603** A118. arXiv: `1703.09705 [astro-ph.SR]` (cit. on p. 64).

Ruffert, M. and H. .-.-T. Janka (1998). *Colliding neutron stars. Gravitational waves, neutrino emission, and gamma-ray bursts*. Astronomy and Astrophysics **338** 535. arXiv: `astro-ph/9804132 [astro-ph]` (cit. on p. 14).

Salpeter, E. E. (1955). *The Luminosity Function and Stellar Evolution.* Astrophysical Journal **121** 161 (cit. on pp. 13, 85, 93, 95, 96).

Sana, H., S. E. de Mink et al. (2012). *Binary Interaction Dominates the Evolution of Massive Stars*. Science **337** 444. arXiv: `1207.6397 [astro-ph.SR]` (cit. on pp. 18, 74, 93).

Sana, H. and C. J. Evans (2011). "The multiplicity of massive stars". *Active OB Stars: Structure, Evolution, Mass Loss, and Critical Limits*. Ed. by C. Neiner et al. Vol. 272. IAU Symposium 474. arXiv: `1009.4197 [astro-ph.SR]` (cit. on p. 74).

Sander, A. A. C. and J. S. Vink (2020). *On the nature of massive helium star winds and Wolf-Rayet-type mass loss*. arXiv e-prints arXiv:2009.01849. arXiv: `2009.01849 [astro-ph.SR]` (cit. on pp. 75, 76, 98).

Sanyal, D. et al. (2015). *Massive main-sequence stars evolving at the Eddington limit*. Astronomy and Astrophysics **580** A20. arXiv: `1506.02997 [astro-ph.SR]` (cit. on p. 75).

Savaglio, S., K. Glazebrook and D. Le Borgne (2009). *The Galaxy Population Hosting Gamma-Ray Bursts*. Astrophysical Journal **691** 182. arXiv: `0803.2718 [astro-ph]` (cit. on p. 15).

Schmutz, W., W. .-.-R. Hamann and U. Wessolowski (1989). *Spectral analysis of 30 Wolf-Rayet stars.* Astronomy and Astrophysics **210** 236 (cit. on p. 80).

Schootemeijer, A. et al. (2019). *Constraining mixing in massive stars in the Small Magellanic Cloud*. Astronomy and Astrophysics **625** A132. arXiv: `1903.10423 [astro-ph.SR]` (cit. on p. 75).

Schulze, S. et al. (2018). *Cosmic evolution and metal aversion in superluminous supernova host galaxies*. Monthly Notices of the RAS **473** 1258. arXiv: `1612.05978 [astro-ph.GA]` (cit. on p. 48).

Shenar, T. et al. (2020). *Why binary interaction does not necessarily dominate the formation of Wolf-Rayet stars at low metallicity*. Astronomy and Astrophysics **634** A79. arXiv: `2001.04476 [astro-ph.SR]` (cit. on pp. 18, 75, 76, 80, 83, 84, 99).

Shivvers, I. et al. (2017). *Revisiting the Lick Observatory Supernova Search Volume-limited Sample: Updated Classifications and Revised Stripped-envelope Supernova Fractions*. Publications of the ASP **129** 054201. arXiv: `1609.02922 [astro-ph.HE]` (cit. on pp. 16, 17, 74).

Smartt, S. J. (2015). *Observational Constraints on the Progenitors of Core-Collapse Supernovae: The Case for Missing High-Mass Stars*. Publications of the Astron. Soc. of Australia **32** e016. arXiv: `1504.02635 [astro-ph.SR]` (cit. on p. 61).

Smartt, S. J. et al. (2009). *The death of massive stars - I. Observational constraints on the progenitors of Type II-P supernovae*. Monthly Notices of the RAS **395** 1409. arXiv: `0809.0403 [astro-ph]` (cit. on pp. 20, 74).

Smith, N. et al. (2007). *SN 2006gy: Discovery of the Most Luminous Supernova Ever Recorded, Powered by the Death of an Extremely Massive Star like η Carinae*. Astrophysical Journal **666** 1116. arXiv: `astro-ph/0612617 [astro-ph]` (cit. on p. 101).

Sorokina, E. et al. (2016). *Type I Superluminous Supernovae as Explosions inside Non-hydrogen Circumstellar Envelopes*. Astrophysical Journal **829** 17. arXiv: `1510.00834 [astro-ph.HE]` (cit. on p. 39).

Springmann, U. (1994). *Multiple resonance line scattering and the 'momentum problem' in Wolf-Rayet star winds*. Astronomy and Astrophysics **289** 505 (cit. on p. 35).

Suijs, M. P. L. et al. (2008). *White dwarf spins from low-mass stellar evolution models*. Astronomy and Astrophysics **481** L87. arXiv: `0802.3286` (cit. on pp. 20, 33).

Sukhbold, T. and S. Adams (2019). *Missing Red Supergiants and Carbon Burning*. arXiv e-prints. arXiv: `1905.00474 [astro-ph.HE]` (cit. on p. 49).

Sukhbold, T. and S. E. Woosley (2014). *The Compactness of Presupernova Stellar Cores*. Astrophysical Journal **783** 10. arXiv: `1311.6546 [astro-ph.SR]` (cit. on pp. 20, 49, 59, 64, 79, 91).

Sukhbold, T., S. E. Woosley and A. Heger (2018). *A High-resolution Study of Presupernova Core Structure*. Astrophysical Journal **860** 93. arXiv: `1710.03243 [astro-ph.HE]` (cit. on pp. 20, 49, 59, 62, 64).

Summa, A. et al. (2018). *Rotation-supported Neutrino-driven Supernova Explosions in Three Dimensions and the Critical Luminosity Condition*. Astrophysical Journal **852** 28. arXiv: `1708.04154 [astro-ph.HE]` (cit. on pp. 59, 71, 91).

Svirski, G. and E. Nakar (2014). *SN 2008D: A Wolf-Rayet Explosion Through a Thick Wind*. Astrophysical Journall **788** L14. arXiv: `1403.3400 [astro-ph.HE]` (cit. on p. 38).

Szécsi, D. et al. (2015). *Low-metallicity massive single stars with rotation. Evolutionary models applicable to I Zwicky 18*. Astronomy and Astrophysics **581** A15. arXiv: `1506.09132 [astro-ph.SR]` (cit. on p. 50).

Takiwaki, T., K. Kotake and Y. Suwa (2016). *Three-dimensional simulations of rapidly rotating core-collapse supernovae: finding a neutrino-powered explosion aided by non-axisymmetric flows*. Monthly Notices of the RAS **461** L112. arXiv: `1602.06759 [astro-ph.HE]` (cit. on pp. 59, 102).

Tauris, T. M., M. Kramer et al. (2017). *Formation of Double Neutron Star Systems*. Astrophysical Journal **846** 170. arXiv: `1706.09438 [astro-ph.HE]` (cit. on p. 19).

Tauris, T. M., N. Langer, T. J. Moriya et al. (2013). *Ultra-stripped Type Ic Supernovae from Close Binary Evolution*. Astrophysical Journal, Letters **778** L23. arXiv: `1310.6356 [astro-ph.SR]` (cit. on p. 87).

Tauris, T. M., N. Langer and P. Podsiadlowski (2015). *Ultra-stripped supernovae: progenitors and fate*. Monthly Notices of the RAS **451** 2123. arXiv: `1505.00270 [astro-ph.SR]` (cit. on p. 74).

Thompson, C. and R. C. Duncan (1993). *Neutron Star Dynamos and the Origins of Pulsar Magnetism*. Astrophysical Journal **408** 194 (cit. on p. 67).

Tramper, F., H. Sana and A. de Koter (2016). *A New Prescription for the Mass-loss Rates of WC and WO Stars*. Astrophysical Journal **833** 133. arXiv: `1610.03800 [astro-ph.SR]` (cit. on pp. 76, 98).

Ugliano, M. et al. (2012). *Progenitor-explosion Connection and Remnant Birth Masses for Neutrino-driven Supernovae of Iron-core Progenitors*. Astrophysical Journal **757** 69. arXiv: `1205.3657 [astro-ph.SR]` (cit. on pp. 20, 49, 59).

Usov, V. V. (1992). *Millisecond pulsars with extremely strong magnetic fields as a cosmological source of gamma-ray bursts*. Nature **357** 472 (cit. on p. 21).

van den Bergh, S., W. Li and A. V. Filippenko (2005). *Classifications of the Host Galaxies of Supernovae, Set III*. Publications of the ASP **117** 773. eprint: `astro-ph/0504668` (cit. on p. 74).

Van Dyk, S. D. et al. (2018). *SN 2017ein and the Possible First Identification of a Type Ic Supernova Progenitor*. Astrophysical Journal **860** 90. arXiv: `1803.01050 [astro-ph.SR]` (cit. on p. 15).

van Marle, A. J. et al. (2008). *The circumstellar medium around a rapidly rotating, chemically homogeneously evolving, possible gamma-ray burst progenitor*. Astronomy and Astrophysics **478** 769. arXiv: `0711.4807 [astro-ph]` (cit. on pp. 35, 68).

Vedrenne, G. and J.-L. Atteia (2009). *Gamma-Ray Bursts* (cit. on p. 48).

Villar, V. A., M. Nicholl and E. Berger (2018). *Superluminous Supernovae in LSST: Rates, Detection Metrics, and Light-curve Modeling*. Astrophysical Journal **869** 166. arXiv: `1809.07343 [astro-ph.HE]` (cit. on pp. 42, 48, 67–69).

Vink, J. S. (2017). *Winds from stripped low-mass helium stars and Wolf-Rayet stars*. Astronomy and Astrophysics **607** L8. arXiv: `1710.02010 [astro-ph.SR]` (cit. on pp. 18, 75, 76, 82, 98).

Vink, J. S., A. de Koter and H. J. G. L. M. Lamers (2001). *Mass-loss predictions for O and B stars as a function of metallicity*. Astronomy and Astrophysics **369** 574. arXiv: `astro-ph/0101509 [astro-ph]` (cit. on p. 50).

von Zeipel, H. (1924). *The radiative equilibrium of a rotating system of gaseous masses*. Monthly Notices of the RAS **84** 665 (cit. on p. 18).

Waxman, E. and B. Katz (2017). "Shock Breakout Theory". *Handbook of Supernovae*. Ed. by A. W. Alsabti and P. Murdin 967 (cit. on p. 38).

White, G. L. and D. F. Malin (1987). *Possible binary star progenitor for SN1987A*. Nature **327** 36 (cit. on p. 15).

Woolley, R. et al. (1970). *Catalogue of stars within twenty-five parsecs of the Sun*. Royal Observatory Annals **5** ill (cit. on p. 6).

Woosley, S. E. (1993). *Gamma-ray bursts from stellar mass accretion disks around black holes*. Astrophysical Journal **405** 273 (cit. on pp. 21, 48, 49).

– (2010). *Bright Supernovae from Magnetar Birth*. Astrophysical Journal, Letters **719** L204. arXiv: `0911.0698 [astro-ph.HE]` (cit. on pp. 42, 48, 49).

– (2017). *Pulsational Pair-instability Supernovae*. Astrophysical Journal **836** 244. arXiv: `1608.08939 [astro-ph.HE]` (cit. on pp. 20, 38, 39, 41, 44, 59).

– (2019). *The Evolution of Massive Helium Stars, Including Mass Loss*. Astrophysical Journal **878** 49. arXiv: `1901.00215 [astro-ph.SR]` (cit. on pp. 26, 74, 77, 85, 87, 91, 99).

Woosley, S. E. and J. S. Bloom (2006). *The Supernova Gamma-Ray Burst Connection*. Annual Review of Astronomy and Astrophysics **44** 507. arXiv: `astro-ph/0609142 [astro-ph]` (cit. on p. 15).

Woosley, S. E. and A. Heger (2006). *The Progenitor Stars of Gamma-Ray Bursts*. Astrophysical Journal **637** 914. arXiv: `astro-ph/0508175 [astro-ph]` (cit. on pp. 44, 49).

Woosley, S. E., N. Langer and T. A. Weaver (1995). *The Presupernova Evolution and Explosion of Helium Stars That Experience Mass Loss*. Astrophysical Journal **448** 315 (cit. on p. 74).

Woosley, S. E., T. Sukhbold and H. .-.-T. Janka (2020). *The Birth Function for Black Holes and Neutron Stars in Close Binaries*. Astrophysical Journal **896** 56. arXiv: `2001.10492 [astro-ph.HE]` (cit. on p. 20).

Worley, A., P. G. Krastev and B.-A. Li (2008). *Nuclear Constraints on the Moments of Inertia of Neutron Stars*. Astrophysical Journal **685** 390 (cit. on pp. 65, 67, 69).

Yan, L. et al. (2017). *Far-ultraviolet to Near-infrared Spectroscopy of a Nearby Hydrogen-poor Superluminous Supernova Gaia16apd*. Astrophysical Journal **840** 57. arXiv: `1611.02782 [astro-ph.SR]` (cit. on p. 44).

Yoon, S.-C., L. Dessart and A. Clocchiatti (2017). *Type Ib and IIb Supernova Progenitors in Interacting Binary Systems*. Astrophysical Journal **840** 10. arXiv: `1701.02089 [astro-ph.SR]` (cit. on p. 77).

Yoon, S.-C. and N. Langer (2005). *Evolution of rapidly rotating metal-poor massive stars towards gamma-ray bursts*. Astronomy and Astrophysics **443** 643. arXiv: `astro-ph/0508242 [astro-ph]` (cit. on pp. 22, 44, 49).

Yoon, S.-C., N. Langer and C. Norman (2006a). *Single star progenitors of long gamma-ray bursts. I. Model grids and redshift dependent GRB rate*. Astronomy and Astrophysics **460** 199. eprint: `astro-ph/0606637` (cit. on p. 44).

– (2006b). *Single star progenitors of long gamma-ray bursts. I. Model grids and redshift dependent GRB rate*. Astronomy and Astrophysics **460** 199. arXiv: `astro-ph/0606637 [astro-ph]` (cit. on pp. 44, 49).

Yoon, S.-C., S. E. Woosley and N. Langer (2010). *Type Ib/c Supernovae in Binary Systems. I. Evolution and Properties of the Progenitor Stars*. Astrophysical Journal **725** 940. arXiv: `1004.0843 [astro-ph.SR]` (cit. on p. 74).

Yoon, S.-C. (2017). *Towards a better understanding of the evolution of Wolf-Rayet stars and Type Ib/Ic supernova progenitors*. Monthly Notices of the RAS **470** 3970. arXiv: `1706.04716 [astro-ph.SR]` (cit. on pp. 25, 26, 74, 76, 83, 84, 87, 98–100).

Yoon, S.-C., W. Chun et al. (2019). *Type Ib/Ic Supernovae: Effect of Nickel Mixing on the Early-time Color Evolution and Implications for the Progenitors*. Astrophysical Journal **872** 174. arXiv: `1810.03108 [astro-ph.HE]` (cit. on pp. 48, 52).

Yoshida, T. et al. (2019). *One-, Two-, and Three-dimensional Simulations of Oxygen-shell Burning Just before the Core Collapse of Massive Stars*. Astrophysical Journal **881** 16. arXiv: `1903.07811 [astro-ph.SR]` (cit. on p. 102).

List of Figures

1.1 Detail of the mural *Historical Representation of Culture* created by Juan O'Gorman, located in the southern façade of the Central Library of the National Autonomous University of Mexico. It represents the Ptolemaic model of the Solar system, with the Earth at the center (left), and the Copernican model, with the Sun at the center. Figures around the two represent the locations of constellations and stars in the Celestial Sphere. Adapted from a photograph by Thomas Guignard. Source: Flickr. 2

1.2 Photograph and recreation of the proposed oldest supernova recorded, a craving on a cave wall in Kashmir, India. Figure adapted from Joglekar et al. (2011). 3

1.3 A Hertzsprung-Russell diagram showing the inferred luminosities (left y-axis, in units of a Solar luminosity $L_\odot$) and equivalent absolute magnitudes (right y-axis), as a function of color index B-V (bottom x-axis) and its equivalent effective temperature and spectral class (top y-axis) of 22,000 nearby stars from the *Hipparcos Catalogue* (Perryman et al., 1997), and 1,000 faint stars from the *Gliese Catalogue of Nearby Stars* (Gliese, 1957; Woolley et al., 1970). Figure adapted from Wikipedia. 6

1.4 A schematic representation of the pp chain (left) and the CNO cycle (right); the nuclear fusion processes that most commonly take place inside of stars, and turn hydrogen into helium. Adapted from Wikipedia. 8

1.5 A schematic representation of the layers of different composition that a massive star will have at the end of its life. Figure adapted from Chaisson et al. (2005). 10

1.6 Example optical spectra near the time of maximum brightness of typical Type Ia (a), Type II (b), Type Ic (c) and Type Ib (d) supernovae. The different features in the spectra are caused by the presence of different elements near the photosphere. The elements and ionization states responsible for some features are highlighted. The variable t in this figure represents the time after B-band maximum, and the variable τ represents time after core collapse. Figure adapted from Filippenko (1997). 12

1.7 Schematic blue magnitude light curves representative of typical supernovae of different types. including a supernova Type II-L, a Type II-P, a Type Ia, a Type Ib, and the peculiar case of SN 1987A. Figure adapted from Filippenko (1997). 13

1.8 Examples of absolute magnitude light curves of superluminous supernovae of Type I (hydrogen poor, pink), Type II (hydrogen rich, red) and Type R (hydrogen poor, likely powered by ^{56}Ni, dark blue). For compatison, typical light curves of other supernova types are shown. Adapted from Gal-Yam (2012). 14

1.9 Pie chart representing the relative fractions of core-collapse supernovae of different types in a volume limited sample of supernovae with well determined type. Figure courtesy of H. F. Stevance, using data from from Shivvers et al. (2017). 17

1.10 A schematic representation of an example evolutionary channel that a massive binary might go through to form a neutron star merger. Represents the evolution of a massive binary system co-evolving from the ZAMS. The system experiences an episode of mass transfer through Roche-lobe overflow (RLO), that strips the donor star from its hydrogen rich envelope. It subsequently evolves as a helium star and explodes as a supernova. The neutron star (NS) remains bound to its companion, and the system becomes a high mass X-ray binary (HMXB). Later, a common envelope (CE) event strips the secondary of its hydrogen-rich envelope, and becomes a helium star. The system experiences Case BB Roche-lobe overflow (after core helium depletion). After the secondary explosion, the system evolves as a neutron star binary, leading to a double neutron star (DNS) merger, creating a stellar mass black hole (BH). Figure adapted from Tauris et al. (2017). . . . 19

1.11 Schematic temperature-density diagram, showing approximate evolutionary tracks of stars of different masses (blue lines). Red shaded regions indicate the parameter space where different equations of state lead to instabilities that result in the formation of either a transient, the formation of a black hole, or the formation of a white dwarf. Fe$\rightleftharpoons \alpha$ indicates the region where iron photodisintegrates into alpha particles, leading to core-collapse supernovae (CCSN) or black hole (BH) formation. $2 \rightleftharpoons e^{+}e^{-}$ indicates the region where pair creation is favored to occur, leading to pair instability supernovae (PISN). Tracks in the e^{-} capture limit end up as electron capture supernovae (ECSN, not further discussed). The yellow region highlights the parameter space for low mass stars that become degenerate, and form white dwarfs (WDs). Adapted from Langer (2012). . 21

1.12 Stellar radius as a function of central temperature of the stellar evolutionary sequences of models of different initial mass in Series A (solid lines) and Series B (dashed lines). The temperature ranges where H (light orange), He (dark orange) and heavy element burning (red) occur are highlighted. This figure shows that massive models from Series A, and Series B models, continuously contract during their evolution. Lower mass Series A models develop hydrogen and helium burning shells, and expand during their late evolution. Adapted from Aguilera Dena (2017). 23

2.1 Mass fractions of the major chemical elements as function of mass in stellar models from two evolutionary sequences of Series A at three different times, during core He burning, at He core depletion, and at C core depletion. Figure adapted from Aguilera-Dena et al. (2018). 31

2.2 As Figure 2.1, but for the corresponding models from the B Series. Figure adapted from Aguilera-Dena et al. (2018). 32

2.3 Integrated angular momentum divided by ($m^{5/3}$ as a function of mass coordinate m, plotted for several models of Series A (top) and Series B (bottom) during the ZAMS (purple), during core helium burning (blue), at core helium depletion (light blue), at the onset of carbon burning (green), at core carbon depletion (orange), and at core oxygen depletion (red). Black lines are contours of constant angular momentum. Figure adapted from Aguilera-Dena et al. (2018). 33

2.4 Mass average of the specific angular momentum of the innermost region of our Series B models as a function of central temperature. Solid lines show the average over the innermost 1.5 $M_\odot$ for models with initial mass below 20 $M_\odot$, representative of the region of the star that is likely to end up as a neutron star. For models with initial mass larger than 20 $M_\odot$, we show the average over the innermost 5 $M_\odot$, representative of the region that is likely to form a black hole, are shown in solid lines. In both cases, the corresponding average over the alternate representative mass of a potential remnant is shown in transparent lines of the same color. Figure adapted from Aguilera-Dena et al. (2018). 34

2.5 Mass loss rates of Series A models (top) and Series B models (bottom) as a function of central temperature. Highlighted areas show the temperature regimes where hydrogen burning (light orange), helium burning (dark orange) and heavy element burning (red) take place. Figure adapted from Aguilera-Dena et al. (2018). 36

2.6 Time integrated mass loss rate with the end of core helium burning as zero point in time, as function of time, for six models of our Series B (bottom). Dots indicate where the mass loss rate becomes 10 times higher than that allowed by the momentum limit. Figure adapted from Aguilera-Dena et al. (2018). 37

2.7 Polar and radial magnetic fields (left y-axis) and rotational frequency (right y-axis) of the final models of 3 different evolutionary sequences from Series B. Figure adapted from Aguilera-Dena et al. (2018). 40

2.8 Average angular momentum at core O depletion of the first 1.5 $M_\odot$, for models with mass $M< 20$ $M_\odot$, and first 5 $M_\odot$ for the rest (left axis, blue triangles); and the ratio between shell and ejecta masses for the same remnant masses (right axis, red pentagons), as a function of initial mass for Series B models. The values for converse masses are added in lower saturation for comparison. The ratio between shell and ejecta mass for models that undergo pulsational pair instability is also calculated (red stars), with ejected shell masses according to S. E. Woosley (2017). 41

2.9 Ejecta masses and magnetar spin periods inferred for the sample in Blanchard et al. (2020) (black points), compared to the values inferred for the models presented in Aguilera-Dena et al. (2018) (yellow stars). Figure adapted from Blanchard et al. (2020). 42

2.10 Inferred luminosity as a function of time, product of the interaction between a spherical SN ejecta and a spherical CSM. The kinetic energy of the SN ejecta is taken as 4×10^{51} erg. Ejecta mass corresponds to the final mass of the Series B models of Aguilera-Dena et al. (2018) with initial masses of 5 (blue), 8 (brown) 13 (red) and 39 $M_\odot$ (orange). The CSM is assumed to be a wind with velocity of 0.2 km s^{-1}, and have a density continuous density distribution given by the mass loss history of each model. Luminosity at each time is calculated using Equation 2.2. The light curve of SN 2015bn (Nicholl et al., 2016) is displayed alongside for comparison. Figure adapted from Aguilera-Dena et al. (2018). 43

3.1 Panels show a comparison of different key properties of core collapse models in this study (represented in orange), with the final models from ALMS18 (represented in blue). Panels show the final masses (top), final helium masses in the envelope (excluding the helium formed in the core due to photodisintegration of iron, middle), and final radii (bottom), as a function of initial mass. 53

3.2 Mass lost between core helium depletion and core collapse ($\Delta M_{He \rightarrow final}$), representative of the CSM mass immediately close to the progenitors at core collapse, as a function of initial mass. Comparison between core collapse models from this study (orange) and the final models from ALMS18 (blue). 54

3.3 Kippenhahn diagram following the efficiency of rotational mixing, and the structure of convective and overshooting regions of the 9 $M_\odot$ evolutionary calculation from ZAMS to core collapse, as a function of the time remaining before core collapse. Color denotes the diffusion coefficient due to rotational mixing (dominated by Eddington-Sweet circulation). Regions hatched with diagonals denote convective regions, whereas the region hatched with perpendicular lines, above the hydrogen burning core, denotes an overshooting region. 56

3.4 Compactness parameter measured at 2.5 $M_\odot$ of the core collapse models in this study, as a function of their initial mass. The dotted line at $\xi_{2.5} = 0.45$ separates models that might explode (below the line) or implode (above the line) according to O'Connor et al. (2011), orange points indicate models that are predicted to explode according to the explodability the B. Müller et al. (2016) and Ertl et al. (2016) tests, blue points are models that are predicted to explode according the B. Müller et al. (2016) test, but not by the Ertl et al. (2016) test, the green point is a model that is predicted to explode according to the Ertl et al. (2016) test but not the B. Müller et al. (2016) test, and grey points are models that would not successfully explode according to both tests. 60

3.5 Iron core mass of the core collapse models in this study, as a function of initial mass. . 62

3.6 Compactness parameter measured at 2.5 $M_\odot$ of the core collapse models in this study, as a function of iron core mass at the moment of core collapse. Crosses indicate models where core carbon burning occurred radiatively, whereas points indicate convective core carbon burning. 63

3.7 Kippenhahn diagrams following the energy generation/loss rate, and the structure of convective regions as a funciton of time remaining until core collapse, from core helium burning until minutes before core collapse. Represented are the evolutionary sequences with initial masses of 7 (left), 8 (middle) and 9 $M_\odot$ (right). Color denotes the intensity of energy generation rate (red), and the energy loss rate (blue). Regions hatched with diagonals denote convective regions. 63

3.8 NS gravitational mass, explosion energy and ^{56}Ni mass resulting from SN explosions produced from our core collapse models, as predicted by the B. Müller et al. (2016) model, as a function of initial mass. 66

3.9 Azimuthal component of the magnetic field, averaged over the innermost 1.5$M_\odot$ of our core collapse models (blue), and assuming this region contracts homologously to a radius of 15 km, and that magnetic flux is conserved during the contraction (orange), as a funciton of initial mass. Compared to the inferred values for the SLSN samples analyzed by Nicholl et al. (2017), Villar et al. (2018) and Blanchard et al. (2018) and and Blanchard et al. (2019) in the context of the magnetar model (histogram on the right). 68

3.10 Pentagons represent the ejecta masses produced by SN explosions produced from the our core collapse models –as predicted by the B. Müller et al. (2016) model– as a function of the spin periods calculated for their remnants, and colored by their initial mass. Spin periods are calculated assuming homologous contraction of the collapsing core to a radius of 15 km, conservation of angular momentum, and NS moment of inertia as prescribed by Worley et al. (2008). Light blue points correspond to the inferred values from observations obtained for observed SLSNe obtained by Nicholl et al. (2017), Villar et al. (2018) and Blanchard et al. (2018) and and Blanchard et al. (2019). 69

3.11 The left y-axis shows the average specific angular momentum in the innermost 1.5 $M_\odot$ (blue) and 5 $M_\odot$ (orange) of core collapse models, chosen as mass coordinates representative of NS and collapsar forming models, respectively.On the right y-axis, the fraction of the kinetic energy that can be converted into radiation by CSM interaction, f_M, is shown. This is calculated assuming that the explosions leave behind a 1.5 $M_\odot$ remnant (red) and a 5 $M_\odot$ remnant (orange), and that the ejected mass interacts with the CSM mass given by $\Delta M_{\mathrm{He}\rightarrow\mathrm{final}}$. Hexagons in the plot correspond to core collapse models that explode as a SLSN according to the Marchant et al. (2016b) model, triangles correspond to models that are expected to form a BH. All quantities shown as a function of initial mass. 70

4.1 Kippenhahn diagrams following the energy generation/loss rate and the structure of convective regions as a function of time remaining until core collapse, from core helium burning until a few days before core collapse. Represented are the evolutionary calculations with initial helium star masses of 8 (left) and 20 (right) $M_\odot$, with metallicities of Z=0.01 (top) and Z=0.04 (bottom). Color denotes the intensity of the energy generation (red) and loss (blue) rate. Hatched regions denote convective regions. 78

4.2 Total life time of helium stars of different initial masses, from the start of helium core burning to core-collapse, as a function of initial helium star mass, for helium stars of different metallicities. 80

4.3 Fraction of the total life time of our helium star models spent as WN stars (helium/nitrogen rich envelope, top), and ratio between WC (carbon/oxygen rich envelope) and WN life times (bottom), as a function of initial mass, for helium stars of different metallicities. . 81

4.4 Evolution of surface luminosity as a function of age, between the He-ZAMS and core carbon depletion, for helium star models with different initial masses, colored by surface helium abundance. Each panel represents a set of models with different metallicity, going from 0.01 (top left) to 0.04 (bottom). Arrows on the right hand side represent the luminosities of observed WC stars in the LMC, in the case of Z=0.01, and the known Galactic WC stars in the case of Z=0.02. 82

4.5 Optical depth at the base of a WR wind, as a function of metallicity and luminosity, obtained from Equation 4.6. It is assumed that the wind depends on metallicity and luminosity as in Equation 4.1. The lines represent the solutions for $\tau = 1$ and $\tau = 2$, and the fit to observations obtained with Equation 7. Star shaped symbols represent the threshold luminosity for observed WR stars in the SMC, LMC and in the Galaxy, as inferred by Shenar et al. (2020). 84

4.6 Optical depth at the base of a WC/WO wind, as a function of metallicity and luminosity, obtained from Equation 4.6. It is assumed that the wind depends on metallicity and luminosity as in Equation 4.2. The lines represent the solutions for $\tau = 1$ and $\tau = 3$. The red line represents the minimum luminosity of WC/WO stars found in our models. Star shaped symbols represent the minimum luminosity of observed WC/WO stars in the SMC, LMC and in the Galaxy. Pentagons represent the minimum luminosity of a WC attained in our models. 85
4.7 Average number ratio of WC to WN stars as a function of metallicity, as estimated by Equation 4.9. This quantity strongly depends on the minimum mass for a star to be observable as a WR. Different lines in this figure correspond to assuming that the minimum mass corresponds to setting the WR wind optical depth in Equation 4.6 to $\tau = 1$ (purple), $\tau = 2$ (green) and the fit to observations in Equation 4.7 (blue). 87
4.8 Final mass (at core-collapse) as a function of initial mass for helium stars of different metallicities. 88
4.9 Final mass of helium in the envelope, as calculated by Equation 4.10, as a function of initial mass for helium stars of different metallicities. 89
4.10 Surface mass fractions of ^{4}He, ^{12}C, ^{14}N and ^{16}O of helium stars at core-collapse, as a function of initial mass, for different metallicities. 90
4.11 Compactness parameter as a function of initial mass (top) and final mass (bottom) for helium stars of different metallicities. 92
4.12 Summary of the key parameters obtained from the core collapse models of helium stars through the explosion model of B. Müller et al. (2016), as a function of initial mass (left) and final mass. We include the NS gravitational mass for core collapse models that successfully explode, the BH mass for models that directly collapse (which corresponds to their final mass), the ejecta mass and explosion energy. Dashed lines indicate the division between Type Ib and Type Ic progenitors. 94
4.13 Cumulative distribution functions of NS gravitational masses, BH masses, explosion energies, ejecta masses for both Type Ib and Ic SNe, kick velocities and nickel masses that result from analyzing our core-collapse models with the B. Müller et al. (2016) model, using the standard parameters, weighted by the IMF from Salpeter (1955). Different color lines represent different metallicities. 95
4.14 Mean values and standard deviation of NS gravitational masses, BH masses, explosion energies, ejecta masses for both Type Ib and Ic SNe, kick velocities and nickel masses at different metallicities, that result from analyzing our core-collapse models with the B. Müller et al. (2016) model, using the standard parameters, weighted by the IMF from Salpeter (1955). 96
4.15 Expected number ratio of Type Ib and Type Ic SNe as a function of metallicity, as estimated by Equation 4.11. 97

List of Tables

2.1 Initial and final parameters of the evolutionary sequences in Series B. Table adapted from Aguilera-Dena et al. (2018). 29
2.2 Initial and final parameters of the evolutionary sequences in Series A. Table adapted from Aguilera-Dena et al. (2018). 30

3.1 Initial mass, final mass, mass lost between ZAMS and the onset of core helium burning, mass lost between the end of helium burning and core collapse of evolutionary sequences in this work, and key parameters of their respective core collapse models. The compactness parameter $\xi_{2.5}$, and the values of M_4 and μ_4 as defined by Equations 3.1, 3.2 and 3.3 respectively. 57
3.2 Explosion parameters inferred from core collapse models in this work analyzed with the B. Müller et al. (2016) model, and rotational energy of the resulting NS, total rotational and absolute value of their total energies (sum of gravitational, internal, kinetic and rotational energies) at core collapse. 64

Acknowledgements

One of greatest breakthroughs in physics and astronomy, perhaps even the greates of all times, was the work that Isaac Newton put forth in his pivotal text, the *PhilosophiæNaturalis Principia Mathematica*. In this work, he explained the motion of celestial bodies according to a few, simple rules. And yet, he humbly (almost too humbly, slightly out of character for a narcissist like Newton) wrote in a letter to his contemporary Robert Hooke "If I have seen further it is by standing on the shoulders of Giants", referring to the work of others in helping him with his own discoveries. In a much (much much!) more modest way, the work in this thesis also was possible because I could stand in the shoulders of giants, some of which I've had the immense pleasure to meet and collaborate with in person, and who deserve mentioning here, in the next few lines.

Most notably, of course, is my supervisor Norbert Langer. He always had an open door (metaphorically during the 2020 COVID-19 pandemic, of course) and a listening ear for me, and beyond all his scientific wisdom, he also supported me personally and made this work become the best that it possibly could. Countless others have lent me a hand to make this work see the light of day, but a few others deserve a special acknowledgement. Particularly, the wisdom of John Antoniadis, Takashi Moriya, Luc Dessart, Abel Schootemeijer, Thomas Tauris, Götz Gräfener, Eva Laplace and Nathan Grin have been pivotal in the making of this work. And that's just the people I've worked with during my thesis, but many others helped me get here in the first place. In particular, I'd like to thank Fabio De Colle and Enrico Ramirez-Ruiz for mentoring me when I was even more unexperienced, and for giving me the first breath of astronomy I ever had.

Beyond the scientific content poured down in this text, I must also give many thanks to those who have contributed to my survival and the retention of the little mental health I have held onto the last few years. Family, friends and those who have become like family have kept me going and this would have been impossible without their support, friendship and shenanigans. This first bit will be in Spanish: Quiero agradecer en especial a mi mamá y hermanas por apoyarme siempre montones con palabras bellas, consejos sabios, y amor incondicional. Es mútuo, obvi, y no podría haber logrado nada de nada sin ustedes! Desde pequeño, las tres me han hecho ver el mundo de una manera especial (cada una de una manera diferente, que resultó ser una combinación genial!), y todo lo que he hecho es gracias a sus enseñanzas. Gracias también a mis dos cuñados por ser bellos con mis hermanas y sobrinos, y también a los dos por enseñarme cosas geniales y echarme porras con mis ideas locas. Gracias a mi archi Paola, y a mis compitas preferidos Angel y Alejandro también por sabiduría y momentos memorables. And back to English: I also want to thank my friends for keeping me relatively sane through this last years. Paola, Malte, Nathan, Abel, Kostas, Eftychia, Eva, Angel, Alejandro, Toma, Ana, Joscha, Gina, Antje, Yannik, Ema, Liza, Chio, Cosima, Ivana, Maude, Diana, Gosia, Rusu, Catalin, Rahul, and many other fantastic individuals I've been lucky to meet during my stay in Germany: You have made me come to this point in one piece, and this period of my life would have a void without your presence.

Thanks as well to past and present members of the Bonn Stellar Group for amazing discussions, great fun, and a fantastic work environment. Special thanks to the people that I've closely collaborated with, and have taught me the most. Nathan, Abel, Götz, Koh, John, Daniel, David (Ohse), Katharina, Carlo, Elvijs, Ben, Johnathan, Koushik: thanks a billion times for the great sciency discussions, fun work environment. Thanks to the subset of the Stellar Group that made up the old lunch crew for the ever enriching conversation.

Also, my past and present roomies deserve a shout out. Thanks to Anni (and Berni, of course), Malte, Eri and Niklas for making up the best home a homie could have found in Bonn. Wouldn't have been the same without you!

List of Publications

First author papers, refereed

I **Aguilera-Dena, David R.**, Langer, Norbert, Moriya, Takashi J. & Schootemeijer, Abel — *2018, ApJ, 858, 115A* — RELATED PROGENITOR MODELS FOR LONG-DURATION GAMMA-RAY BURSTS AND TYPE IC SUPERLUMINOUS SUPERNOVAE

II **Aguilera-Dena, David R.**, Langer, Norbert, Antoniadis, John & Müller, Bernhard — *2020, ApJ, 901, 114A* — PREEXPLOSION CORE PROPERTIES OF SUPERLUMINOUS SUPERNOVA AND LONG GAMMA-RAY BURST PROGENITORS

Second-or-later author papers, refereed

i De Colle, Fabio, Kumar, Pawan & **Aguilera-Dena, David R.** — *2018, ApJ, 863, 32D* — RADIO EMISSION FROM THE COCOON OF A GRB JET: IMPLICATIONS FOR RELATIVISTIC SUPERNOVAE AND OFF-AXIS GRB EMISSION

ii Misra, Devina, Fragos, Tassos, Tauris, Thomas, Zapartas, Emmanouil & **Aguilera-Dena, David R.** — *Accepted for publication in Astronomy & Astrophysics* — THE ORIGIN OF PULSATING ULTRA-LUMINOUS X-RAY SOURCES: INTERMEDIATE-MASS X-RAY BINARIES CONTAINING NEUTRON STAR ACCRETORS

iii Dessart, Luc, Yoon, Sung-Chul, **Aguilera-Dena, David R.** & Langer, Norbert — *Accepted for publication in Astronomy & Astrophysics* — SUPERNOVAE IB AND IC FROM THE EXPLOSION OF HELIUM STARS

Curriculum Vitae

Personal Details

Name	David Ramon Aguilera Dena
Date of Birth	14-01-1991
Email	davidrad@astro.uni-bonn.de

Education

2009–2015	BSc in Physics, Universidad Nacional Autónoma de México, Mexico City, Mexico.
2015–2017	MSc in Astronomy & Astrophysics, Rheinische Friedrich-Wilhelms-Universität, Bonn, Germany.
2017–2020	PhD in Astrophysics, Rheinische Friedrich-Wilhelms-Universität, Bonn, Germany.

Professional Experience

2014-2015	Teaching assistant for various Physics and Mathematics undergraduate university courses. Universidad Nacional Autónoma de México, Mexico City, Mexico.
2016-2020	Teaching assistant for various Astrophysics graduate university courses. Rheinische Friedrich-Wilhelms-Universität, Bonn, Germany.
2018	Teaching assistant at the “Simulating Stars Summer School”, University of Chinese Academy of Sciences, China.
2017-2020	Doctoral work at the University of Bonn, Germany.

Languages

Spanish	Native speaker
English	Fluent
French	Intermediate
German	Basic